Development of analogous piezoelectric networks for the vibration damping of complex structures

Robin Darleux

HESAM UNIVERSITÉ

le cnam

ÉCOLE DOCTORALE Sciences des Métiers de l'Ingénieur

Laboratoire de Mécanique des Structures et des Systèmes Couplés

THÈSE

présentée par : **Robin DARLEUX**
soutenue le : **19 juin 2020**

pour obtenir le grade de : **Docteur d'HESAM Université**

préparée au : **Conservatoire national des arts et métiers**

Discipline : **Mécanique, génie mécanique, génie civil**

Spécialité : **Mécanique**

Development of analogous piezoelectric networks for the vibration damping of complex structures

THÈSE dirigée par :
M. Jean-François DEÜ Professeur des Universités, Cnam Paris

et co-encadrée par :
M. Boris LOSSOUARN Maître de Conférences, Cnam Paris

Jury

M. Gaëtan KERSCHEN	Full Professor, Université de Liège	Président
M. Morvan OUISSE	Professeur des Universités, ENSMM Besançon	Rapporteur
M. Dejan VASIC	Maître de Conférences HDR, Université de Cergy-Pontoise	Rapporteur
Mme Marta BERARDENGO	Associate Professor, Università degli Studi di Genova	Examinateur
M. Francesco DELL'ISOLA	Full Professor, Università di Roma La Sapienza	Examinateur
M. Jean-François DEÜ	Professeur des Universités, Cnam Paris	Examinateur
M. Mickaël LALLART	Professeur des Universités, INSA Lyon	Examinateur
M. Boris LOSSOUARN	Maître de Conférences, Cnam Paris	Examinateur

THÈSE

Remerciements

Cette thèse de doctorat a été menée au Laboratoire de Mécanique des Structures et des Systèmes Couplés du Conservatoire national des arts et métiers de Paris, dans le cadre d'un Contrat Doctoral Spécifique Normalien (CDSN).

S'il y a une chose que j'ai retenue des présentations que j'ai données et des rapports que j'ai rédigés lors de mes années d'études, c'est qu'une information redondante doit être présentée de façon concise. À défaut d'un manuscrit synthétique, essayons de l'être dans ces remerciements...

Merci à...	**Raisons**
Jean-François Deü	De m'avoir proposé ce sujet, et pour la confiance et la gentillesse dont tu as toujours fait preuve à mon égard.
Boris Lossouarn	De m'avoir formé au monde de la recherche, d'avoir toujours été à l'écoute, d'avoir systématiquement pris le temps de répondre à mes questions, d'avoir supporté mes égarements expérimentaux, d'avoir toléré mes approximations scientifiques, de m'avoir inspiré par ta ténacité et ta passion durant ces trois années. Merci pour ta patience et pour ton amitié.
Morvan Ouisse Dejan Vasic	D'avoir accepté la lourde charge de rapporter mon travail de thèse. J'espère que celui-ci sera à la hauteur de vos attentes, et que vous m'excuserez pour le peu de temps que je vous laisse pour vous y atteler...
Marta Berardengo Francesco dell'Isola Gaëtan Kerschen Mickaël Lallart	D'avoir accepté de faire partie de mon jury de thèse. J'espère que les échanges que nous aurons à ce propos seront enrichissants, et que vous y trouverez votre intérêt.

Fred et Philippe	De m'avoir rendu cette thèse facile et agréable et d'avoir toujours pris le temps de m'aider. Sans votre duo de choc, je n'aurais certainement pas obtenu de tels résultats expérimentaux et numériques ! Nos discussions me manqueront. Prévenez-moi quand vous voulez qu'on se fasse un concert !
Mathieu, Lucie, JBD, Olivier, Luc, Antoine, Xavier, Claude, Éric...	Pour les échanges scientifiques, pédagogiques, littéraires, vidéoludiques (et j'en passe !) que nous avons pu avoir. Merci de m'avoir fait confiance pour donner des heures d'enseignements pour vous. Merci pour les gâteaux faits maison, pour les fous rires à la cantine, pour les tournées de café. Et surtout merci d'avoir toujours pris le temps de répondre à mes nombreuses interrogations.
Roger	Pour tous les gâteaux que vous nous avez offerts ! Mais surtout pour vos conseils avisés, que je n'ai certainement pas encore complètement assimilés. Merci enfin de m'avoir officieusement remis "Le grand prix du pianiste" (comme le chantait Michel Berger, n'est-ce pas ?).
Chaima, Sylvain, Christophe, Hadrien, Martin, Aro	D'avoir supporté mon tempérament variable, ma musique qui va trop fort et mes blagues foireuses. Vous avez été des cat-marades irrépro-chat-bles ! Faites-moi signe quand vous êtes partants pour un bowling (je ne parle pas de laser game, on connaît déjà le résultat...) !
Naim, JBG, JBB, Julien, Pedro	De prendre la relève ! Que ce BDD soit toujours rempli à ras-bord... de bonne humeur, évidemment !
Laëtitia, Isadora, Nadège, Roger, Chloé	D'avoir fait parti de mon aventure dans la recherche ! J'espère que nos routes se croiseront à nouveau.
Aux personnes du labo que j'ai pu oublier	De m'excuser...
Benji, Gab, Chef, Kirchhof, Shilt, Le Cador, Momo, Matthias, Hugo...	De toujours accepter d'aller boire des canons quand vous êtes dans le coin. Gageons toutefois que les occasions se multiplieront une fois nos thèses respectives achevées !
Faf et Sandra	De m'avoir donné l'occasion de me changer les idées en organisant le meilleur jeu de piste qu'il m'ait été donné d'organiser ! Votre amitié m'est précieuse.
Ma mère et mes grands-parents	Pour tout ce que vous avez fait, et pour tout ce que vous continuez de faire pour moi. Je ne serais jamais arrivé jusqu'ici sans votre soutien et votre amour depuis maintenant 27 ans. Je n'ai pas été très disponible ces dernières années pour vous. C'est à moi de faire en sorte que cela change.
Joséphine	Merci de partager ma vie. Tu m'es indispensable...

Résumé

Cette thèse de doctorat s'intéresse au développement de réseaux piézoélectriques analogues pour l'amortissement vibratoire de structures complexes. L'objectif est d'atténuer les vibrations des modes de plus grandes longueurs d'ondes de structures qu'on recouvre de patchs piézoélectriques, afin de les coupler à des réseaux qui présentent des propriétés identiques de propagation d'onde. Pour ce faire, on détaille une méthode permettant de définir l'analogue électrique de toute structure mécanique. On applique cette méthode à des cas standards de propagation d'ondes mécaniques pour former une bibliothèque de cellules électriques analogues. Le cas d'une plaque rectangulaire recouverte de patchs piézoélectriques est ensuite traité. On assemble un réseau analogue à l'aide d'éléments de la bibliothèque précédemment obtenue. Un dimensionnement adéquat des composants magnétiques du réseau assure qu'il soit de nature purement passive. La connexion de la plaque à son réseau analogue résulte en un amortissement multimodal, ce qui illustre l'efficacité de cette solution d'amortissement. En parallèle, un modèle éléments finis d'une structure couplée à un réseau électrique par des patchs piézoélectriques est développé. La comparaison entre résultats expérimentaux et simulés permet de valider ce modèle. Il est par conséquent utilisé pour finalement aborder l'amortissement large bande de structures complexes à travers des exemples numériques de plaques complexes et de structures à une courbure. Les résultats sont prometteurs, puisqu'ils illustrent la possibilité d'appliquer à des structures complexes l'amortissement multimodal par couplage à des réseaux piézoélectriques analogues purement passifs.

Mots-clefs: Couplage piézoélectrique, Amortissement vibratoire multimodal, Réseau analogue passif, Structures complexes, Analogie électromécanique directe, Modélisation éléments finis, Comparaisons calculs-essais.

Abstract

This doctoral thesis focuses on the development of analogous piezoelectric networks for broadband damping of complex structures. The objective is to damp the modes of largest wavelengths of mechanical structures, which are covered by piezoelectric patches in order to couple them to fully passive electrical networks which exhibit similar wave propagating properties. To do so, we first propose a method to derive the electrical analogue of any mechanical structure. It is applied to create a library of elementary analogues that represent classical wave propagation cases. Then, the electrical analogue of a rectangular plate covered by piezoelectric transducers is assembled with elements from the library. Following design methods of passive inductors and transformers, the produced network is fully passive. Vibration tests highlight the mitigation efficiency of the concept when the plate is connected to its analogous network. Meanwhile, we develop a finite element model of a structure covered with thin piezoelectric transducers connected to a lumped electrical network. Comparisons with experiments validate this model. Thus it is used to finally investigate the achievable performance of piezoelectric network damping applied to complex structures, such as complex plates and single curved structures numerical examples. Results are promising: they highlight it might be possible to develop fully passive piezoelectric analogous networks to damp vibrations of complex structures.

Keywords: Piezoelectric coupling, Broadband vibration mitigation, Passive analogous network, Complex structures, Direct electromechanical analogy, Finite element modeling, Experimental comparisons.

Résumé étendu

I Introduction

Les vibrations de structures minces en ingénierie mécanique génèrent de l'endommagement et du bruit, et donc une réduction de la durée de vie des pièces concernées. De ce fait, de nombreuses solutions d'amortissement des vibrations mécaniques continuent d'être développées. On se concentre dans cette thèse sur la solution consistant à recouvrir une structure de transducteurs piézoélectriques et à les interconnecter par des composants électriques. L'avantage des réseaux piézoélectriques ainsi formés par rapport aux solutions de shunts multi-résonants [31] ou d'ensembles de patchs piézoélectriques indépendamment shuntés [36] est que tous les patchs participent au couplage électromécanique sur la plage de fréquence considérée. Cela permet de maximiser les facteurs de couplage électromécanique, et donc la performance théorique d'atténuation. En outre, on réduit ainsi les valeurs des composants inductifs nécessaires [51], ce qui rend envisageable une intégration purement passive [85].

Par ailleurs, Vidoli et dell'Isola ont démontré l'intérêt de coupler une structure à un milieu qui présente des propriétés de propagation d'ondes similaires dans un contexte d'amortissement large bande des vibrations [63]. Cela revient à coupler une structure à un amortisseur à masse accordée multimodal réparti sur la structure. La situation présentée sur la figure 1 est une illustration mécanique du phénomène étudié: deux plaques identiques P_1 et P_2 sont couplées par des ressorts longitudinaux. La formulation éléments finis du système couplé utilisée pour les simulations en régime harmonique à la pulsation Ω est la suivante:

$$\left[\begin{pmatrix} \boldsymbol{K_1} & -\boldsymbol{K_c} \\ -\boldsymbol{K_c}^{\mathrm{T}} & (1+2\mathrm{j}\xi)\,\boldsymbol{K_2} \end{pmatrix} - \Omega^2 \begin{pmatrix} \boldsymbol{M_1} & \boldsymbol{0} \\ \boldsymbol{0} & \boldsymbol{M_2} \end{pmatrix}\right] \begin{pmatrix} \boldsymbol{U_1} \\ \boldsymbol{U_2} \end{pmatrix} = \begin{pmatrix} \boldsymbol{F_1} \\ \boldsymbol{F_2} \end{pmatrix}, \tag{1}$$

avec respectivement $\boldsymbol{M}_j$, $\boldsymbol{K}_j$, $\boldsymbol{U}_j$ et $\boldsymbol{F}_j$ représentant la matrice de masse, la matrice de rigidité, le vecteur des déplacements nodaux et le vecteur des chargements mécaniques externes pour la plaque P_j.

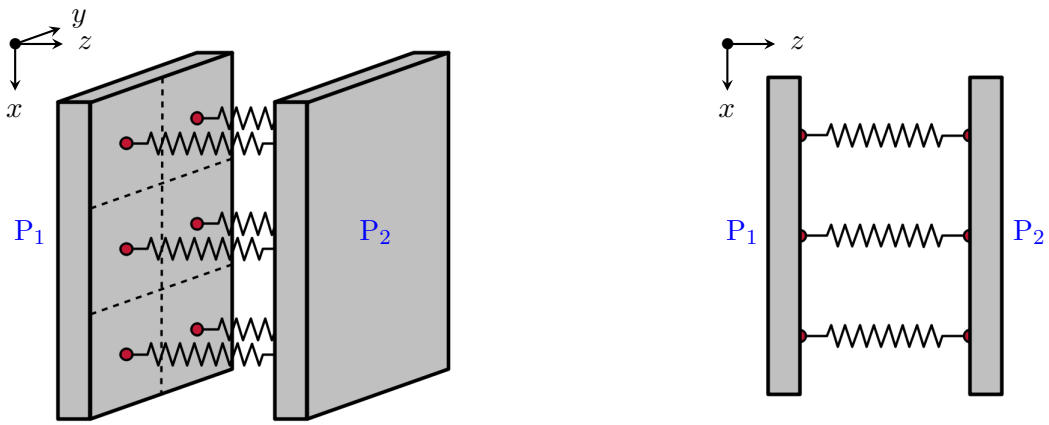

Figure 1: Couplage de deux structures analogues par des ressorts longitudinaux. Bien qu'elles ne soient pas représentées, les conditions aux limites sont similaires pour les deux structures.

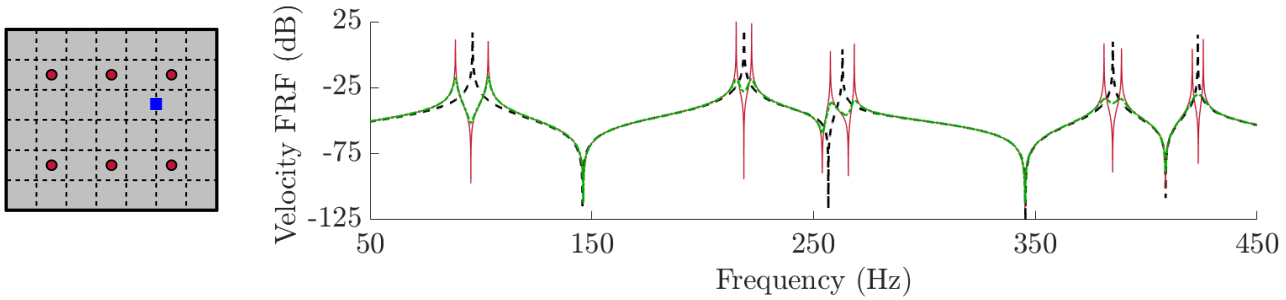

Figure 2: À gauche: • (x, y) emplacements des ressorts reliant les déplacements suivant z de deux plaques identiques, et ■ (x, y) emplacement de l'excitation et de la mesure. À droite: FRF correspondante quand la plaque P_1 ---- n'est pas couplée à la plaque P_2, —— est couplée à une plaque P_2 avec $\xi = 0$, et -·-·- est couplée à une plaque P_2 avec $\xi = 1$ %.

$\boldsymbol{K_c}$ désigne la matrice de couplage, qui dépend des raideurs des ressorts reliant les deux plaques, ξ est le coefficient d'amortissement mécanique pris en compte dans le modèle de la plaque P_2, et $j^2 = -1$. Un exemple du couplage simulé pour des ressorts adaptés aux plaques considérées est représenté sur la figure 2. La fonction de réponse en fréquence (FRF) montre qu'un couplage multimodal se produit entre les deux plaques conservatives. En effet, pour tout mode de la plaque P_1, on constate deux modes résultants lorsque P_1 et P_2 sont couplés. C'est un résultat classique pour les systèmes résonants couplés. Enfin, on parvient à amortir les premiers modes de vibration de la plaque P_1 dès que ξ est non nul.

La possibilité de reproduire les résultats de la figure 2 avec un couplage piézoélectrique est étudiée dans ce manuscrit. En d'autres termes, le but est de remplacer l'absorbeur P_2 par un réseau multi-résonant, qui est l'analogue électrique de la structure vibrante. Les ressorts sont donc remplacés

par des transducteurs piézoélectriques, et des résistances ajoutées dans le réseau servent à amortir les vibrations. Environ quinze ans après l'article de Vidoli et dell'Isola, des démonstrations expérimentales de l'efficacité d'un couplage à un réseau analogue ont été menées pour les barres [70], les poutres [71] et les plaques [72]. Il reste maintenant à prouver l'efficacité de la méthode pour des structures plus complexes. Cela nécessite donc de développer les analogues électriques de structures quelconques, ainsi qu'un modèle prédictif du couplage d'une structure à un réseau électrique par transducteurs piézoélectriques. Ce résumé étendu synthétise les méthodes proposées et les avancées liées à ce sujet.

Objectifs

Les objectifs de ce travail sont les suivants:

- Créer une bibliothèque d'analogues électriques élémentaires.
- Proposer une méthode d'obtention d'analogues électriques de structures complexes à basse fréquence, basée sur l'assemblage d'analogues élémentaires de la bibliothèque.
- Développer un modèle prédictif éléments finis d'une structure couverte par des patchs piézoélectriques et couplée à un réseau électrique.
- Développer des outils pour valider l'analogie entre une structure et un réseau électrique.
- Étudier l'amortissement multimodal par couplage à un réseau piézoélectrique analogue, tout en s'assurant qu'une réalisation entièrement passive serait réalisable en pratique.

II Bibliothèque d'analogues électriques de structures mécaniques

Dans ce chapitre, on propose une méthode de développement d'analogues électriques passifs de structures mécaniques, ainsi que les outils de validation associés. Cette méthode est ensuite appliquée à des cas de barres en traction/compression ou en torsion, poutres droites et courbes, plaques et tubes.

II.1 Méthode

Puisqu'on se concentre sur le développement d'analogues électriques purement passifs de structures mécaniques, seuls les composants électriques représentés sur la figure 3 peuvent être utilisés. Ces composants sont une bobine d'inductance L, un condensateur de capacité C, une résistance de valeur R, et un transformateur de rapport $\hat{a}$. On donne leurs relations caractéristiques:

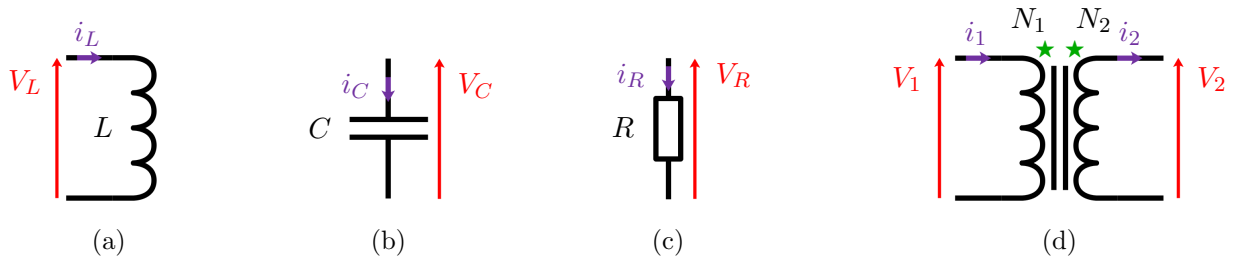

(a) (b) (c) (d)

Figure 3: Représentation des quatre composants idéaux purement passifs: (a) une bobine d'inductance L, (b) un condensateur de capacité C, (c) une résistance de valeur R, et (d) un transformateur à N_1 tours au primaire et N_2 tours au secondaire.

$$V_L = L\,\frac{di_L}{dt}, \qquad i_C = C\,\frac{dV_C}{dt}, \qquad V_R = R\,i_R, \qquad \hat{a} = \frac{N_1}{N_2} = \frac{i_2}{i_1} = \frac{V_1}{V_2}. \tag{2}$$

Les vibrations des milieux mécaniques continus peuvent être décrites par des équations différentielles partielles reliant les déplacements aux actions mécaniques extérieures. Ces équations découlent des théories des vibrations des barres minces, des poutres droites et courbes d'Euler-Bernoulli et des plaques de Kirchhoff-Love. On écrit ces équations en régime harmonique, ce qui correspond donc à remplacer la dérivée temporelle de toute quantité g par $\mathrm{j}\Omega g$, avec Ω la pulsation et $\mathrm{j}^2 = -1$. Ces équations différentielles sont généralement d'ordre supérieur à 1. Au regard des équations caractéristiques (2), il est nécessaire d'exprimer la dynamique de la structure par un système équivalent d'équations différentielles du premier ordre ou d'ordre zéro. On définit donc des quantités mécaniques intermédiaires, comme par exemple le moment de flexion, l'effort tranchant et l'inclinaison pour une poutre d'Euler-Bernoulli. On applique ensuite un schéma différences finies au système d'équations obtenues, ce qui résulte en un modèle mécanique discret de la structure.

Puis, on applique l'analogie électromécanique directe [77] qui est résumée dans le tableau 1. Cette analogie stipule que la vitesse est analogue au courant électrique, et que les actions mécaniques sont analogues aux tensions. On obtient ainsi un circuit électrique qui représente la dynamique de la structure mécanique discrétisée. En assemblant plusieurs de ces cellules élémentaires électriques, on crée un réseau qui reproduit dans le domaine électrique la dynamique de la structure mécanique complète. Le réseau ainsi développé est un système multirésonant, dont les propriétés modales peuvent être modifiées en agissant sur ses conditions aux limites et sur les caractéristiques de ses composants. Par conséquent, des conditions doivent s'appliquer pour que le réseau présente les propriétés de propagation d'ondes souhaitées:

Quantités mécaniques	Quantités électriques
Effort $-F$ et moment $-M$	Tension V
Vitesse en translation $\dot{u}$ et vitesse de rotation $\dot{\theta}$	Courant électrique i
Déplacement u et orientation θ	Charge électrique q
Souplesse	Capacité C
Masse et inertie en rotation	Inductance L
Amortissement visqueux	Résistance R

Tableau 1: Analogie électromécanique directe.

La condition de cohérence spatiale: Le réseau électrique doit présenter les mêmes formes modales que la structure. Pour ce faire, il faut d'une part que le réseau soit composé de cellules électriques qui représentent correctement le comportement dynamique de la structure. D'autre part, les conditions limites doivent être reproduites de façon analogue dans le réseau. Enfin, le nombre d'éléments du réseau doit être suffisant pour que le mode de plus petite longueur d'onde de la plage de fréquence considérée soit convenablement reproduit. Un critère usuel est d'utiliser au moins dix éléments par longueur d'onde. La vérification de la condition de cohérence spatiale peut être menée à l'aide du Modal Assurance Criterion (MAC) [87].

La condition de cohérence fréquentielle: Si la condition de cohérence spatiale est vérifiée, alors assurer les mêmes propriétés de propagation d'ondes dans les deux milieux est équivalent à imposer des fréquences propres mécaniques et électriques égales. Par conséquent, les composants électriques du réseau doivent être réglés dans cette optique. La vérification de la condition de cohérence fréquentielle est menée par une comparaison directe des fréquences propres.

II.2 Bibliothèque

En appliquant la méthode décrite, on obtient les analogues électriques de structures soumises à des sollicitations classiques. La bibliothèque de cellules unitaires est présentée à la page suivante. On suggère donc d'assembler des éléments issus de cette bibliothèque afin de reproduire dans le domaine électrique le comportement mécanique de structures plus complexes discrétisées.

Bibliothèque d'analogues électriques élémentaires de structures mécaniques

Barre en traction/compression	Traction/compression 1D	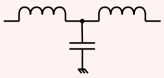
Barre en torsion	Torsion 1D	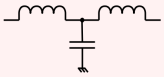
Poutre	Flexion 1D	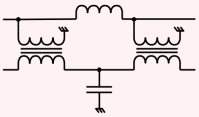
Plaque carrée	Flexion 2D	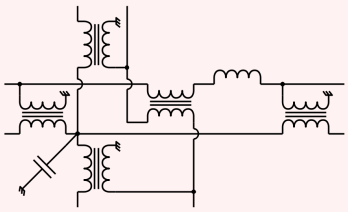
Poutre courbe	Couplage flexion /traction 1D	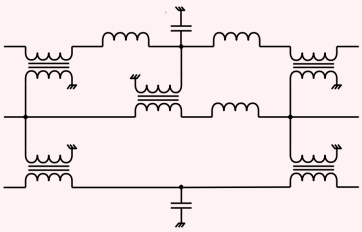
Tube	Flexion 2D et couplage flexion/traction 1D	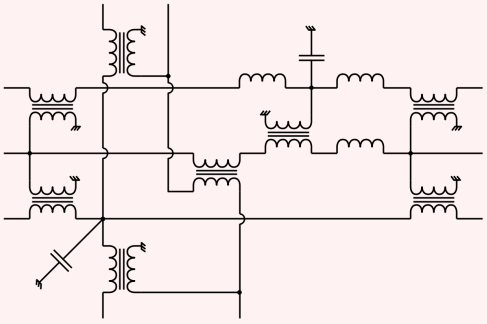

III Modèle éléments finis d'une structure couplée à un réseau électrique

Dans ce manuscrit, nous rappelons d'abord la formulation éléments finis d'une structure recouverte par des transducteurs piézoélectriques fins [92]. Ce modèle est validé par comparaison à l'expérience. Nous construisons ensuite une formulation du problème d'une structure couplée à un réseau électrique assemblé à partir de cellules élémentaires.

III.1 Modèle d'une structure recouverte de patchs piézoélectriques

Nous faisons les hypothèses suivantes:

- La théorie des petites déformations s'applique.
- Le champ électrique $\boldsymbol{E}$ dérive d'un potentiel scalaire V.
- La couche adhésive entre la structure et les transducteurs piézoélectriques est négligée.
- Les épaisseurs des électrodes sont négligées, et les électrodes basses sont mises à la terre.
- Il n'y a pas de charges électriques libres sur les côtés des patchs piézoélectriques.
- Les transducteurs piézoélectriques sont fins et polarisés dans les directions orthogonales aux électrodes, et le matériau est modélisé comme un milieu transverse isotrope.
- La structure hôte est modélisée comme un milieu élastique linéaire homogène isotrope.

La formulation éléments finis du problème ainsi posé est la suivante:

$$\left[\begin{pmatrix} \boldsymbol{K_m} + \boldsymbol{K_c}\boldsymbol{K_e}{\boldsymbol{K_c}}^{\mathrm{T}} & \boldsymbol{K_c}\boldsymbol{K_e} \\ (\boldsymbol{K_c}\boldsymbol{K_e})^{\mathrm{T}} & \boldsymbol{K_e} \end{pmatrix} + \mathrm{j}\Omega \begin{pmatrix} \boldsymbol{D_m} & \boldsymbol{0} \\ \boldsymbol{0} & \boldsymbol{0} \end{pmatrix} - \Omega^2 \begin{pmatrix} \boldsymbol{M_m} & \boldsymbol{0} \\ \boldsymbol{0} & \boldsymbol{0} \end{pmatrix}\right] \begin{pmatrix} \boldsymbol{U} \\ \boldsymbol{Q} \end{pmatrix} = \begin{pmatrix} \boldsymbol{F} \\ \boldsymbol{V} \end{pmatrix}. \tag{3}$$

Avec ces notations, $\boldsymbol{F}$ contient les actions mécaniques extérieures appliquées à la structure, tandis que $\boldsymbol{Q}$ et $\boldsymbol{V}$ contiennent respectivement les charges et potentiels électriques sur les électrodes supérieures des patchs piézoélectriques. Par ailleurs, $\boldsymbol{M_m}$, $\boldsymbol{D_m}$ et $\boldsymbol{K_m}$ sont respectivement les matrices de masse, d'amortissement et de rigidité de la structure, $\boldsymbol{K_c}$ est la matrice de couplage, et $\boldsymbol{K_e}$ est une matrice diagonale dans laquelle le j-ème terme est l'inverse de la capacité piézoélectrique bloquée $C^{\varepsilon(j)}$, qui peut être estimée à partir de constantes matériaux.

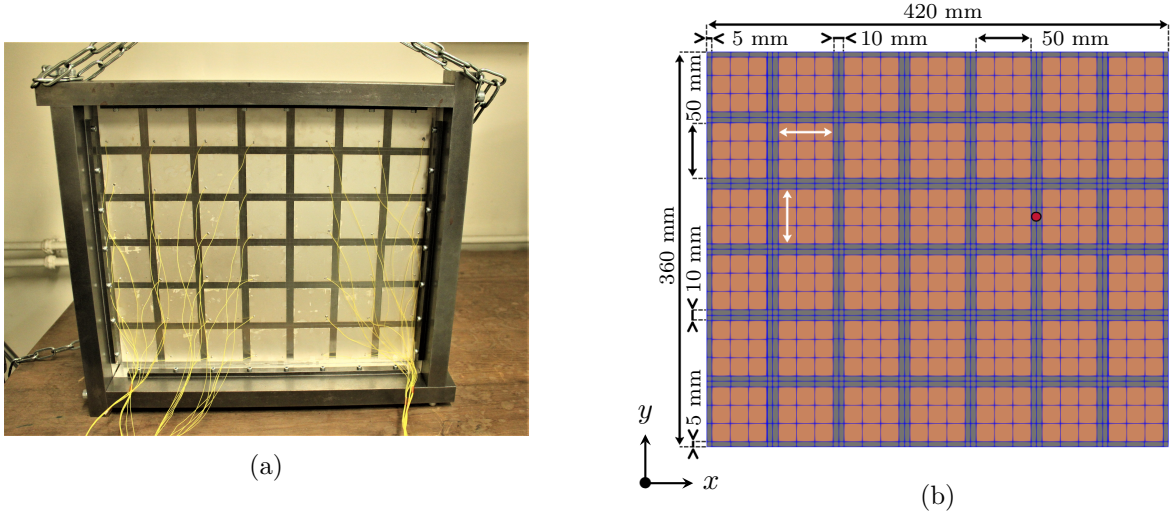

(a) (b)

Figure 4: (a) Plaque en alliage d'aluminium périodiquement recouverte de 42 patchs piézoélectriques et en appuis simples sur un cadre en acier. (b) Dimensions de la structure et maillage correspondant, sur lequel • (x, y) l'emplacement des mesures d'excitation et de vitesse est indiqué.

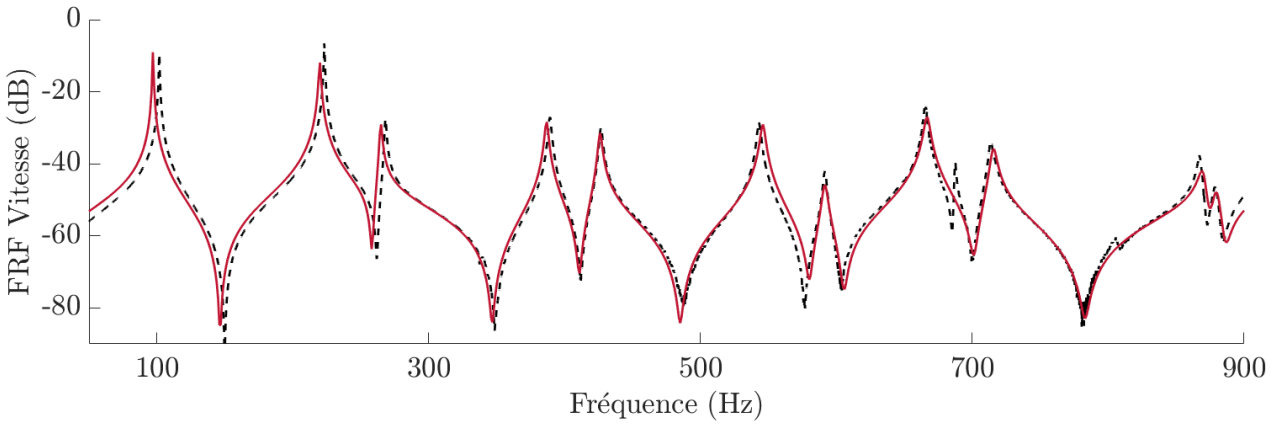

Figure 5: Comparaison de la —— FRF simulée à la - - - - FRF mesurée lorsque les patchs piézoélectriques sont connectés en court-circuit.

Ce modèle est validé par comparaison avec une mesure effectuée sur la structure représentée en figure 4: il s'agit d'une plaque rectangulaire en alliage d'aluminium, d'épaisseur constante et périodiquement recouverte de patchs piézoélectriques carrés en matériau PIC 153. Un effort ponctuel est appliqué sur la surface de la plaque recouverte de patchs piézoélectriques à la position (x, y) indiquée sur la figure 4b. On mesure la vitesse au point de mêmes coordonnées (x, y) situé sur la face nue de la plaque. La comparaison en figure 5 entre résultats expérimentaux et simulés à l'aide de l'équation (3) avec des patchs piézoélectriques court-circuités prouve que le modèle développé est capable de prédire le comportement de la structure.

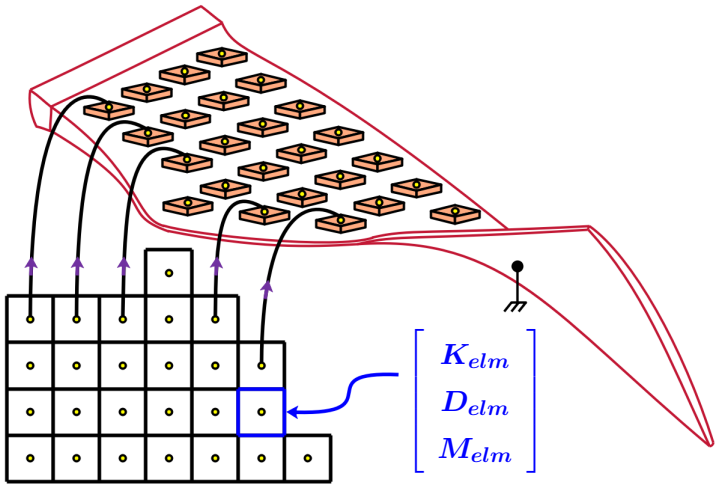

Figure 6: Couplage d'une structure à un réseau électrique par un ensemble de patchs piézoélectriques. Pour des raisons de lisibilité, seuls quelques fils de connexion sont représentés.

III.2 Modèle d'une structure couplée à un réseau électrique

Pour modéliser le comportement d'une structure couplée par des patchs piézoélectriques à un réseau électrique, comme représenté sur la figure 6, on fait deux hypothèses supplémentaires:

- La dynamique des cellules élémentaires du réseau est décrite par des matrices élémentaires de "raideur" électrique $\boldsymbol{K_{elm}}$, d'amortissement électrique $\boldsymbol{D_{elm}}$ et de "masse" électrique $\boldsymbol{M_{elm}}$. Celles-ci dépendent respectivement des composants capacitifs, dissipatifs et inductifs du réseau, ainsi que des rapports des transformateurs éventuellement inclus. Elles permettent de relier localement les courants électriques et les tensions aux bords des cellules.

- Les composants du réseau se comportent linéairement, et on reste dans le cadre de la piézoélectricité linéaire. Ainsi, le réseau électrique se comporte linéairement avec les sources d'excitation.

Par conséquent, suite à un assemblage géométrique similaire à celui de la méthode des éléments finis, on obtient des matrices générales de "masse" électrique $\boldsymbol{M_N}$, d'amortissement électrique $\boldsymbol{D_N}$ et de "raideur" électrique $\boldsymbol{K_N}$ à partir des modèles de comportement des cellules élémentaires du réseau. Ces matrices permettent de relier les vecteurs de tensions $\boldsymbol{V_N}$ et de courants $\boldsymbol{Q_N}$ du réseau lorsque celui-ci n'est pas couplé à la structure:

$$\boldsymbol{V_N} = \left(\boldsymbol{K_N} + \mathrm{j}\Omega\boldsymbol{D_N} - \Omega^2\boldsymbol{M_N}\right)\boldsymbol{Q_N}. \tag{4}$$

Le couplage de la structure à un réseau électrique se fait donc en combinant les équations (3) et (4). Une matrice $\boldsymbol{P}$ doit être définie pour prendre en compte la façon dont la structure est connectée au réseau. La formulation obtenue est alors

$$\left[\begin{pmatrix} \boldsymbol{K_m} + \boldsymbol{K_c}\boldsymbol{K_e}\boldsymbol{K_c}^{\mathrm{T}} & \boldsymbol{K_c}\boldsymbol{K_e}\boldsymbol{P} \\ (\boldsymbol{K_c}\boldsymbol{K_e}\boldsymbol{P})^{\mathrm{T}} & \boldsymbol{K_N} \end{pmatrix} + \mathrm{j}\Omega \begin{pmatrix} \boldsymbol{D_m} & \boldsymbol{0} \\ \boldsymbol{0} & \boldsymbol{D_N} \end{pmatrix} - \Omega^2 \begin{pmatrix} \boldsymbol{M_m} & \boldsymbol{0} \\ \boldsymbol{0} & \boldsymbol{M_N} \end{pmatrix}\right] \begin{pmatrix} \boldsymbol{U} \\ \boldsymbol{Q_N} \end{pmatrix} = \begin{pmatrix} \boldsymbol{F} \\ \boldsymbol{V_N} \end{pmatrix}. \quad (5)$$

Cette expression est similaire à l'équation (1), à ceci près que des matrices d'amortissement électrique et mécanique ont été rajoutées. L'originalité de ce modèle réside dans le couplage d'un modèle éléments finis 3D à un réseau décrit par un ensemble d'équations discrètes. En outre, cette formulation présente l'avantage de pouvoir être appliquée après les assemblages indépendants des systèmes mécaniques et électriques.

IV Amortissement d'une plaque par couplage à un réseau piézoélectrique analogue

Le but de ce chapitre est de concevoir l'analogue électrique de la plaque rectangulaire en appuis simples visible sur la figure 4a. On détaille pour cela les méthodes de conception des bobines et des transformateurs pour s'assurer que le réseau assemblé soit peu résistif. L'analogie entre la structure et le réseau électrique est ensuite validée. Enfin, on vérifie qu'on obtient bien une atténuation multimodale des vibrations de la plaque, et les résultats expérimentaux sont utilisés pour valider le modèle éléments finis couplé représenté par l'équation (5).

IV.1 Dimensionnement de bobines et de transformateurs

Tous les circuits électriques définis dans la bibliothèque d'éléments analogues contiennent des bobines, et certains incluent des transformateurs. Leur conception est donc primordiale. En effet, le but reste de concevoir des réseaux analogues purement passifs et dont les éléments dissipatifs sont suffisamment faibles pour éviter le sur-amortissement de la structure à laquelle ils seront couplés. Les méthodes de dimensionnement qu'on suit [101, 106, 3] permettent d'atteindre ces objectifs.

On propose de réaliser une bobine par l'enroulement de N tours de fil conducteur autour d'un circuit magnétique de perméabilité μ, fait en matériau ferrite et comprenant un entrefer δ, comme représenté sur la figure 7a. À basses fréquences et bas niveaux de courants électriques, un modèle réaliste des

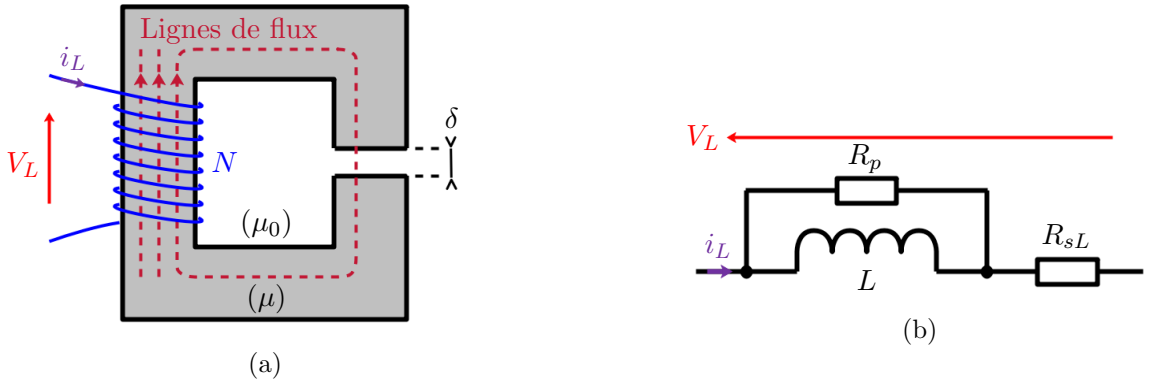

Figure 7: (a) Circuit magnétique avec entrefer autour duquel du fil conducteur est enroulé, et (b) modèle électrique du composant inductif ainsi réalisé.

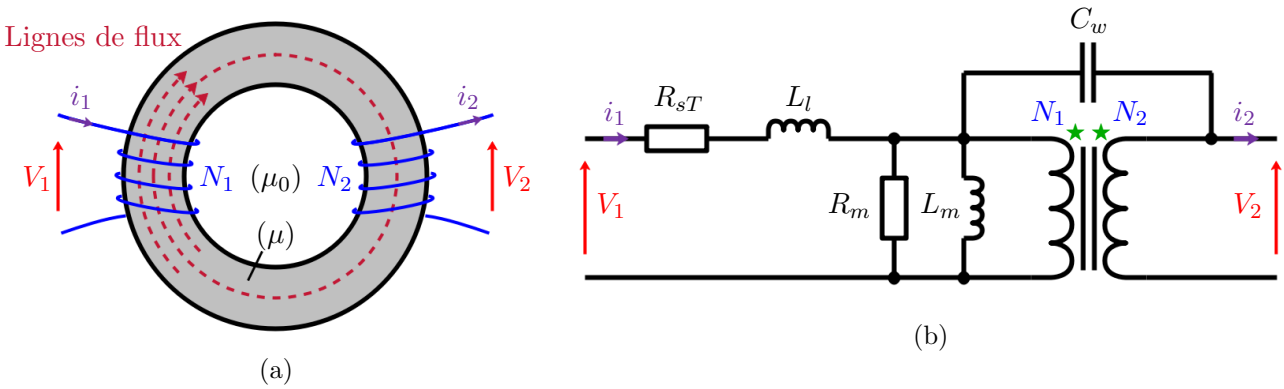

Figure 8: (a) Circuit magnétique torique sans entrefer et avec deux enroulements de fil conducteur, et (b) modèle électrique à basse fréquence du transformateur non-idéal ainsi réalisé.

bobines est dessiné sur la figure 7b et comprend une inductance L, une résistance série R_{sL} qui modélise les pertes cuivre et une résistance parallèle R_p modélisant les pertes magnétiques. Il convient de choisir le matériau ferrite et les caractéristiques géométriques du circuit magnétique en fonction de l'application. En effet, le volume et la masse des composants magnétiques dépend principalement de l'énergie qu'ils doivent pouvoir stocker. Par ailleurs, on montre que des compromis sont à trouver entre des bobines peu dissipatives et des inductances peu dépendantes des facteurs environnementaux.

Quant aux transformateurs, on propose de les réaliser grâce à deux enroulements de N_1 et N_2 tours de fil conducteur autour d'un même circuit magnétique en matériau nanocristallin, comme dessiné sur la figure 8a. Un modèle de transformateur à basses fréquences et bas niveaux de courants électriques est présenté sur la figure 8b. Le circuit équivalent fait intervenir une inductance magnétisante L_m et une inductance de fuite L_l qui modélisent une perméabilité finie du circuit magnétique, une résistance

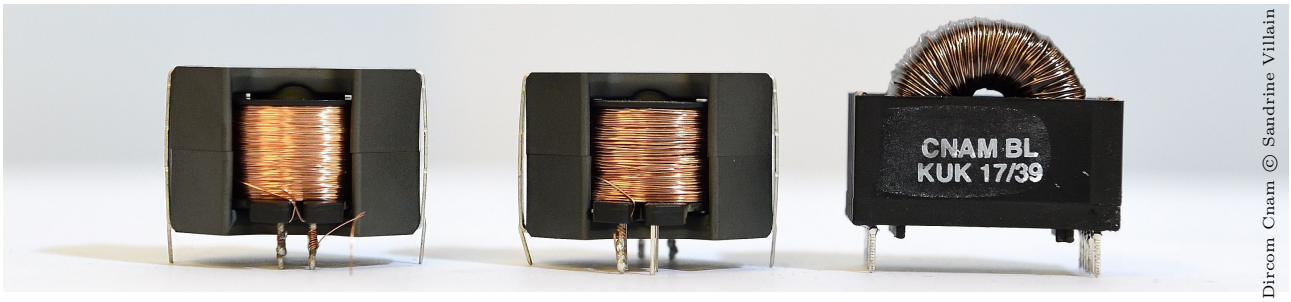

Figure 9: Deux bobines et un transformateur réalisés par enroulements de fil conducteur autour de circuits magnétiques.

série R_{sT} qui représente les pertes cuivre, une résistance parallèle R_m qui modélise les pertes fer, et une capacité inter-enroulements C_w qui représente l'interaction électrostatique entre les enroulements du transformateur. Les transformateurs étant usuellement les composants les plus volumineux en électrotechnique, le choix sur des critères énergétiques du matériau nanocristallin dont est fait le circuit magnétique revêt une grande importance. De plus, on montre qu'un doit trouver un compromis entre des transformateurs peu dissipatifs et des transformateurs ayant une influence limitée sur le comportement fréquentiel du réseau.

Dans la mesure du possible, les problématiques explicitées ci-dessus ont été prises en compte pour fabriquer les composants requis. La figure 9 montre quelques composants réalisés dans le cadre de cette thèse. Ces composants ont été caractérisés à basses fréquences et faibles courants électriques afin d'identifier les valeurs requises pour les modèles présentés en figures 7b et 8b.

IV.2 Validation du réseau assemblé

L'objectif est de développer l'analogue électrique de la plaque rectangulaire recouverte de patchs piézoélectriques précédemment décrite. Parmi les éléments de la bibliothèque d'analogues électriques, on sélectionne la plaque carrée comme cellule unitaire du réseau. Ce dernier est composé de 7 éléments sur la longueur et de 6 éléments sur la largeur. Ainsi, un réseau composé de 42 cellules unitaires identiques a été assemblé. La structure et son réseau analogue sont photographiés en figures 10a et 10b. La figure 11b permet d'examiner une cellule unitaire de plus près. Elle peut être comparée au circuit issu de la bibliothèque d'éléments analogues dessiné en figure 11a. Les bobines et transformateurs du réseau sont les composants photographiés en figure 9.

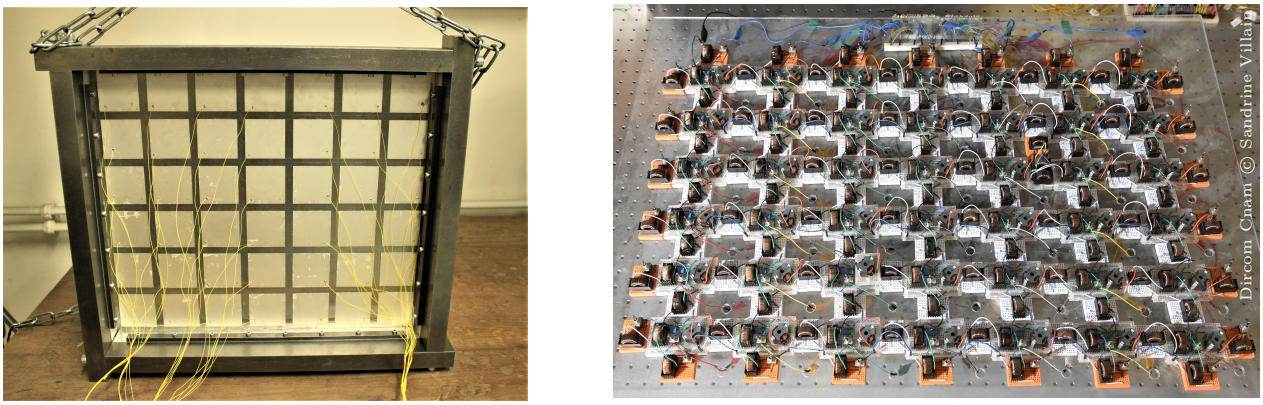

(a) (b)

Figure 10: (a) Plaque rectangulaire recouverte de 42 patchs piézoélectriques et (b) son réseau analogue formé de 42 cellules unitaires.

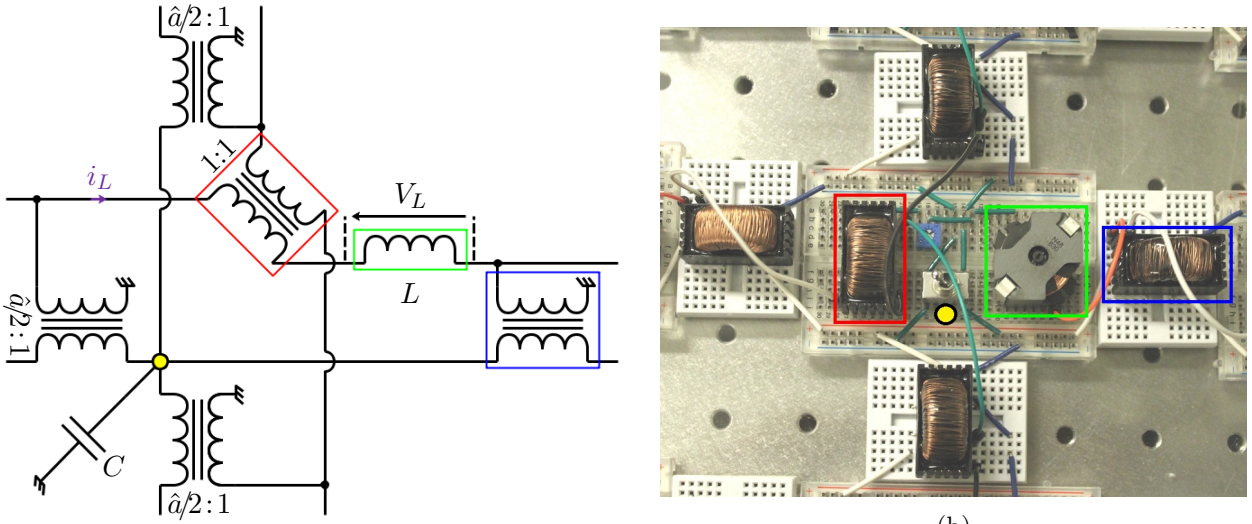

(a) (b)

Figure 11: (a) Représentation idéale schématique et (b) photographie de l'analogue électrique d'une plaque carrée, sur lesquelles sont encadrés le transformateur central en rouge, un transformateur de bord de cellule en bleu, une bobine en vert, et le point de connexion avec les condensateurs en jaune.

On procède ensuite à la validation du modèle du réseau décrit par l'équation (4). Pour cela, on impose une tension kV_{exc} entre deux cellules du réseau, ce qui est analogue à imposer un effort ponctuel sur la structure. On trace ensuite l'évolution avec la fréquence de la tension V_L aux bornes d'une bobine du réseau. Les résultats simulés prennent en compte uniquement les résistances séries R_{sL} et RsT parmi les imperfections représentées sur les circuits des figures 7b et 8b. En figure 12, la comparaison aux mesures permet de valider le modèle du réseau électrique.

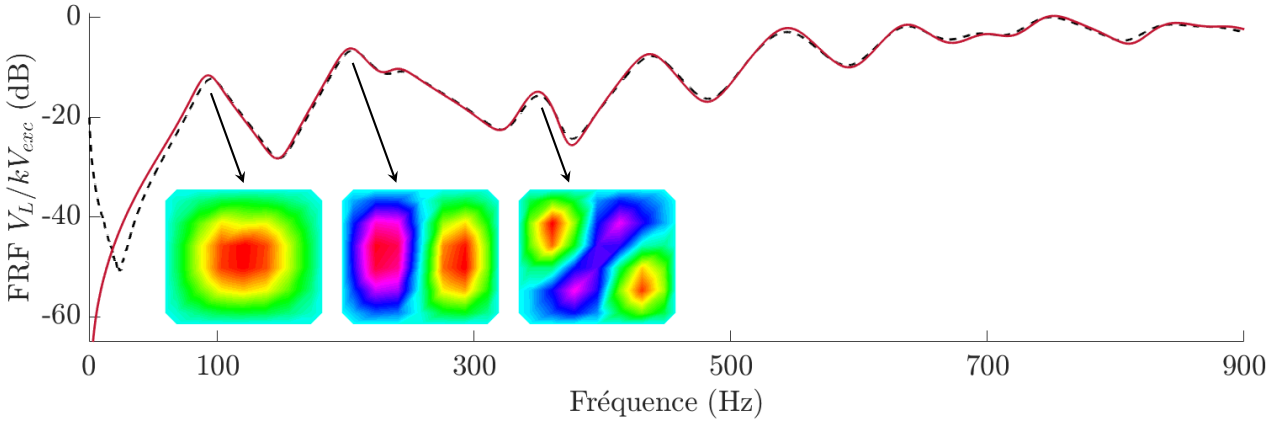

Figure 12: FRF de V_L/kV_{exc} ---- mesurée et —— simulée. Quelques déformées opérationnelles mesurées de courant électrique sont représentées aux pics de la FRF mesurée.

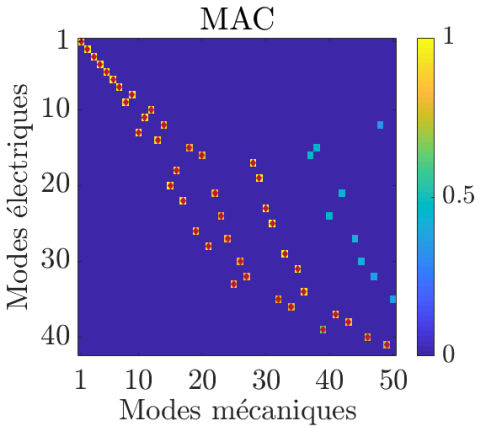

Figure 13: MAC entre les 50 premiers modes de vitesse de la plaque recouverte de patchs piézoélectriques et les 42 premiers modes de courant électrique du réseau. Les petits marqueurs ♦ indiquent les couples de modes clairement identifiés, qui sont par conséquent reportés sur la figure 14.

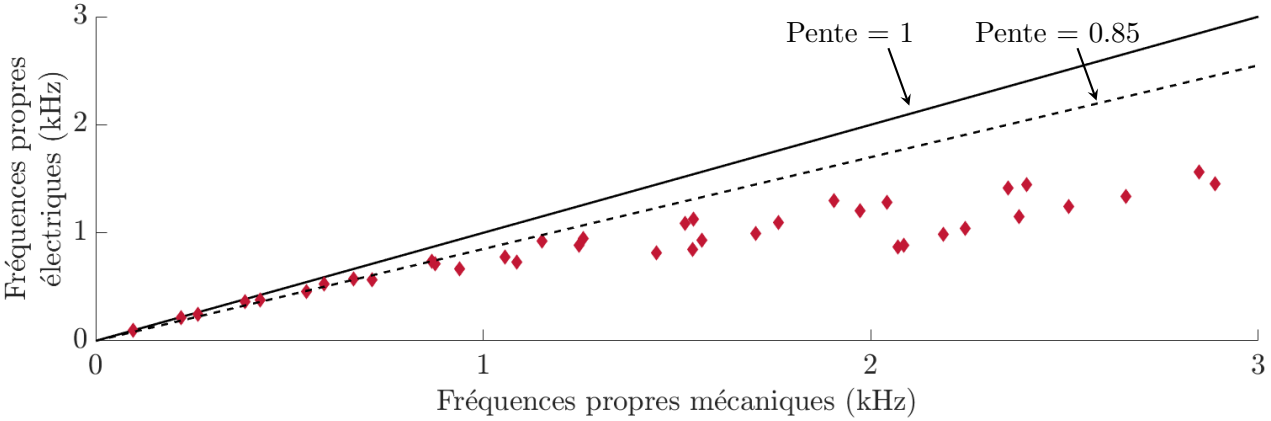

Figure 14: Comparaison entre les fréquences propres électriques du réseau et mécaniques de la plaque.

IV.3 Validation de l'analogie

Les composants électriques du réseau sont réglés en appliquant la condition de cohérence fréquentielle. Celle-ci est spécifique à l'analogue électrique de la plaque carrée qu'on a sélectionné dans la bibliothèque:

$$\frac{1}{a^2}\,\frac{K_\theta^E}{m} = \frac{1}{\hat{a}^2}\,\frac{1}{LC_{st}}. \tag{6}$$

Dans cette expression, a représente le côté de la cellule unitaire, m sa masse, et K_θ^E sa raideur en flexion lorsque les patchs piézoélectriques sont court-circuités. De plus, $\hat{a}$ intervient dans les rapports de transformation des transformateurs de bord de cellule, L est l'inductance centrale, et C_{st} est la capacité piézoélectrique statique, supposée égale à la capacité à 0 Hz. Ces composants sont indiqués sur la figure 11a, où C devrait être remplacé par C_{st}. Les paramètres mécaniques de l'équation (6) sont estimés à partir de modèles mécaniques simples, et C_{st} à partir du modèle éléments finis de l'équation (3). En fixant $\hat{a}$, on déduit donc la valeur de L requise.

Une fois les composants du réseau définis, on procède à la validation de l'analogie entre le réseau et la plaque. Pour cela, on compare les modes simulés à l'aide des modèles prédictifs exprimés par les équations (3) et (4). La matrice de MAC obtenue est tracée en figure 13. Elle n'est pas diagonale, puisqu'on compare des résultats issus d'un modèle continu à des résultats simulés à l'aide d'un modèle différences finies. Cela étant, on visualise que la condition de cohérence spatiale est vérifiée pour un grand nombre de modes. Puis, les fréquences propres des paires de modes clairement identifiées sont reportées et comparées en figure 14. En supposant un écart acceptable de 15 % entre elles, la condition de cohérence fréquentielle est validée pour les onze premiers modes, ce qui représente une bande de fréquences de près de 900 Hz. On peut donc donc considérer que le réseau assemblé se comporte bel et bien en analogue de la plaque étudiée jusqu'à environ 900 Hz.

Par ailleurs, on peut montrer que l'augmentation du nombre de cellules du réseau fait converger ses propriétés modales vers celles de la plaque estimées par le modèle éléments finis. Cela permet ainsi de faire tendre la matrice de MAC vers une matrice diagonale. Autrement dit, discrétiser davantage le réseau électrique permet d'élargir la bande de fréquence sur laquelle l'analogie entre la structure et le réseau est validée.

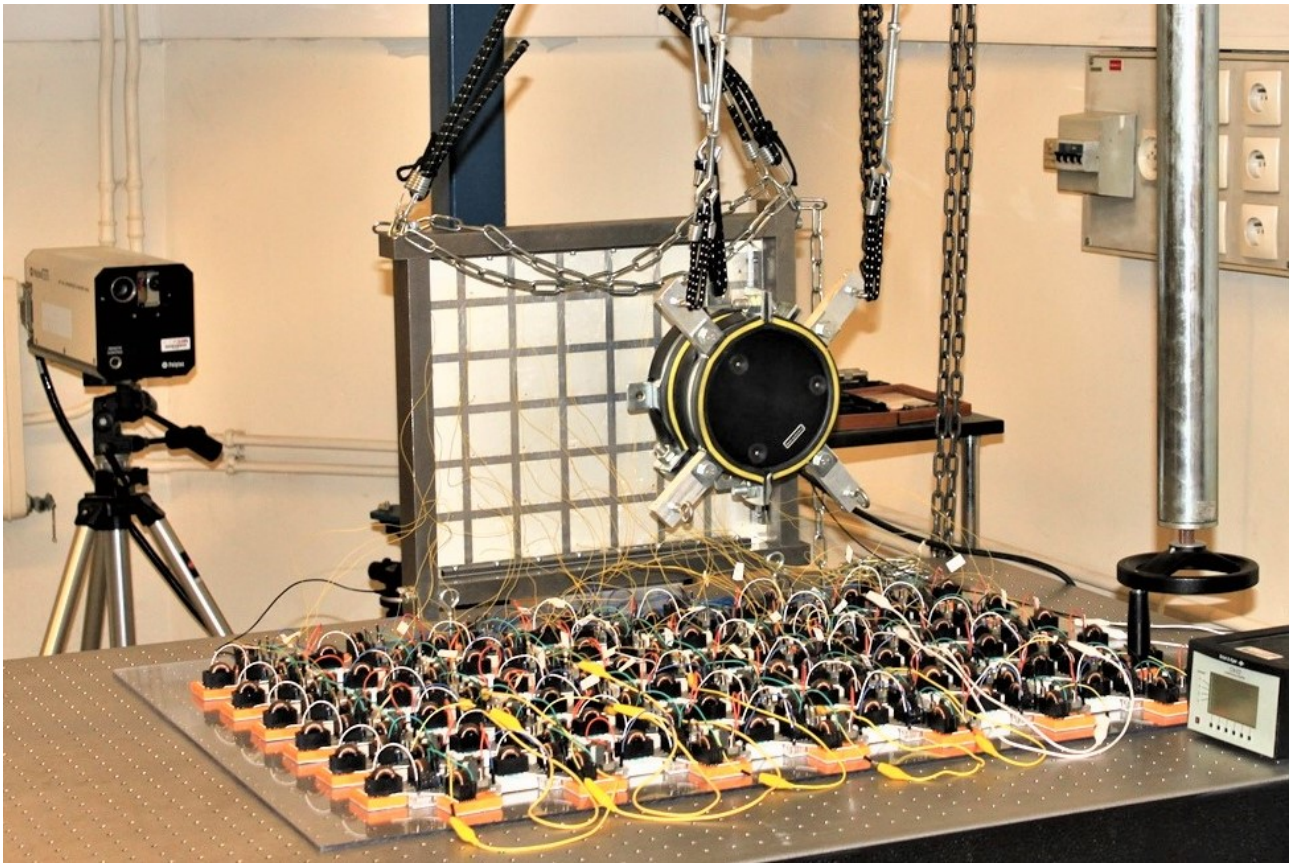

Figure 15: Photographie du montage expérimental, comprenant la plaque recouverte de transducteurs piézoélectriques, un pot vibrant, un vibromètre laser et le réseau électrique analogue.

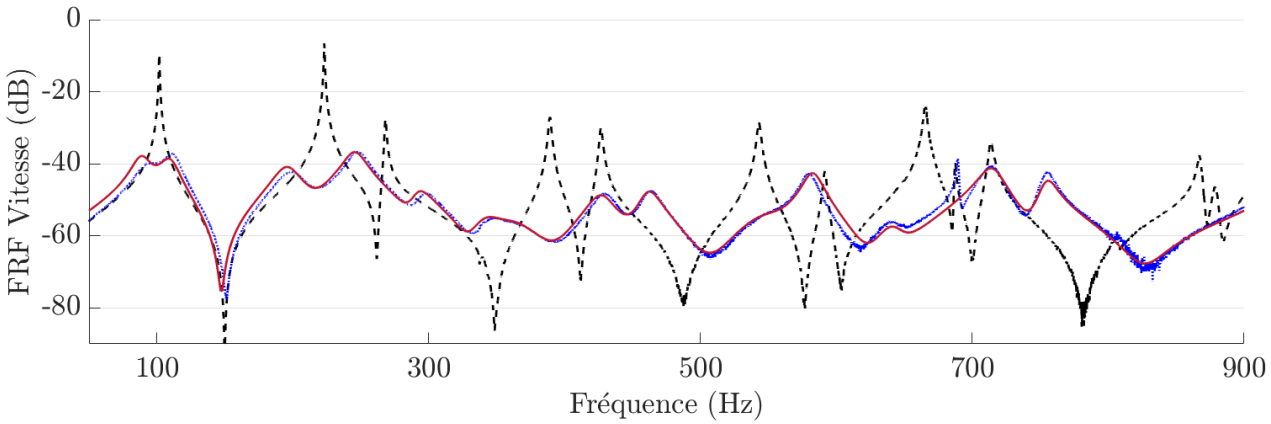

Figure 16: Comparaison de FRFs en vitesse obtenues par - - - - mesure avec les patchs piézoélectriques en court-circuit, ····· mesure et —— simulation quand la plaque est connectée à son réseau électrique analogue.

IV.4 Amortissement multimodal de la structure

Le cas de la structure couplée à son analogue électrique passif est finalement étudié. Le montage expérimental est photographié en figure 15. Un pot vibrant applique une charge ponctuelle sur la surface de la plaque sur laquelle les patchs piézoélectriques sont collés, et un vibromètre laser mesure le mouvement induit de l'autre côté de la plaque. Comme le montre la figure 16, le comportement dynamique de la structure est nettement altéré par la connexion au réseau électrique. Après les montages expérimentaux proposés dans [70, 71, 72], il s'agit ici d'une illustration supplémentaire qu'il est possible d'atténuer les vibrations sur une large gamme de fréquences au moyen du couplage piézoélectrique d'une plaque à son analogue électrique.

De plus, le modèle de l'équation (5) est capable de prédire la dynamique de la structure couplée à un réseau électrique. Ce résultat est d'une importance primordiale pour aller vers des structures complexes. En effet, il valide le modèle précédemment développé: alors qu'on prédit le comportement de la structure par un modèle éléments finis, on peut y connecter un réseau électrique indépendamment assemblé par une approche de type éléments finis. Le cas particulier ici traité est le couplage d'un modèle mécanique 3D à un réseau électrique 2D. On considère donc qu'il peut être utilisé pour le couplage de toute structure mécanique 3D modélisée par la méthode des éléments finis à un réseau électrique 1D ou 2D.

V Amortissement de structures complexes par couplage à des réseaux piézoélectriques

L'objectif du dernier chapitre de ce manuscrit est d'étendre le concept d'amortissement vibratoire par couplage via patchs piézoélectriques à un réseau électrique analogue à des structures complexes. Le principe est d'assembler des cellules de la bibliothèque d'analogues électriques pour former des réseaux analogues adéquats. Un premier cas non périodique permet de valider le modèle de l'équation (5) dans un cas complexe par comparaison entre mesures et simulations. Les autres structures traitées sont des exemples numériques d'une plaque à épaisseur variable, d'une plaque avec diverses conditions aux limites, d'une arche et d'un anneau. L'amortissement vibratoire de ces structures est atteint par couplage à des réseaux électriques purement passifs.

Plusieurs sources de complexités de structure peuvent être combinées en pratique. Nous choisissons de les considérer séparément afin de distinguer leurs effets sur la performance d'amortissement. Les complexités qu'on est capable de traiter peuvent se classer en trois catégories:

Structures non périodiques: Une fois la structure discrétisée, la distribution des paramètres discrets peut être non uniforme. Cela peut être dû à des paramètres géométriques variables, tels que l'épaisseur ou la courbure, ou à des modifications locales induites par des contacts avec des pièces extérieures.

Complexités de conditions limites: Les seuls cas étudiés dans la littérature scientifique jusqu'à présent appliquaient les mêmes conditions limites à toutes les extrémités de la structure. Mixer ces conditions limites est donc une complexité à étudier.

Recouvrement des fréquences propres: Certaines structures peuvent présenter des modes très proches les uns des autres. C'est le cas notamment des structures presque axisymétriques. Une autre complexité apparaît pour les structures dont des modes de différentes natures se situent dans l'intervalle fréquentiel d'intérêt.

V.1 Méthode

On applique la même méthode pour étudier l'amortissement vibratoire des structures complexes recouvertes de patchs piézoélectriques de ce chapitre:

- Le point de départ est la sélection de cellules élémentaires dans la bibliothèque d'éléments analogues. Le choix est basé sur la nature des modes de vibration qu'on souhaite atténuer. Un assemblage géométrique de ces cellules élémentaires forme le réseau analogue de la structure.

- On estime ensuite les paramètres mécaniques et électriques apparaissant dans la condition de cohérence fréquentielle correspondante. On en déduit les degrés de liberté restants parmi les composants électriques du réseau en appliquant cette même condition de cohérence fréquentielle.

- Puis, on valide l'analogie entre la structure et le réseau proposé en comparant leurs caractéristiques modales. Celles-ci sont estimées via les modèles des équations (3) et (4). Si les deux conditions de cohérence sont vérifiées, alors on parlera de **couplage modal** lors du couplage entre les systèmes mécaniques et électriques considérés.

- Une fois la **condition de couplage modal** vérifiée, on s'attend à obtenir un amortissement vibratoire multimodal de la structure. La formulation de l'équation (5) sert alors à estimer la performance d'amortissement atteinte. On y implémente des composants magnétiques certes non optimisés, mais conçus de façon réaliste.

V.2 Plaque avec une masse ajoutée

Le premier cas de plaque complexe traité ici est l'ajout d'une masse importante sur le côté de la plaque qui n'est pas recouvert par des patchs piézoélectriques, comme illustré par la figure 17. Cet ajout permet de rompre la symétrie de la structure. Son réseau analogue devient donc non périodique. Quelques unes des déformées opérationnelles du réseau adapté, tracées sur la figure 18, en témoignent.

On adapte localement le réseau à la modification de la structure. L'ajout local de masse se traduit dans le domaine électrique par une augmentation de l'inductance de la cellule correspondante du réseau. On vérifie par comparaison entre calculs et essais que les modèles des équations (3) et (4) prédisent correctement le comportement dynamique de la structure et du réseau non périodique. La comparaison des réponses en fréquence du réseau est notamment illustrée par la figure 18. Puis, on utilise ces mêmes modèles pour estimer les caractéristiques modales des deux systèmes non couplés. On estime que l'analogie entre la structure et le réseau est vérifiée pour les sept premiers modes et jusqu'à environ 600 Hz.

La plaque non périodique est finalement couplée à son analogue électrique passif. La mesure de FRF est effectuée dans la même configuration que celle présentée en figure 15. Comme le montre la figure 19, on obtient un amortissement multimodal dans ce cas aussi. Ces résultats valident l'approche consistant à coupler une structure non périodique à son analogue électrique entièrement passif à des fins d'amortissement large bande. Par ailleurs, les simulations correspondent assez bien aux mesures. En l'état, nous supposons par conséquent que le modèle éléments finis développé dans ce manuscrit et exprimé par l'équation (5) peut prédire la dynamique d'une structure complexe couplée à un réseau électrique.

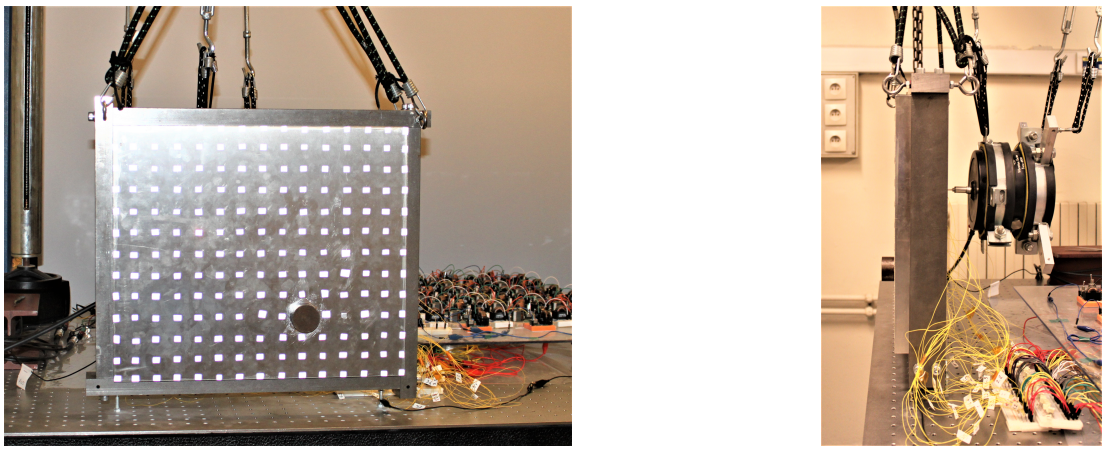

Figure 17: Vues de face et de côté de la plaque sur laquelle une masse est ajoutée.

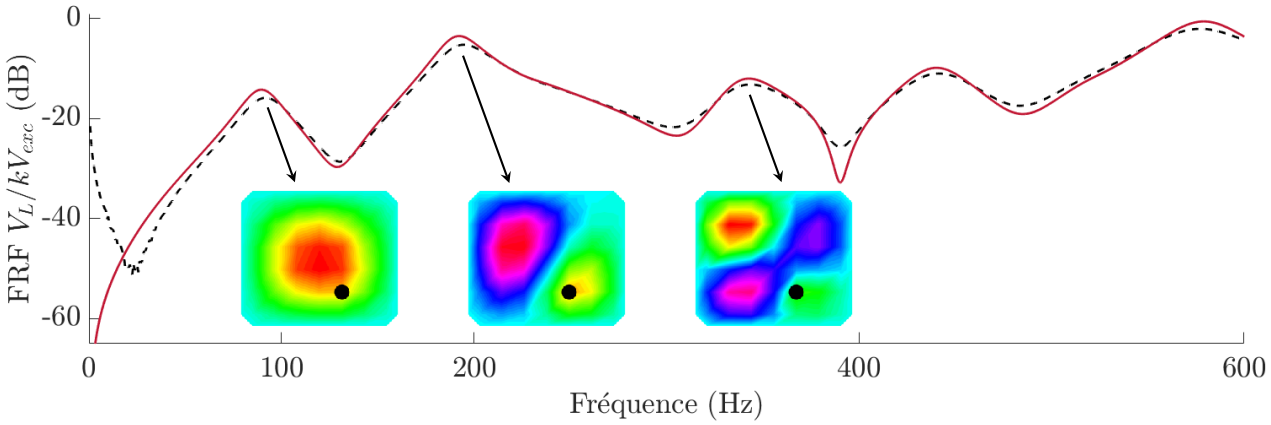

Figure 18: FRF de V_L/kV_{exc} ---- mesurée et —— simulée. Quelques déformées opérationnelles mesurées de courant électrique du réseau non périodique sont représentées aux pics de la FRF mesurée, et la position de la masse ajoutée est représentée en noir.

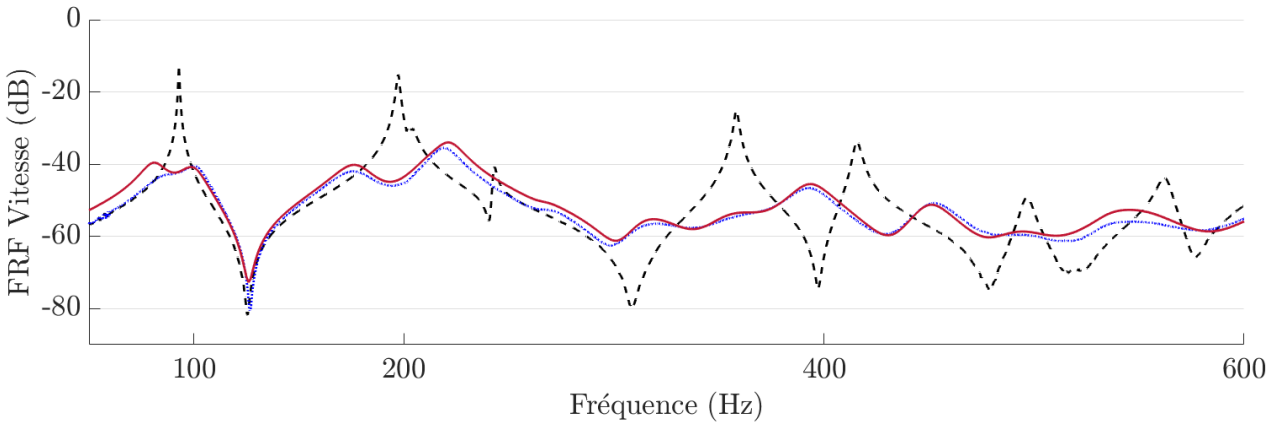

Figure 19: Comparaison de FRFs en vitesse obtenues par ---- mesure avec les patchs piézoélectriques en court-circuit, ····· mesure et —— simulation quand la plaque avec masse ajoutée est connectée à son réseau électrique analogue.

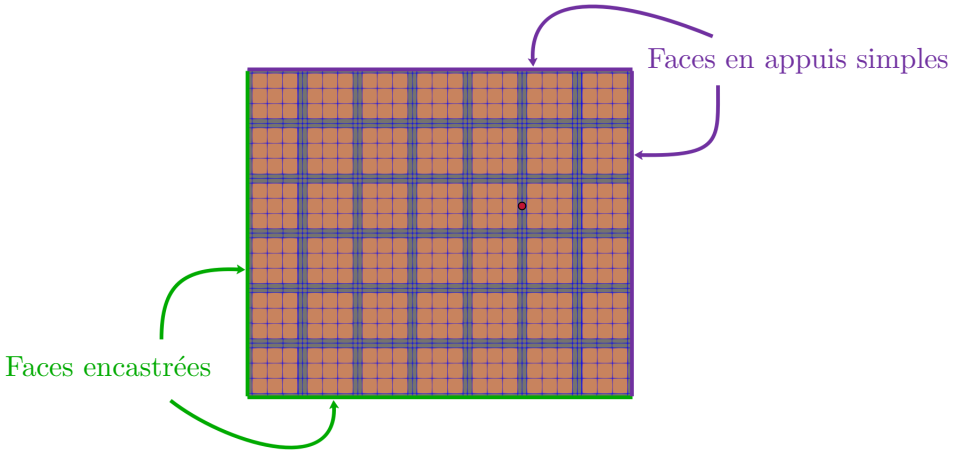

Figure 20: Plaque rectangulaire recouverte de patchs piézoélectriques et aux conditions limites variées.

V.3 Exemples numériques de structures complexes

Deux autres cas de plaques complexes sont étudiés dans ce manuscrit. Le premier est une plaque à épaisseur linéairement variable, recouverte de patchs piézoélectriques d'épaisseurs constantes. Ce cas permet d'étudier une structure dont le réseau analogue est complètement non périodique. Le second cas est une plaque à épaisseur constante qui est soumise à des conditions limites variées, comme schématisée en figure 20.

Enfin, deux autres exemples numériques sont traités et concernent des structures courbes. Le premier exemple est l'amortissement vibratoire d'une arche, qui est le premier cas abordé de développement d'un réseau électrique analogue d'une structure courbe. Cet exemple permet notamment de discuter du problème de recouvrement des domaines fréquentiels de modes de natures différentes. Le dernier exemple est un anneau, qui se distingue des autres cas par l'absence de conditions limites et par le fait que le réseau obtenu soit fermé sur lui-même.

Les quatre exemples numériques proposés permettent donc de traiter les différentes sources de complexités précédemment mises en évidence. La méthode décrite en début de chapitre leur est appliquée, et mène à une conclusion identique à chaque fois: le concept d'amortissement vibratoire par couplage à un réseau analogue via des éléments piézoélectriques peut s'appliquer aux structures considérées. De plus, la conception de composants électriques réalistes rend envisageable une intégration purement passive de la solution proposée.

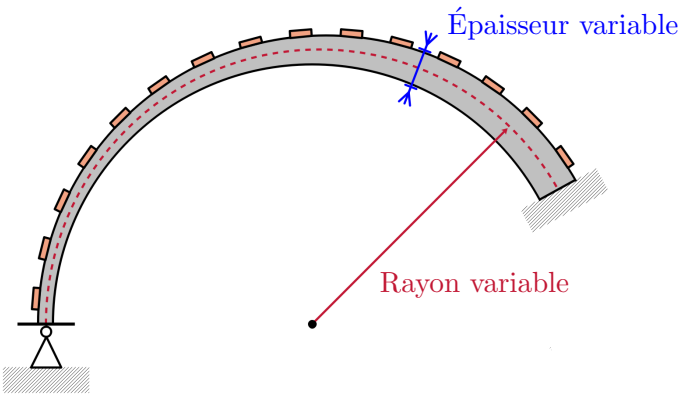

Figure 21: Segment d'arche de rayon et d'épaisseur variables recouvert par des patchs piézoélectriques.

VI Conclusions et perspectives

Principales contributions reportées dans ce manuscrit de thèse

- Description d'une méthode de conception d'analogues électriques passifs.
- Définition d'une bibliothèque d'analogues électriques, qui comprend notamment des éléments courbes 1D et 2D.
- Développement d'un outil numérique pour la modélisation du couplage à un réseau électrique d'une structure 3D recouverte de patchs piézoélectriques.
- Validation de cet outil par comparaison calculs/essais sur des structures périodiques et non périodiques.
- Preuve numérique de l'efficacité de l'amortissement par couplage à un réseau piézoélectrique analogue pour les plaques complexes et les structures courbes 1D.
- Obtention d'un amortissement multimodal en considérant des composants électriques réalistes et donc purement passifs.

Au-delà des résultats obtenus durant ce doctorat, il reste des problématiques à aborder pour assurer le potentiel déploiement des solutions d'amortissement proposées à des cas industriels. Des cas de structures encore plus complexes, comme dessiné sur la figure 21, peuvent être envisagés. De plus, l'influence de facteurs environnementaux tels que la température et la nature et l'amplitude de l'excitation sont des éléments déterminants dans la conception des composants électriques. Un travail de fond sur l'intégration des réseaux piézoélectriques analogues est à mener dans ce sens.

Contents

List of Tables

List of Figures

Chapter 1

Introduction

This short chapter gives some context about the work recorded in this manuscript. The distinction between active and passive damping solutions is explained, and we give references to past and recent works about vibration mitigation by piezoelectric coupling. A numerical example is treated to highlight the interest in piezoelectric analogous network damping, which helps explaining the objectives of the present thesis.

Content

1.1 Motivations and context

Reducing the power consumption in transports has been an issue for the last decades. The main motivations for it were economic reasons. Moreover, the topic of limiting the environmental impact, which has been raised to public knowledge in the last few years, has given incentives to further carry out research on this domain. One way to decrease the power consumption in transports is to reduce the embedded mass. This has finally led to using thinner structures in mechanical engineering. The problem that has consequently appeared is the need for vibration mitigation. Indeed, while thinner structures meet the requirement of reducing the embedded mass, their deflections might be more significant in the case of dynamic loads, which in turn induce noise issues, discomfort, mechanical damage and thus reduced lifespan. Therefore, mechanical vibration damping has been widely studied and remains a current field of research. The common damping solutions include friction dampers, hydraulic dampers, dissipative viscoelastic materials being spread on the structure or electromagnetic systems. There are numerous existing damping solutions, and the present manuscript does not aim at being exhaustive about these.

We concentrate on solutions which involve piezoelectric coupling. The piezoelectric effect allows some materials under stress to generate an electric field. Conversely, these materials are strained when subjected to an electrical field. These are called the direct and inverse piezoelectric effects, respectively. By inserting piezoelectric material in the structure or by bonding piezoelectric elements to its surface, an electromechanical coupling is created. Thus, if the piezoelectric elements are connected to an electrical device, a transfer of energy between the structure and the electrical circuit occurs when the structure vibrates. The ability of the piezoelectric materials to transform mechanical energy into electrical energy has garnered a significant interest in the energy harvesting community [1]. In the present case, however, the goal is not to harvest the vibrating energy, but to damp vibrations. The dissipative elements of the circuits are thus tuned in order not to optimize the power output in the electrical device, but to optimize the vibration mitigation performance.

1.2 Active, passive and in-between solutions

The literature on vibration damping using piezoelectric material is abundant. One way to classify the developed solutions is to separate them between the active ones and the passive ones. The active solutions require external power supplies to work, while the passive solutions do not, as there are composed of passive components or because they use local energy scavengers as power sources. However, this classification is too simplistic to represent the variety of existing possibilities [2]. Thus, we suggest classifying the developed solutions into four main categories:

- **Active**: Active solutions require an external energy source to power the electronic device. Sensors inform about the vibration state of the structure. A command board then adapts the control of actuators according to the perceived information and to the operator orders. In other words, a feedback loop is implemented. This kind of solution leans towards automation, as the design of the actuators command is of prime importance. Sensors or actuators, or both, can be piezoelectric transducers.

- **Semi-active**: Semi-active solutions include components which cannot be passively realized for physical reasons. In this category, we include the use of negative capacitors, inductors or resistors. In most cases, these negative components are realized by specific electronic circuits made of passive components and operational amplifiers. Therefore, they require powering. As opposed to the active solutions previously defined, these solutions do not explicitly include feedback loops nor actuators, but electromechanical transducers.

- **Semi-passive**: Semi-passive solutions require external power supplies to simulate electrical components which are physically realistic. Examples can include synthetic inductors. Note that we do not classify into this category the studies in which inductors of low values are required and are realized using synthetic inductors for practical reasons. We rather categorize as semi-passive solutions the ones involving inductors of very high values, which might be difficult to produce, or the ones using synthetic inductors to adapt the inductance value over time.

- **Fully passive**: For quite some time, fully passive realizations of piezoelectric damping solutions such as the resonant shunt were considered nearly impossible in practice. The reason for this is that the produced inductors should exhibit high inductance and low resistance values for vibra-

tion mitigation at low frequencies, and it was believed to result in large and heavy components. However, the dimensions and the mass of inductors mostly depend on the energy it should store, and not on its inductance value. Hence it has been shown that designing reasonable inductors meeting these criteria is possible [3]. As a consequence, fully passive solutions are made with realizable components that require no external source of power to work.

1.3 Vibration mitigation by piezoelectric coupling

1.3.1 Unimodal damping

Mitigation of mechanical vibrations by piezoelectric coupling has first been proposed by Forward [4], and Hagood and von Flotow derived the equations for the resistive and resonant shunts [5]. The resistive shunt can be described as an electromechanical Lanchester damper [6], or viscoelastic damper: its influence is restricted to a given frequency range, and the resistance is optimized for only one frequency. The interest in this solution is consequently limited.

Therefore, over the years more focus has been given to the resonant shunt, which is an electromechanical tuned mass damper [6] whose absorber is an electrical circuit made of a resistor and an inductor. These electrical components can either be connected in series [7, 8, 9, 10] or in parallel [11, 7, 12, 13]. Meanwhile, the piezoelectric transducer serves as a capacitance in terms of electrical behavior. The association of a capacitance and an inductance generates an electrical resonance. Correctly tuning this resonance, and then adequately setting the resistance of the shunt, allows mitigating the mechanical mode. The efficiency of such a solution is recognized for unimodal damping. However, while several methods have been suggested to tune the electrical components [13, 14, 9, 15], it is commonly accepted that the main limitation of the resonant shunt is that it requires a precise tuning [8, 16, 9] to be efficient. Recent contributions show that research is still conducted on the topic of improving the reliability and the attained performance by resonant shunts and associated circuits [17].

Semi-passive [18, 19] and fully passive non-linear switched shunts [20, 21, 22, 23, 24] have also been developed. Though the switching techniques are more complicated to design and usually reject energy at higher frequencies, hence generating noise, they do not require an as fine tuning as a fully passive resonant shunt. This explains the interest in such solutions.

1.3.2 Multimodal damping with a single piezoelectric transducer

Solutions of piezoelectric coupling have also been developed in order to achieve broadband damping while bonding only one patch on the vibrating structure. Attempts appear in [25], where multi-branch shunts are proposed, whose components are set in order to damp the targeted modes. A few years later, Wu suggested using branches which are described as current-blocking [26], while Behrens et al. developed a multi-mode resonant shunt with current-flowing branches [27]. The team of Moheimani and Fleming then worked on comparing and combining these solutions [28, 29, 27, 30] in semi-passive damping setups. A generalization of such circuits is developed in [31], where the optimized quantity is the shunt impedance. This allows not prescribing the number and placement of electrical components, while still imposing the passivity of the resulting circuit.

Other semi-active proposals notably include negative capacitors [32, 33, 34], for which the interest stems from the virtual increase of the coupling factor by connecting them in parallel with the piezoelectric capacitance. Negative capacitance setups are suited for unimodal and multimodal damping.

All these solutions are limited by the fact that using only one piezoelectric transducer does not allow maximizing the electromechanical coupling for all considered modes [35]. This means that the overall damping performance is limited. Hence, solutions using several piezoelectric transducers have been developed.

1.3.3 Multiple patch-based multimodal damping

Electromechanical dampers involving arrays of piezoelectric transducers can lead to significant and broadband coupling. Moreover, periodically bonding piezoelectric transducers on mechanical structures generates bandgaps, which has garnered interest from researchers of the metamaterials community [36]. While bandgaps usually appear at small wavelengths, and hence are out of scope of the present manuscript, we note that they have been realized for rods [37], beams [38, 39, 40, 41, 42] shells [43] and plates [44, 45, 46, 47, 48, 49, 50]. Nonetheless, higher electromechanical coupling factors can be attained by interconnecting the piezoelectric transducers with electrical components. This is the difference between the solutions based on arrays of independently shunted piezoelectric transducers and structures connected to electrical networks.

1.4 Piezoelectric network damping

1.4.1 Bibliography

Covering a structure with piezoelectric transducers, and interconnecting them with electrical components allows each transducer to participate in the modal coupling. Moreover, it reduces the requirements on the inductance values [51]. The first studied setup proposed by Valis et al. in [52] consists in interconnecting the piezoelectric elements by inductors to create a flexural waves coupler. Substantial coupling is achieved this way. Several other networks have been studied to mitigate vibrations, such as resistive networks [53], networks made of resistors, inductors and capacitors [54, 55, 56, 57], sometimes enhanced with negative capacitors [58], or networks with switching branches composed of inductors and resistors [59, 60, 61, 62].

In the meantime, the principle of piezoelectric network damping emerged in the early 2000s. Vidoli and dell'Isola highlighted the interest in coupling a structure to a medium which exhibits similar wave propagation properties in a context of broadband vibration damping [63]. As a consequence, the electrical analogues of mechanical structures have been revived [64], and the piezoelectric network damping of beams [65, 66, 67] and plates [68, 69] has been investigated. More than ten years later, experimental demonstrations of the concept effectiveness have been conducted for rods [70], beams [71] and plates [72].

Note that the scientific literature referring to the electrical analogues of mechanical structures had not been used to its full potential for nearly fifty years. Before being replaced by the finite element method during the 1960s, mechanical analogues, then called analog computers, were developed as simulation tools. Back then, MacNeal et al. derived the electrical analogues of classical mechanical structures such as beams [73, 74], plates [73, 75] and shells [76] by applying electromechanical analogies [77, 78]. An example of analog computer is given in [79], where the dynamics of an air-frame is simulated with analogous electrical networks.

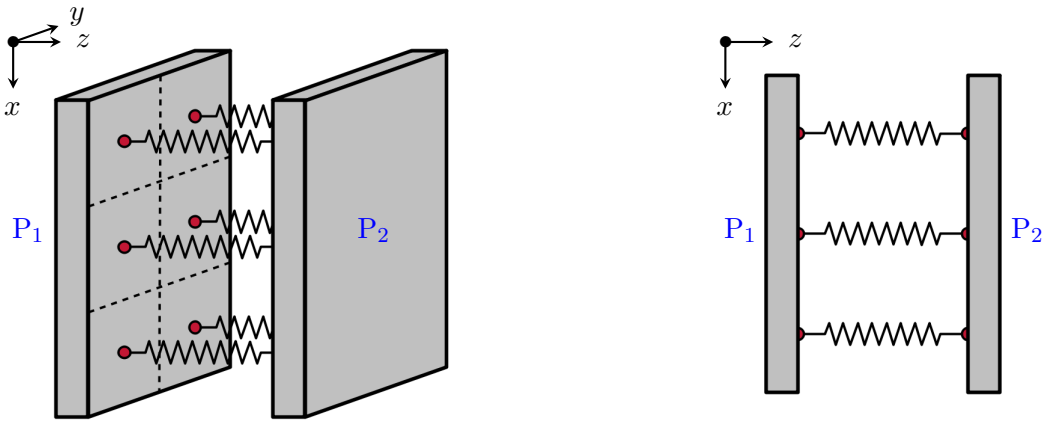

Figure 1.1: Coupling of two analogous plates by longitudinal springs. Though not represented, the boundary conditions are similar for the two plates.

1.4.2 Numerical illustration of the coupling of two analogous structures

Consider the situation presented in figure 1.1: two simply-supported plates are coupled with extension springs. We denote P_1 and P_2 the plates drawn on the left and on the right sides of the illustration, respectively. In this subsection, the subscript 1 means that the quantity refers to the plate P_1, while the subscript 2 refers to the plate P_2. The two structures are analogous to each other. The extension springs prescribe a relationship between the transverse displacements of the upper surface of P_1 and the lower surface of P_2. We propose to study the effect of coupling these two plates on the dynamic response of P_1. A point load is applied to P_1 along the z axis on the location indicated by a ■ marker in figure 1.2.

A finite element formulation of the coupled system in harmonic motion at angular frequency Ω is as follows:

$$\left[\begin{pmatrix} \boldsymbol{K_1} & -\boldsymbol{K_c} \\ -\boldsymbol{K_c}^{\mathrm{T}} & \boldsymbol{K_2} \end{pmatrix} - \Omega^2 \begin{pmatrix} \boldsymbol{M_1} & \boldsymbol{0} \\ \boldsymbol{0} & \boldsymbol{M_2} \end{pmatrix}\right] \begin{pmatrix} \boldsymbol{U_1} \\ \boldsymbol{U_2} \end{pmatrix} = \begin{pmatrix} \boldsymbol{F_1} \\ \boldsymbol{F_2} \end{pmatrix}, \tag{1.1}$$

with $\boldsymbol{M_j}$, $\boldsymbol{K_j}$, $\boldsymbol{U_j}$ and $\boldsymbol{F_j}$ respectively standing for the mass matrix, the stiffness matrix, the vector of nodal displacements and the vector of external loads for the plate P_j. Meanwhile, $\boldsymbol{K_c}$ denotes the coupling matrix. If there are n springs linking the plates, then there are n non-zero terms in $\boldsymbol{K_c}$. All these terms are equal to K_s, which denotes the common spring stiffness, and relate the degrees of freedom of P_1 and P_2 along the z axis at the corresponding nodes. If K_s is too small when compared to the terms in $\boldsymbol{K_1}$ and $\boldsymbol{K_2}$, then P_1 and P_2 have no influence on each other. On the contrary, if K_s is too large, then this means that the springs are nearly rigid, and thus P_2 and P_1 are bonded together.

Length l_x	**Width** l_y	**Thickness**	**Young's modulus**	**Poisson's ratio**	**Density**	K_s
(mm)	(mm)	(mm)	(GPa)	(-)	$(\mathrm{kg/m^3})$	(N/m)
420	360	3	69	0.35	2800	10^4

Table 1.1: Parameters considered to compute the finite element modeling results in figure 1.2.

Therefore, to avoid these uncoupled situations, K_s should be tuned at an intermediate value. This value has been numerically set in order to enhance the visualization of results in figure 1.2. We do not give details about the finite element model here developed, as it is the topic of chapter 3. However, the parameters required to conduct the simulations are recorded in table 1.1.

The results of coupling P_1 and P_2 for different numbers n of springs are shown in figure 1.2. The Frequency Response Functions (FRFs) show that a coupling occurs between the two plates. Note that no damping is taken into account in these simulations. Therefore the peaks in the plotted FRFs in figure 1.2 are infinite, and their heights depend on the frequency step. Even for $n = 1$ in figure 1.2a, multimodal coupling is achieved, as there are antiresonances appearing near the first and fifth modes of P_1. However, no coupling is achieved for the second, third and fourth modes of P_1, which are respectively (2,1), (1,2) and (2,2) plate modes, because the only spring is located on their nodal lines. This illustrates the principle that even though the secondary system is multi-resonant and perfectly tuned, the choice of the locations and design of the coupling elements is significant, whether they are springs or piezoelectric transducers [80].

Therefore, several springs are then considered. Their locations on figures 1.2b, 1.2c and 1.2d ensure a coupling for all modes in the studied frequency range. Indeed, for any mode of the plate P_1, we notice two resulting modes when P_1 and P_2 are coupled. This is a typical result for coupled resonant systems. Meanwhile, the fact that the frequency step between each resulting pair of modes increases with n is an indication that the coupling increases as well, which was expected. In the end, these results induce that broadband energy transfer from a structure to its analogue is possible when coupling them by well-located transducers. For vibration damping purposes, dissipating elements should then be added in P_2 or in the springs.

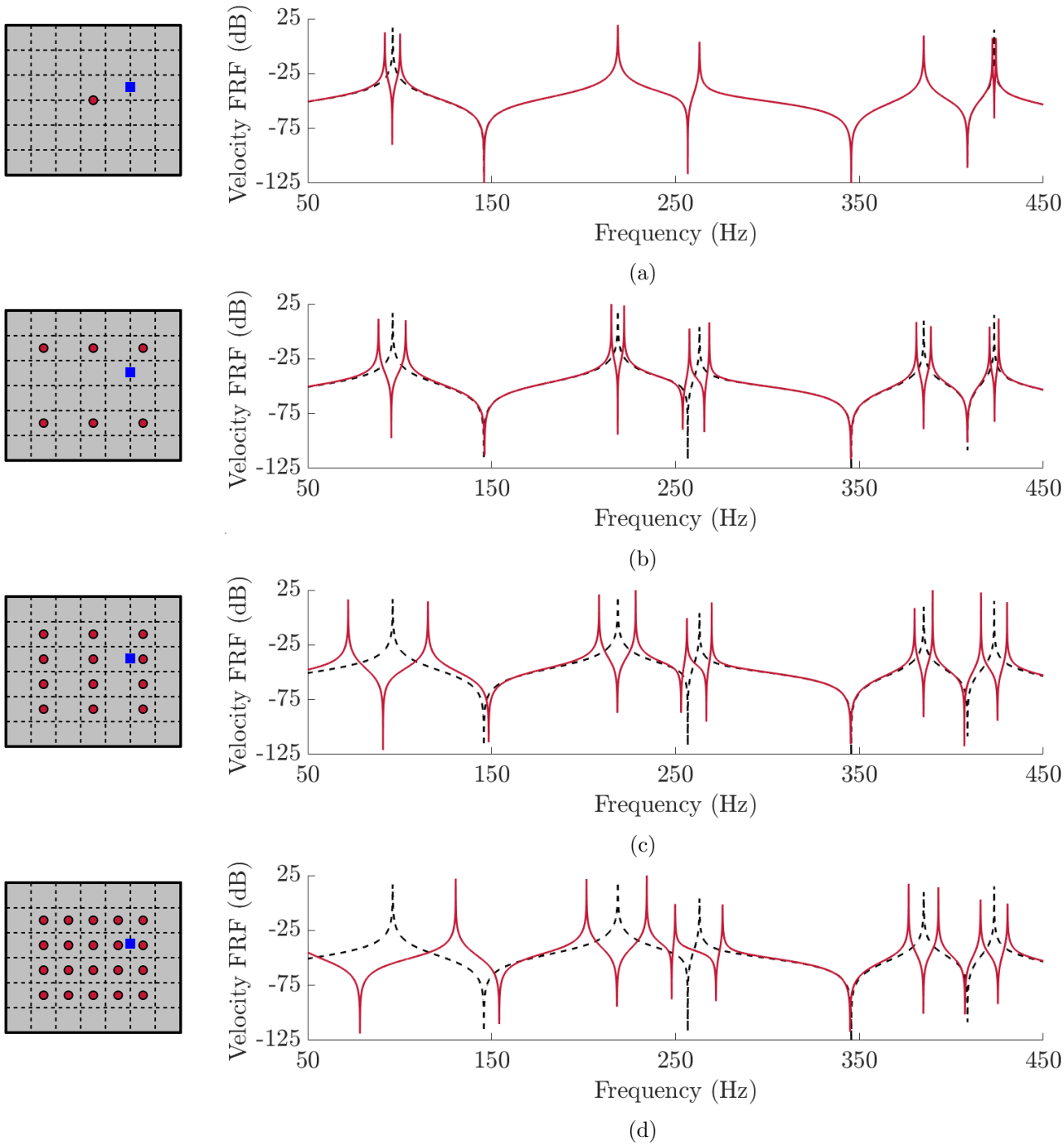

Figure 1.2: On the left-hand side: • (x, y) locations of springs connecting out-of-plane displacements of P_1 and P_2, and ■ (x, y) location of both the point load and the measurement. On the right-hand side: corresponding FRFs when ---- $K_s = 0$ N/m and when —— $K_s = 10^4$ N/m.

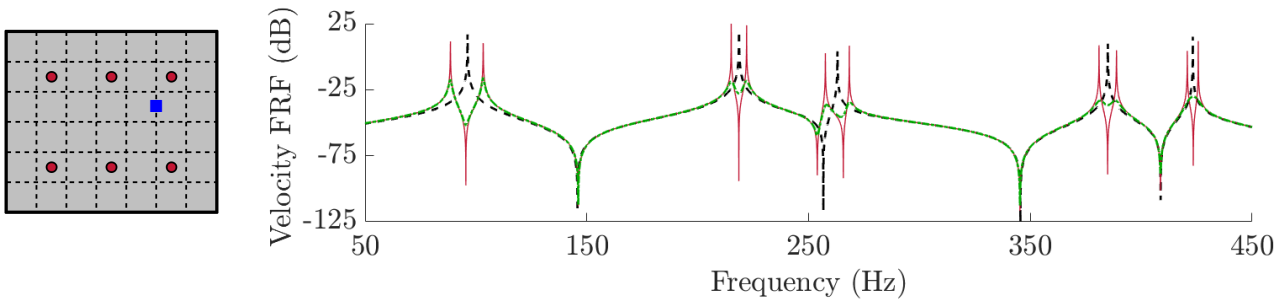

Figure 1.3: On the left-hand side: • (x, y) locations of springs connecting out-of-plane displacements of P_1 and P_2, and ■ (x, y) location of both the point load and the measurement. On the right-hand side: corresponding FRFs when ---- $K_s = 0$ N/m, —— $K_s = 10^4$ N/m and $\xi = 0$, and when -·-·- $K_s = 10^4$ N/m and $\xi = 1$ %.

1.4.3 "Mechanical network" damping

Damping is now taken into account in the numerical model of the plate P_2. In other words, P_2 becomes a vibration absorber for the host structure P_1. A simple way to make the coupled system non-conservative is to implement hysteretic damping in P_2. The mechanical damping matrix $\boldsymbol{D_2}$ is therefore related to the stiffness matrix $\boldsymbol{K_2}$ by a damping coefficient ξ:

$$\boldsymbol{K_2} + \mathrm{j}\Omega\boldsymbol{D_2} = (1 + 2\mathrm{j}\xi)\,\boldsymbol{K_2}, \qquad \text{which is equivalent to} \qquad \boldsymbol{D_2} = \frac{2\xi}{\Omega}\,\boldsymbol{K_2}, \tag{1.2}$$

with $\mathrm{j}^2 = -1$. The finite element formulation of the coupled system thus becomes:

$$\left[\begin{pmatrix} \boldsymbol{K_1} & -\boldsymbol{K_c} \\ -\boldsymbol{K_c}^{\mathrm{T}} & (1 + 2\mathrm{j}\xi)\,\boldsymbol{K_2} \end{pmatrix} - \Omega^2 \begin{pmatrix} \boldsymbol{M_1} & \boldsymbol{0} \\ \boldsymbol{0} & \boldsymbol{M_2} \end{pmatrix}\right] \begin{pmatrix} \boldsymbol{U_1} \\ \boldsymbol{U_2} \end{pmatrix} = \begin{pmatrix} \boldsymbol{F_1} \\ \boldsymbol{F_2} \end{pmatrix}. \tag{1.3}$$

An example of resulting FRF is plotted in figure 1.3. It shows that for a non-zero damping coefficient ξ, broadband damping is achieved. A value of 1 % is the limit value of ξ over which the fifth plate mode becomes overdamped and the associated damping performance decreases. This numerical example illustrates that there is a significant interest in coupling a structure to an analogous absorber for multimodal vibration damping purposes. Several models of damping could then be considered in the absorber to optimize the damping over the frequency range of interest.

Spatial and frequency coherence conditions

In this numerical example, the two coupled plates are identical: they are made of the same material, share the same dimensions, and are subjected to the same boundary conditions. However, a similar dynamics is attained if P_1 is coupled to a structure P_2 which behaves as its analogue. This means that P_2 can have different dimensions while keeping the same overall shape, and can be made in another material, as long as its modal properties are identical to those of P_1. More details are given in chapter 2.

1.4.4 Extension to various kinds of coupling

An observation of significant importance is that any coupling between two analogous structures would result in the same broadband transfer of energy, and thus in vibration mitigation if the absorber include dissipative elements. Indeed, any coupled system that can be formulated as in the equation (1.1) behaves similarly. In other words, for a vibrating structure P_1, several situations are conceivable for the absorber P_2 and the coupling between them. To this end, analogies between mechanical, electrical, acoustical and hydraulic systems could be considered [77, 78, 81]. Meanwhile, the coupling matrix $\boldsymbol{K_c}$ can be induced by springs connections, such as in figure 1.1, or by piezoelectric or electromagnetic transducers in the case of electromechanical systems. Another potential case of application is the vibroacoustic coupling between a structure and its analogous cavity.

In this manuscript, we investigate replicating the results in figure 1.2 with piezoelectric coupling. In other words, we want to replace the absorber P_2 by a multi-resonant network, which is the electrical analogue of the vibrating structure. Meanwhile, the springs are replaced by piezoelectric transducers. Damping would then be added through electrical resistance in the absorber in order to improve the vibration mitigation performance.

1.5 Assumptions and manuscript outline

1.5.1 Fully passive solutions

Nowadays, there are solutions to integrate complex electrical devices into limited space. Using active and programmable components, or 3D printing miniaturized components, are examples of such solutions. However, the present work aims at developing fully passive electrical networks for vibration mitigation purposes. This choice is mainly motivated by three reasons:

- **Treating physics-related problems**:

  Developing active solutions requires considering elements which are not directly influential on the damping performance, such as the power sources of the active components. Besides, active solutions might lead to instabilities which can annihilate the damping performance if not compensated [82]. We choose not to consider these options. Indeed, the study of piezoelectric network damping requires first answering other questions related to the development of electrical analogues and their coupling with mechanical structures, before thinking about the potential integration of such electrical dampers.

- **Avoiding the difficulties related to certification processes**:

  Designed vibration damping devices in industrial applications must be submitted to certification bodies to ensure their compliance with predefined criteria. This certification is more complicated to obtain for damping solutions which require powering, as more proofs should be given. This is done to ensure that the powering system cannot amplify the structure vibrations or deteriorate parts of the electromechanical system. Though the piezoelectric network damping solutions we develop are not matured enough for industrial integration, this stands as a reason against leaning towards active control for now.

- **Avoiding power supplies connection problems**:

  In some cases, connecting an active solution to its energy source remains a problem. The situation of a rotating machine comes to mind. Consider the example of a turbine blade whose vibrations should be damped by piezoelectric coupling. Powering the electronic device requires connecting the piezoelectric transducers attached to the blade to the energy source which is attached to the frame. Therefore a specific connection technology is needed, such as brushes for DC electric motors, whose lifespan is limited.

Even though we do not close the door on developing semi-passive, semi-active or active solutions in future works, we thus commit to design fully passive solutions in this manuscript. The long-term objective is to highlight the limits of such solutions, which might then justify going towards more integrated electronic devices.

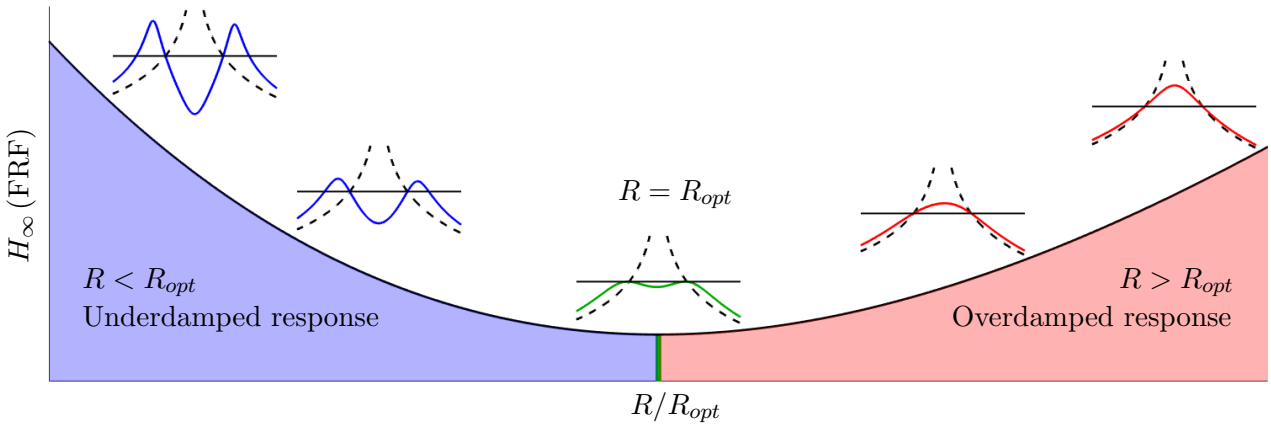

Figure 1.4: Principle of resistance value tuning based on the computation of the infinite norm of a FRF for the coupled system.

1.5.2 Tuning of the resistive components

The objective is to damp the structural modes of largest wavelengths, as they usually are the most energetic ones. In most cases, for thin structures this corresponds to modes at frequencies between tens of Hertz and several kHz. However, low frequencies often present challenges in terms of passive components production. This is mostly due to passive inductors, which exhibit poor quality factors at low frequencies. Consequently, low resistance values are required to avoid overdamping the coupled system. Though each situation has its own particularities, in most cases the objective is to design inductors and transformers so that their internal resistance R is inferior to an optimal value R_{opt}. Assume that the frequency range of interest is limited by the minimum f_{min} and maximum f_{max} frequencies, then we suggest using the infinite norm H_∞ of a FRF of the coupled system to evaluate the vibration mitigation performance:

$$\underset{[f_{\min}:f_{\max}]}{H_\infty}(\mathrm{FRF}) = \mathrm{Max}\left(\left|\mathrm{FRF}\left(2\pi f\right)\right|, f_{\min} \leq f \leq f_{\max}\right). \tag{1.4}$$

The notions of underdamped and overdamped responses are illustrated in figure 1.4. For R above the optimal value R_{opt}, the infinite norm of the FRF increases, and the vibration mitigation thus deteriorates. Besides, if R is below R_{opt}, R can be virtually increased by adding a resistor in series with it. Thus, in this manuscript we ensure that every developed network can be produced with fully passive components while avoiding overdamping the coupled system.

Note that different optimization processes exist. In the case of the resonant shunt, other criteria have been investigated in the frequency domain [9], though most of them lead to resistors of the same order of magnitude. In the time domain, an example of vibration damping optimization through pole-placement technique consists in maximizing the damping ratio [83, 84, 8]. This last kind of tuning leads to higher values of resistance than obtained with the H_∞-norm minimization presented in figure 1.4. In other words, the criterion we use is more restrictive in terms of produced components than the one classically used in the time domain.

1.5.3 Outline of the manuscript

In chapter 2, we suggest a method to derive passive electrical analogues of mechanical structures. This method most notably defines the spatial and frequency coherence conditions, which are the requirements for ensuring identical wave propagation properties in the electrical and mechanical media. It is then applied to cases of rods, bars, straight and curved beams, plates and tubes. Deriving their analogues brings the opportunity to develop tools for the study of piezoelectric network damping for complex structures.

In chapter 3, we recall the finite element model of a structure covered by thin piezoelectric transducers. A setup of a simply-supported plate covered by piezoelectric patches is then realized, and is used to conduct the validation of the developed model. Then, finite element formulations of a structure coupled by piezoelectric patches to electrical circuits are derived. The treated cases of electrical circuits are shunts and electrical networks, for which the finite element formulation is similar to the one in equation (1.1).

In chapter 4, we produce the simply-supported plate electrical analogue. Design methods for inductors and transformers are detailed and applied to ensure that the network is not too resistive once vibration damping tests are conducted. The network behavior is validated by comparison with experiments. Finally, broadband vibration mitigation is achieved, and experimental results are used to validate the coupled finite element formulation derived in the previous chapter.

In chapter 5, we finally extend the concept of piezoelectric network damping to complex structures. The principle is to assemble unit cells of the library created in chapter 2 to make up adequate electrical analogues. A first non-periodic case allows validating the finite element electromechanical model by comparison with experiments in a complex case. The other treated structures are numerical examples of a variable thickness plate, a plate with various boundary conditions, an arch and a ring. Piezoelectric network damping with fully passive networks is performed for all these structures.

In chapter 6, we evaluate the results and the contributions of the present thesis. After that, we suggest potential future works. These include investigating piezoelectric network damping of even more complex structures by assembling networks made of previously derived electrical unit cells. There is also interest in designing passive electrical components by taking energetic and temperature considerations into account for the integration of analogous networks in practical applications.

Objectives

The objectives of this work are to:

- Create a library of elementary electrical analogues.
- Propose a method to derive low-frequency electrical analogues of complex structures, based on assembling elementary analogues from the library.
- Develop a predictive finite element model of a structure covered by thin piezoelectric transducers and coupled to an electrical network.
- Develop tools for the analogy validation between a structure and an electrical network.
- Investigate the piezoelectric network damping of complex structures, while assuring that a fully passive realization would be achievable in practice.

Chapter 2

Electrical analogues of mechanical structures

The objective of the present chapter is to create a library of electrical analogues of mechanical structures. Only inductors, capacitors, resistors and transformers can be used so that the resulting electrical network is fully passive. The derivation of the electrical analogues of the library is conducted by applying an electromechanical analogy to a discretized mechanical model. Electrical analogues are finally validated if they exhibit similar wave propagation properties as their analogous mechanical structures. This is ensured by comparing mechanical and electrical modal properties. The design method is detailed in this chapter, and is then applied to mechanical structures such as rods, straight and curved beams, plates and tubes. The analogy validation is conducted on several numerical examples.

Content

2.1 Introduction

The use of the finite element method as a modeling tool for static or low-frequency dynamic problems is widespread nowadays. The first digital computers which were able to run small finite element simulations date back to the 1950s, but it is only during the 1960s that we witnessed a gain of popularity for this method. The rise of the finite element method coincides with the extension of processing power. Before that, simulations or experiments could be made with analog computers. In particular, the behavior of mechanical systems could be simulated by using electrical networks. These networks were designed to exhibit similar static or dynamic behavior as their associated mechanical systems. Researchers and engineers could then access internal variables such as displacements or shear forces by measuring electrical currents or voltages in the produced physical networks. For these reasons, developing electrical analogues was a prolific field of interest back then. R. H. MacNeal and his colleagues did an extensive work about designing electrical analogues of mechanical structures. More precisely, they proposed electrical analogues of beams [73, 79, 74], plates [73] and shells [76].

Most of these works have been left out once the finite element method became a global standard for mechanical simulations. However, the concept of designing analogous structures has been revived at the beginning of the 2000s for vibration damping purposes [64]. Indeed, Vidoli and dell'Isola showed that coupling the vibrating structure to a network that has the same modal properties ensures that there is as much electrical energy as mechanical energy involved in the coupled system [63]. As a consequence, the principle of piezoelectric network damping emerged [51, 54, 55].

One way to define electrical analogues is to use an electromechanical analogy [77, 78]. In the early 2000s, piezoelectric network damping of beams [65, 66, 67] and plates [68, 69] has been studied. Most of these works are based on the application of the force-current and velocity-voltage analogy, also called indirect analogy [77]. In the present work, the force-voltage and velocity-current analogy, also called direct electromechanical analogy, is applied. Indeed, this analogy allows representing the electromechanical converter of a coupled system with passive electrical components when this converter uses the action of electrostatic forces [77]. Thus, it is a convenient analogy to use to represent piezoelectric coupling with passive electrical components. Hence, one can derive a fully passive repre-

sentation of a mechanical structure coupled to an electrical network via piezoelectric transducers. The resulting electrical analogues have been implemented recently for the vibration mitigation of rods [70], beams [71] and plates [72, 85].

The long-term objective is to define analogous electrical networks in order to damp vibrations of complex structures, which include curvatures, varying geometrical parameters and anisotropic materials. A solution would be to define an electrical analogue for each considered structure. However, it might become difficult to do so for any 3D structure. Therefore, rather than defining ever more complex analogous networks, the idea is to create a library of basic analogous unit cells. Different unit cells could then be assembled to model the dynamics of the complex structure. An example of this is available in [79], where the dynamics of an air-frame is replicated by an assembly of beam elements in bending and torsion. The vibration analysis of the structure is then conducted by making measurements in the network.

The present chapter aims at creating this library of simple electrical analogues. After exposing the available electrical components in section 2.2 and describing the method to derive an electrical analogue in section 2.3, different unit cells are developed. In the end, the library is composed of electrical analogues of rods, bars, straight and curved beams, plates and tubes.

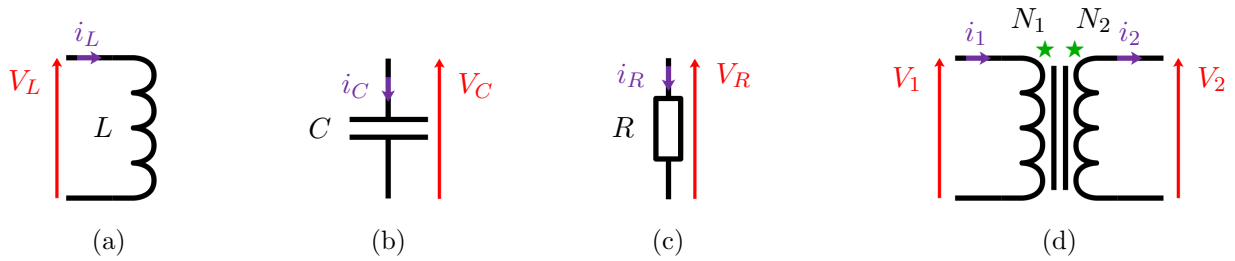

(a) (b) (c) (d)

Figure 2.1: Schematic representation of the four ideal purely passive electrical components: (a) an inductor, (b) a capacitor, (c) a resistor and (d) a transformer.

2.2 Available ideal passive electrical components

The focus of this work is to find purely passive electrical analogues of mechanical structures. For this reason, only passive electrical components should be part of the resulting analogue. The four classical passive components are sketched in their ideal versions in figure 2.1. An inductor of inductance L and a capacitor of capacitance C relate the respective electrical currents i_L and i_C flowing through them to the voltages V_L and V_C at their terminals by first order time differential equations:

$$V_L = L\,\frac{di_L}{dt}, \qquad i_C = C\,\frac{dV_C}{dt}. \tag{2.1}$$

On the other hand, a resistor of resistance R demands a linear relation between the electrical current i_R flowing through it and the voltage drop V_R across it:

$$V_R = R\,i_R. \tag{2.2}$$

Lastly, a transformer is a two-port circuit which has two windings of conductive wire: a primary one of N_1 turns, and a secondary one of N_2 turns. Its related terminals, which are indicated by star symbols ★ in figure 2.1d, inform about the winding direction. With the electrical currents i_1 and i_2 and the voltages V_1 and V_2 pointing towards the related terminals, a transformer of ratio $\hat{a} = N_1/N_2$ gives the following characteristic:

$$\hat{a} = \frac{N_1}{N_2} = \frac{i_2}{i_1} = \frac{V_1}{V_2}. \tag{2.3}$$

Commonly accepted representations of transformers do not indicate the position of the related terminals. Indeed, most representations implicitly place them on the same side of the transformer, such as in figure 2.1d. As a consequence, the related terminals not appearing on sketches thereafter follow this implicit rule.

As a side note: only the resistor is a dissipative component in its ideal representation. Indeed, ideal inductors and capacitors store and release electrical energy but do not dissipate it. Meanwhile, the transformer characteristic of equation (2.3) shows that $V_1\, i_1 = V_2\, i_2$, which means that there is no loss in the power transfer from the primary to the secondary. Models of non-ideal components, which include internal resistances and parasitic elements will be discussed later on.

2.3 Design of electrical analogues of mechanical structures

2.3.1 Mechanical continuous equation in harmonic motion

Vibrations of continuous mechanical media can be described by partial differential equations relating displacements to external loads. These commonly accepted equations derive from the vibration theories of thin rods, straight and curved Euler-Bernoulli beams and Kirchhoff-Love plates. They represent the starting points of the analysis.

Moreover, we assume the separation of the space and time variables. If M denotes the position and t the time, this means that any function $u(M,t)$ can be expressed by a product of independent functions, so that $u(M,t) = U(M) \cdot g(t)$. By relating u to its time derivatives thanks to the angular frequency Ω, the dynamics of a structure in harmonic motion is derived from its motion equation in the time domain by applying $dg/dt = \mathrm{j}\Omega g$, and thus $\partial u/\partial t = \mathrm{j}\Omega u$, with $\mathrm{j}^2 = -1$.

2.3.2 Set of zero or first order mechanical continuous equations

To design a purely passive electrical analogue of a mechanical structure, only the passive electrical components described in section 2.2 can be used. The characteristics of said-passive components are written in equations (2.1), (2.2) and (2.3). These equations relating voltages to electrical currents are either linear or first order differential equations. Hence, it is required to replace the partial differential equation describing the structure dynamics by a set of zero or first order differential equations as well. Since the dynamics of mechanical structures is usually described by partial differential equations whose orders are superior to two, intermediate quantities should be introduced. For example, these intermediate quantities can be the bending moment, the shear force and the slope for an Euler-Bernoulli beam. Besides, we will highlight in sections 2.6 and 2.7 that the design of an electrical analogue depends on the chosen set of intermediate quantities, which is not unique.

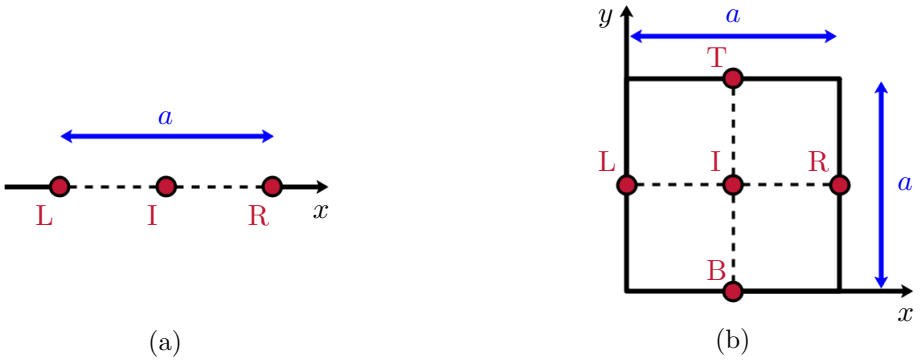

(a) (b)

Figure 2.2: (a) 1D and (b) 2D discretization schemes, where I, B, L, R, T refer to the central, bottom, left, right and top positions, respectively.

2.3.3 Finite difference scheme

The next step is to define a discrete model of the mechanical structure. The choice of the discretization grid is important since it leads to more or less complex discrete systems [86]. We choose to use the simplest discretization grid so that the resulting number of components in the discrete unit cell is as low as possible. This is done by applying a first order finite difference pattern to the set of continuous mechanical equations previously obtained. The discretization scheme which is used to derive a 1D discrete model of the structure is represented in figure 2.2a. We consider the following finite difference expressions for any physical quantity g:

$$\left(\frac{\partial g}{\partial x}\right)_{\mathrm{I}} = \frac{g_{\mathrm{R}} - g_{\mathrm{L}}}{a}, \qquad \left(\frac{\partial g}{\partial x}\right)_{\mathrm{L}} = \frac{g_{\mathrm{I}} - g_{\mathrm{L}}}{a/2}, \qquad \left(\frac{\partial g}{\partial x}\right)_{\mathrm{R}} = \frac{g_{\mathrm{R}} - g_{\mathrm{I}}}{a/2}. \tag{2.4}$$

The derivation of a 2D discrete model of a mechanical structure involves the grid in figure 2.2b and some additional finite difference equations:

$$\left(\frac{\partial g}{\partial y}\right)_{\mathrm{I}} = \frac{g_{\mathrm{T}} - g_{\mathrm{B}}}{a}, \qquad \left(\frac{\partial g}{\partial y}\right)_{\mathrm{B}} = \frac{g_{\mathrm{I}} - g_{\mathrm{B}}}{a/2}, \qquad \left(\frac{\partial g}{\partial y}\right)_{\mathrm{T}} = \frac{g_{\mathrm{T}} - g_{\mathrm{I}}}{a/2}. \tag{2.5}$$

Refined finite difference schemes exist, in order to take second order variations into account for example. These refined schemes are not considered since they would lead to circuits with more electrical components.

Mechanical quantities	**Electrical quantities**	
	Direct analogy	Indirect analogy
Force $-F$ and moment $-M$	Voltage V	Electrical current i
Linear velocity $\dot{u}$ and angular velocity $\dot{\theta}$	Electrical current i	Voltage V
Displacement u and orientation θ	Electrical charge q	Voltage primitive $\int V$
Compliance	Capacitance C	Inductance L
Mass and rotational inertia	Inductance L	Capacitance C
Viscous damping	Resistance R	Conductance $1/R$

Table 2.1: Direct and indirect electromechanical analogies. When possible, the color coding of representing forces, moments and voltages in red and displacements, velocities, electrical charges and electrical currents in purple will be applied in the drawings and circuits of the present manuscript.

2.3.4 Electromechanical analogy

An electromechanical analogy [77, 78] is then applied to the resulting set of discrete mechanical equations. The indirect analogy, which states that velocities are analogous to voltages and forces are analogous to electrical currents, is considered in some works [73, 68]. This analogy is summed up in table 2.1. It is particularly well suited to the study of electromagnetic systems, as it allows the passive representation of the electromagnetic coupling [77].

In the present work, we consider the direct electromechanical analogy [77], which states that voltages and electrical currents are respectively analogous to forces and velocities. It is summed up in table 2.1. Once the electrical equations are written, the mechanical structure and its electrical analogue can both be represented by a lumped-element electrical circuit. Note that this analogy is preferred because it allows the fully passive representation of piezoelectric transducers [77]. Moreover, in most cases, the electrical analogues of clamped, simply-supported and free edges can be obtained with fully passive electrical components by applying this analogy.

Finally, several analogous unit cells are assembled to produce a structure analogue. The assembled network is a multi-resonant system, whose modal properties can be modified by acting on its boundary conditions and on its components characteristics. Therefore, conditions should be applied to ensure that the network exhibits the desired dynamics.

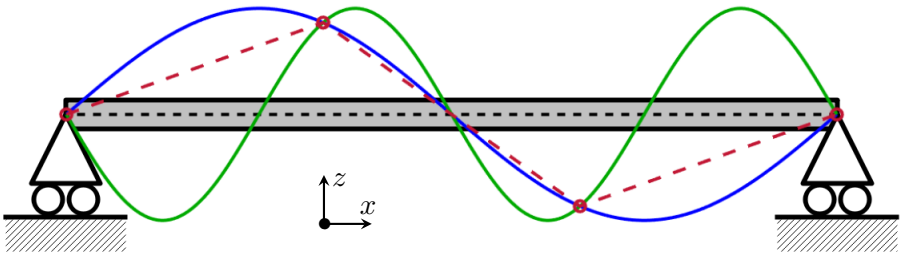

Figure 2.3: —— Second and —— fourth bending mode deflection shapes of a simply-supported beam, as well as – – the aliased visualization with 3 elements.

2.3.5 Spatial and frequency coherence conditions

The next objective is that the mechanical structure and its analogous electrical network have the same modal properties. This means that the electrical analogue should meet:

- **The spatial coherence condition**: The electrical network should exhibit the same mode shapes as the mechanical structure. To meet this condition, the electrical unit cell can be derived from the discrete mechanical model which forecasts the dynamic behavior of the structure well enough. Furthermore, the mechanical boundary conditions should be adequately reproduced in the electrical network. Finally, a requirement is to adapt the structure discretization to the frequency range over which the analogy should be validated. Indeed, having too few elements leads to a poor discretization of the mode shapes. An example of the spatial aliasing induced by having too few elements is drawn in figure 2.3. A first criterion to meet the spatial coherence condition can be to consider at least ten elements per wavelength:

$$\frac{n_{elm}}{N_{max}} \geq 10, \tag{2.6}$$

  where n_{elm} is the number of elements of the structure, and N_{max} is the maximum number of wavelengths among the modes of the considered frequency range. This criterion can be part of the design process: once the frequency range is fixed, the natural frequencies and mode shapes can be predicted. We can forecast the value of N_{max}, and so an approximation of n_{elm}. In the numerical examples later on, this condition is met by increasing the number of elements.

- **The frequency coherence condition**: The electrical network and the mechanical structure should have similar wave propagation properties. If the spatial coherence condition is met, then ensuring that they share the same natural frequencies is equivalent to ensuring that they exhibit the same wave propagation properties. Therefore, the electrical components of the network should be tuned to meet this condition.

  Note that applying a strict electromechanical analogy is not mandatory: while setting each inductance of the network to the value of the corresponding discrete mass of the discrete mechanical model is a possibility, the network can exhibit similar natural frequencies as the structure with different sets of electrical components. In other words, there are degrees of freedom in the network tuning. This principle can be understood in the case of a tuned mass damper [6], which can be regarded as a one-degree-of-freedom absorber that is coupled to the structure. Without considering performance issues, an infinite number of combinations of stiffness and mass can be used to mitigate the structure vibrations at a targeted frequency. One constraint is that the square root of the ratio stiffness over mass of the absorber should be tuned to the targeted frequency to be damped: this is the frequency coherence condition of the tuned mass damper.

  The derivation of the frequency coherence condition is based on the 1D unit cells representations in figure 2.4. The notations are adapted from the table 2.1 and the figure 2.2a: u, F, q and V respectively denote displacements, mechanical loads, electrical charges and voltages, while the L and R subscripts signal the left and right positions of the unit cells. Finally, the $\star$ superscript indicates nondimensionalized quantities. The mechanical and electrical transfer matrices $\boldsymbol{T}_{\boldsymbol{m}}^{\star}$ and $\boldsymbol{T}_{\boldsymbol{e}}^{\star}$ of the discretized systems relate quantities on the left-hand side to quantities on the right-hand side of the unit cells:

$$\begin{pmatrix} u_{\mathrm{R}}^{\star} \\ -F_{\mathrm{R}}^{\star} \end{pmatrix} = \boldsymbol{T}_{\boldsymbol{m}}^{\star} \begin{pmatrix} u_{\mathrm{L}}^{\star} \\ -F_{\mathrm{L}}^{\star} \end{pmatrix}, \qquad \begin{pmatrix} q_{\mathrm{R}}^{\star} \\ V_{\mathrm{R}}^{\star} \end{pmatrix} = \boldsymbol{T}_{\boldsymbol{e}}^{\star} \begin{pmatrix} q_{\mathrm{L}}^{\star} \\ V_{\mathrm{L}}^{\star} \end{pmatrix}. \tag{2.7}$$

  Consequently, the frequency coherence condition is met when $\boldsymbol{T}_{\boldsymbol{e}}^{\star} = \boldsymbol{T}_{\boldsymbol{m}}^{\star}$. Both systems would then have similar wave propagation properties, and thus equal natural frequencies if exhibiting analogous boundary conditions.

(a) (b)

Figure 2.4: Schematic representation of (a) a mechanical unit cell and (b) an electrical unit cell of the corresponding discrete models.

2.3.6 Unit cells assembly

To define an electrical analogue of a continuous mechanical structure, several unit cells should be assembled. As stated before, the more cells used to discretize the network, the wider the frequency range over which the analogy will be validated. To model the behavior of the assembled network, we propose to assemble elementary matrices just like in the finite element method. These matrices should relate external voltages to electrical charges, such as prescribed by the direct electromechanical analogy in table 2.1. Using the notations of equation (2.7), the electrical transfer matrix $\boldsymbol{T_e^{\star}}$ can be separated in four square submatrices:

$$\boldsymbol{T_e^{\star}} = \left(\begin{array}{c|c} \boldsymbol{A} & \boldsymbol{B} \\ \hline \boldsymbol{C} & \boldsymbol{D} \end{array}\right), \tag{2.8}$$

so that

$$q_{\mathrm{R}}^{\star} = \boldsymbol{A} q_{\mathrm{L}}^{\star} + \boldsymbol{B} V_{\mathrm{L}}^{\star}, \qquad V_{\mathrm{R}}^{\star} = \boldsymbol{C} q_{\mathrm{L}}^{\star} + \boldsymbol{D} V_{\mathrm{L}}^{\star}. \tag{2.9}$$

The objective is to derive the elementary dynamic matrix $\boldsymbol{D_e^{\star}}$, which is defined by:

$$\begin{pmatrix} V_{\mathrm{L}}^{\star} \\ -V_{\mathrm{R}}^{\star} \end{pmatrix} = \boldsymbol{D_e^{\star}} \begin{pmatrix} q_{\mathrm{L}}^{\star} \\ q_{\mathrm{R}}^{\star} \end{pmatrix}. \tag{2.10}$$

Starting from equations (2.9), $\boldsymbol{D_e^{\star}}$ can be identified:

$$\boldsymbol{D_e^{\star}} = \left(\begin{array}{c|c} -\boldsymbol{B}^{-1}\boldsymbol{A} & \boldsymbol{B}^{-1} \\ \hline \boldsymbol{D}\boldsymbol{B}^{-1}\boldsymbol{A} - \boldsymbol{C} & -\boldsymbol{D}\boldsymbol{B}^{-1} \end{array}\right). \tag{2.11}$$

Note that the dynamic matrix is defined only if $\boldsymbol{B}$ is invertible. This condition can be interpreted from equation (2.9), in which setting $q_{\mathrm{L}}^{\star} = 0$ for comprehension purposes does not restrain the problem: if $\boldsymbol{B}$ is invertible, then $V_{\mathrm{L}}^{\star}$ can be calculated once the electrical charges $q_{\mathrm{R}}^{\star}$ are set. In a more general way,

this means that imposing the boundary electrical charges of the unit cell allows deriving the boundary voltages. From a mechanical point of view, this corresponds to being able to determine the boundary mechanical loads when the displacements are prescribed. If the discrete model is ill-defined, that is to say if $\boldsymbol{B}$ is singular, then some numerical parameter must be added to enable further simulations. This is the case for the electrical analogue of beams in section 2.6, plates in section 2.7, curved beams in section 2.8 and tubes in section 2.9.

We want to point out that the dynamic matrix $\boldsymbol{D}_e^\star$ relating nondimensionalized voltages to nondimensionalized electrical charges is not the required matrix going forward. The needed matrix is denoted $\boldsymbol{D_e}$, and relates dimensionalized quantities:

$$\begin{pmatrix} V_{\mathrm{L}} \\ -V_{\mathrm{R}} \end{pmatrix} = \boldsymbol{D_e} \begin{pmatrix} q_{\mathrm{L}} \\ q_{\mathrm{R}} \end{pmatrix}. \tag{2.12}$$

If $\boldsymbol{B}$ is invertible, then the dynamic matrix $\boldsymbol{D_e}$ can be expressed, and so the elementary matrices of electrical "mass" $\boldsymbol{M_{elm}}$ and of electrical "stiffness" $\boldsymbol{K_{elm}}$ can be extracted. The suggested method is to set the angular frequency Ω at zero to derive $\boldsymbol{K_{elm}}$, and to calculate $\boldsymbol{M_{elm}}$ afterwards:

$$\boldsymbol{K_{elm}} = \boldsymbol{D_e}|_{\Omega=0} \qquad \text{and} \qquad \boldsymbol{M_{elm}} = \frac{\boldsymbol{K_{elm}} - \boldsymbol{D_e}}{\Omega^2}. \tag{2.13}$$

According to the direct electromechanical analogy in table 2.1, $\boldsymbol{M_{elm}}$ should depend on the inductive quantities of the unit cell, while $\boldsymbol{K_{elm}}$ should depend on the capacitive quantities.

Then, following a geometric assembly process, the vectors $\boldsymbol{Q_N}$ and $\boldsymbol{V_N}$ which contain the values of electrical charges and external voltages in the entire network are related to each other by

$$\boldsymbol{V_N} = \left(\boldsymbol{K_N} - \Omega^2 \boldsymbol{M_N}\right) \boldsymbol{Q_N}, \tag{2.14}$$

with $\boldsymbol{M_N}$ and $\boldsymbol{K_N}$ being respectively the assembled matrices of electrical "mass" and electrical "stiffness". The equation (2.14) is the matrix formulation from which all further electrical analogues models will be developed.

Electrical damping matrix

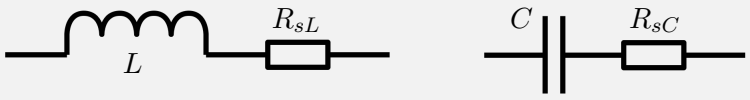

Figure 2.5: Inductor and capacitor with series resistors.

In the following chapters, electrical damping is added in order to mitigate mechanical vibrations. Thus it should be included in the unit cell formulation. The simplest way to do so is to model the capacitive and inductive components as non-ideal, such as represented in figure 2.5. Let us assume that $\boldsymbol{K_{elm}}$ and $\boldsymbol{M_{elm}}$ are respectively proportional to the inverse of a capacitance $1/C$ and an inductance L:

$$\boldsymbol{K_{elm}} = \frac{1}{C}\,\boldsymbol{K_0} \qquad \text{and} \qquad \boldsymbol{M_{elm}} = L\boldsymbol{M_0}. \tag{2.15}$$

Depending on the network topology, these two relations might get more complicated and involve different terms corresponding to different parasitic elements. We only explain the case of the series resistances here, as it is the most basic one. Indeed, in harmonic behavior at angular frequency Ω, the parasitic series resistances can be included in the model by replacing $1/C$ by $1/C + \mathrm{j}\Omega R_{sC}$ and L by $L + R_{sL}/\mathrm{j}\Omega$, with $\mathrm{j}^2 = -1$. This means that we can define an electrical damping matrix $\boldsymbol{D_{elm}}$:

$$\left(\frac{1}{C} + \mathrm{j}\Omega R_{sC}\right)\boldsymbol{K_0} - \Omega^2\left(L + \frac{R_{sL}}{\mathrm{j}\Omega}\right)\boldsymbol{M_0} = \boldsymbol{K_{elm}} + \mathrm{j}\Omega\boldsymbol{D_{elm}} - \Omega^2\boldsymbol{M_{elm}},$$
$$\text{with } \boldsymbol{D_{elm}} = R_{sC}\boldsymbol{K_0} + R_{sL}\boldsymbol{M_0}. \tag{2.16}$$

This expression of $\boldsymbol{D_{elm}}$ is an electrical analogue of the mechanical model of Rayleigh damping. Therefore, series resistances can directly be included in the following network models, since assembling elementary matrices $\boldsymbol{D_{elm}}$ would make the equation (2.14) include an assembled damping matrix $\boldsymbol{D_N}$:

$$\boldsymbol{V_N} = \left(\boldsymbol{K_N} + \mathrm{j}\Omega\boldsymbol{D_N} - \Omega^2\boldsymbol{M_N}\right)\boldsymbol{Q_N}. \tag{2.17}$$

We do not use this equation before chapter 3, since the notion of damping does not appear in the process of defining electrical analogues of mechanical structures. Indeed, note that the objective is not to design electrical analogues exhibiting damping properties which are analogous to those of mechanical structures: structures are supposedly slightly damped, while assembled networks for vibration damping purposes exhibit non-negligible electrical damping. This is illustrated by measurements conducted in section 4.4 on an assembled plate electrical analogue.

2.3.7 Analogy validation

The designed electrical analogue should have the same modal properties as the mechanical structure. These modal properties can be either extracted from experiments following an experimental modal analysis, or simulated. Simulations are the chosen path in this chapter. Modal properties of the electrical network are obtained by solving the eigenvalue problem associated to the equation (2.14) in harmonic behavior at angular frequency Ω:

$$\left(\boldsymbol{K_N} - \Omega^2 \boldsymbol{M_N}\right) \boldsymbol{Q_N} = \boldsymbol{0}. \tag{2.18}$$

Meanwhile, in this chapter, a 3D finite element model of a given mechanical structure is taken as reference. The designed electrical network should approach its modal properties. Few details about this method are given in the current chapter, as it is more precisely described in chapter 3. Note that the modes and natural frequencies of the structure are computed by resolving an eigenvalue problem that is analogous to the one of equation (2.18):

$$\left(\boldsymbol{K_m} - \Omega^2 \boldsymbol{M_m}\right) \boldsymbol{U} = \boldsymbol{0}, \tag{2.19}$$

where $\boldsymbol{K_m}$ is the assembled stiffness matrix, $\boldsymbol{M_m}$ is the assembled mass matrix and $\boldsymbol{U}$ is the vector of nodal displacements.

Conducting the analogy validation requires checking if the frequency coherence condition is met. This is done by a direct quantitative comparison of electrical and mechanical natural frequencies. In the meantime, the analogy between the mechanical structure and the electrical network is validated if the spatial coherence condition is met. To this end, we propose to involve the Modal Assurance Criterion (MAC) [87]. For any two eigenvectors Φ_1 and Φ_2 of same length, its definition is

$$\mathrm{MAC}\left(\Phi_1, \Phi_2\right) = \frac{\left|\Phi_1 \cdot \bar{\Phi}_2\right|^2}{\left(\Phi_1 \cdot \bar{\Phi}_1\right)\left(\Phi_2 \cdot \bar{\Phi}_2\right)}. \tag{2.20}$$

In this expression, $\bar{\Phi}$ indicates the conjugate vector of the eigenvector Φ. This criterion indicates if the tested mode shapes look alike. If the MAC matrix contains values close to 1, this means that the associated mode shapes are similar. On the other hand, low values in the MAC matrix are attained for two nearly orthogonal mode shapes.

2.3.8 Capsulized design method

In the following sections, electrical analogues of basic mechanical structures are derived. The suggested electrical analogue design process is recorded in the summary below. Though not represented, a feedback loop can be implemented starting from the last step, denoted Step 6, if the analogy is not validated. Besides, this last step is not conducted for all the analogues of this chapter. The validation of only the most complex ones is detailed on numerical examples.

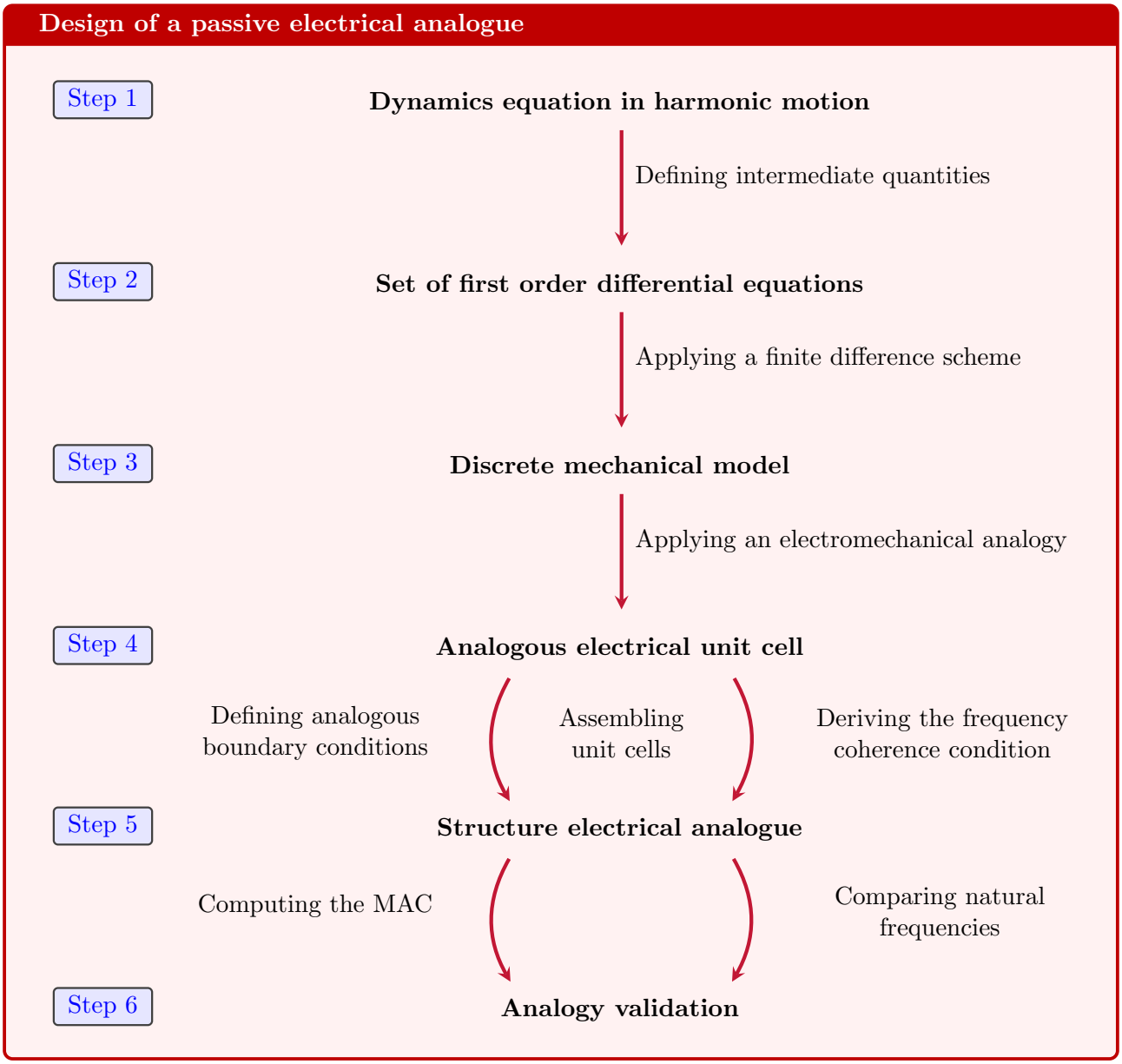

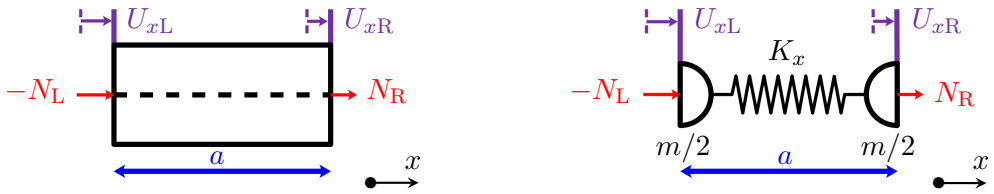

Figure 2.6: (a) Continuous rod segment and (b) associated discrete model.

2.4 Rod electrical analogue

Vibrations of a thin rod segment of density ρ and Young's modulus Y, such as represented in figure 2.6a, are described by the wave equation:

$$Y \frac{\partial^2 u_x}{\partial x^2} = \rho \frac{\partial^2 u_x}{\partial t^2}. \tag{2.21}$$

Assuming the separation of the space and time variables, the longitudinal displacement u_x can be written $u_x(x,t) = U_x(x) \cdot g(t)$, with U_x its amplitude and g its time variations. Then, in harmonic motion at angular frequency Ω, the equation (2.21) becomes

Step 1

$$Y \frac{d^2 U_x}{dx^2} = -\rho \Omega^2 U_x. \tag{2.22}$$

The equation (2.22) is a second order differential equation. As such, one intermediate quantity should be introduced in order to form an equivalent set of first order differential equations. This quantity is the normal force in the rod, denoted N. With S being the structure cross-section, one shows that the equation (2.22) is equivalent to

Step 2

$$\begin{aligned} \frac{dN}{dx} &= -\rho S \Omega^2 U_x, \\ N &= YS \frac{dU_x}{dx}. \end{aligned} \tag{2.23}$$

Applying the finite difference scheme presented in figure 2.2a and by equations (2.4) to the set of equations (2.23) leads to a discrete model of the rod:

Step 3

$$\begin{aligned} N_{\mathrm{I}} - N_{\mathrm{L}} &= -\frac{m}{2} \Omega^2 U_{x\mathrm{L}}, \\ N_{\mathrm{R}} - N_{\mathrm{I}} &= -\frac{m}{2} \Omega^2 U_{x\mathrm{R}}, \\ N_{\mathrm{I}} &= K_x \left(U_{x\mathrm{R}} - U_{x\mathrm{L}} \right), \end{aligned} \tag{2.24}$$

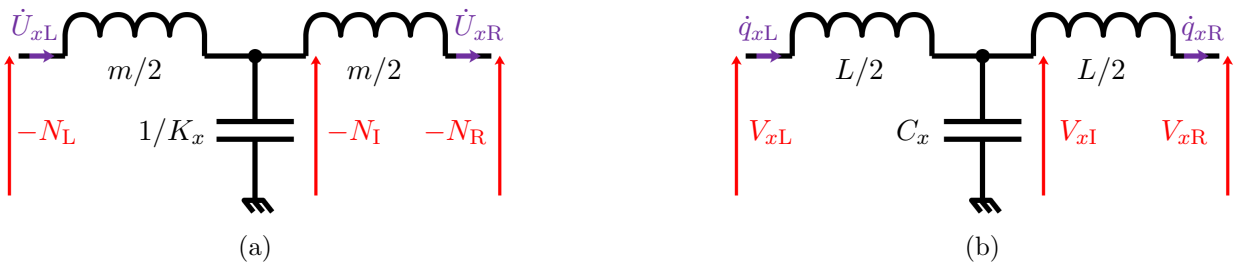

Figure 2.7: (a) Electrical representation of the discrete mechanical model of equations (2.24), and (b) analogous electrical model of equations (2.25).

with $m = \rho S a$ the mass of the rod segment, and $K_x = YS/a$ its longitudinal stiffness. This discrete mechanical model is represented in electrical fashion in figure 2.7a.

Then, the electrical analogue of the rod segment is derived from equations (2.24) by replacing K_x by $1/C_x$ and m by L according to the direct electromechanical analogy summed up in table 2.1. The resulting electrical model is defined by the following equations, and is sketched in figure 2.7b:

Step 4

$$\begin{aligned} V_{x\mathrm{L}} - V_{x\mathrm{I}} &= -\frac{L}{2}\,\Omega^2 q_{x\mathrm{L}}, \\ V_{x\mathrm{I}} - V_{x\mathrm{R}} &= -\frac{L}{2}\,\Omega^2 q_{x\mathrm{R}}, \\ C_x V_{x\mathrm{I}} &= q_{x\mathrm{L}} - q_{x\mathrm{R}}. \end{aligned} \tag{2.25}$$

Analogous boundary conditions: In case of a free boundary, the normal effort N vanishes while the displacement u_x can vary. The analogous boundary conditions are to set the V_x voltage to zero while letting the electrical current $\dot{q}_x$ freely flow. This corresponds to a short-circuit electrical condition.

Besides, if a boundary of the mechanical unit cell in figure 2.6b is blocked, then the longitudinal displacement u_x is forced at zero. Meanwhile, the normal force N has an unassigned value. The corresponding electrical boundary condition involves preventing the electrical current $\dot{q}_x$ to flow while letting the voltage V_x freely evolve: this is an open-circuit electrical condition.

Therefore, the free and blocked mechanical boundary conditions have direct electrical analogues. In the case of the right-side of the unit cells being a boundary, the associated discrete equations and schemes are gathered in table 2.2.

Boundary condition	Mechanical equations	Electrical equations	Scheme
Free	$N_{\mathrm{R}} = 0$	$V_{x\mathrm{R}} = 0$	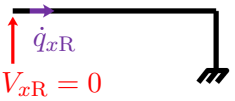
	$U_{x\mathrm{R}}$ free	$\dot{q}_{x\mathrm{R}}$ free	
Blocked	N_{R} free	$V_{x\mathrm{R}}$ free	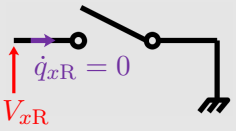
	$U_{x\mathrm{R}} = 0$	$\dot{q}_{x\mathrm{R}} = 0$	

Table 2.2: Rod analogous boundary conditions for a boundary on the right-side of the mechanical and electrical unit cells, respectively represented in figures 2.6b and 2.7b.

Frequency coherence condition: We define nondimensionalized displacements and forces by $U_x^\star = U_x/a$ and $N^\star = N/(aK_x)$, as well as analogous electrical charges and voltages by $q_x^\star = q_x/a$ and $V^\star = C_x V/a$. To derive the frequency coherence condition, the quantities on the right-hand side of the mechanical unit cell in figure 2.6b are related to the quantities on the left-hand side:

$$\begin{pmatrix} U^\star_{x\mathrm{R}} \\ -N^\star_{\mathrm{R}} \end{pmatrix} = \begin{pmatrix} 1-\delta_m & -1 \\ \delta_m\,(2-\delta_m) & 1-\delta_m \end{pmatrix} \begin{pmatrix} U^\star_{x\mathrm{L}} \\ -N^\star_{\mathrm{L}} \end{pmatrix} \qquad \text{with } \delta_m = \frac{m\Omega^2}{2K_x}. \tag{2.26}$$

Moreover, the quantities on the right-hand side of the electrical circuit in figure 2.7b are related to the quantities on the left-hand side:

$$\begin{pmatrix} q^\star_{x\mathrm{R}} \\ V^\star_{\mathrm{R}} \end{pmatrix} = \begin{pmatrix} 1-\delta_e & -1 \\ \delta_e\,(2-\delta_e) & 1-\delta_e \end{pmatrix} \begin{pmatrix} q^\star_{x\mathrm{L}} \\ V^\star_{\mathrm{L}} \end{pmatrix} \qquad \text{with } \delta_e = \frac{LC_x\Omega^2}{2}. \tag{2.27}$$

In other words, we identify that the mechanical and electrical transfer matrices are

$$\boldsymbol{T}^\star_{\boldsymbol{m}} = \begin{pmatrix} 1-\delta_m & \boxed{-1} \\ \delta_m\,(2-\delta_m) & 1-\delta_m \end{pmatrix} \quad \text{and} \quad \boldsymbol{T}^\star_{\boldsymbol{e}} = \begin{pmatrix} 1-\delta_e & \boxed{-1} \\ \delta_e\,(2-\delta_e) & 1-\delta_e \end{pmatrix} \tag{2.28}$$

($\boldsymbol{B}$)

The electrical circuit in figure 2.7b would have identical longitudinal wave propagation properties as the discrete mechanical model in figure 2.6b if $\boldsymbol{T}^\star_{\boldsymbol{m}} = \boldsymbol{T}^\star_{\boldsymbol{e}}$, which is equivalent to command that $\delta_m = \delta_e$. This means that the frequency coherence condition is

$$\frac{K_x}{m} = \frac{1}{LC_x}. \tag{2.29}$$

Unit cells assembly: Taking equations (2.8) and (2.28) into account, we can identify that $\boldsymbol{B}$ is invertible, therefore the dynamic matrix $\boldsymbol{D_e}$ can be derived. Using the notations in figure 2.7b, the values of the electrical charges and the voltages in one unit cell of the network are denoted $\boldsymbol{q_N}$ and $\boldsymbol{v_N}$:

$$\boldsymbol{q_N} = \begin{pmatrix} q_{x\mathrm{L}} & q_{x\mathrm{R}} \end{pmatrix}^{\mathrm{T}}, \qquad \boldsymbol{v_N} = \begin{pmatrix} V_{x\mathrm{L}} & -V_{x\mathrm{R}} \end{pmatrix}^{\mathrm{T}}. \tag{2.30}$$

Thus we derive the expression of $\boldsymbol{D_e}$:

$$\boldsymbol{D_e} = \begin{pmatrix} \frac{1}{C_x} - \frac{L}{2}\Omega^2 & \frac{-1}{C_x} \\ \frac{-1}{C_x} & \frac{1}{C_x} - \frac{L}{2}\Omega^2 \end{pmatrix}. \tag{2.31}$$

We then apply equations (2.13). The resulting electrical elementary matrices are

$$\boldsymbol{K_{elm}} = \begin{pmatrix} \frac{1}{C_x} & \frac{-1}{C_x} \\ \frac{-1}{C_x} & \frac{1}{C_x} \end{pmatrix} \qquad \text{and} \qquad \boldsymbol{M_{elm}} = \begin{pmatrix} \frac{L}{2} & 0 \\ 0 & \frac{L}{2} \end{pmatrix}. \tag{2.32}$$

The elementary "mass" matrix $\boldsymbol{M_{elm}}$ is a function of the inductance value L, which is the electrical analogous quantity of the mass. The elementary "stiffness" matrix $\boldsymbol{K_{elm}}$ is a function of the capacitance C_x, which is the analogous quantity of the longitudinal compliance. Then, after defining a number of cells to form the network and following an assembly process, the vectors $\boldsymbol{Q_N}$ and $\boldsymbol{V_N}$ which contain the values of electrical charges and external voltages in the entire network are related to each other by

Step 5

$$\boldsymbol{V_N} = \left(\boldsymbol{K_N} - \Omega^2 \boldsymbol{M_N}\right) \boldsymbol{Q_N}, \tag{2.33}$$

with $\boldsymbol{M_N}$ and $\boldsymbol{K_N}$ being respectively the assembled matrices of electrical "mass" and electrical "stiffness". After that, the mode shapes and natural frequencies of the electrical circuit can be estimated to be compared to those of the mechanical structure.

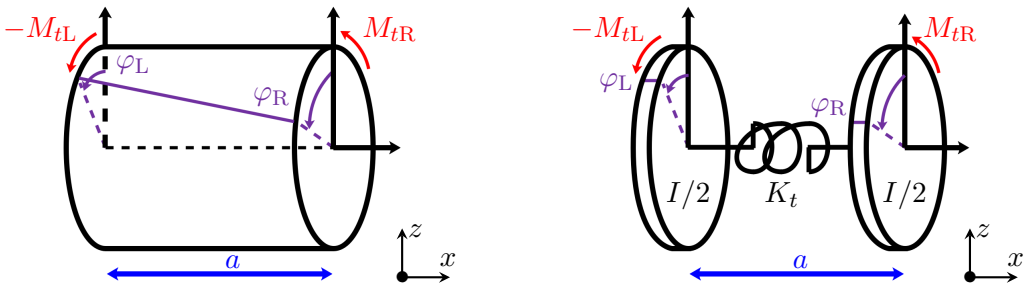

(a) (b)

Figure 2.8: (a) Continuous bar segment and (b) associated discrete model.

2.5 Bar electrical analogue

Torsional vibrations of a bar segment of density ρ, polar moment of inertia I_t, torsion constant J, and shear modulus G, such as represented in figure 2.8a, are described by a wave equation. Denoting φ the twisting angle amplitude and Ω the angular frequency, this equation in harmonic motion is of the same form as the equation (2.22) describing rod vibrations:

Step 1

$$GJ\,\frac{d^2\varphi}{dx^2} = -\rho I_t \Omega^2 \varphi. \tag{2.34}$$

Just like in the case of the rod of section 2.4, the harmonic motion of the considered structure is described by a second order differential equation. As such, one intermediate quantity should be introduced in order to form an equivalent set of first order differential equations. This quantity is the twisting moment M_t. One can show that the equation (2.34) is equivalent to

Step 2

$$\begin{aligned} \frac{dM_t}{dx} &= -\rho I_t \Omega^2 \varphi, \\ M_t &= GJ\,\frac{d\varphi}{dx}. \end{aligned} \tag{2.35}$$

Denoting $I = \rho a I_t$ the rotational inertia of the bar segment and $K_t = GJ/a$ its torsional stiffness, the discrete model of the bar in figure 2.8b, also represented in electrical fashion in figure 2.9a, is obtained by applying the finite difference scheme presented in figure 2.2a and by equations (2.4) to the set of equations (2.35):

Step 3

$$\begin{aligned} M_{t\mathrm{I}} - M_{t\mathrm{L}} &= -\frac{I}{2}\,\Omega^2 \varphi_{\mathrm{L}}, \\ M_{t\mathrm{R}} - M_{t\mathrm{I}} &= -\frac{I}{2}\,\Omega^2 \varphi_{\mathrm{R}}, \\ M_{t\mathrm{I}} &= K_t\,(\varphi_{\mathrm{R}} - \varphi_{\mathrm{L}})\,. \end{aligned} \tag{2.36}$$

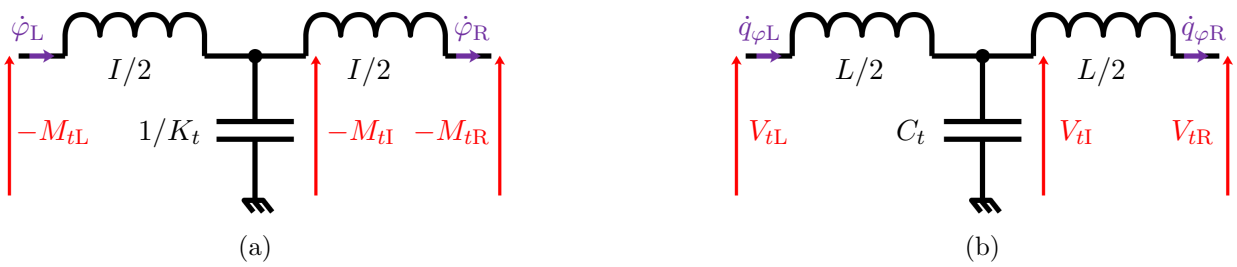

Figure 2.9: (a) Electrical representation of the discrete mechanical model of equations (2.36), and (b) analogous electrical model of equations (2.37).

Then, the model of the discretized bar electrical analogue is derived by replacing K_t by $1/C_t$ and I by L in equations (2.36) according to the direct electromechanical analogy summed up in table 2.1:

Step 4

$$\begin{aligned} V_{t\mathrm{L}} - V_{t\mathrm{I}} &= -\frac{L}{2}\,\Omega^2 q_{\varphi\mathrm{L}}, \\ V_{t\mathrm{I}} - V_{t\mathrm{R}} &= -\frac{L}{2}\,\Omega^2 q_{\varphi\mathrm{R}}, \\ C_t V_{t\mathrm{I}} &= q_{\varphi\mathrm{L}} - q_{\varphi\mathrm{R}}. \end{aligned} \tag{2.37}$$

The resulting electrical circuit is sketched in figure 2.9b. Though the components values have different interpretations, the circuit topology is the same as for the rod electrical analogue presented in figure 2.7b. This is coherent with rod and bar vibrations both being described by a wave equation.

Analogous boundary conditions: Electrical analogues of the free and blocked boundary conditions are similar to the ones recorded in table 2.2. The only differences are that the normal force N_{R}, the longitudinal displacement $U_{x\mathrm{R}}$, the voltage $V_{x\mathrm{R}}$ and the electrical current $\dot{q}_{x\mathrm{R}}$ are respectively replaced by the twisting moment $M_{t\mathrm{R}}$, the twisting angle φ_{R}, the voltage $V_{t\mathrm{R}}$ and the electrical current $\dot{q}_{\varphi\mathrm{R}}$.

Frequency coherence condition: We define nondimensionalized angles and moments by $\varphi^\star = \varphi$ and $M_t^\star = M_t/K_t$. Just like in the case of the rod electrical analogue, relating quantities on the sides of the unit cells in figures 2.8b and 2.9b allows defining the frequency coherence condition:

$$\frac{K_t}{I} = \frac{1}{LC_t}. \tag{2.38}$$

Unit cells assembly: Since the electrical dynamic matrix can be computed, one can derive electrical elementary matrices which are similar to the ones for the rod electrical analogue previously treated:

$$\boldsymbol{K_{elm}} = \begin{pmatrix} \frac{1}{C_t} & \frac{-1}{C_t} \\ \frac{-1}{C_t} & \frac{1}{C_t} \end{pmatrix} \qquad \text{and} \qquad \boldsymbol{M_{elm}} = \begin{pmatrix} \frac{L}{2} & 0 \\ 0 & \frac{L}{2} \end{pmatrix}. \tag{2.39}$$

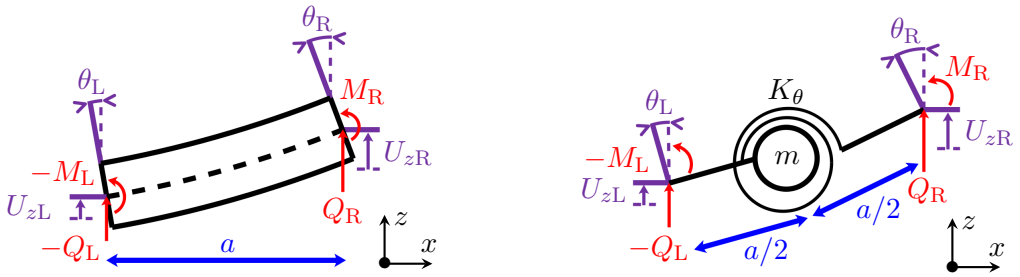

Figure 2.10: (a) Continuous beam segment and (b) associated discrete model.

2.6 Beam electrical analogue

The Euler-Bernoulli model of a beam describes the dynamics of a thin beam segment in harmonic motion at angular frequency Ω by

Step 1

$$YI\,\frac{\partial^4 U_z}{\partial x^4} = \rho S \Omega^2 U_z, \tag{2.40}$$

where U_z is the displacement amplitude, ρ is the density, S is the cross-section, Y is the Young's modulus and I is the second moment of area. The equation (2.40) is a fourth order differential equation. As such, three intermediate quantities should be introduced in order to form an equivalent set of first order differential equations. These quantities are the shear force Q, the bending moment M, and the rotation of the cross-section θ. One can show that the equation (2.40) is equivalent to

Step 2

$$\begin{aligned} \frac{dQ}{dx} &= -\rho S \Omega^2 U_z, & M &= YI\,\frac{d\theta}{dx}, \\ Q &= -\frac{dM}{dx}, & \theta &= \frac{dU_z}{dx}. \end{aligned} \tag{2.41}$$

Applying the finite difference scheme presented in figure 2.2a and in the equations (2.4) to the set of equations (2.41) leads to a discrete model of the beam:

Step 3

$$\begin{aligned} Q_R - Q_L &= -m\Omega^2 U_{zI}, & M_I &= K_\theta\,(\theta_R - \theta_L)\,, \\ \frac{a}{2}\,Q_L &= M_L - M_I, & \frac{a}{2}\,\theta_L &= U_{zI} - U_{zL}, \\ \frac{a}{2}\,Q_R &= M_I - M_R, & \frac{a}{2}\,\theta_R &= U_{zR} - U_{zI}, \end{aligned} \tag{2.42}$$

with $m = \rho S a$ the mass of the beam segment, and $K_\theta = YI/a$ its bending stiffness. The discrete mechanical model in figure 2.10b is also sketched in electrical fashion in figure 2.11a.

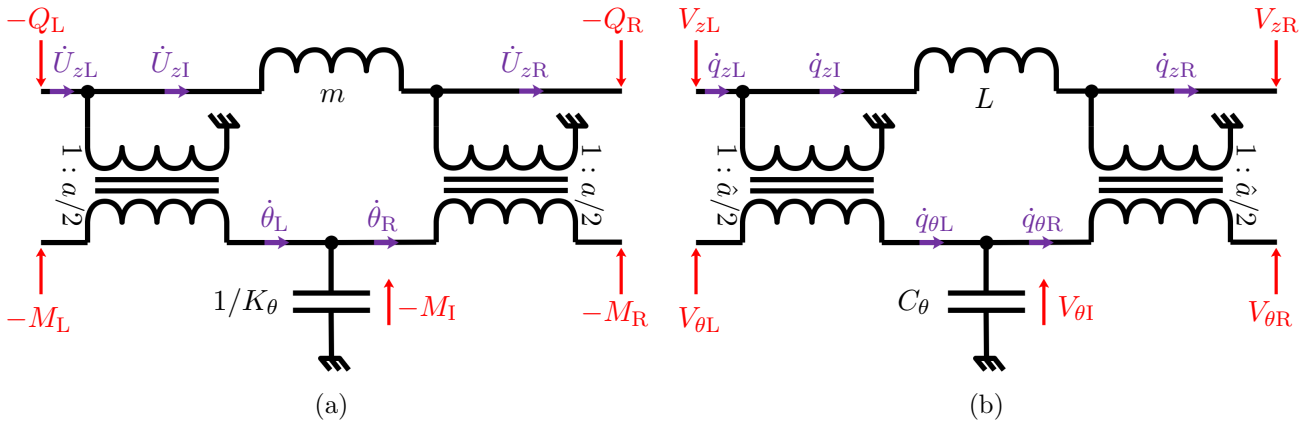

Figure 2.11: (a) Electrical representation of the discrete mechanical model of equations (2.42) and (b) analogous electrical model of equations (2.43).

Then, the electrical analogue of the beam segment is derived by replacing a by the electric "length" $\hat{a}$, K_θ by $1/C_\theta$ and m by L according to the direct electromechanical analogy summed up in table 2.1. The resulting electrical unit cell is characterized by the following equations, and by the circuit drawn in figure 2.11b:

Step 4

$$\begin{aligned} V_{zL} - V_{zR} &= -L\Omega^2 q_{zI}, & C_\theta V_{\theta I} &= q_{\theta L} - q_{\theta R}, \\ \frac{\hat{a}}{2} V_{zL} &= V_{\theta L} - V_{\theta I}, & \frac{\hat{a}}{2} q_{\theta L} &= q_{zI} - q_{zL}, \\ \frac{\hat{a}}{2} V_{zR} &= V_{\theta I} - V_{\theta R}, & \frac{\hat{a}}{2} q_{\theta R} &= q_{zR} - q_{zI}. \end{aligned} \tag{2.43}$$

Analogous boundary conditions: In case of a free boundary, the shear force Q and the bending moment M vanish at the boundary, while the displacement u_z and the slope θ can vary. This corresponds to short-circuit conditions for both branches of the electrical unit cell in figure 2.11b.

If a boundary of the mechanical unit cell in figure 2.10 is simply-supported, then the transverse displacement u_z is forced at zero while the slope θ is left unassigned. Moreover, at the boundary, the shear force Q is undefined while the bending moment M is equal to zero. This corresponds to an open-circuit electrical connection on the transverse displacement grid, and to a short-circuit electrical connection on the slope grid.

Boundary condition	Mechanical equations	Electrical equations	Scheme
Free	$Q_{\mathrm{R}} = 0$	$V_{z\mathrm{R}} = 0$	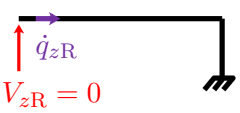
	$M_{\mathrm{R}} = 0$	$V_{\theta\mathrm{R}} = 0$	
	$U_{z\mathrm{R}}$ free	$\dot{q}_{z\mathrm{R}}$ free	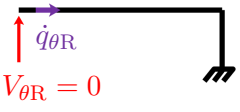
	θ_{R} free	$\dot{q}_{\theta\mathrm{R}}$ free	
Simply-supported	Q_{R} free	$V_{z\mathrm{R}}$ free	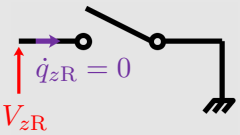
	$M_{\mathrm{R}} = 0$	$V_{\theta\mathrm{R}} = 0$	
	$U_{z\mathrm{R}} = 0$	$\dot{q}_{z\mathrm{R}} = 0$	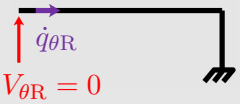
	θ_{R} free	$\dot{q}_{\theta\mathrm{R}}$ free	
Clamped	Q_{R} free	$V_{z\mathrm{R}}$ free	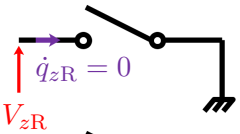
	M_{R} free	$V_{\theta\mathrm{R}}$ free	
	$U_{z\mathrm{R}} = 0$	$\dot{q}_{z\mathrm{R}} = 0$	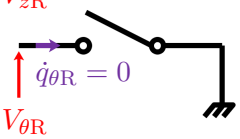
	$\theta_{\mathrm{R}} = 0$	$\dot{q}_{\theta\mathrm{R}} = 0$	

Table 2.3: Beam analogous boundary conditions for a boundary on the right-side of the mechanical and electrical unit cells, respectively represented in figures 2.10b and 2.11b.

Finally, we consider the case of a clamped boundary condition. In this case, both the transverse displacement u_z and the slope θ are set at zero, while the boundary mechanical loads Q and M have unassigned values. These represent open-circuit electrical conditions on both branches of the electrical unit cell represented in figure 2.11b.

Hence, the free, simply-supported and clamped mechanical boundary conditions have direct electrical analogues. In the case of the right-side of the unit cells being a boundary, the associated discrete equations and schemes are gathered in table 2.3.

Frequency coherence condition: We define nondimensionalized displacements by $U_z^\star = U_z/a$, rotations by $\theta^\star = \theta$, shear forces by $Q^\star = aQ/K_\theta$ and bending moments by $M^\star = M/K_\theta$. To derive the frequency coherence condition, the quantities on the right-hand side of the mechanical unit cell in figure 2.10b are related to the quantities on the left-hand side :

$$\begin{pmatrix} U^\star_{z\mathrm{R}} \\ \theta^\star_{\mathrm{R}} \\ -Q^\star_{\mathrm{R}} \\ -M^\star_{\mathrm{R}} \end{pmatrix} = \begin{pmatrix} 1 & 1 & \frac{1}{4} & \frac{-1}{2} \\ 0 & 1 & \frac{1}{2} & -1 \\ \delta & \frac{\delta}{2} & 1 & 0 \\ \frac{-\delta}{2} & \frac{-\delta}{4} & -1 & 1 \end{pmatrix} \begin{pmatrix} U^\star_{z\mathrm{L}} \\ \theta^\star_{\mathrm{L}} \\ -Q^\star_{\mathrm{L}} \\ -M^\star_{\mathrm{L}} \end{pmatrix} \qquad \text{with } \delta = \frac{ma^2\Omega^2}{K_\theta}. \tag{2.44}$$

Hence we deduce that the electrical circuit in figure 2.11b would have identical bending wave propagation properties as the discrete mechanical model in figure 2.10b if they share the same ratio δ. This means that the frequency coherence condition is

$$\frac{1}{a^2}\frac{K_\theta}{m} = \frac{1}{\hat{a}^2}\frac{1}{LC_\theta}. \tag{2.45}$$

Unit cells assembly: Taking equations (2.8) and (2.44) into account, we identify $\boldsymbol{B}$ as a singular matrix. As a consequence, we cannot compute the electrical dynamic matrix $\boldsymbol{D_e}$ from the set of equations (2.43). This can be understood by analyzing the figure 2.11b: once $q_{z\mathrm{L}} = 0$ and $q_{\theta\mathrm{L}} = 0$, $q_{z\mathrm{I}} = 0$ and thus $q_{z\mathrm{R}}$ is directly proportional to $q_{\theta\mathrm{R}}$ because of the right-side transformer. In other words: $q_{z\mathrm{R}}$ and $q_{\theta\mathrm{R}}$ cannot be independently set. This can also be understood from a mechanical point of view. Imagining the sketch in figure 2.10b with $U_{z\mathrm{L}} = 0$ and $\theta_{\mathrm{L}} = 0$ shows that $U_{z\mathrm{R}} = a/2 \cdot \theta_{\mathrm{R}}$. Therefore $U_{z\mathrm{R}}$ and θ_{R} cannot be independently fixed. In both cases, the system is ill-defined since it is overconstrained.

A way to overcome this problem is to introduce fictive degrees of freedom in the unit cell. One possibility is to add capacitors of C_0 value between unit cells, such as drawn in figure 2.12. This is analogous to consider additional rotary springs between unit cells of the discretized mechanical structure. Integrating these components to the beam electrical analogue model defined by equations (2.43) leads to a more complicated transfer matrix. Though not detailed here, the new $\boldsymbol{B}$ matrix is

$$\boldsymbol{B} = \begin{pmatrix} \frac{1}{4} & -\frac{1+\epsilon}{2} \\ \frac{1+\epsilon}{2} & -\left(1+\epsilon+\frac{\delta}{16}\epsilon^2\right) \end{pmatrix} \qquad \text{with } \epsilon = \frac{C_0}{C_\theta}. \tag{2.46}$$

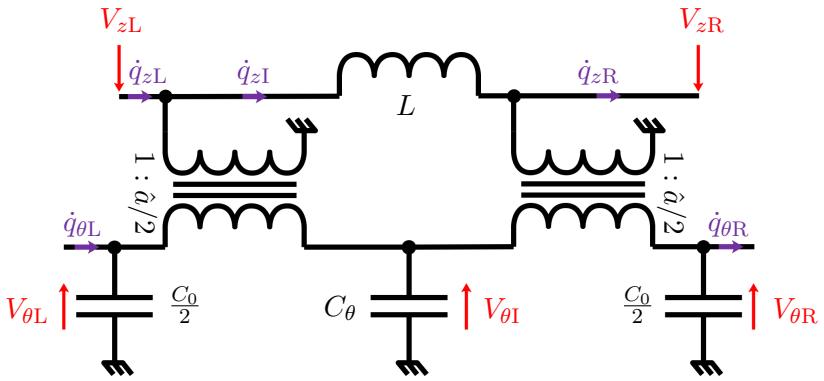

Figure 2.12: Modified unit cell of the beam electrical analogue.

Notice that setting $C_0 = 0$, i.e. $\epsilon = 0$, in this new expression of $\boldsymbol{B}$ leads to the previously identified singular matrix. One can show that the determinant of this new matrix is

$$\det(\boldsymbol{B}) = \frac{\epsilon}{4}\left[1 + \epsilon\left(1 - \frac{\delta}{16}\right)\right] \approx \frac{\epsilon}{4} \qquad \text{if } \epsilon \ll 1. \tag{2.47}$$

As expected, the C_0 capacitance should be different from zero to avoid numerical singularity, but should be small enough so that it remains a numerical trick. Setting ϵ at around 10^{-6} is adequate in most cases. By doing so, $\boldsymbol{B}$ is not singular anymore, and the electrical dynamic matrix $\boldsymbol{D_e}$ can thus be derived. Using the notations in figure 2.12, the values of the electrical charges and the voltages in one unit cell of the network are denoted $\boldsymbol{q_N}$ and $\boldsymbol{v_N}$:

$$\boldsymbol{q_N} = \begin{pmatrix} q_{z\mathrm{L}} & q_{\theta\mathrm{L}} & q_{z\mathrm{R}} & q_{\theta\mathrm{R}} \end{pmatrix}^{\mathrm{T}}, \qquad \boldsymbol{v_N} = \begin{pmatrix} V_{z\mathrm{L}} & V_{\theta\mathrm{L}} & -V_{z\mathrm{R}} & -V_{\theta\mathrm{R}} \end{pmatrix}^{\mathrm{T}}. \tag{2.48}$$

After deriving the dynamic matrix $\boldsymbol{D_e}$ and applying equations (2.13), we derive the elementary "mass" matrix $\boldsymbol{M_{elm}}$, which is a function of the inductance value L, and the elementary "stiffness" matrix $\boldsymbol{K_{elm}}$, which depends on the capacitance C_θ and the numerical parameter C_0:

$$\boldsymbol{K_{elm}} = \frac{1}{\hat{a}C_0}\begin{pmatrix} \frac{4}{\hat{a}} & 2 & \frac{-4}{\hat{a}} & 2 \\ 2 & \frac{\hat{a}(2C_0+C_\theta)}{C_0+C_\theta} & -2 & \frac{\hat{a}C_\theta}{C_0+C_\theta} \\ \frac{-4}{\hat{a}} & -2 & \frac{4}{\hat{a}} & -2 \\ 2 & \frac{\hat{a}C_\theta}{C_0+C_\theta} & -2 & \frac{\hat{a}(2C_0+C_\theta)}{C_0+C_\theta} \end{pmatrix} \quad \text{and} \quad \boldsymbol{M_{elm}} = \frac{L}{16}\begin{pmatrix} 4 & 2\hat{a} & 4 & -2\hat{a} \\ 2\hat{a} & \hat{a}^2 & 2\hat{a} & -\hat{a}^2 \\ 4 & 2\hat{a} & 4 & -2\hat{a} \\ -2\hat{a} & -\hat{a}^2 & -2\hat{a} & \hat{a}^2 \end{pmatrix}. \tag{2.49}$$

Influence of C_0 capacitors on the network model

The addition of C_0 capacitors on the sides of the unit cell of the beam electrical analogue may alter the behavior of the assembled network. The network dynamics is influenced by the value of $\epsilon = C_0/C_\theta$. A numerical example highlighting the effect of said-capacitors on the behavior of a plate electrical analogue is recorded in the aside of subsection 4.4.3.

Alternative electrical analogues in case of bending motion

Apart from the rod and bar vibrations studied in sections 2.4 and 2.5, the designed electrical analogues of the present chapter are related to bending wave propagation. The same numerical problem arises in all these problems: the system of discrete mechanical equations is ill-defined, so the $\boldsymbol{B}$ matrix is not invertible. Therefore, numerical parameters in the form of capacitors C_0 are connected at the unit cell boundaries. Setting C_0 at a small value when compared with the element bending stiffness C_θ leads to adequate formulations in all cases.

A way to avoid these fictive degrees of freedom is to offset the finite different scheme of $a/2$ along the beam main direction. This means that the equations (2.43) would become:

$$\begin{aligned} V_{z\mathrm{I}} - V_{z\mathrm{R}} &= -\frac{L}{2}\,\Omega^2 q_{z\mathrm{R}}, & \frac{C_\theta}{2}\,V_{\theta\mathrm{L}} &= q_{\theta\mathrm{L}} - q_{\theta\mathrm{I}}, \\ V_{z\mathrm{L}} - V_{z\mathrm{I}} &= -\frac{L}{2}\,\Omega^2 q_{z\mathrm{L}}, & \frac{C_\theta}{2}\,V_{\theta\mathrm{R}} &= q_{\theta\mathrm{I}} - q_{\theta\mathrm{R}}, \\ \hat{a}\,V_{z\mathrm{I}} &= V_{\theta\mathrm{L}} - V_{\theta\mathrm{R}}, & \hat{a}\,q_{\theta\mathrm{I}} &= q_{z\mathrm{R}} - q_{z\mathrm{L}}. \end{aligned} \tag{2.50}$$

The corresponding unit cell of the beam electrical analogue is sketched below. One can show that in this case, the identified $\boldsymbol{B}$ matrix is $\begin{pmatrix} 0 & -1/2 \\ 1/2 & 1 \end{pmatrix}$, and thus it is invertible. This unit cell could be used to avoid implementing the numerical parameters C_0. However, we prefer centering the piezoelectric capacitance on the unit cells going forward. Indeed, the coupling of mechanical structures to piezoelectric networks is considered in the following chapters. It is then more practical to center the piezoelectric patches on the corresponding unit cells of the discretized structure.

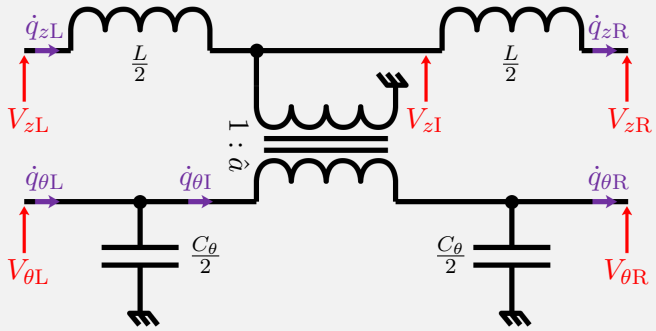

Figure 2.13: Alternative unit cell of the beam electrical analogue.

2.7 Square plate electrical analogue

2.7.1 Design of an electrical analogue

In harmonic motion at angular frequency Ω, the dynamics of a plate of thickness h, mass density ρ and bending stiffness K_θ is described by the Kirchhoff-Love plate theory, so that

Step 1

$$K_\theta \left(\frac{\partial^4 U_z}{\partial x^4} + 2 \frac{\partial^4 U_z}{\partial x^2 \partial y^2} + \frac{\partial^4 U_z}{\partial y^4} \right) = \rho h \Omega^2 U_z, \tag{2.51}$$

where U_z stands for the transverse displacement amplitude. This equation is a fourth order equation. To define an equivalent set of first order equations, it is convenient to describe the plate dynamics by the combination of membrane equations [88], which are second order differential equations:

$$K_\theta \left(\frac{\partial^2}{\partial x^2} + \frac{\partial^2}{\partial y^2} \right) \left(\frac{\partial^2 U_z}{\partial x^2} + \frac{\partial^2 U_z}{\partial y^2} \right) = \rho h \Omega^2 U_z. \tag{2.52}$$

The intermediate quantities we define are:

Step 2

$$\begin{aligned} \theta_x &= \frac{\partial U_z}{\partial x}, & Q_x &= -\frac{\partial M}{\partial x}, \\ \theta_y &= \frac{\partial U_z}{\partial y}, & Q_y &= -\frac{\partial M}{\partial y}, \\ M &= a K_\theta \left(\frac{\partial \theta_x}{\partial x} + \frac{\partial \theta_y}{\partial y} \right), & \frac{\partial Q_x}{\partial x} + \frac{\partial Q_y}{\partial y} &= -\rho h a \Omega^2 U_z, \end{aligned} \tag{2.53}$$

The first intermediate quantities are the slopes θ_x and θ_y along the principal directions. Then, we introduce the bending moment M, whose expression is in fact a linear combination of the usual bending moments about the x and y directions of the plate theory [88]. It is adapted to the study of a square plate of side a, though it is different from the expression that Timoshenko and Woinowsky-Krieger proposed: it was chosen to multiply their expression by a to ensure M is actually of the same unit as a moment. We finally introduce the shear forces Q_x and Q_y as the partial derivatives of M. As a consequence, the equation (2.52) is equivalent to the set of equations (2.53).

Applying the finite difference scheme presented in figure 2.2b and by equations (2.4) and (2.5) to the set of equations (2.53) leads to a discrete model of the square plate:

Step 3

$$\begin{aligned}
&\frac{a}{2}\,\theta_{\mathrm{B}} = U_{z\mathrm{I}} - U_{z\mathrm{B}}, && \frac{a}{2}\,Q_{\mathrm{B}} = M_{\mathrm{B}} - M_{\mathrm{I}},\\
&\frac{a}{2}\,\theta_{\mathrm{L}} = U_{z\mathrm{I}} - U_{z\mathrm{L}}, && \frac{a}{2}\,Q_{\mathrm{L}} = M_{\mathrm{L}} - M_{\mathrm{I}},\\
&\frac{a}{2}\,\theta_{\mathrm{R}} = U_{z\mathrm{R}} - U_{z\mathrm{I}}, && \frac{a}{2}\,Q_{\mathrm{R}} = M_{\mathrm{I}} - M_{\mathrm{R}},\\
&\frac{a}{2}\,\theta_{\mathrm{T}} = U_{z\mathrm{T}} - U_{z\mathrm{I}}, && \frac{a}{2}\,Q_{\mathrm{T}} = M_{\mathrm{I}} - M_{\mathrm{T}},\\
&M_{\mathrm{I}} = K_{\theta}\left(\theta_{\mathrm{T}} - \theta_{\mathrm{B}} + \theta_{\mathrm{R}} - \theta_{\mathrm{L}}\right), && Q_{\mathrm{T}} - Q_{\mathrm{B}} + Q_{\mathrm{R}} - Q_{\mathrm{L}} = -m\Omega^2 U_{z\mathrm{I}},
\end{aligned} \tag{2.54}$$

with $m = \rho h a^2$ the mass of the square plate.

Then, the electrical analogue of the plate is derived by replacing mechanical quantities by electrical quantities according to the direct electromechanical analogy summed up in table 2.1, and by replacing the cell side a by the electric "length" $\hat{a}$. The resulting electrical unit cell is characterized by the following equations, and is shown in figure 2.14:

Step 4

$$\begin{aligned}
&\frac{\hat{a}}{2}\,q_{\theta\mathrm{B}} = q_{z\mathrm{I}} - q_{z\mathrm{B}}, && \frac{\hat{a}}{2}\,V_{z\mathrm{B}} = V_{\theta\mathrm{B}} - V_{\theta\mathrm{I}},\\
&\frac{\hat{a}}{2}\,q_{\theta\mathrm{L}} = q_{z\mathrm{I}} - q_{z\mathrm{L}}, && \frac{\hat{a}}{2}\,V_{z\mathrm{L}} = V_{\theta\mathrm{L}} - V_{\theta\mathrm{I}},\\
&\frac{\hat{a}}{2}\,q_{\theta\mathrm{R}} = q_{z\mathrm{R}} - q_{z\mathrm{I}}, && \frac{\hat{a}}{2}\,V_{z\mathrm{R}} = V_{\theta\mathrm{I}} - V_{\theta\mathrm{R}},\\
&\frac{\hat{a}}{2}\,q_{\theta\mathrm{T}} = q_{z\mathrm{T}} - q_{z\mathrm{I}}, && \frac{\hat{a}}{2}\,V_{z\mathrm{T}} = V_{\theta\mathrm{I}} - V_{\theta\mathrm{T}},\\
&C_{\theta} V_{\theta\mathrm{I}} = q_{\theta\mathrm{B}} - q_{\theta\mathrm{T}} + q_{\theta\mathrm{L}} - q_{\theta\mathrm{R}}, && V_{z\mathrm{B}} - V_{z\mathrm{T}} + V_{z\mathrm{L}} - V_{z\mathrm{R}} = -L\Omega^2 q_{z\mathrm{I}}.
\end{aligned} \tag{2.55}$$

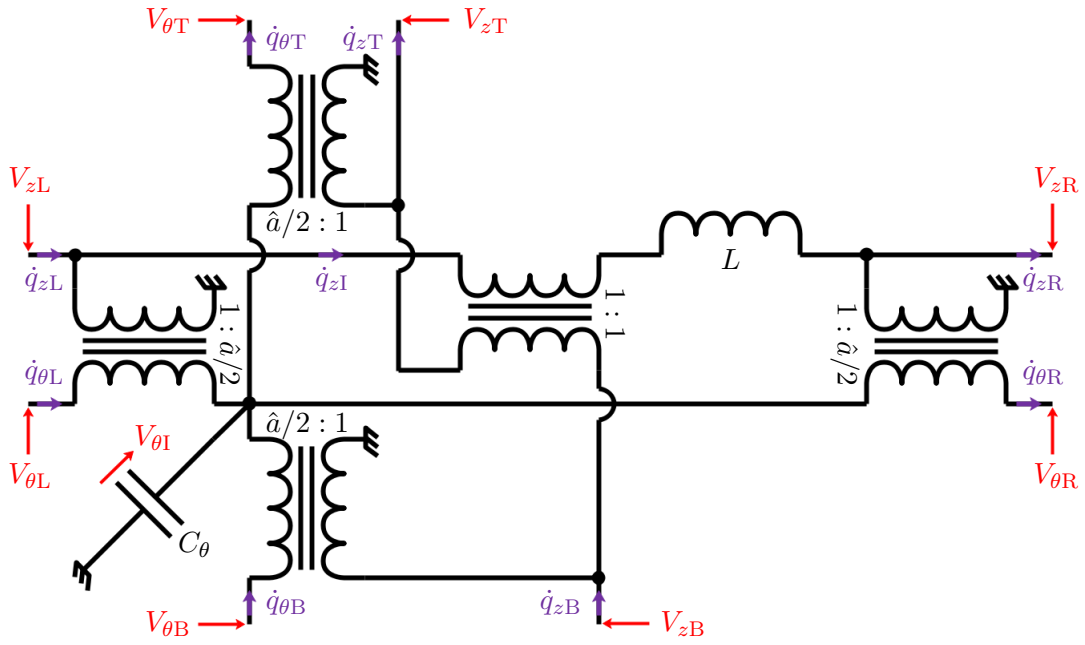

Figure 2.14: Unit cell of the plate electrical analogue, which is defined by the set of equations (2.55).

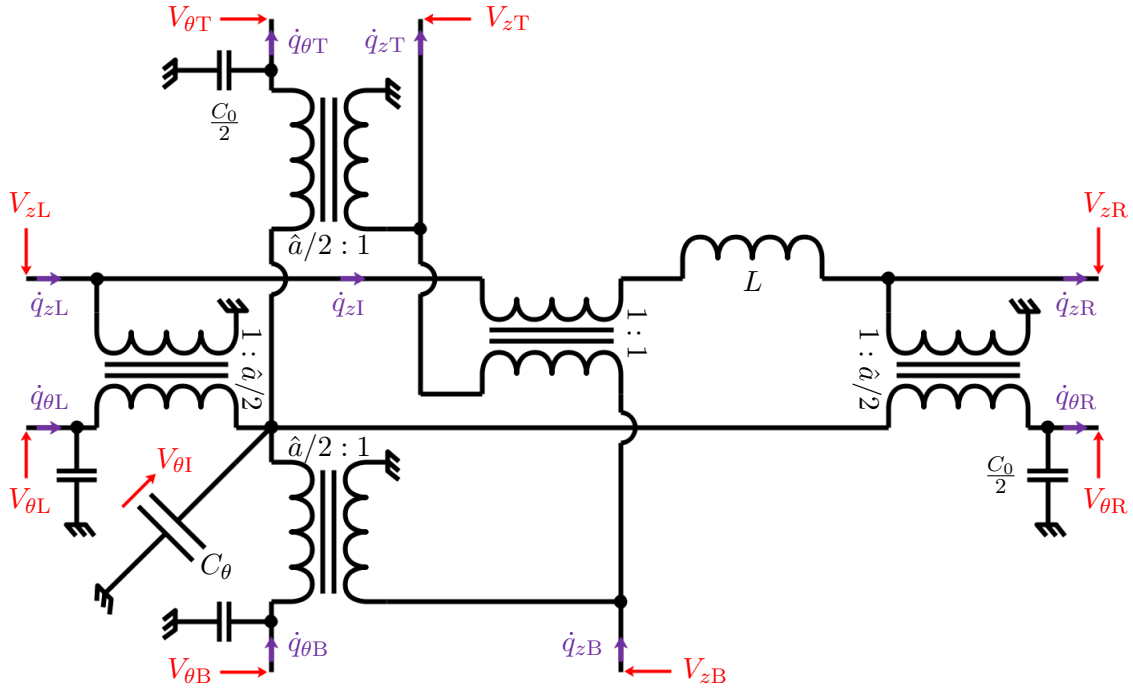

Figure 2.15: Unit cell of the plate electrical analogue, which is defined by the set of equations (2.55), with added capacitors on the sides.

Boundary condition	Mechanical equations	Electrical equations	Scheme
Simply-supported	Q_{R} free	$V_{z\mathrm{R}}$ free	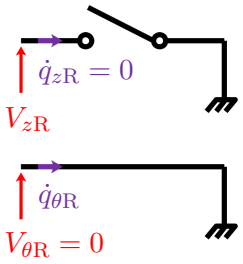
	$M_{\mathrm{R}} = 0$	$V_{\theta\mathrm{R}} = 0$	
	$U_{z\mathrm{R}} = 0$	$\dot{q}_{z\mathrm{R}} = 0$	
	θ_{R} free	$\dot{q}_{\theta\mathrm{R}}$ free	
Clamped	Q_{R} free	$V_{z\mathrm{R}}$ free	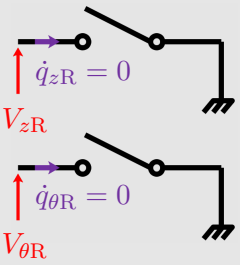
	M_{R} free	$V_{\theta\mathrm{R}}$ free	
	$U_{z\mathrm{R}} = 0$	$\dot{q}_{z\mathrm{R}} = 0$	
	$\theta_{\mathrm{R}} = 0$	$\dot{q}_{\theta\mathrm{R}} = 0$	

Table 2.4: Plate analogous boundary conditions for a boundary on the right-side of the mechanical and electrical unit cells, the latest being represented in figure 2.14.

Analogous boundary conditions: Suppose that the boundary is parallel to the y direction. If it is simply-supported, then the transverse displacement U_z and the bending moment M are equal to zero [88, 72]. Indeed, the choice of intermediate quantities in equations (2.53) is particularly well adapted to simply-supported plates, as the defined bending moment M vanishes on any simply-supported boundary that is parallel to the x or the y direction [88]. Meanwhile, the slope θ_x and the shear force Q can freely vary. Finally, the slope θ_y is not a boundary quantity on the right-side of the unit cell. These conditions, applied to the electrical unit cell in figure 2.14, lead to an open-circuit condition on the displacement branch and to a short-circuit on the slope branch.

If the boundary is now fully clamped, then the transverse displacement U_z and the slope θ_x are forced at zero, while the shear force Q and the bending moment M are unconstrained. Besides, the slope θ_y is not a boundary quantity. Hence, the analogous electrical boundary conditions are open-circuit connections on both branches of the unit cell in figure 2.14.

Consequently, the simply-supported and clamped mechanical boundary conditions have direct electrical analogues. In the case of the right-side of the unit cell being a boundary, the associated discrete equations and sketches are gathered in table 2.4.

Electrical analogue of a plate free edge

A plate free edge is the boundary condition whose electrical analogue remains undefined with the method described in section 2.3. This is a limitation of the designed plate electrical analogue. The problem of the free edge plate analogue, as well as potential solutions, are discussed in appendix A.

Frequency coherence condition: The discrete model of a square Kirchhoff-Love plate is the 2D extension of the Euler-Bernoulli beam discrete model previously developed. Indeed, the circuit in figure 2.14 represents the coupling by a 1:1 central transformer of two orthogonal electrical circuits sketched in figure 2.11b. Thus, the frequency coherence condition is an extension of the condition expressed by equation (2.45), as we still have:

$$\frac{1}{a^2}\,\frac{K_\theta}{m} = \frac{1}{\hat{a}^2}\,\frac{1}{LC_\theta}. \tag{2.56}$$

Unit cells assembly: To overcome the overconstrained nature of the equations system (2.55), we propose a solution which is similar than depicted for the Euler-Bernoulli beam electrical analogue: we suggest adding numerical degrees of freedom by connecting capacitances C_0 on the sides of the unit cell represented in figure 2.14. This is analogous to interconnect mechanical unit cells by rotary springs. The resulting unit cell is sketched in figure 2.15. These numerical parameters are required to compute the electrical dynamic matrix $\boldsymbol{D_e}$, but should be small when compared to C_θ to mitigate their influence on the network dynamics. Again, setting ϵ at around 10^{-6} is adequate in most cases.

Using the notations in figure 2.15, the values of the electrical charges and the voltages in one unit cell of the network are denoted $\boldsymbol{q_N}$ and $\boldsymbol{v_N}$:

$$\begin{aligned}\boldsymbol{q_N} &= \begin{pmatrix} q_{z\mathrm{B}} & q_{\theta\mathrm{B}} & q_{z\mathrm{L}} & q_{\theta\mathrm{L}} & q_{z\mathrm{R}} & q_{\theta\mathrm{R}} & q_{z\mathrm{T}} & q_{\theta\mathrm{T}} \end{pmatrix}^{\mathrm{T}},\\ \boldsymbol{v_N} &= \begin{pmatrix} V_{z\mathrm{B}} & V_{\theta\mathrm{B}} & V_{z\mathrm{L}} & V_{\theta\mathrm{L}} & -V_{z\mathrm{R}} & -V_{\theta\mathrm{R}} & -V_{z\mathrm{T}} & -V_{\theta\mathrm{T}} \end{pmatrix}^{\mathrm{T}}.\end{aligned} \tag{2.57}$$

Following the derivation of the dynamic matrix $\boldsymbol{D_e}$, we apply equations (2.13). The resulting electrical elementary matrices are recorded in appendix B. Note that the elementary electrical "stiffness" matrix $\boldsymbol{K_{elm}}$ is a function of the added capacitance C_0 and of C_θ, which is the analogous quantity of the bending compliance of the square plate. Meanwhile, the elementary electrical "mass" matrix $\boldsymbol{M_{elm}}$ is a function of the inductance value L, which is the electrical analogous quantity of the mass of the square plate.

Then, following an assembly process, the vectors $\boldsymbol{Q_N}$ and $\boldsymbol{V_N}$ which contain the values of electrical charges and external voltages in the entire network are related to each other by

Step 5

$$\boldsymbol{V_N} = \left(\boldsymbol{K_N} - \Omega^2 \boldsymbol{M_N}\right) \boldsymbol{Q_N}, \tag{2.58}$$

with $\boldsymbol{M_N}$ and $\boldsymbol{K_N}$ being respectively the assembled matrices of electrical "mass" and "stiffness".

2.7.2 Electrical analogue validation

2.7.2.1 Structure and analogous network development

Now that a plate electrical analogue is proposed, it should be validated by checking if the spatial and frequency coherence conditions are met. The validation is conducted on a numerical example of a simply-supported duralumin rectangular plate of dimensions $l_x = 420$ mm, $l_y = 360$ mm, $h_s = 3$ mm, whose Poisson's ratio ν, density ρ and Young's modulus Y are respectively set at 0.35, 2800 kg/m^3 and 69 GPa. Its mode shapes and natural frequencies are obtained via a finite element model, which is supposedly precise enough to serve as the reference. The modeling hypotheses are not detailed here, as it is the topic of the section 3.2. We just recall that the structure material is assumed to exhibit isotropic and homogeneous properties and that it stays in linear elasticity. The structure is modeled with 20-node hexahedral elements and one element in depth. Some of these meshes are illustrated in figure 2.16.

The electrical analogue of this structure is composed of identical square plate electrical analogues, whose lumped-element representation is in figure 2.14. According to the plate dimensions, the network should be made of $7n_0$ by $6n_0$ square elements, n_0 being integer. To tune the network components, the parameters appearing in the frequency coherence condition of equation (2.56) should be estimated:

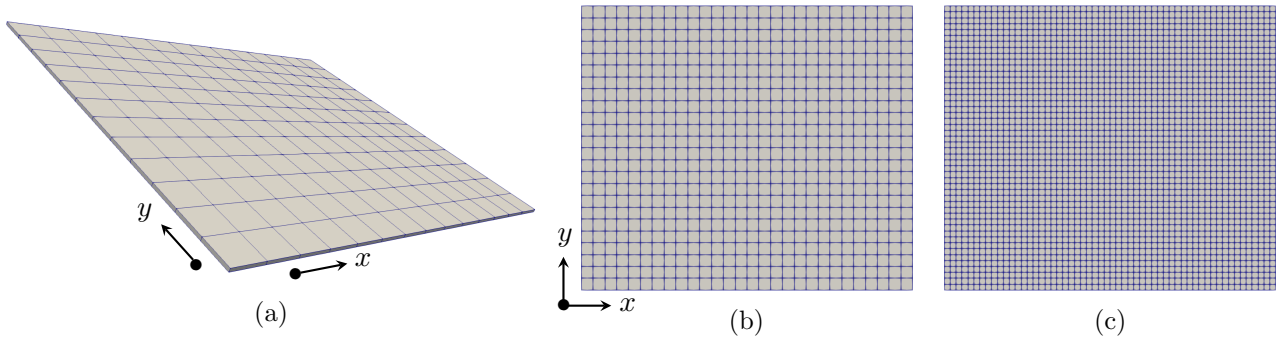

Figure 2.16: Meshes of the plate corresponding to elements densities of (a) $n_0 = 1$, (b) $n_0 = 2$ and (c) $n_0 = 4$.

- The cell side a depends on the considered discretization density:

$$a = \frac{l_x}{7n_0} = \frac{l_y}{6n_0}. \tag{2.59}$$

- The discrete mass m is estimated knowing the mass density ρ:

$$m = \rho h_s a^2. \tag{2.60}$$

- The classical expression for the bending stiffness K_θ of a square plate is

$$K_\theta = \frac{Y h_s^3}{12\left(1-\nu^2\right)}. \tag{2.61}$$

- The main capacitance is given by

$$C_\theta = \frac{150 \cdot 10^{-9}}{n_0^2}. \tag{2.62}$$

  This means that C_θ is equal to 150 nF for $n_0 = 1$, and that it is proportional to the unit cell surface. Even though this numerical example does not involve piezoelectric coupling, this capacitance evolution is inspired from the piezoelectric capacitance dependence on the surface of the transducers, which is explained in chapter 3.

- The transformer ratio is arbitrary set at $\hat{a} = 4$.

- The inductance is deduced by applying the equation (2.56):

$$\begin{aligned} L &= \left(\frac{a}{\hat{a}}\right)^2 \frac{m}{K_\theta C_\theta} \\ &= \frac{\rho h_s l_x^4}{\hat{a}^2 K_\theta \left(150 \cdot 10^{-9} \cdot 7^4\right)} \frac{1}{n_0^2}. \end{aligned} \tag{2.63}$$

n_0	**Elements**	**Nodes**	a (mm)	m (g)	C_θ (nF)	L (mH)	**Meshing**	**MAC matrix**	**Marker**
1	7×6	139	60	30.2	150	257.2	Fig. 2.16a	Fig. 2.19a	♦
2	14×12	530	30	7.6	37.5	64.3	Fig. 2.16b	Fig. 2.19b	▼
3	21×18	1173	20	3.4	16.7	28.6	/	Fig. 2.19c	■
4	28×24	2068	15	1.9	9.4	16.1	Fig. 2.16c	Fig. 2.19d	●

Table 2.5: Electrical modeling parameters for different discretizations of the plate analogue.

The values of these parameters for n_0 from 1 to 4 are recorded in table 2.5. Note that the inductance value in equation (2.63) is proportional to $1/n_0^2$, which highlights the potential decrease of inductance requirements when piezoelectric coupling will be considered in next chapters.

2.7.2.2 Spatial coherence condition validation

As far as the spatial coherence validation goes: velocity and electrical current modes should be compared at the same locations. On one hand, the electrical current modes are estimated with the equation (2.58) at the unit cell centers and at the boundaries between cells. For $n_0 = 1$, there are 139 available nodes, as depicted by red markers in figure 2.17. On the other hand, the velocity modes should be estimated at the positions that correspond to the network nodes. To ensure the meshing compatibility, the velocity modes are simulated with different meshes, as drawn in figure 2.16.

Now that the nodes for comparison have been set, we compute the AutoMAC. This is the particular case of the comparison of normal modes between themselves using the MAC. Computing it allows verifying if all normal modes can be distinguished. If all modes are supposedly different from each other and the AutoMAC matrix is not diagonal, then there is a spatial aliasing problem, such as illustrated in figure 2.3. For $n_0 = 1$, the figure 2.18b highlights that we can tell the difference between all electrical modes. Meanwhile, the mechanical AutoMAC in figure 2.18a is obtained with the mesh in figure 2.16a, which is compatible with a density of $n_0 = 1$. It indicates that the nodes locations allow to reliably represent the first velocity plate modes as well. As a consequence, all meshes of the plate and of its analogous network for $n_0 \geq 1$ allow genuinely representing and distinguishing their respective first normal modes, since they include more nodes for comparison.

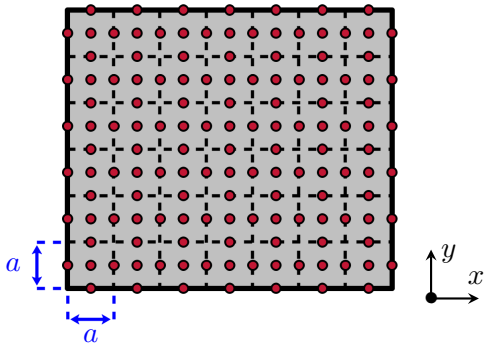

Figure 2.17: Nodes locations for the electrical current modes estimation in the network with $n_0 = 1$.

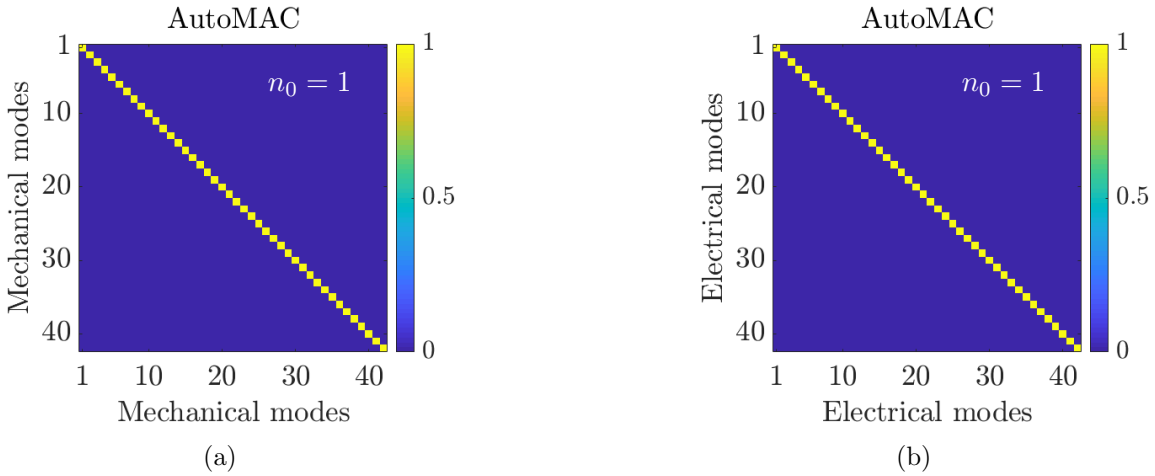

Figure 2.18: AutoMAC of the first 42 (a) velocity modes of the plate and (b) electrical current modes of the analogous network.

Then, the MAC matrix between electrical current modes of the network and velocity modes of the plate is plotted for n_0 from 1 to 4 in figure 2.19. This is equivalent to comparing plate modes estimated by a finite difference model on one hand, and by a finite element model on the other hand. Since we compare results issued from a continuous model to results issued from a discrete representation of the structure, it makes sense that the modes might not be similarly arranged. This is the case for $n_0 = 1$ in figure 2.19a, where the MAC matrix is not diagonal after the seventh mode. However, when n_0 increases, the MAC matrix tends to the identity matrix. This is equivalent to visualizing the convergence of a finite difference model towards a finite element model. Besides, each electrical mode in figure 2.19 is clearly identified and uniquely associated with a mechanical mode, even though they do not appear in the same order. For these reasons, we consider that the spatial coherence condition is met over the first tens of modes of the systems.

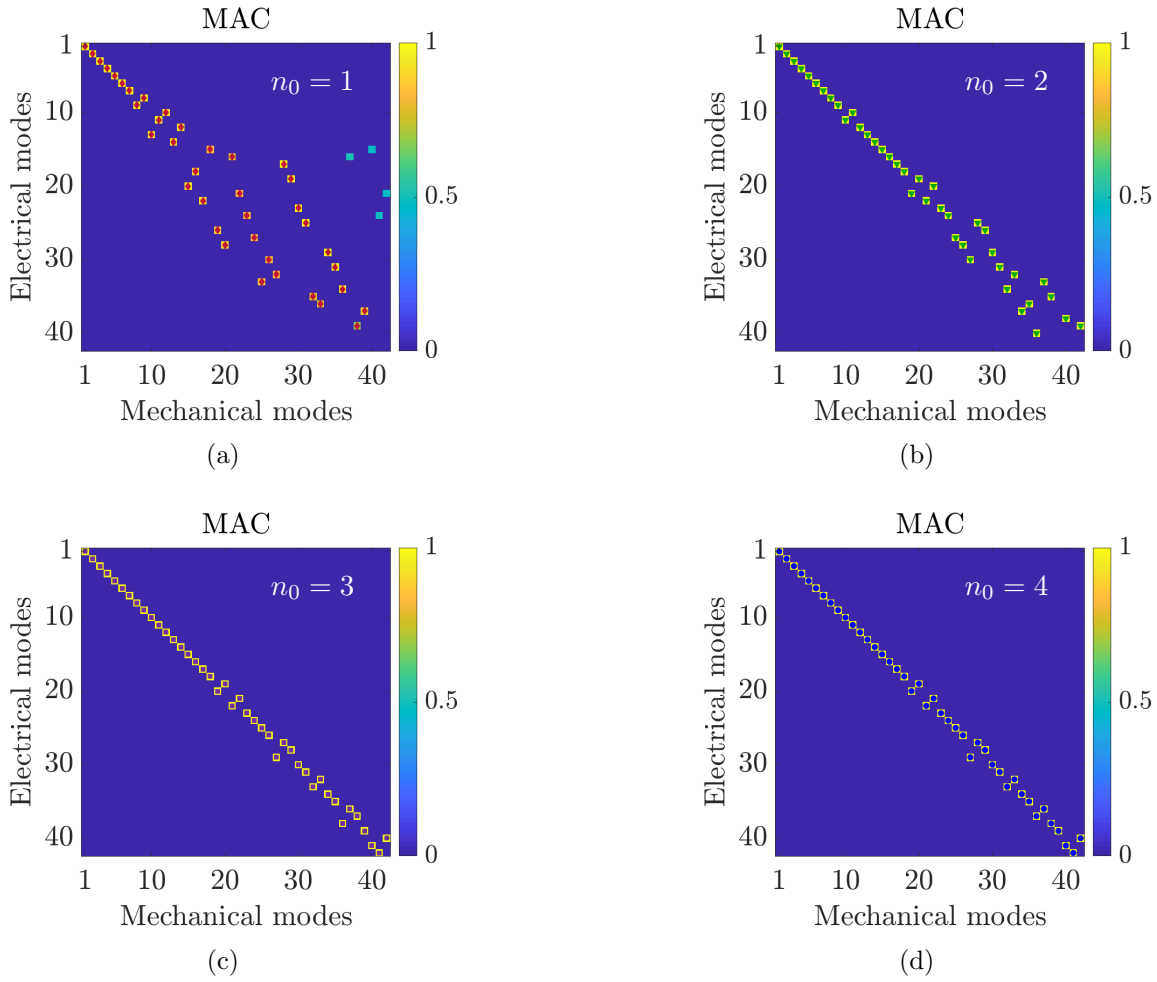

Figure 2.19: MAC between the 42 first velocity modes of the plate and electrical current modes of the network for (a) $n_0 = 1$, (b) $n_0 = 2$, (c) $n_0 = 3$ and (d) $n_0 = 4$. The tiny ♦, ▼, ■ and ● markers indicate which couple of modes are deemed clearly identified, so that they can be plotted in figure 2.20.

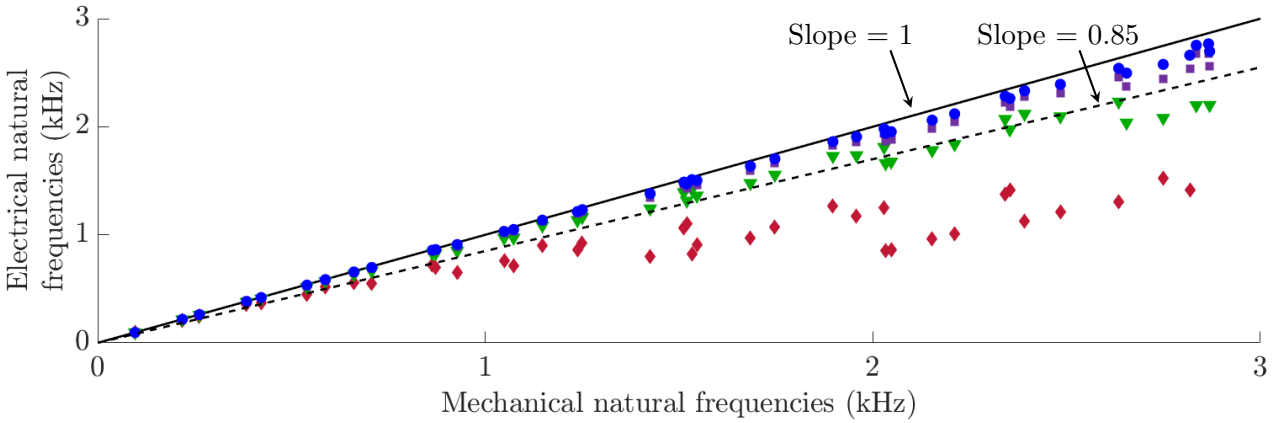

Figure 2.20: Comparison of mechanical and electrical natural frequencies for (♦) $n_0 = 1$, (▼) $n_0 = 2$, (■) $n_0 = 3$ and (●) $n_0 = 4$.

2.7.2.3 Frequency coherence condition validation

Now that we have verified that the plate and the developed electrical network share similar mode shapes, we should verify if they exhibit the same natural frequencies. The electrical components of the network have been tuned with this in mind. The natural frequencies of the electrical network, estimated thanks to the model of equation (2.58), are then compared to the plate natural frequencies estimated by a finite element model. Note that the mechanical natural frequencies are calculated with the finest mesh in figure 2.16c. The comparison is plotted in figure 2.20. It shows here as well that the finite difference results tend towards the finite element results when n_0 increases, as expected. For $n_0 = 1$, we can consider that the frequency coherence condition is verified for the first eleven modes and over nearly 1 kHz of frequency range.

As a conclusion, we have illustrated by a numerical example that the spatial and frequency coherence conditions are validated upon a given frequency range. This frequency range depends on the number of elements the electrical network is made of. In other words, increasing the number of elements in the network will make it tend towards a continuous structure, and therefore will extend the range over which the analogy is validated. Moreover, this example has given the opportunity to develop tools for the analogy validation between a mechanical structure and an electrical network, which will be useful in the following chapters.

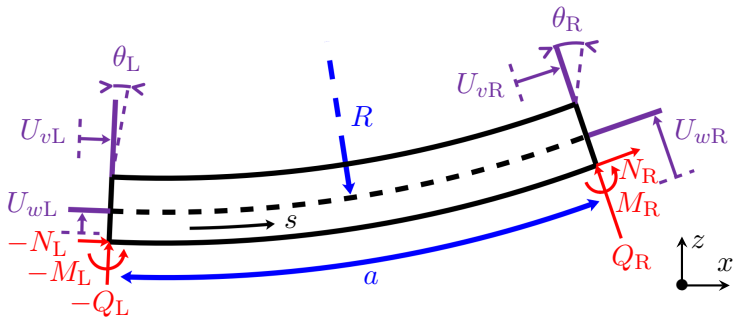

Figure 2.21: Continuous curved beam segment.

2.8 Curved beam electrical analogue

2.8.1 Model A: From the constitutive equations

Literature is abundant on the analytic study of curved structures, such as beams, rings and arches [89]. In the case of an elongated structure, the simplest model to implement is to apply the same hypotheses as the Euler-Bernoulli beam theory. Hence we study the motion of a curved beam of mass density ρ, cross-section S and radius of curvature R. Displacements amplitudes are denoted U_v in the direction which is parallel to the neutral axis, and U_w in the direction which is orthogonal to the neutral axis. All quantities depend on the arc length s. One can show that the curved beam dynamics in harmonic motion at angular frequency Ω is ruled by the following set of differential equations:

Step 1

$$\begin{aligned} -\rho S\Omega^2 U_v &= \frac{dN}{ds} + \frac{Q}{R}, \\ -\rho S\Omega^2 U_w &= \frac{dQ}{ds} - \frac{N}{R}, \end{aligned} \tag{2.64}$$

where N and Q respectively denote the normal and shear forces in the beam. Thus, constitutive equations are required to completely define the structure behavior. One of them is the relation between the bending moment M and the shear force Q when neglecting the rotational inertia, which is a classical hypothesis of the Euler-Bernoulli beam theory. In this theory, shear deformations are neglected as well. As a consequence, the slope θ of the beam is related to the displacements. Finally, assuming a linear elastic material, the constitutive equations of the medium relate the normal force N and the bending moment M to the displacements. These hypotheses create a set of four equations which, combined with the dynamic behavior described by equations (2.64), form the set of first-order

differential equations we look for:

Step 2

$$\begin{aligned} Q &= -\frac{dM}{ds}, & \theta &= \frac{dU_w}{ds} - \frac{U_v}{R}, \\ M &= EI\,\frac{d\theta}{ds}, & N &= ES\left(\frac{dU_v}{ds} + \frac{U_w}{R}\right). \end{aligned} \tag{2.65}$$

Applying the finite difference scheme presented in figure 2.2a and by equations (2.4) to the set of equations (2.65) leads to a discrete model of the curved beam:

Step 3

$$\begin{aligned} -\frac{m}{2}\,\Omega^2 U_{v\mathrm{L}} &= N_\mathrm{I} - N_\mathrm{L} + \frac{a}{2R}\,Q_\mathrm{L}, & \frac{a}{2}\,\theta_\mathrm{L} &= U_{w\mathrm{I}} - U_{w\mathrm{L}} - \frac{a}{2R}\,U_{v\mathrm{L}}, \\ -\frac{m}{2}\,\Omega^2 U_{v\mathrm{R}} &= N_\mathrm{R} - N_\mathrm{I} + \frac{a}{2R}\,Q_\mathrm{R}, & \frac{a}{2}\,\theta_\mathrm{R} &= U_{w\mathrm{R}} - U_{w\mathrm{I}} - \frac{a}{2R}\,U_{v\mathrm{R}}, \\ -m\Omega^2 U_{w\mathrm{I}} &= Q_\mathrm{R} - Q_\mathrm{L} - \frac{a}{R}\,N_\mathrm{I}, & \frac{a}{2}\,Q_\mathrm{L} &= M_\mathrm{L} - M_\mathrm{I}, \\ N_\mathrm{I} &= K_v\left(U_{v\mathrm{R}} - U_{v\mathrm{L}} + \frac{a}{R}\,U_{w\mathrm{I}}\right), & \frac{a}{2}\,Q_\mathrm{R} &= M_\mathrm{I} - M_\mathrm{R}, \\ M_\mathrm{I} &= K_\theta\left(\theta_\mathrm{R} - \theta_\mathrm{L}\right), \end{aligned} \tag{2.66}$$

with $m = \rho S a$ the mass of the beam segment, $K_v = ES/a$ its longitudinal stiffness and $K_\theta = EI/a$ its bending stiffness.

Then, the electrical analogue of the curved beam is derived by replacing mechanical quantities by electrical quantities according to the direct electromechanical analogy summed up in table 2.1, and by replacing the curved length a and the radius R by the electric "lengths" $\hat{a}$ and $\hat{R}$, respectively. The resulting electrical unit cell is characterized by the following equations, and is shown in figure 2.22:

Step 4

$$\begin{aligned} -\frac{L}{2}\,\Omega^2 q_{v\mathrm{L}} &= V_{v\mathrm{L}} - V_{v\mathrm{I}} - \frac{\hat{a}}{2\hat{R}}\,V_{w\mathrm{L}}, & \frac{\hat{a}}{2}\,q_{\theta\mathrm{L}} &= q_{w\mathrm{I}} - q_{w\mathrm{L}} - \frac{\hat{a}}{2\hat{R}}\,q_{v\mathrm{L}}, \\ -\frac{L}{2}\,\Omega^2 q_{v\mathrm{R}} &= V_{v\mathrm{I}} - V_{v\mathrm{R}} - \frac{\hat{a}}{2\hat{R}}\,V_{w\mathrm{R}}, & \frac{\hat{a}}{2}\,q_{\theta\mathrm{R}} &= q_{w\mathrm{R}} - q_{w\mathrm{I}} - \frac{\hat{a}}{2\hat{R}}\,q_{v\mathrm{R}}, \\ -L\Omega^2 q_{w\mathrm{I}} &= V_{w\mathrm{L}} - V_{w\mathrm{R}} + \frac{\hat{a}}{\hat{R}}\,V_{v\mathrm{I}}, & \frac{\hat{a}}{2}\,V_{w\mathrm{L}} &= V_{\theta\mathrm{L}} - V_{\theta\mathrm{I}}, \\ C_v V_{v\mathrm{I}} &= q_{v\mathrm{L}} - q_{v\mathrm{R}} - \frac{\hat{a}}{\hat{R}}\,q_{w\mathrm{I}}, & \frac{\hat{a}}{2}\,V_{w\mathrm{R}} &= V_{\theta\mathrm{I}} - V_{\theta\mathrm{R}}. \\ C_\theta V_{\theta\mathrm{I}} &= q_{\theta\mathrm{L}} - q_{\theta\mathrm{R}}, \end{aligned} \tag{2.67}$$

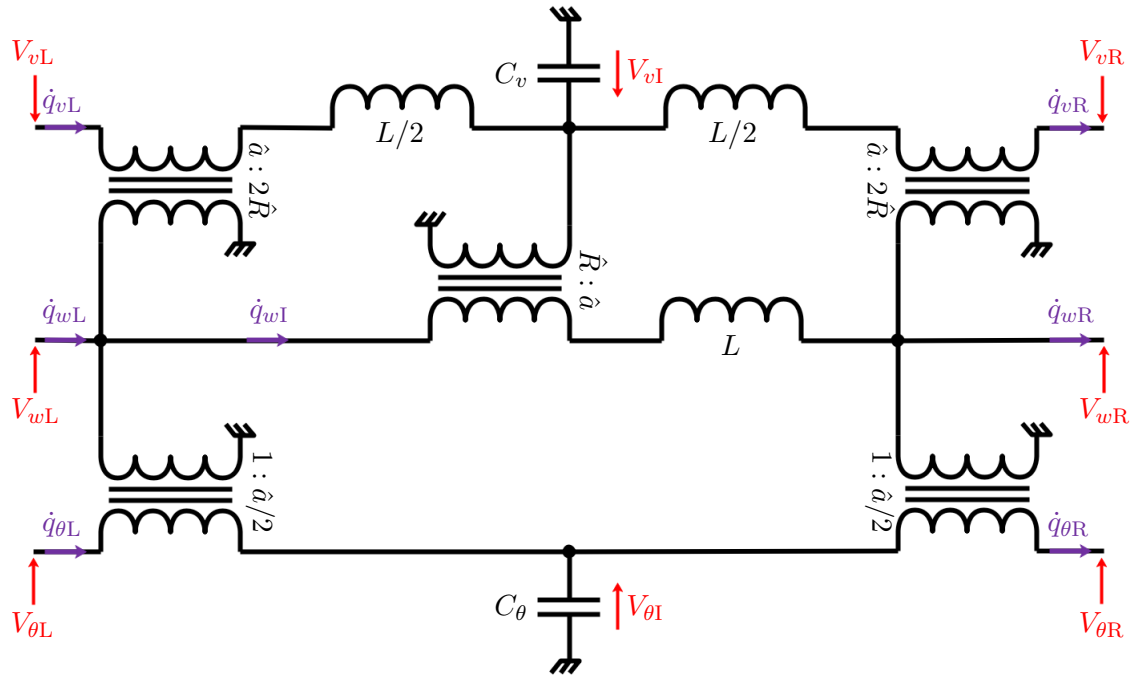

Figure 2.22: Unit cell of the model A of the curved beam electrical analogue, which is defined by the set of equations (2.67).

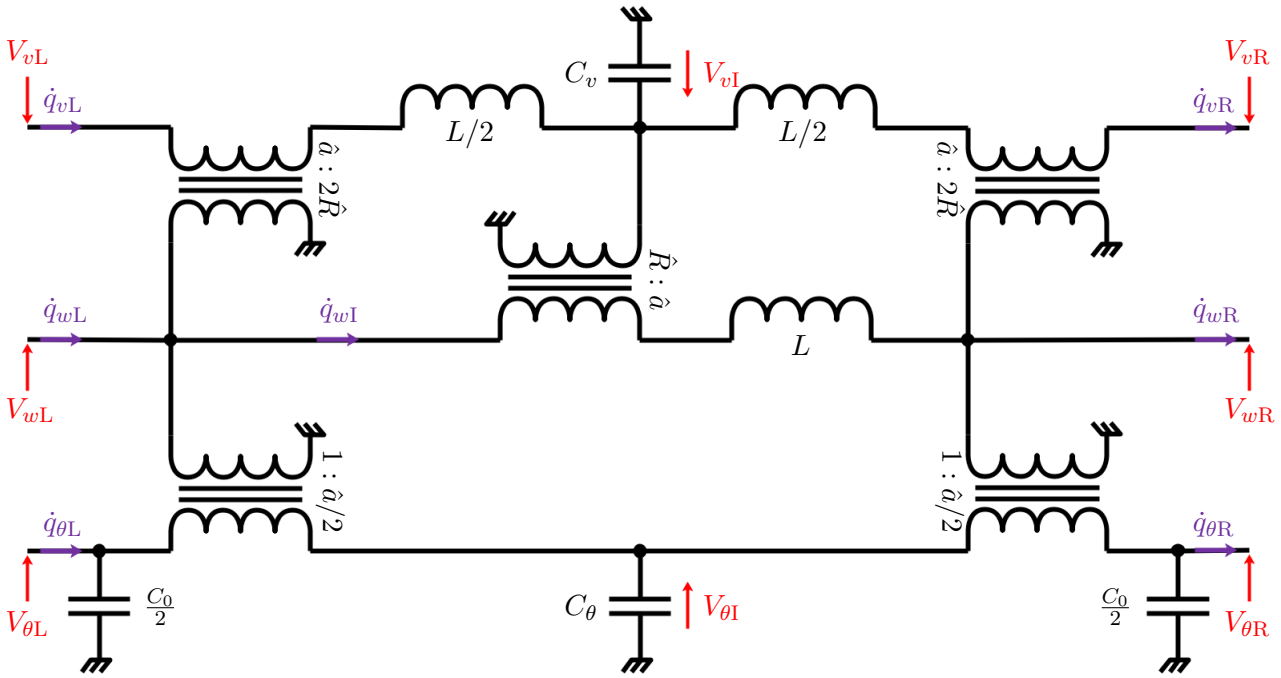

Figure 2.23: Unit cell of the model A of the curved beam electrical analogue, which is defined by the set of equations (2.67), with added capacitors on the sides.

Boundary condition	Mechanical equations	Electrical equations	Scheme
Free	$N_{\mathrm{R}} = 0$	$V_{v\mathrm{R}} = 0$	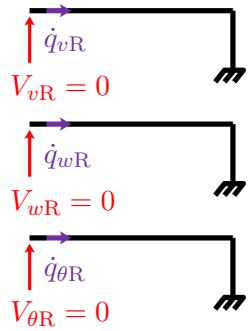
	$Q_{\mathrm{R}} = 0$	$V_{w\mathrm{R}} = 0$	
	$M_{\mathrm{R}} = 0$	$V_{\theta\mathrm{R}} = 0$	
	$U_{v\mathrm{R}}$ free	$\dot{q}_{v\mathrm{R}}$ free	
	$U_{w\mathrm{R}}$ free	$\dot{q}_{w\mathrm{R}}$ free	
	θ_{R} free	$\dot{q}_{\theta\mathrm{R}}$ free	
Simply-supported	N_{R} free	$V_{v\mathrm{R}}$ free	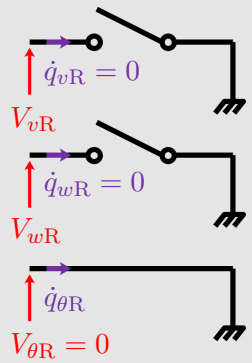
	Q_{R} free	$V_{w\mathrm{R}}$ free	
	$M_{\mathrm{R}} = 0$	$V_{\theta\mathrm{R}} = 0$	
	$U_{v\mathrm{R}} = 0$	$\dot{q}_{v\mathrm{R}} = 0$	
	$U_{w\mathrm{R}} = 0$	$\dot{q}_{w\mathrm{R}} = 0$	
	θ_{R} free	$\dot{q}_{\theta\mathrm{R}}$ free	
Clamped	N_{R} free	$V_{v\mathrm{R}}$ free	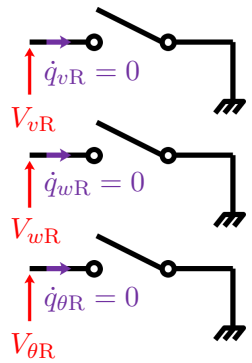
	Q_{R} free	$V_{w\mathrm{R}}$ free	
	M_{R} free	$V_{\theta\mathrm{R}}$ free	
	$U_{v\mathrm{R}} = 0$	$\dot{q}_{v\mathrm{R}} = 0$	
	$U_{w\mathrm{R}} = 0$	$\dot{q}_{w\mathrm{R}} = 0$	
	$\theta_{\mathrm{R}} = 0$	$\dot{q}_{\theta\mathrm{R}} = 0$	

Table 2.6: Curved beam analogous boundary conditions for a boundary on the right-side of the mechanical and electrical unit cells, the latest being represented in figure 2.22.

Analogous boundary conditions: In the case of a free boundary, the normal force N, the shear force Q and the bending moment M vanish at the boundary, while the displacements U_v and U_w and the slope θ can vary. This corresponds to a short-circuit condition on each of the three branches on the right-side of the electrical unit cell in figure 2.22.

If a boundary of the mechanical unit cell is simply-supported, then the displacements U_v and U_w are forced at zero while the slope θ is left unassigned. Moreover, at the boundary, the normal and shear forces N and Q are undefined while the bending moment M is equal to zero. For the unit cell in figure 2.22, this corresponds to a short-circuit electrical connection on the slope grid, and to an open-circuit electrical connection on the two remaining displacements grids.

Finally, we consider the case of a clamped boundary condition. In this case, the transverse displacement U_v, the longitudinal displacement U_w and the slope θ are all equal to zero, while all mechanical loads at the boundary are unconstrained. These represent open-circuit electrical conditions on the three branches of the unit cell in figure 2.22.

As a consequence, the free, simply-supported and clamped mechanical boundary conditions have direct electrical analogues. In the case of the right-side of the unit cells being a boundary, the associated discrete equations and sketches are gathered in table 2.6.

Frequency coherence conditions: Lastly, we give the expressions of nondimensionalized displacements by $U_v^\star = U_v/a$ and $U_w^\star = U_w/a$, rotations by $\theta^\star = \theta$, normal forces by $N^\star = N/(aK_v)$, shear forces by $Q^\star = aQ/K_\theta$ and bending moments by $M^\star = M/K_\theta$. To derive the frequency coherence conditions, the quantities on the right-hand side of the mechanical unit cell in figure 2.21 that has been discretized are related to the quantities on the left-hand side:

$$\begin{pmatrix} U^\star_{v\mathrm{R}} \\ U^\star_{w\mathrm{R}} \\ \theta^\star_{\mathrm{R}} \\ -N^\star_{\mathrm{R}} \\ -Q^\star_{\mathrm{R}} \\ -M^\star_{\mathrm{R}} \end{pmatrix} = \begin{pmatrix} 1-\frac{\delta^2+\beta}{2} & -\delta & \frac{-\delta}{2} & \multicolumn{3}{c}{\multirow{3}{*}{$\boldsymbol{B}$}} \\ \delta\left(1-\frac{\delta^2+\beta}{4}\right) & 1-\frac{\delta^2}{2} & 1-\frac{\delta^2}{4} & & & \\ 0 & 0 & 1 & & & \\ \beta\left(1-\frac{3\delta^2+\beta}{4}\right) & -\delta\beta & \frac{-\delta\beta}{2} & 1-\frac{\delta^2+\beta}{2} & \frac{\beta\delta}{\gamma}\left(\frac{\delta^2+\beta}{4}-1\right) & 0 \\ \delta\gamma & \gamma & \frac{\gamma}{2} & \frac{\delta\gamma}{\beta} & 1-\frac{\delta^2}{2} & 0 \\ \frac{-\delta\gamma}{2} & \frac{-\gamma}{2} & \frac{-\gamma}{4} & \frac{-\delta\gamma}{2\beta} & \frac{\delta^2}{4}-1 & 1 \end{pmatrix} \begin{pmatrix} U^\star_{v\mathrm{L}} \\ U^\star_{w\mathrm{L}} \\ \theta^\star_{\mathrm{L}} \\ -N^\star_{\mathrm{L}} \\ -Q^\star_{\mathrm{L}} \\ -M^\star_{\mathrm{L}} \end{pmatrix},$$

$$\text{with} \qquad \delta = \frac{a}{R}, \qquad \beta = \frac{m\Omega^2}{K_v} \qquad \text{and} \qquad \gamma = \frac{ma^2\Omega^2}{K_\theta}. \tag{2.68}$$

Thus we deduce that the electrical circuit in figure 2.22 would have identical bending wave propagation properties as the discrete mechanical model if they share the same ratios δ, β and γ. This means that the frequency coherence conditions are

$$\frac{a}{R} = \frac{\hat{a}}{\hat{R}}, \qquad \frac{K_v}{m} = \frac{1}{LC_v}, \qquad \frac{1}{a^2}\frac{K_\theta}{m} = \frac{1}{\hat{a}^2}\frac{1}{LC_\theta}. \tag{2.69}$$

We find two frequency coherence conditions which are identical to those of the rod and beam electrical analogues, written in equations (2.29) and (2.45). The last condition concerns the ratio of the unit cell length a over the curvature R. It represents the coupling between traction and bending in the curved structure, whose influence is modeled by the three transformers of ratio $\hat{a} : \hat{R}$ or $\hat{a} : 2\hat{R}$ in figure 2.22.

Unit cells assembly: Taking equations (2.8) and (2.68) into account, we identify that $\boldsymbol{B}$ is a singular matrix. As a consequence, we cannot compute the electrical dynamic matrix $\boldsymbol{D_e}$. The reason for this is the same as for the Euler-Bernoulli beam and the Kirchhoff-Love plate discrete models previously derived: the system of equations (2.67) is ill-defined and cannot be solved. Hence we suggest adding side capacitors of capacitance C_0 as a numerical trick to avoid singularity problems. Figure 2.23 shows the adapted electrical unit cell. Integrating these components to the curved beam electrical analogue described by equations (2.67) leads to a more complicated transfer matrix. Though not detailed here, the new $\boldsymbol{B}$ matrix is

$$\boldsymbol{B} = \begin{pmatrix} -1 & \frac{\delta\beta}{2\gamma} & \frac{\delta\epsilon}{4} \\ \frac{-\delta}{2} & \frac{1}{4}\left(1+\frac{\beta\delta^2}{\gamma}\right) & \frac{1}{2}\left(\frac{\epsilon\delta^2}{4}-\epsilon-1\right) \\ \frac{\delta\gamma\epsilon}{4\beta} & \frac{1}{2}\left(1+\epsilon-\frac{\epsilon\delta^2}{4}\right) & -\left(1+\epsilon+\frac{\gamma\epsilon^2}{16}\right) \end{pmatrix} \qquad \text{with } \epsilon = \frac{C_0}{C_\theta}. \tag{2.70}$$

Notice that setting $C_0 = 0$, i.e. $\epsilon = 0$, in this new expression of $\boldsymbol{B}$ leads to the previously identified singular matrix. One can show that the determinant of this new matrix is

$$\det(\boldsymbol{B}) = -\frac{\epsilon}{4}\left[1 + \epsilon\left(1 + \frac{\gamma}{16\beta}\left(\delta^2 - \gamma\beta\right)\right)\right] \approx -\frac{\epsilon}{4} \qquad \text{if } \epsilon \ll 1. \tag{2.71}$$

As expected, the C_0 capacitance should be different from zero to avoid numerical singularity, but should small enough so that it remains a numerical trick. As previously stated, setting ϵ at around 10^{-6} is adequate in most cases.

Now that $\boldsymbol{B}$ is not singular anymore, the dynamic matrix can be derived. Using the notations in figure 2.23, the values of the electrical charges and the voltages in one unit cell of the network are denoted $\boldsymbol{q_N}$ and $\boldsymbol{v_N}$:

$$\begin{aligned} \boldsymbol{q_N} &= \begin{pmatrix} q_{v\mathrm{L}} & q_{w\mathrm{L}} & q_{\theta\mathrm{L}} & q_{v\mathrm{R}} & q_{w\mathrm{R}} & q_{\theta\mathrm{R}} \end{pmatrix}^{\mathrm{T}}, \\ \boldsymbol{v_N} &= \begin{pmatrix} V_{v\mathrm{L}} & V_{w\mathrm{L}} & V_{\theta\mathrm{L}} & -V_{v\mathrm{R}} & -V_{w\mathrm{R}} & -V_{\theta\mathrm{R}} \end{pmatrix}^{\mathrm{T}}. \end{aligned} \tag{2.72}$$

Following the derivation of the dynamic matrix $\boldsymbol{D_e}$, we apply equations (2.13). Because of their large size, the resulting electrical elementary matrices are recorded in appendix B. The elementary "mass" matrix $\boldsymbol{M_{elm}}$ is a function of the inductance value L, which is the electrical analogous quantity of the mass. The elementary "stiffness" matrix $\boldsymbol{K_{elm}}$ is a function of the capacitances C_v and C_θ, which are the respective analogous quantities of the longitudinal and bending compliances, as well as the numerical parameter C_0.

Then, following an assembly process, the vectors $\boldsymbol{Q_N}$ and $\boldsymbol{V_N}$ which contain the values of electrical charges and external voltages in the entire network are related to each other by

Step 5

$$\boldsymbol{V_N} = \left(\boldsymbol{K_N} - \Omega^2 \boldsymbol{M_N}\right) \boldsymbol{Q_N}, \tag{2.73}$$

with $\boldsymbol{M_N}$ and $\boldsymbol{K_N}$ being respectively the assembled matrices of electrical "mass" and electrical "stiffness". After that, the mode shapes and natural frequencies of the electrical circuit can be estimated to be compared to those of the mechanical structure.

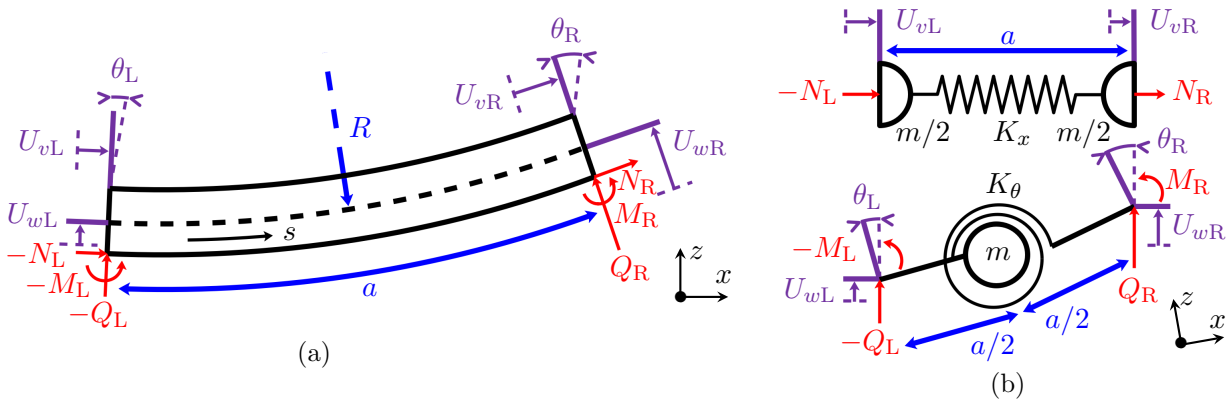

Figure 2.24: (a) Continuous curved beam segment and (b) associated discrete model.

2.8.2 Model B: From assembling existing analogous elements

Going towards complex structures, we aim at creating a library of electrical analogues that could be assembled to replicate the dynamic behavior of a mechanical system. In the previous subsection, we have defined a curved beam electrical analogue starting from its dynamics equations. We have now the opportunity to define another analogue by assembling previously derived unit cells. This approach intends on verifying that it is possible to assemble basic unit cells in order to estimate the mechanical behavior of a more complex structure. This method is different from what is proposed in section 2.3.

If the structure is discretized enough, then a model of a curved beam can be seen as an assembly of straight elements with independent responses to traction and bending loads. A mechanical representation of one element is sketched in figure 2.24b. It combines longitudinal and transverse vibrations, and hence independently associates the discrete rod model in figure 2.6b and the discrete beam model in figure 2.10b. Therefore, the electrical analogue of such an element is defined by independently combining the rod electrical analogue in figure 2.7b and the beam electrical analogue in figure 2.12. The resulting curved beam electrical analogue is drawn in figure 2.25.

The electrical unit cell represented in figure 2.25 assumes that the structure is straight, and so that traction and bending vibrations are not correlated. Let us consider the curved beam electrical analogue designed from its dynamics equations, which is shown in figure 2.23. In the case of a nearly straight structure, the radius of curvature R is much greater than the unit cell length a. Thus, according to one of the frequency coherence conditions written in equation (2.69), the ratio $\hat{R}/\hat{a}$ is much larger

than 1. Consequently, considering the notations in figure 2.26, we have:

$$V_{v\mathrm{I}} = \frac{\hat{R}}{\hat{a}}\, V_{T1}, \qquad V_{w\mathrm{L}} = \frac{2\hat{R}}{\hat{a}}\, V_{T2}, \qquad V_{w\mathrm{R}} = \frac{2\hat{R}}{\hat{a}}\, V_{T3}. \tag{2.74}$$

Since $V_{v\mathrm{I}}$, $V_{w\mathrm{L}}$ and $V_{w\mathrm{R}}$ have finite values while the ratio $\hat{R}/\hat{a} \to \infty$, one deduces that V_{T1}, V_{T2} and V_{T3} are all equal to zero. Thus the three transformers involving this ratio are short-circuited on one of their sides. Therefore the bending-traction coupling does not occur anymore. As depicted in figure 2.26, we can identify the rod and beam electrical analogues as a limit case. This shows that the two unit cells of the electrical curved beam analogues are mutually consistent.

To take the structure curvature into account, the elementary cells should be angularly offset according to the structure geometry. Supposing that deflections are small and linear, we can define a nominal angle α around which vibrations occur. The clamped condition between the two straight structure segments allows defining the transmission of efforts and movements in both normal and transverse directions. The figure 2.27 highlights this concept. To electrically simulate the angularly orientated junction between two elements, an electrical analogue of a rotation matrix should be designed. If "1" and "2" respectively designate the left and right side of the junction, then

$$\begin{pmatrix} U_{v2} \\ U_{w2} \\ U_{\theta 2} \end{pmatrix} = \begin{pmatrix} \cos\alpha & \sin\alpha & 0 \\ -\sin\alpha & \cos\alpha & 0 \\ 0 & 0 & 1 \end{pmatrix} \begin{pmatrix} U_{v1} \\ U_{w1} \\ U_{\theta 1} \end{pmatrix} \quad \text{and} \quad \begin{pmatrix} N_2 \\ Q_2 \\ M_2 \end{pmatrix} = \begin{pmatrix} \cos\alpha & \sin\alpha & 0 \\ -\sin\alpha & \cos\alpha & 0 \\ 0 & 0 & 1 \end{pmatrix} \begin{pmatrix} N_1 \\ Q_1 \\ M_1 \end{pmatrix}. \tag{2.75}$$

Applying the direct electromechanical analogy summed up in table 2.1, one obtains the analogous electrical equations of a rotation transformation:

$$\begin{pmatrix} q_{v2} \\ q_{w2} \\ q_{\theta 2} \end{pmatrix} = \begin{pmatrix} \cos\alpha & \sin\alpha & 0 \\ -\sin\alpha & \cos\alpha & 0 \\ 0 & 0 & 1 \end{pmatrix} \begin{pmatrix} q_{v1} \\ q_{w1} \\ q_{\theta 1} \end{pmatrix} \quad \text{and} \quad \begin{pmatrix} V_{v2} \\ V_{w2} \\ V_{\theta 2} \end{pmatrix} = \begin{pmatrix} \cos\alpha & \sin\alpha & 0 \\ -\sin\alpha & \cos\alpha & 0 \\ 0 & 0 & 1 \end{pmatrix} \begin{pmatrix} V_{v1} \\ V_{w1} \\ V_{\theta 1} \end{pmatrix}. \tag{2.76}$$

These set of equations can be passively represented in the form of an electrical circuit, in which the transformers ratios involve the α angle. These cells were first shown in [79], and are sketched in figure 2.28.

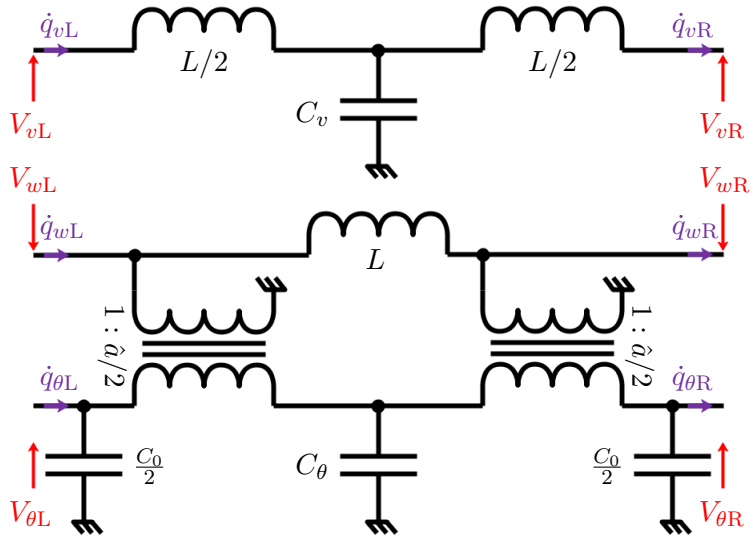

Figure 2.25: Unit cell of the model B of the curved beam electrical analogue, which is defined by the set of equations (2.25) and (2.43) with adapted notations and added capacitors on the sides.

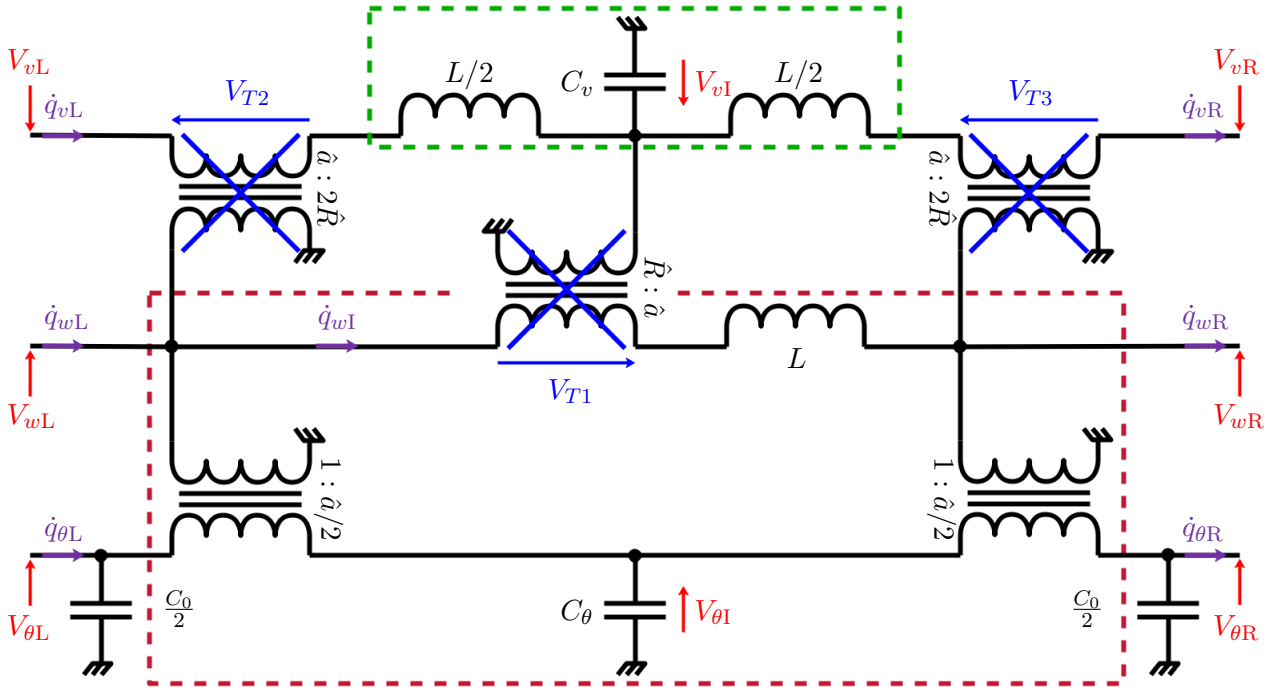

Figure 2.26: Limit case when $\hat{R}/\hat{a} \to \infty$ of the unit cell of the model A of the curved beam electrical analogue, initially represented in figure 2.23. The identified ---- rod electrical analogue and ---- beam electrical analogue are framed.

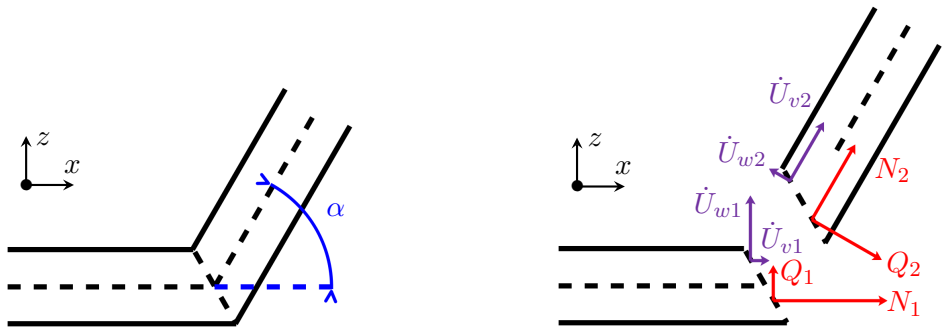

Figure 2.27: Transmission of efforts and displacements through a tilted clamping.

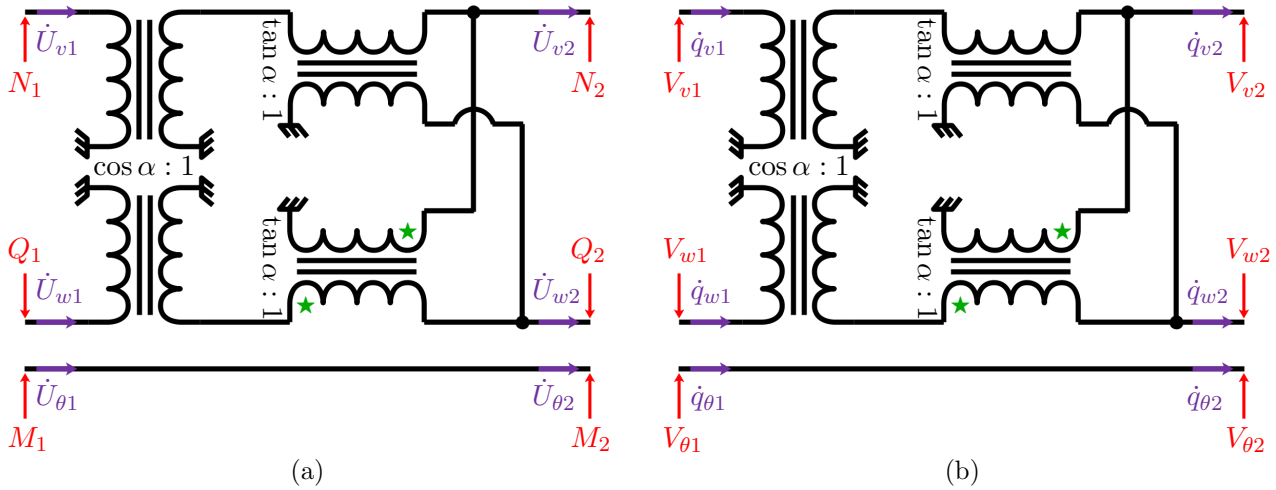

Figure 2.28: (a) Electrical representation of the mechanical rotation of equations (2.75) and (b) analogous electrical model of equations (2.76).

As a conclusion, it is possible to define another curved beam electrical analogue. It is done by considering previously derived electrical circuits modeling traction and bending wave propagation, and interconnecting them by electrical analogues of rotation matrices. The comparison between these two analogues is conducted in the following subsection.

Number of components and integration

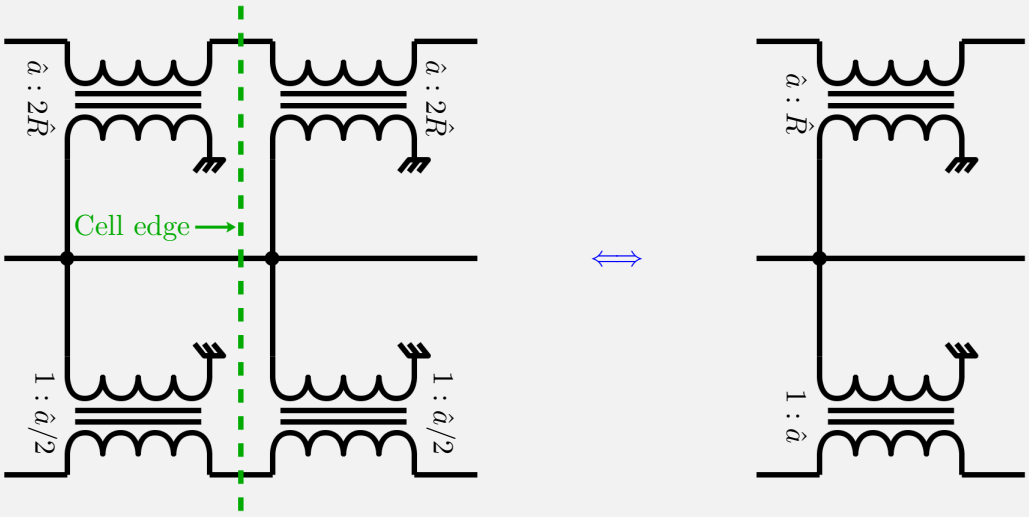

Figure 2.29: Simplification of the network transformers by interconnection of unit cells represented in figure 2.22.

It is important to note that the number of components is different for the two derived curved beam electrical analogues. The unit cell in figure 2.22 contains three inductors, two capacitors and five transformers. However, the side transformers of ratios $\hat{a} : 2\hat{R}$ and $1 : \hat{a}/2$ could be merged with the similar transformer of the adjacent cell to form transformers of ratios $\hat{a}/\hat{R}$ and $1 : \hat{a}$, respectively. This simplification is illustrated by figure 2.29. Therefore, each unit cell virtually contains three inductors, two capacitors and three transformers (one being in the center, and four halves of side transformers).

Meanwhile, the unit cell in figure 2.25 contains three inductors, two capacitors and two transformers. Moreover, the figure 2.28b shows that four transformers are required between two unit cells to make the rotation transformation. Hence, four transformers virtually belong to the unit cell as well. This gets the unit cell number of components up to three inductors, two capacitors and six transformers.

This difference between components amount in the unit cells highlight that the method of electrical analogue derivation has a significant impact on the potential integration of such analogues. More electrical components leads to more parasitic elements, an increased embedded mass and a greater cost as well. These drawbacks might be unavoidable going towards complex structures, because the objective is to create a library of electrical circuits whose assembly replicates a 3D dynamics behavior.

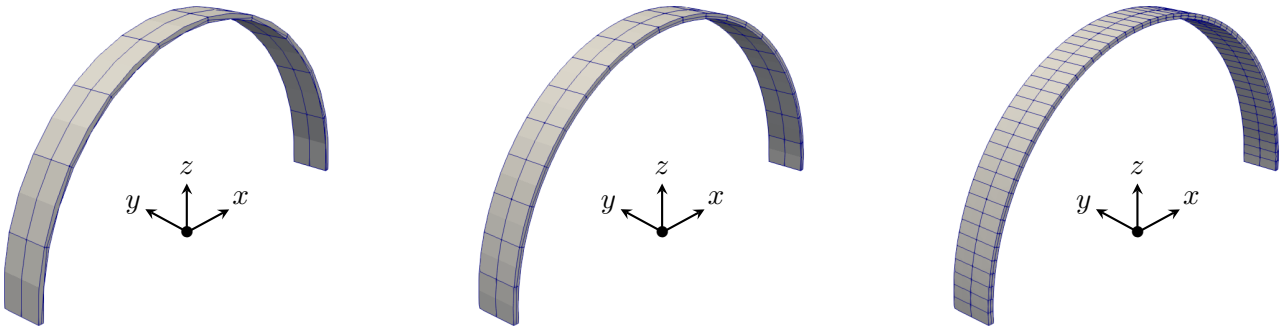

(a) (b) (c)

Figure 2.30: Meshes of the arch corresponding to (a) $n_{elm} = 10$ elements, (b) $n_{elm} = 20$ elements and (c) $n_{elm} = 60$ elements along the curvature.

2.8.3 Electrical analogue validation

2.8.3.1 Structure and analogous network development

We suggest validating the curved beam electric analogue derived in this section by treating a numerical example. We study a fully-clamped duralumin semi-circular arch of radius $R = 200$ mm, width $b = 40$ mm and thickness $h_s = 5$ mm, whose Poisson's ratio ν, density ρ and Young's modulus Y are respectively set at 0.35, 2800 kg/m^3 and 69 GPa. Its mode shapes and natural frequencies are estimated via the same finite element model as the one in subsection 2.7.2. The structure material exhibits isotropic and homogeneous properties and stays in linear elasticity. It is modeled with 20-node hexahedral elements. We use one element in depth, and two elements in width. Some meshes are illustrated in figure 2.30.

The electrical analogue of this structure is composed of identical curved beam electrical unit cells, whose lumped-element representation is either sketched in figure 2.23 for the model A, or in figure 2.25 for the model B. We choose to discretize the structure with a number of elements n_{elm} equal to 10, 20, 30 or 60. To tune the network components, the parameters appearing in the frequency coherence conditions of equation (2.69) should be estimated:

- The length a depends on the considered discretization:

$$a = \frac{\pi R}{n_{elm}}. \tag{2.77}$$

- The discrete mass m is estimated knowing the mass density ρ:

$$m = \rho a b h_s. \tag{2.78}$$

- The longitudinal stiffness is estimated by its classical expression:

$$K_v = Y\,\frac{b h_s}{a}. \tag{2.79}$$

- Denoting (v, w, y) the local coordinate system, the bending stiffness K_θ can be computed using the following expressions:

$$\frac{1}{K_\theta} = \frac{1}{Y}\int_0^a \frac{1}{I(v)}\,dv, \qquad \text{with } I(v) = \int_0^b \int_{-h_s/2}^{h_s/2} w^2\,dy\,dw. \tag{2.80}$$

  In the present situation, it leads to the classical expression of the bending stiffness of a beam:

$$K_\theta = Y\,\frac{b h_s^3}{12 a}. \tag{2.81}$$

- The main capacitance is given by

$$C_\theta = \frac{150 \cdot 10^{-9}}{n_{elm}/10}. \tag{2.82}$$

  This means that C_θ is equal to 150 nF for $n_{elm} = 10$, and that it is proportional to the unit cell surface, which decreases along the curvature when n_{elm} increases. Even though this numerical example does not involve piezoelectric coupling, this capacitance evolution is inspired from the piezoelectric capacitance dependence on the surface of the transducers, which is explained in chapter 3.

- The transformer ratio is arbitrary set at $\hat{a} = 4$.

- The electrical radius, the inductance and the longitudinal capacitance are derived thanks to the coherence conditions of equation (2.69):

$$\hat{R} = \frac{\hat{a} R}{a}, \qquad L = \left(\frac{a}{\hat{a}}\right)^2 \frac{m}{K_\theta C_\theta}, \qquad C_v = \frac{m}{L K_v}. \tag{2.83}$$

  In this case, one can prove that L is proportional to $1/n_{elm}^3$. Thus, there is an interest in increasing the number of components to reduce the requirements on the inductors to be produced.

The values of these parameters for n_{elm} from 10 to 60 are recorded in table 2.7.

n_{elm}	**Nodes**	a (mm)	m (g)	K_v (GN/m)	K_θ (N.m)	C_θ (nF)	$\hat{R}$ (-)	L (mH)	C_v (nF)
10	11	62.8	35.2	0.22	458	150	12.7	126.5	1.3
20	21	31.4	17.6	0.44	915	75	25.5	15.8	2.5
30	31	20.9	11.7	0.66	1373	50	38.2	4.7	3.8
60	61	10.5	5.9	1.3	2745	25	76.4	0.6	7.6

n_{elm}	**Meshing**	**MAC matrix**	**Marker**
10	Fig. 2.30a	Fig. 2.32a	♦
20	Fig. 2.30b	Fig. 2.32b	▼
30	/	Fig. 2.32c	■
60	Fig. 2.30c	Fig. 2.32d	●

Table 2.7: Electrical modeling parameters for different discretizations of the curved beam analogue of model A.

2.8.3.2 Spatial coherence condition validation

Firstly, we plot the AutoMAC matrices of the mechanical and electrical systems to verify if the meshes are sufficiently fine. The electrical AutoMAC matrices shown in figures 2.31b and 2.31c indicate that all electrical current modes of both networks can be easily distinguished from each other, even for $n_{elm} = 10$. It is thus possible to make the difference between the first 20 electrical modes for a greater number of elements as well.

The mechanical AutoMAC in figure 2.31a illustrates a problem of spatial aliasing. While it is possible to distinguish most of the 40 first modes of the arch, some are not clearly and uniquely identified. It is the case for example of modes number 2, 5 and 8, among others. These modes are actually either torsional or out-of-plane bending modes. As written before, and as can be seen in figure 2.30, we use only two elements in width and one element in depth. The discretization along these two directions is not fine enough to obtain a completely diagonal AutoMAC matrix, and refining the mesh along the curve would not improve it. Therefore, we assume that all mechanical meshes for $n_{elm} \geq 10$ allow making the difference between mechanical modes we are interested in.

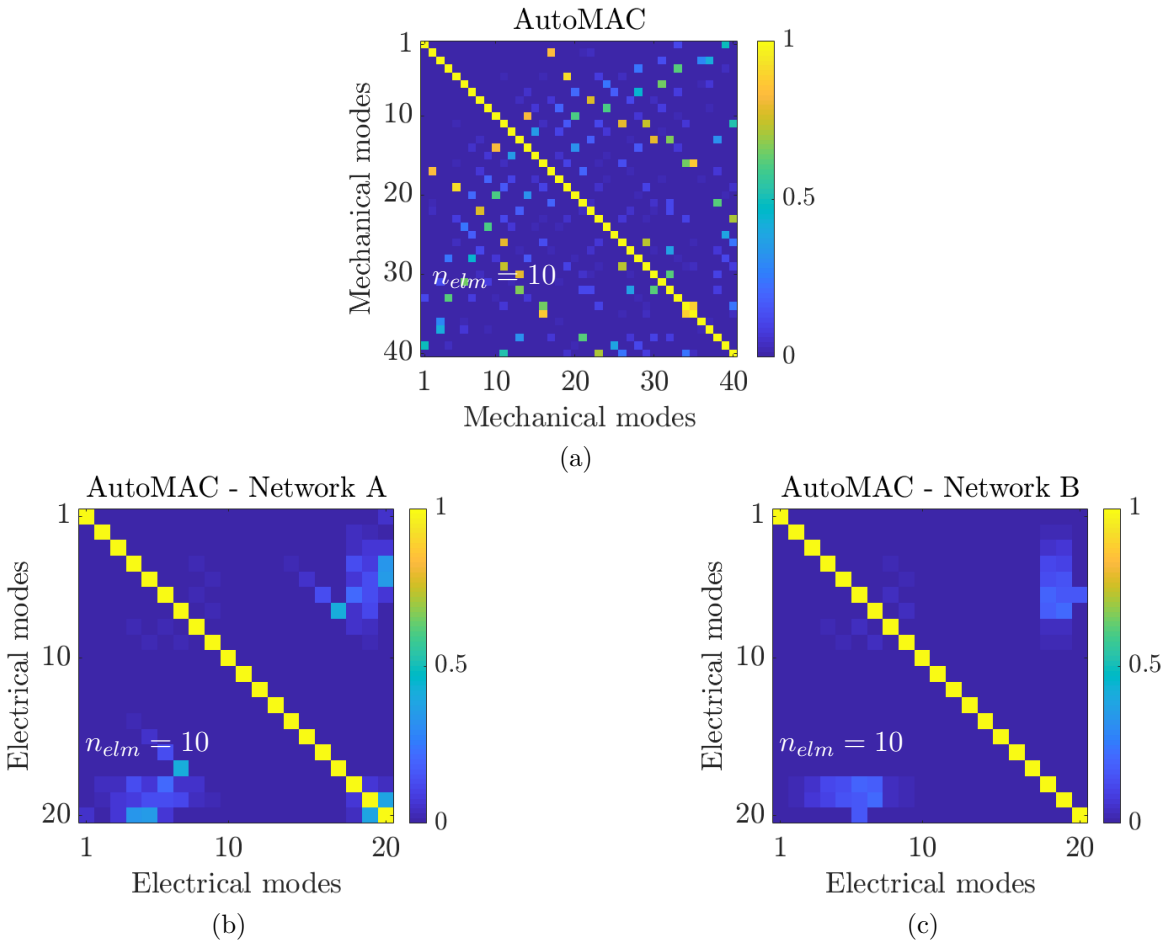

Figure 2.31: (a) AutoMAC of the first 40 velocity modes of the arch, and AutoMAC of the first 20 electrical current modes of the analogous network assembled with unit cells (b) in figure 2.23 or (c) in figure 2.25.

The MAC matrices between electrical current modes of the two assembled networks and velocity modes of the curved beam are plotted for different values of n_{elm} in figures 2.32 and 2.33. This is equivalent to comparing arch modes estimated by a finite difference model on one hand, and by a finite element model on the other hand. One can notice that the torsional and out-of-plane bending modes of the arch do not appear in networks A and B. Indeed, these kind of loads cannot be predicted by the present networks, which only represent in-plane bending. This is why there are some columns of the MAC matrices which completely remain at zero. In both cases however, the finite difference models indeed converge towards the finite element model, which is assumed to be precise enough to serve as the reference. Consequently, the spatial coherence condition is met over the first in-plane bending modes of the arch.

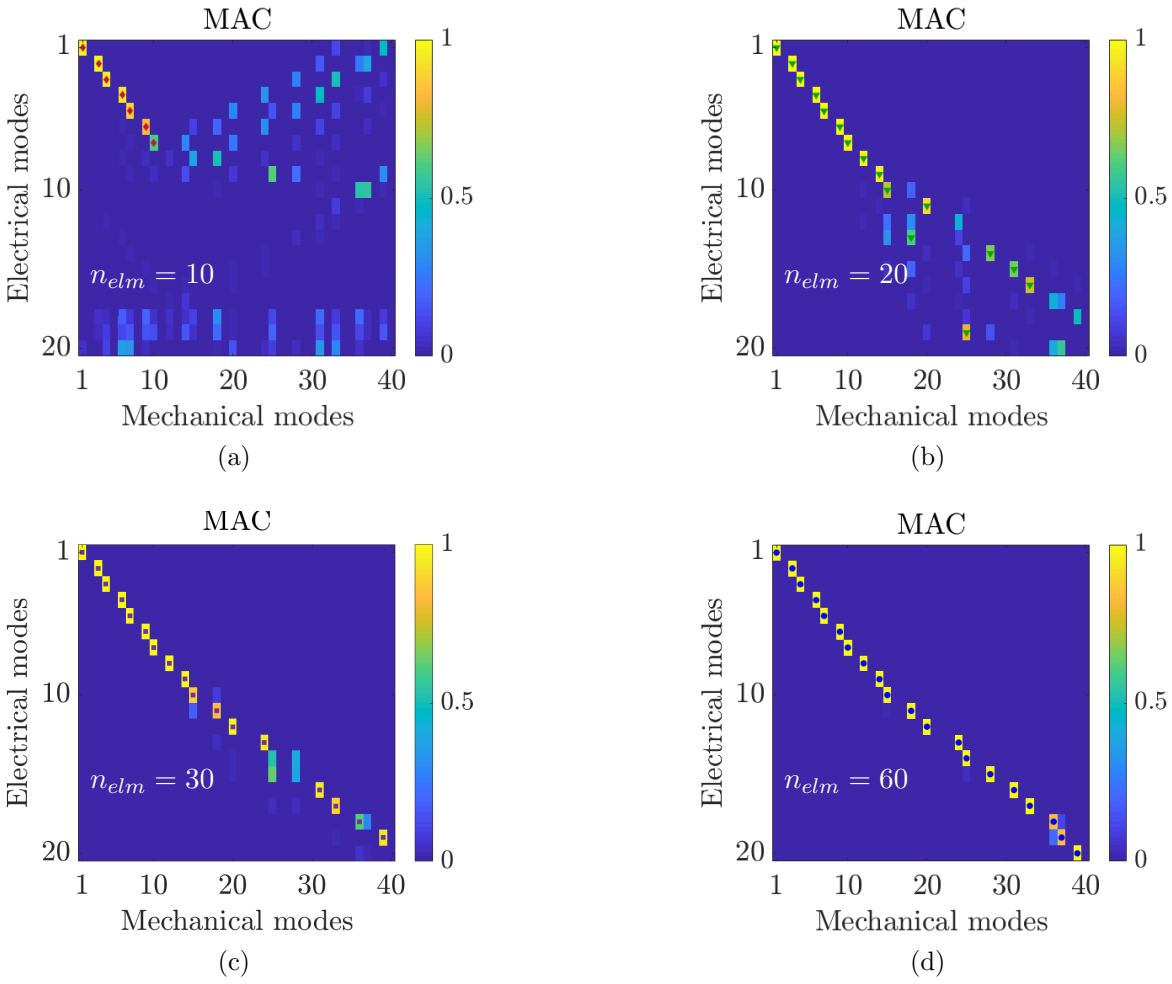

Figure 2.32: MAC between the 40 first velocity modes of the arch and the 20 first electrical current modes of the network A for (a) $n_{elm} = 10$, (b) $n_{elm} = 20$, (c) $n_{elm} = 30$ and (d) $n_{elm} = 60$. The tiny ♦, ▼, ■ and ● markers indicate which couple of modes are deemed clearly identified, so that they can be plotted in figure 2.34.

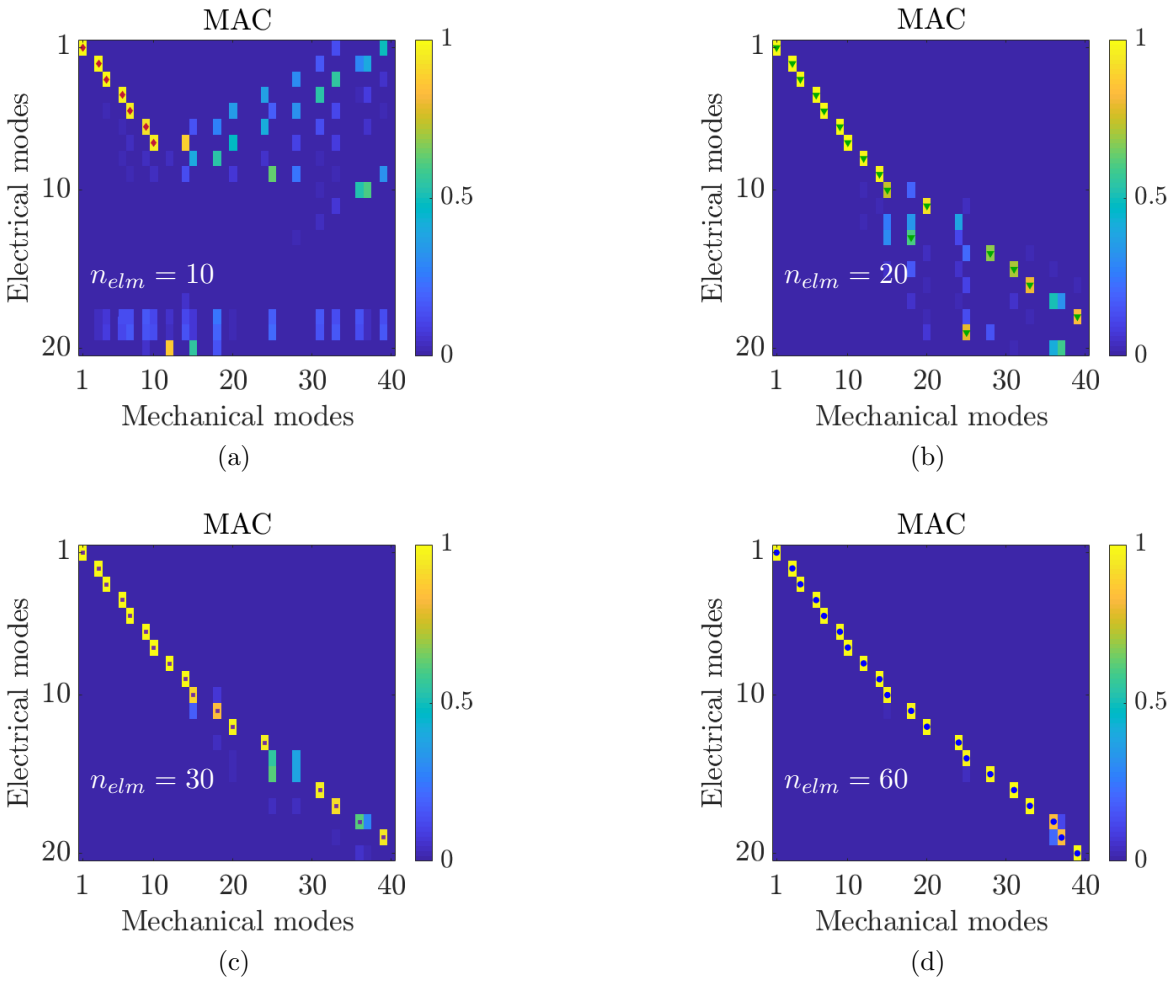

Figure 2.33: MAC between the 40 first velocity modes of the arch and the 20 first electrical current modes of the network B for (a) $n_{elm} = 10$, (b) $n_{elm} = 20$, (c) $n_{elm} = 30$ and (d) $n_{elm} = 60$. The tiny ♦, ▼, ■ and ● markers indicate which couple of modes are deemed clearly identified, so that they could be plotted in figure 2.34.

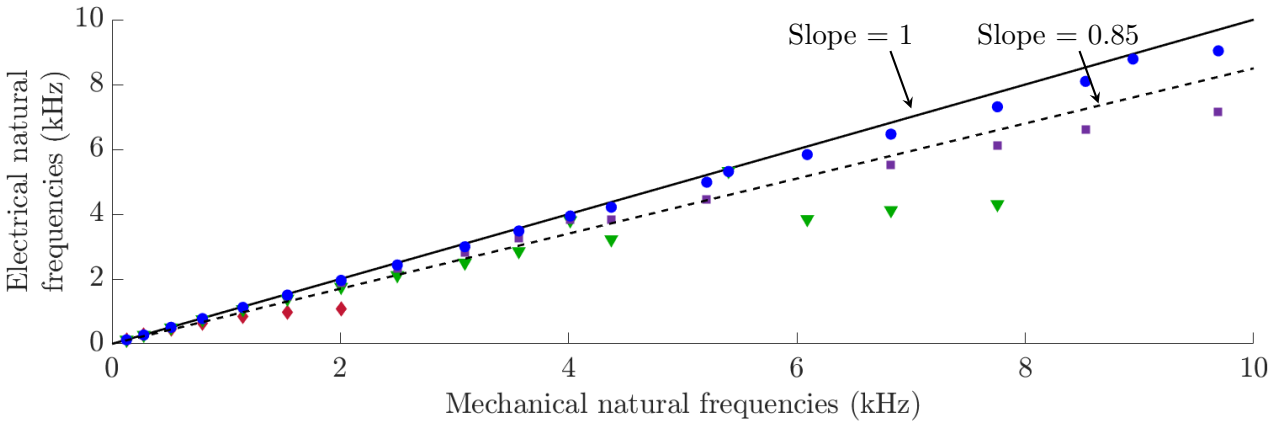

Figure 2.34: Comparison of mechanical natural frequencies of the arch and electrical natural frequencies of the network A for (♦) $n_{elm} = 10$, (▼) $n_{elm} = 20$, (■) $n_{elm} = 30$ and (●) $n_{elm} = 60$.

2.8.3.3 Frequency coherence condition validation

The natural frequencies of the electrical networks A and B are then compared to the arch natural frequencies estimated by a finite element model. We use the mesh presented in figure 2.30c to ensure computing converged mechanical natural frequencies. The comparison is made in figure 2.34 for several numbers of elements n_{elm}. However, only the natural frequencies of the network A are plotted. Indeed, the networks A and B exhibit close natural frequencies: all the natural frequencies of the network B are nearly 3.5 % superior to the ones of the network A for $n_{elm} = 10$ elements, but this gap decreases to less than 1 % for $n_{elm} \geq 20$ elements. Hence, the figure 2.34 shows three things. Firstly, the two developed networks are interchangeable in terms of modal properties. It is a promising result, since the objective for complex structures is to assemble previously developed electrical unit cells rather than creating new ones. Secondly, the two developed networks converge towards the arch dynamics when the number of elements increases. This can be regarded as the convergence of finite difference models towards a finite element model. Finally, we can say that the frequency range upon which the frequency coherence condition is met depends on the structure discretization. For $n_{elm} = 10$ elements, we can consider that the frequency coherence condition is verified for the first six modes.

As a conclusion, we have illustrated by a numerical example that the spatial and frequency coherence conditions are validated upon a given frequency range. As expected, increasing the number of elements in the network makes it tend towards a continuous structure, and therefore extends the frequency range over which the analogy is validated.

2.9 Tube electrical analogue

In the present section, we study the case of the tube electrical analogue. One possibility to derive it is to follow the method that is detailed in section 2.3. It involves applying the direct electromechanical analogy to a finite difference mechanical model stemming from the constitutive equations of shells in harmonic motion. We choose to avoid this because of the potential complexity of the resulting finite difference mechanical model. Besides, the previous section hinted at the possibility to use a different method to derive an electrical analogue. By adequately assembling known unit cells, one can produce an electrical analogue that replicates the physical properties of the structure.

One way to do so is to describe the in-plane bending wave propagation with the curved beam electrical analogue that we have defined in section 2.8. Meanwhile, the bending wave propagation along the longitudinal direction can be modeled using the straight beam electrical analogue of section 2.6. Connecting these circuits together leads to a unit cell whose topology is sketched in figure 2.35a.

Another way to model the 2D bending wave propagation in the tube is to use the plate electrical analogue of section 2.7. The effect of curvature should then be taken into account. We can connect the coupling between bending and traction as represented in figure 2.22 to each plate element. This latest proposal is sketched in figure 2.35b.

Both cases lead to the tube electrical analogue that is represented in figure 2.36, whose notations are the same as for the previously studied analogues. By connecting electrical unit cells according to the dynamics to be represented, we jumped straight to the Step 4 of the capsulized method of subsection 2.3.8.

Another aside on the number of components and integration

As highlighted in the aside of subsection 2.8.2, the tube analogue of figure 2.36 might not be optimized in terms of number of components. Moreover, a tube electrical analogue could be assembled from interconnecting square plate unit cells represented in figure 2.14 with rotation elements as sketched in figure 2.28b. This network would include even more transformers, which probably makes its fully passive integration very complicated in practice. Therefore, deriving another analogue starting from the constitutive equations of shells might lead to a more compact network, that would thus be easier to integrate.

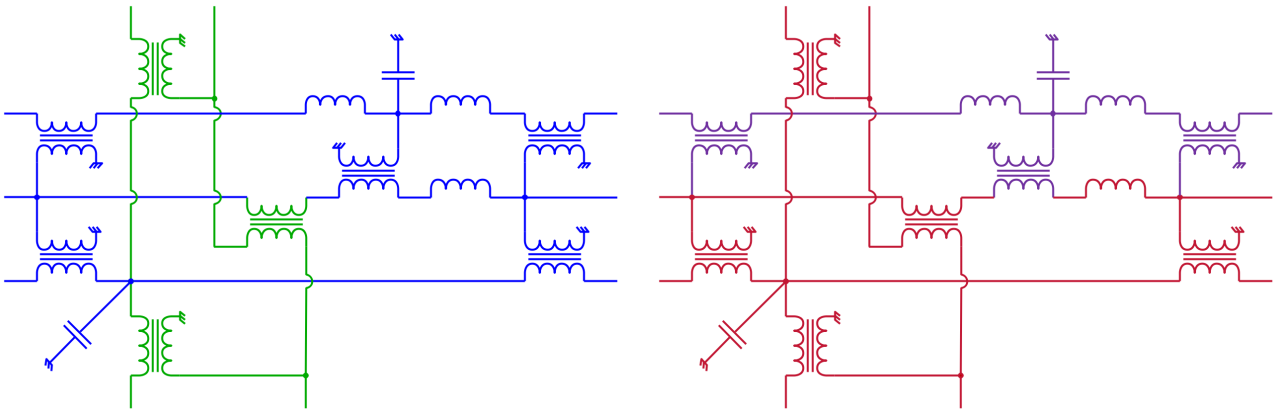

(a) (b)

Figure 2.35: Unit cell of the tube electrical analogue represented as (a) the curved beam analogue of figure 2.22 in blue, extended along the second axis by the beam analogue of figure 2.11b in green, or as (b) an interconnection of the plate analogue of figure 2.14 in red and the traction wave propagation line of figure 2.22 in purple.

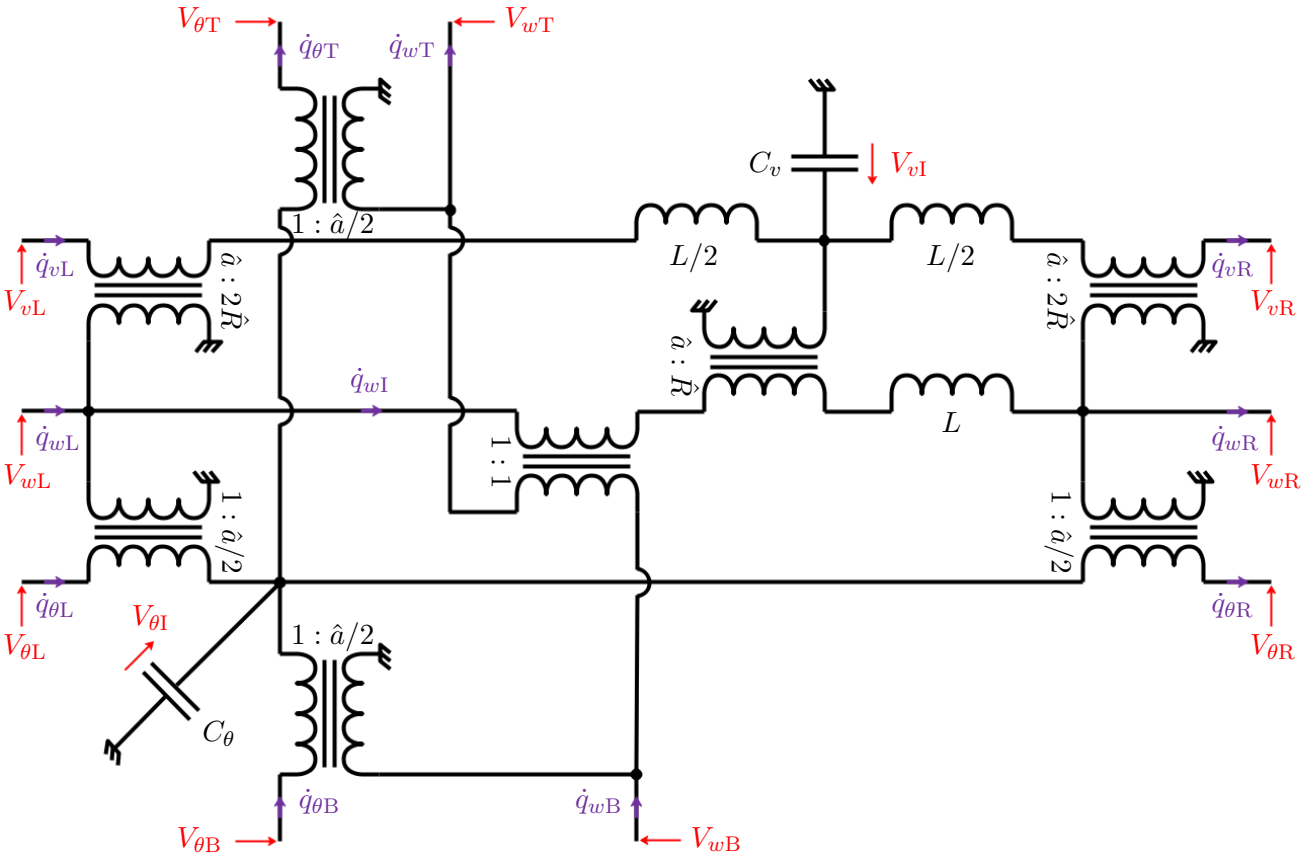

Figure 2.36: Unit cell of the tube electrical analogue. The required added capacitors on the sides are not sketched.

Analogous boundary conditions: The tube analogue is an extension of previously derived unit cells. Therefore, the boundary conditions are deduced from the case of the curved beam or the case of the square plate, depending on the side of the unit cell in figure 2.36 which is the boundary. If the boundary is directly connected to the traction wave propagation line, such as the left and right boundaries of the unit cell in figure 2.36, then the boundary conditions of table 2.6 apply. However, if the boundary is only connected to the bending wave propagation lines, such as the bottom and top boundaries of the unit cell in figure 2.36, then the boundary conditions of table 2.4 apply.

Frequency coherence conditions: The tube electrical analogue is an extension of the plate analogue developed in section 2.7 and of the curved beam analogue developed in subsection 2.8.1. Thus, the frequency coherence conditions of the tube are similar to those of equations (2.56) and (2.69):

$$\frac{a}{R} = \frac{\hat{a}}{\hat{R}}, \qquad \frac{K_v}{m} = \frac{1}{LC_v}, \qquad \frac{1}{a^2}\,\frac{K_\theta}{m} = \frac{1}{\hat{a}^2}\,\frac{1}{LC_\theta}. \tag{2.84}$$

Unit cells assembly: The system of equations corresponding to the electrical unit cell in figure 2.36 is ill-defined. The suggested solution to avoid singularity problems is to add side capacitors of capacitance C_0 in this case as well. They are not represented in figure 2.36 for the sake of readability.

Using the notations in figure 2.36, the values of the electrical charges and the voltages in one unit cell of the network are denoted $\boldsymbol{q_N}$ and $\boldsymbol{v_N}$:

$$\begin{aligned}
\boldsymbol{q_N} &= \begin{pmatrix} q_{w\mathrm{B}} & q_{\theta\mathrm{B}} & q_{v\mathrm{L}} & q_{w\mathrm{L}} & q_{\theta\mathrm{L}} & q_{v\mathrm{R}} & q_{w\mathrm{R}} & q_{\theta\mathrm{R}} & q_{w\mathrm{T}} & q_{\theta\mathrm{T}} \end{pmatrix}^{\mathrm{T}}, \\
\boldsymbol{v_N} &= \begin{pmatrix} V_{w\mathrm{B}} & V_{\theta\mathrm{B}} & V_{v\mathrm{L}} & V_{w\mathrm{L}} & V_{\theta\mathrm{L}} & -V_{v\mathrm{R}} & -V_{w\mathrm{R}} & -V_{\theta\mathrm{R}} & -V_{w\mathrm{T}} & -V_{\theta\mathrm{T}} \end{pmatrix}^{\mathrm{T}}.
\end{aligned} \tag{2.85}$$

Following the derivation of the dynamic matrix $\boldsymbol{D_e}$, we apply equations (2.13). Because of their lengths, the resulting electrical elementary matrices are recorded in appendix B. The elementary "mass" matrix $\boldsymbol{M_{elm}}$ is a function of the inductance value L, which is the electrical analogous quantity of the mass. The elementary "stiffness" matrix $\boldsymbol{K_{elm}}$ is a function of the capacitances C_v and C_θ, which are the respective analogous quantities of the longitudinal and bending compliances, as well as the numerical parameter C_0.

2.10 Conclusions

Library of unit cells of electrical analogues of mechanical structures

Rod	1D Traction	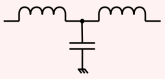
Bar	1D Torsion	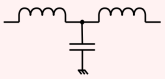
Beam	1D Bending	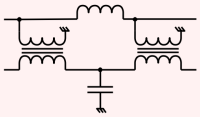
Square plate	2D Bending	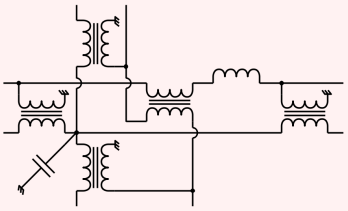
Curved beam	Coupled in-plane bending and traction	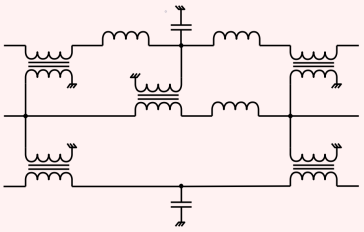
Tube	Longitudinal bending and coupled in-plane bending and traction	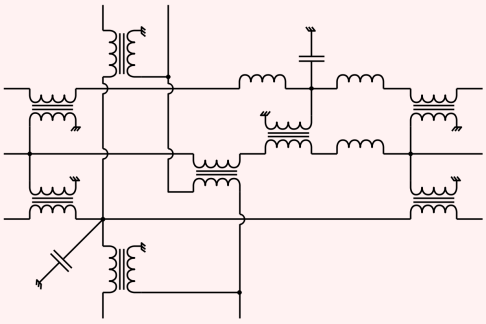

In this chapter, we have detailed a method to derive electrical analogues of mechanical structures. The main principle is to apply the direct electromechanical analogy to a discrete mechanical model of the considered structure. The developed electrical network is the analogue of a mechanical structure if it meets two conditions. The first one is the spatial coherence condition, which states that the network should represent the structure physical behavior. The network should thus be composed of enough unit cells so that the smaller wavelength of the frequency range of interest is sufficiently discretized. This condition is numerically verified by comparing the velocity mode shapes of the structure to the electrical current mode shapes of the network. The second condition is the frequency coherence condition, which states that the network should exhibit the same wave propagation properties as the structure. Once analogous boundary conditions are obtained in the electrical system, it is verified if the structure and the network have equal natural frequencies. All developed unit cells are composed of ideal components such as capacitors, inductors and transformers.

The analogues which have been derived are gathered in the aside above. Though not sketched, the electrical analogue of a rotation matrix has been detailed as well. The most common mechanical structures that are rods, bars, beams and plates are studied. Furthermore, the classical loads, which are traction, torsion and bending, are considered at least once. The library of electrical analogues can therefore be used to quite a wide variety of cases. Finally, some of the most complex derived electrical analogues have been validated on numerical examples.

Several other unit cells could be derived to expand the library of electrical analogues. Examples of potential future electrical analogues include a 2D membrane element or a rectangular plate element. However, we suggest not to derive the analogues of the most complex structures, as the number of electrical components might significantly increase. Future works might consider assembling different elements of the developed library in order to approximate the dynamic behavior of complex structures.

Chapter 3

Finite element model of a structure coupled to an electrical network

This chapter is about the development of a finite element model of a structure coupled via thin piezoelectric transducers to a lumped electrical network. A finite element formulation of a structure covered by piezoelectric patches is first derived. A setup of a simply-supported rectangular plate covered with piezoelectric material is then used to validate the model by comparison with experiments. Finally, the connection to an electrical network is accounted for.

Content

3.1 Introduction

The main objective of this thesis is to investigate the broadband vibration mitigation of complex structures by coupling them to electrical networks. The literature is abundant on finite element modeling of piezoelectric coupling [90, 91]. Our bibliography on the subject is not exhaustive, as it is not the aim of this manuscript. The work of Thomas et al. [92] concerning a structure covered by thin piezoelectric patches is taken as the starting point. The main originality of their work is to consider only one electrical degree of freedom by piezoelectric patch, as they impose the equipotentiality over the electrodes. Therefore, the voltage on the upper electrode of each piezoelectric patch is a global variable appearing in the formulation. Implementing the connection of the structure to lumped-element models of electronic circuits is then convenient.

The development of a modeling tool for structures whose vibrations are mitigated by piezoelectric coupling to an electrical network presents several interests:

- **To avoid conducting experimental validation for all examples we want to treat.**

  Since experimental setups will not be developed for all future numerical examples, having a predictive model of the behavior of a structure being coupled to an electrical network becomes necessary. It will be especially useful for the numerical examples of chapter 5.

- **To optimize electrical components to improve the vibration mitigation performance.**

  Indeed, numerically optimizing the electrical damping provided by resistances in the network is possible once a simulating tool is available. Several damping strategies could thus be explored.

- **To compute the dynamic piezoelectric capacitance.**

  In most solutions of vibration damping by piezoelectric coupling, an estimation of the piezoelectric capacitance is required to tune the electrical components. However, the piezoelectric capacitance depends on the frequency and on the structure modal properties [33, 84, 34]. Hence we suggest it is a more accurate approach to use a 3D finite element model for the estimation, rather than only referring to the manufacturer's data.

In section 3.2, the main steps to obtain a finite element model of a structure covered by piezoelectric patches are detailed. This model is validated by comparison with experiments conducted on a setup of a simply-supported plate in section 3.3. The coupling of the vibrating structure to an electrical circuit which is described by discrete equations is then considered in section 3.4. This process results in a finite element model of a structure being coupled to an electrical network, which will be validated in the chapter 4.

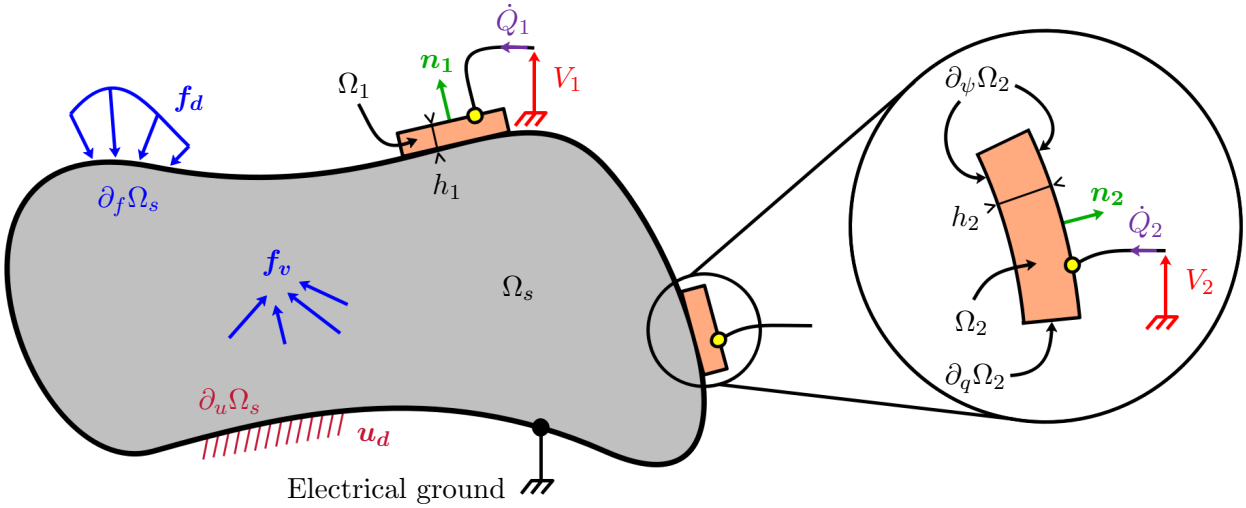

Figure 3.1: Mechanical structure covered by piezoelectric transducers, whose electrodes are not represented. The adhesive layer is not sketched either.

Medium	**Subscript**
Generic	$(\cdot)_0$
Structure	$(\cdot)_s$
j-th piezoelectric transducer	$(\cdot)_j\,,\ \ j=1,\ldots,p$
Structure $\oplus$ Piezoelectric transducers	None

Boundary surface	**Prescribed quantity**	**Value notation**
$\partial_f\Omega_0$	Surface force density	$\boldsymbol{f_d}$
$\partial_u\Omega_0$	Displacement	$\boldsymbol{u_d}$
$\partial_\psi\Omega_0$	Electrostatic potential	ψ_d
$\partial_q\Omega_0$	Electric charges surface density	q_d

Table 3.1: Medium subscript notations and boundary conditions applied to the surface $\partial\Omega_0$ of the generic medium Ω_0.

3.2 Structure covered by thin piezoelectric transducers

3.2.1 Notations

The mechanical medium is sketched in figure 3.1. Ω_0 denotes the volume of a generic medium, either piezoelectric or not, while $\partial\Omega_0$ denotes its boundary surface. Eventually, the subscript 0 denoting a generic structure will be replaced either to designate the host structure, which exhibits no piezoelectric properties, or to designate a piezoelectric transducer that is bonded to it. The corresponding notations are summed up in table 3.1. Besides, the boundary partitions verify that

$$\begin{aligned} \partial\Omega_0 &= (\partial_f\Omega_0) \cup (\partial_u\Omega_0) = (\partial_\psi\Omega_0) \cup (\partial_q\Omega_0)\,, \\ \varnothing &= (\partial_f\Omega_0) \cap (\partial_u\Omega_0) = (\partial_\psi\Omega_0) \cap (\partial_q\Omega_0)\,. \end{aligned} \tag{3.1}$$

3.2.2 Local equations

To model the mechanical behavior of the system, the elastodynamic equation is considered. Then, Gauss's law involving no free charges is considered to model its electrical behavior. The two equations describing in Ω_0 the mechanical and the electrical dynamics behaviors of the system are then

$$\mathbf{div}\,\overline{\overline{\boldsymbol{\sigma}}} + \boldsymbol{b} = \rho\,\frac{\partial^2 \boldsymbol{u}}{\partial t^2}, \tag{3.2}$$

$$\operatorname{div}\boldsymbol{D} = 0, \tag{3.3}$$

where $\overline{\overline{\boldsymbol{\sigma}}}$ is the linearized stress tensor, $\boldsymbol{b}$ are the prescribed body forces, ρ is the mass density, $\boldsymbol{u}$ is the displacement field and $\boldsymbol{D}$ is the electric displacement. Furthermore, the boundary conditions of the problem are

$$\overline{\overline{\boldsymbol{\sigma}}} \cdot \boldsymbol{n} = \boldsymbol{f_d} \quad \text{on } \partial_f\Omega_0, \tag{3.4}$$

$$\boldsymbol{u} = \boldsymbol{u_d} \quad \text{on } \partial_u\Omega_0, \tag{3.5}$$

$$\psi = \psi_d \quad \text{on } \partial_\psi\Omega_0, \tag{3.6}$$

$$\boldsymbol{D} \cdot \boldsymbol{n} = -q_d \quad \text{on } \partial_q\Omega_0. \tag{3.7}$$

Meanwhile, the strain tensor is related to the displacement field in the infinitesimal strain theory by

$$\overline{\overline{\boldsymbol{\varepsilon}}} = \frac{1}{2}\left(\overline{\overline{\mathbf{grad}}}\,(\boldsymbol{u}) + \overline{\overline{\mathbf{grad}}}\,(\boldsymbol{u})^{\mathrm{T}}\right). \tag{3.8}$$

	Stresses						**Strains**					
Tensor	σ_{xx}	σ_{yy}	σ_{zz}	σ_{yz}	σ_{xz}	σ_{xy}	ε_{xx}	ε_{yy}	ε_{zz}	$2\varepsilon_{yz}$	$2\varepsilon_{xz}$	$2\varepsilon_{xy}$
Voigt	σ_1	σ_2	σ_3	σ_4	σ_5	σ_6	ε_1	ε_2	ε_3	ε_4	ε_5	ε_6

Table 3.2: Equivalence between the tensor notation and the Voigt notation.

Besides, the electrical phenomena are assumed to happen much faster than the mechanical ones in the piezoelectric medium, which means that an electrostatic potential ψ can be related to the electric field $\boldsymbol{E}$ by

$$\boldsymbol{E} = -\mathbf{grad}\,\psi. \tag{3.9}$$

Finally, we suppose that each piezoelectric transducer is polarized in its transverse direction $\boldsymbol{n}^{(j)}$, where the index j is associated to the j-th piezoelectric patch. The patches thicknesses, denoted $h^{(j)}$, are considered small when compared to their longitudinal dimensions. For this reason, the electrical field $\boldsymbol{E}^{(j)}$ is supposed uniform and orthogonal to the electrodes, and can be expressed as a function of the potential difference $V^{(j)}$ between electrodes of each patch:

$$\boldsymbol{E}^{(j)} = -\frac{V^{(j)}}{h^{(j)}}\,\boldsymbol{n}^{(j)}. \tag{3.10}$$

3.2.3 Constitutive equations

The stresses and strains in a mechanical medium are represented by the stress tensor $\overline{\overline{\boldsymbol{\sigma}}}$ and by the strain tensor $\overline{\overline{\boldsymbol{\varepsilon}}}$. Their expressions in the $(\vec{x},\vec{y},\vec{z})$ basis are

$$\overline{\overline{\boldsymbol{\sigma}}} = \begin{pmatrix} \sigma_{xx} & \sigma_{xy} & \sigma_{xz} \\ \sigma_{yx} & \sigma_{yy} & \sigma_{yz} \\ \sigma_{zx} & \sigma_{zy} & \sigma_{zz} \end{pmatrix}_{(\vec{x},\vec{y},\vec{z})} \quad \text{and} \quad \overline{\overline{\boldsymbol{\varepsilon}}} = \begin{pmatrix} \varepsilon_{xx} & \varepsilon_{xy} & \varepsilon_{xz} \\ \varepsilon_{yx} & \varepsilon_{yy} & \varepsilon_{yz} \\ \varepsilon_{zx} & \varepsilon_{zy} & \varepsilon_{zz} \end{pmatrix}_{(\vec{x},\vec{y},\vec{z})} \qquad \begin{matrix} \text{with } \overline{\overline{\boldsymbol{\sigma}}} = \overline{\overline{\boldsymbol{\sigma}}}^{\mathrm{T}} \\ \text{and } \overline{\overline{\boldsymbol{\varepsilon}}} = \overline{\overline{\boldsymbol{\varepsilon}}}^{\mathrm{T}}. \end{matrix} \tag{3.11}$$

However, the Voigt notation is used going forward. Indeed, the stress and strain tensors being symmetric, $\overline{\overline{\boldsymbol{\sigma}}}$ and $\overline{\overline{\boldsymbol{\varepsilon}}}$ both include only six independent terms. This means that the same information can be stored in a six-element vector. The equivalence between the tensor notation and the Voigt notation is detailed in table 3.2. The linearized stress $\boldsymbol{\sigma}$ and strain $\boldsymbol{\varepsilon}$ vectors are then

$$\boldsymbol{\sigma} = \begin{pmatrix} \sigma_1 & \sigma_2 & \sigma_3 & \sigma_4 & \sigma_5 & \sigma_6 \end{pmatrix}^{\mathrm{T}}, \qquad \boldsymbol{\varepsilon} = \begin{pmatrix} \varepsilon_1 & \varepsilon_2 & \varepsilon_3 & \varepsilon_4 & \varepsilon_5 & \varepsilon_6 \end{pmatrix}^{\mathrm{T}}. \tag{3.12}$$

On one hand, there are several forms of the electromechanical constitutive equations linking the mechanical quantities $\boldsymbol{\sigma}$ and $\boldsymbol{\varepsilon}$ to the electrical ones $\boldsymbol{E}$ and $\boldsymbol{D}$ [93]. Choosing to use one constitutive equation form rather than the others stems from the electrical, mechanical and geometrical specificities of the study. The most widespread constitutive equations are suitable to the present work:

$$\boldsymbol{\sigma} = \boldsymbol{C}^{\boldsymbol{E}}\boldsymbol{\varepsilon} - \boldsymbol{e}^{\mathrm{T}}\boldsymbol{E}, \tag{3.13}$$

$$\boldsymbol{D} = \boldsymbol{e}\boldsymbol{\varepsilon} + \boldsymbol{\epsilon}^{\boldsymbol{\varepsilon}}\boldsymbol{E}. \tag{3.14}$$

With these notations, $\boldsymbol{C}^{\boldsymbol{E}}$ is the matrix of elastic coefficients at constant electric field, $\boldsymbol{e}$ is the matrix of piezoelectric coefficients, and $\boldsymbol{\epsilon}^{\boldsymbol{\varepsilon}}$ is the matrix of dielectric permittivities at constant strain. We assume that the piezoelectric transducers exhibit transverse isotropic properties and are polarized in their transverse directions, which is labeled as direction "3". Under these assumptions, the constitutive equations (3.13) and (3.14) are simplified and can be written in matrix form:

$$\left(\begin{array}{c} \sigma_1 \\ \sigma_2 \\ \sigma_3 \\ \sigma_4 \\ \sigma_5 \\ \sigma_6 \\ \hline D_1 \\ D_2 \\ D_3 \end{array}\right) = \left(\begin{array}{cccccc|ccc} c_{11}^E & c_{12}^E & c_{13}^E & 0 & 0 & 0 & 0 & 0 & -e_{31} \\ c_{12}^E & c_{11}^E & c_{13}^E & 0 & 0 & 0 & 0 & 0 & -e_{31} \\ c_{13}^E & c_{13}^E & c_{33}^E & 0 & 0 & 0 & 0 & 0 & -e_{33} \\ 0 & 0 & 0 & c_{44}^E & 0 & 0 & 0 & -e_{15} & 0 \\ 0 & 0 & 0 & 0 & c_{44}^E & 0 & -e_{15} & 0 & 0 \\ 0 & 0 & 0 & 0 & 0 & c_{66}^E & 0 & 0 & 0 \\ \hline 0 & 0 & 0 & 0 & e_{15} & 0 & \epsilon_{11}^{\varepsilon} & 0 & 0 \\ 0 & 0 & 0 & e_{15} & 0 & 0 & 0 & \epsilon_{11}^{\varepsilon} & 0 \\ e_{31} & e_{31} & e_{33} & 0 & 0 & 0 & 0 & 0 & \epsilon_{33}^{\varepsilon} \end{array}\right) \left(\begin{array}{c} \varepsilon_1 \\ \varepsilon_2 \\ \varepsilon_3 \\ \varepsilon_4 \\ \varepsilon_5 \\ \varepsilon_6 \\ \hline E_1 \\ E_2 \\ E_3 \end{array}\right). \tag{3.15}$$

Note that eleven materials constants are required to model the piezoelectric transducer behavior. Six of them are elastic coefficients, three of them are piezoelectric coefficients, and the remaining two are dielectric coefficients.

Moreover, another classical formulation for the constitutive equations of linear piezoelectricity [93] involves the matrices of compliance coefficients $\boldsymbol{S}^{\boldsymbol{E}}$, of piezoelectric strain constants $\boldsymbol{d}$ and of dielectric permittivities at constant stress $\boldsymbol{\epsilon}^{\boldsymbol{\sigma}}$. We recall their expressions, as they will be used in section 3.3:

$$\boldsymbol{S}^{\boldsymbol{E}} = \boldsymbol{C}^{\boldsymbol{E}^{-1}}, \qquad \boldsymbol{d} = \boldsymbol{e}\boldsymbol{S}^{\boldsymbol{E}}, \qquad \boldsymbol{\epsilon}^{\boldsymbol{\sigma}} = \boldsymbol{\epsilon}^{\boldsymbol{\varepsilon}} - \boldsymbol{d}\boldsymbol{e}^{\mathrm{T}}. \tag{3.16}$$

On the other hand, the host structure is a medium which exhibits no piezoelectric properties. Therefore its constitutive equations are similar to equations (3.13) and (3.14) with $\boldsymbol{e} = \boldsymbol{0}$. We choose

to model the structure as an isotropic homogeneous linear elastic medium. Applying these assumptions leads to classical constitutive equations in which only the two independent Lamé parameters remain:

$$\overline{\overline{\boldsymbol{\sigma}}} = 2\mu\overline{\overline{\boldsymbol{\varepsilon}}} + \lambda \mathrm{Tr}\left(\overline{\overline{\boldsymbol{\varepsilon}}}\right) \boldsymbol{I_d}, \tag{3.17}$$

where $\mathrm{Tr}\left(\overline{\overline{\boldsymbol{\varepsilon}}}\right)$ is the trace of the strain tensor, $\boldsymbol{I_d}$ is the identity matrix, and λ and μ are the Lamé parameters, which are related to Young's modulus E and Poisson's ratio ν by

$$\lambda = \frac{\nu E}{(1+\nu)(1-2\nu)}, \qquad \mu = \frac{E}{2(1+\nu)}. \tag{3.18}$$

3.2.4 Variational formulation in terms of displacement and electrostatic potential

Going towards the finite element formulation of the problem, one must derive the variational formulation. It is first developed with the displacement field $\boldsymbol{u}$ and the electrostatic potential ψ as variables. Applying the test-function method, we multiply the equations (3.2) and (3.3) by kinematic admissible test functions $\delta\boldsymbol{u}$ and $\delta\psi$, respectively. The resulting mechanical equation is

$$\begin{aligned}\int_{\Omega_0} \boldsymbol{\delta u} \cdot \rho \frac{\partial^2 \boldsymbol{u}}{\partial t^2}\, d\Omega + \int_{\Omega_0} \boldsymbol{\varepsilon}\left(\boldsymbol{\delta u}\right) \cdot \boldsymbol{C^E} \boldsymbol{\varepsilon}\left(\boldsymbol{u}\right)\, d\Omega \\ - \int_{\Omega_0} \boldsymbol{\varepsilon}\left(\boldsymbol{\delta u}\right) \cdot \boldsymbol{e}^{\mathrm{T}} \boldsymbol{E}\left(\psi\right)\, d\Omega = \int_{\partial_f \Omega_0} \boldsymbol{\delta u} \cdot \boldsymbol{f_d}\, dS + \int_{\Omega_0} \boldsymbol{\delta u} \cdot \boldsymbol{b}\, d\Omega,\end{aligned} \tag{3.19}$$

while the resulting electrical equation is

$$\int_{\Omega_0} \boldsymbol{E}\left(\delta\psi\right) \cdot \boldsymbol{e}\, \boldsymbol{\varepsilon}\left(\boldsymbol{u}\right)\, d\Omega + \int_{\Omega_0} \boldsymbol{E}\left(\delta\psi\right) \cdot \boldsymbol{\epsilon^\varepsilon} \boldsymbol{E}\left(\psi\right)\, d\Omega = \int_{\partial_q \Omega_0} \delta\psi q_d\, dS + \int_{\partial_\psi \Omega_0} \delta\psi q_r\, dS. \tag{3.20}$$

In this last equation, q_r stands for the free electric charge density appearing on $\partial_\psi \Omega_0$.

3.2.5 Variational formulation in terms of displacement and potential difference

The objective is to incorporate global variables in the variational formulation, as it is convenient to then simulate the structure connection to a lumped-element electrical circuit. Among these global variables are the voltage drops $V^{(j)}$ across the electrodes of each patch. Assuming all lower electrodes are connected to the electric ground, such as drawn in figure 3.1, the voltage drops $V^{(j)}$ are equal to the potentials on the upper electrodes. The electric charges $Q^{(j)}$ on the upper electrodes of the piezoelectric patches should be implemented in the model as well. Besides, we make the hypothesis that there are no electric charges on the piezoelectric lateral surfaces, thus $q_d = 0$.

The whole system denoted Ω includes the structure, as well as the p piezoelectric transducers covering it. Therefore, the integral of any function g over Ω is obtained from the sum of its integrals over the subdomains of Ω:

$$\int_{\Omega} g \, d\Omega = \int_{\Omega_s} g \, d\Omega + \sum_{j=1}^{p} \int_{\Omega_j} g \, d\Omega. \tag{3.21}$$

Applying the mechanical equation (3.19) of the variational formulation to all subdomains of Ω, and then adding the $p+1$ derived equations term by term considering the equation (3.21) leads to

$$\begin{aligned} \int_{\Omega} \boldsymbol{\delta u} \cdot \rho \, \frac{\partial^2 \boldsymbol{u}}{\partial t^2} \, d\Omega + \int_{\Omega} \boldsymbol{\varepsilon}\left(\boldsymbol{\delta u}\right) \cdot \boldsymbol{C^E} \boldsymbol{\varepsilon}\left(\boldsymbol{u}\right) \, d\Omega \\ + \sum_{j=1}^{p} \int_{\Omega_j} \frac{V^{(j)}}{h^{(j)}} \, \boldsymbol{\varepsilon}\left(\boldsymbol{\delta u}\right) \boldsymbol{e}^{\mathrm{T}} \boldsymbol{n}^{(j)} \, d\Omega = \int_{\partial_f \Omega} \boldsymbol{\delta u} \cdot \boldsymbol{f_d} \, dS + \int_{\Omega} \boldsymbol{\delta u} \cdot \boldsymbol{b} \, d\Omega. \end{aligned} \tag{3.22}$$

Meanwhile, applying the electrical equation (3.20) of the variational formulation to all subdomains of Ω, and then adding the p derived equations term by term considering the equation (3.21) leads to

$$\sum_{j=1}^{p} \delta V^{(j)} C^{\varepsilon(j)} V^{(j)} - \sum_{j=1}^{p} \int_{\Omega_j} \frac{\delta V^{(j)}}{h^{(j)}} \, \boldsymbol{\delta n} \cdot \boldsymbol{e} \, \boldsymbol{\varepsilon}\left(\boldsymbol{u}\right) \, d\Omega = \sum_{j=1}^{p} \delta V^{(j)} Q^{(j)}. \tag{3.23}$$

With these notations, $C^{\varepsilon(j)}$ and $Q^{(j)}$ represent for the j-th piezoelectric patch its blocked piezoelectric capacitance and the electric charges on its upper electrode, respectively. Denoting $S^{(j)}$ the mean surface of the j-th piezoelectric patch, and $\epsilon_{33}^{\varepsilon}$ the transverse permittivity of the piezoelectric medium with no strain, their expressions are

$$C^{\varepsilon(j)} = \frac{\epsilon_{33}^{\varepsilon} S^{(j)}}{h^{(j)}}, \tag{3.24}$$

$$Q^{(j)} = \int_{\partial_\psi \Omega_j} q_r \, dS. \tag{3.25}$$

3.2.6 Finite element formulation

We note $\boldsymbol{U}$ the vector containing the nodal values of the displacement field and $\boldsymbol{V} = \left(V^{(1)}, \ldots, V^{(p)}\right)$ the vector containing the electric potential values on the upper electrodes of the piezoelectric patches. Their test functions counterparts are respectively denoted $\delta\boldsymbol{U}$ and $\delta\boldsymbol{V}$. The next step is to discretize each term of equations (3.22) and (3.23). Following a geometric assembly that is classical in the finite element theory, the resulting terms are as follows:

$$\int_\Omega \boldsymbol{\delta u} \cdot \rho \, \frac{\partial^2 \boldsymbol{u}}{\partial t^2} \, d\Omega \qquad \Longrightarrow \qquad \delta \boldsymbol{U}^{\mathrm{T}} \boldsymbol{M_m} \ddot{\boldsymbol{U}}, \tag{3.26a}$$

$$\int_\Omega \boldsymbol{\varepsilon}\left(\boldsymbol{\delta u}\right) \cdot \boldsymbol{C^E} \boldsymbol{\varepsilon}\left(\boldsymbol{u}\right) \, d\Omega \qquad \Longrightarrow \qquad \delta \boldsymbol{U}^{\mathrm{T}} \boldsymbol{K_m} \boldsymbol{U}, \tag{3.26b}$$

$$\sum_{j=1}^{p} \int_{\Omega_j} \frac{V^{(j)}}{h^{(j)}} \, \boldsymbol{\varepsilon}\left(\boldsymbol{\delta u}\right) \boldsymbol{e}^{\mathrm{T}} \boldsymbol{n}^{(j)} \, d\Omega \qquad \Longrightarrow \qquad \delta \boldsymbol{U}^{\mathrm{T}} \boldsymbol{K_c} \boldsymbol{V}, \tag{3.26c}$$

$$\int_{\partial_f \Omega} \boldsymbol{\delta u} \cdot \boldsymbol{f_d} \, dS + \int_\Omega \boldsymbol{\delta u} \cdot \boldsymbol{b} \, d\Omega \qquad \Longrightarrow \qquad \delta \boldsymbol{U}^{\mathrm{T}} \boldsymbol{F}, \tag{3.26d}$$

$$\sum_{j=1}^{p} \delta V^{(j)} C^{(j)} V^{(j)} \qquad \Longrightarrow \qquad \delta \boldsymbol{V}^{\mathrm{T}} \boldsymbol{K_e}^{-1} \boldsymbol{V}, \tag{3.26e}$$

$$\sum_{j=1}^{p} \int_{\Omega_j} \frac{\delta V^{(j)}}{h^{(j)}} \, \boldsymbol{\delta n} \cdot \boldsymbol{e} \, \boldsymbol{\varepsilon}\left(\boldsymbol{u}\right) \, d\Omega \qquad \Longrightarrow \qquad \delta \boldsymbol{V}^{\mathrm{T}} \boldsymbol{K_c} \boldsymbol{U}, \tag{3.26f}$$

$$\sum_{j=1}^{p} \delta V^{(j)} Q^{(j)} \qquad \Longrightarrow \qquad \delta \boldsymbol{V}^{\mathrm{T}} \boldsymbol{Q}. \tag{3.26g}$$

These terms lead to the finite element model of a mechanical structure being covered by thin piezoelectric transducers:

$$\begin{pmatrix} \boldsymbol{M_m} & \boldsymbol{0} \\ \boldsymbol{0} & \boldsymbol{0} \end{pmatrix} \begin{pmatrix} \ddot{\boldsymbol{U}} \\ \ddot{\boldsymbol{V}} \end{pmatrix} + \begin{pmatrix} \boldsymbol{K_m} & \boldsymbol{K_c} \\ -\boldsymbol{K_c}^{\mathrm{T}} & \boldsymbol{K_e}^{-1} \end{pmatrix} \begin{pmatrix} \boldsymbol{U} \\ \boldsymbol{V} \end{pmatrix} = \begin{pmatrix} \boldsymbol{F} \\ \boldsymbol{Q} \end{pmatrix}. \tag{3.27}$$

Another equivalent formulation is to write the electrical equation with the electrical charges as state variables. Hence the equation (3.27) becomes

$$\begin{pmatrix} \boldsymbol{M_m} & \boldsymbol{0} \\ \boldsymbol{0} & \boldsymbol{0} \end{pmatrix} \begin{pmatrix} \ddot{\boldsymbol{U}} \\ \ddot{\boldsymbol{Q}} \end{pmatrix} + \begin{pmatrix} \boldsymbol{K_m} + \boldsymbol{K_c} \boldsymbol{K_e} \boldsymbol{K_c}^{\mathrm{T}} & \boldsymbol{K_c} \boldsymbol{K_e} \\ \left(\boldsymbol{K_c} \boldsymbol{K_e}\right)^{\mathrm{T}} & \boldsymbol{K_e} \end{pmatrix} \begin{pmatrix} \boldsymbol{U} \\ \boldsymbol{Q} \end{pmatrix} = \begin{pmatrix} \boldsymbol{F} \\ \boldsymbol{V} \end{pmatrix}. \tag{3.28}$$

With these notations, $\boldsymbol{F}$ contains the external mechanical forces applied to the structure, while in $\boldsymbol{Q} = \left(Q^{(1)}, \ldots, Q^{(p)}\right)$ are the electrical charges on the transducers electrodes. $\boldsymbol{K_c}$ is the coupling matrix. $\boldsymbol{M_m}$ and $\boldsymbol{K_m}$ are the mechanical mass and stiffness matrices, respectively. $\boldsymbol{K_e}$ is a diagonal matrix in which the j-th term is the inverse of the blocked piezoelectric capacitance $C^{\varepsilon(j)}$ defined in equation (3.24).

Finite element modeling hypotheses

The main assumptions to derive the finite element formulation of equation (3.28) are:

- The infinitesimal strain theory applies.
- The electric phenomena characteristic time in the piezoelectric domain is much smaller than the one of the mechanical phenomena, hence the electric field $\boldsymbol{E}$ is described in terms of a scalar potential V.
- The thicknesses of the adhesive layers between the structure and the piezoelectric transducers are neglected.
- The electrodes thicknesses are neglected, and the lower ones are connected to the ground.
- There are no free electric charges on the sides of the piezoelectric patches.
- The piezoelectric transducers are thin and polarized in the electrodes orthogonal directions, and they exhibit transverse isotropic properties.
- The host structure is modeled as an isotropic homogeneous linear elastic medium.

3.2.7 Short-circuit and open-circuit formulations

Two particular cases of electrical connections are regularly used as references to describe the dynamics of a structure covered by piezoelectric elements. The first one is the short-circuit connection, when lower and upper electrodes of the piezoelectric transducers are connected to the electrical ground. The second one is the open-circuit connection, when lower electrodes on one hand and upper electrodes on the other hand share common voltages. The finite element formulations of equations (3.27) and (3.28) should be adapted to conveniently describe such connections.

The particular case of all voltages in $\boldsymbol{V}$ being equal to a common voltage V_G is interesting. Indeed, not prescribing any value to V_G is the open-circuit connection while setting $V_G = 0$ afterwards corresponds to the short-circuit connection. We introduce the total electric charge Q_t on the upper electrodes of the piezoelectric transducers, which allows modifying the electrical equation in (3.27):

$$
\begin{aligned}
Q_t &= \sum_{j=1}^{p} Q^{(j)} \\
&= \sum_{j=1}^{p} C^{\varepsilon(j)} V^{(j)} - \left(\sum_{j=1}^{p} \boldsymbol{K_c}^{(j)} \right)^{\mathrm{T}} \boldsymbol{U} \qquad \text{with } \boldsymbol{K_c}^{(j)} \text{ being the } j\text{-th column of } \boldsymbol{K_c} \\
&= V_G \sum_{j=1}^{p} C^{\varepsilon(j)} - \left(\sum_{j=1}^{p} \boldsymbol{K_c}^{(j)} \right)^{\mathrm{T}} \boldsymbol{U} \qquad \text{in case of a common voltage } V_G.
\end{aligned} \tag{3.29}
$$

Therefore, the finite element formulation of a structure being covered by piezoelectric transducers sharing a common voltage difference V_G between their terminals is

$$
\begin{pmatrix} \boldsymbol{M_m} & \boldsymbol{0} \\ \boldsymbol{0} & 0 \end{pmatrix} \begin{pmatrix} \ddot{\boldsymbol{U}} \\ \ddot{V}_G \end{pmatrix} + \begin{pmatrix} \boldsymbol{K_m} & \sum_{j=1}^{p} \boldsymbol{K_c}^{(j)} \\ -\left(\sum_{j=1}^{p} \boldsymbol{K_c}^{(j)} \right)^{\mathrm{T}} & \sum_{j=1}^{p} C^{\varepsilon(j)} \end{pmatrix} \begin{pmatrix} \boldsymbol{U} \\ V_G \end{pmatrix} = \begin{pmatrix} \boldsymbol{F} \\ Q_t \end{pmatrix}. \tag{3.30}
$$

An equivalent finite element formulation using the electrical charge Q_t as a state variable rather than the common voltage V_G is given below:

$$
\begin{pmatrix} \boldsymbol{M_m} & \boldsymbol{0} \\ \boldsymbol{0} & 0 \end{pmatrix} \begin{pmatrix} \ddot{\boldsymbol{U}} \\ \ddot{Q}_t \end{pmatrix} + \begin{pmatrix} \boldsymbol{K_m} + \dfrac{\left(\sum_{j=1}^{p} \boldsymbol{K_c}^{(j)} \right) \left(\sum_{j=1}^{p} \boldsymbol{K_c}^{(j)} \right)^{\mathrm{T}}}{\sum_{j=1}^{p} C^{\varepsilon(j)}} & \dfrac{\sum_{j=1}^{p} \boldsymbol{K_c}^{(j)}}{\sum_{j=1}^{p} C^{\varepsilon(j)}} \\ \dfrac{\left(\sum_{j=1}^{p} \boldsymbol{K_c}^{(j)} \right)^{\mathrm{T}}}{\sum_{j=1}^{p} C^{\varepsilon(j)}} & \dfrac{1}{\sum_{j=1}^{p} C^{\varepsilon(j)}} \end{pmatrix} \begin{pmatrix} \boldsymbol{U} \\ Q_t \end{pmatrix} = \begin{pmatrix} \boldsymbol{F} \\ V_G \end{pmatrix}. \tag{3.31}
$$

At last, commanding $V_G = 0$ is the case of short-circuited piezoelectric transducers, while commanding $Q_t = 0$ is the case of open-circuited piezoelectric transducers. Using the finite element formulations of equations (3.30) and (3.31) allows computing the structure natural frequencies in short-circuit and open-circuit, and then to estimate the modal coupling factors when all the piezoelectric transducers are connected in parallel. Besides, these formulations are convenient to predict the impact of shunting all the piezoelectric transducers with one impedance. This is the topic of the subsection 3.4.1.

A third type of electrical connection that garners interest is the case of independent open-circuited piezoelectric transducers. While all lower electrodes are connected to a common voltage, the upper electrodes are left in open-circuit independently. In other words, the upper electrodes do not share a common voltage. This is specific to a situation with multiple piezoelectric transducers covering a structure. The interest with such a connection stems from the possibility to compute the maximum achievable coupling factors for all modes. Indeed, connecting all upper electrodes together can lead to vanishing coupling factors for several modes. To model the independent open-circuit case, it is sufficient to command that $\boldsymbol{Q} = \boldsymbol{0}$ in the equation (3.28).

3.3 Validation of the finite element model

3.3.1 Structure description

We propose to conduct the validation of the developed finite element model by comparison with experiments on a simply-supported duralumin rectangular plate of lengths $l_x = 420$ mm and $l_y = 360$ mm, and of thickness $h_s = 3$ mm. The simply-supported plate setup has been described by Robin et al. in [94]. Their instructions about the assembly process are detailed enough so that it can be replicated. Besides, they have performed vibration tests of the setup, and have conducted a comparison between experimental and simulated results. They have shown that the plate dynamics can be predicted by a finite element model. The largest difference they have computed between simulated and measured natural frequencies is 4 % on the first value. This stems from the flexibility of the blades linking the plate to the steel frame built around it, which adds some stiffness to the setup. Furthermore, we made several threaded blind holes in the frame to create fixations to suspend the plate.

To create the piezoelectric coupling required to perform vibration mitigation, piezoelectric elements are bonded on one side of the plate. Pictures in figure 3.2 illustrate the bonding process. The principle is to gently fix patches on the plate using tape. A sealed cavity is then created around the structure with a thin layer of plastic material. A vacuum pump is connected to the inside of the cavity, and sucks the air up from it. This way, the layer of plastic material applies a normal load on the upper surfaces of the piezoelectric patches. We let the pump working for several hours, so that the epoxy adhesive, which has been chosen for its mechanical properties [80], dries. To soak up the adhesive leaking from under the patches, an absorbing tissue is placed between the structure and the plastic layer. The resulting layers of epoxy adhesive are very thin, and thus can be neglected during simulations. Their eventual non-uniform distributions under the patches allow for a direct contact between the plate and the lower electrodes of the piezoelectric patches. It is recommended to make a test with only one piezoelectric patch first, before bonding the rest of them.

The resulting structure periodically covered by 42 square piezoelectric patches is pictured in figure 3.3. The sides and thicknesses of the piezoelectric transducers are respectively $l_p = 50$ mm and $h_p = 3$ mm. All measurements are indicated in figure 3.4. Finally, wires have been soldered on the upper electrodes of the piezoelectric patches.

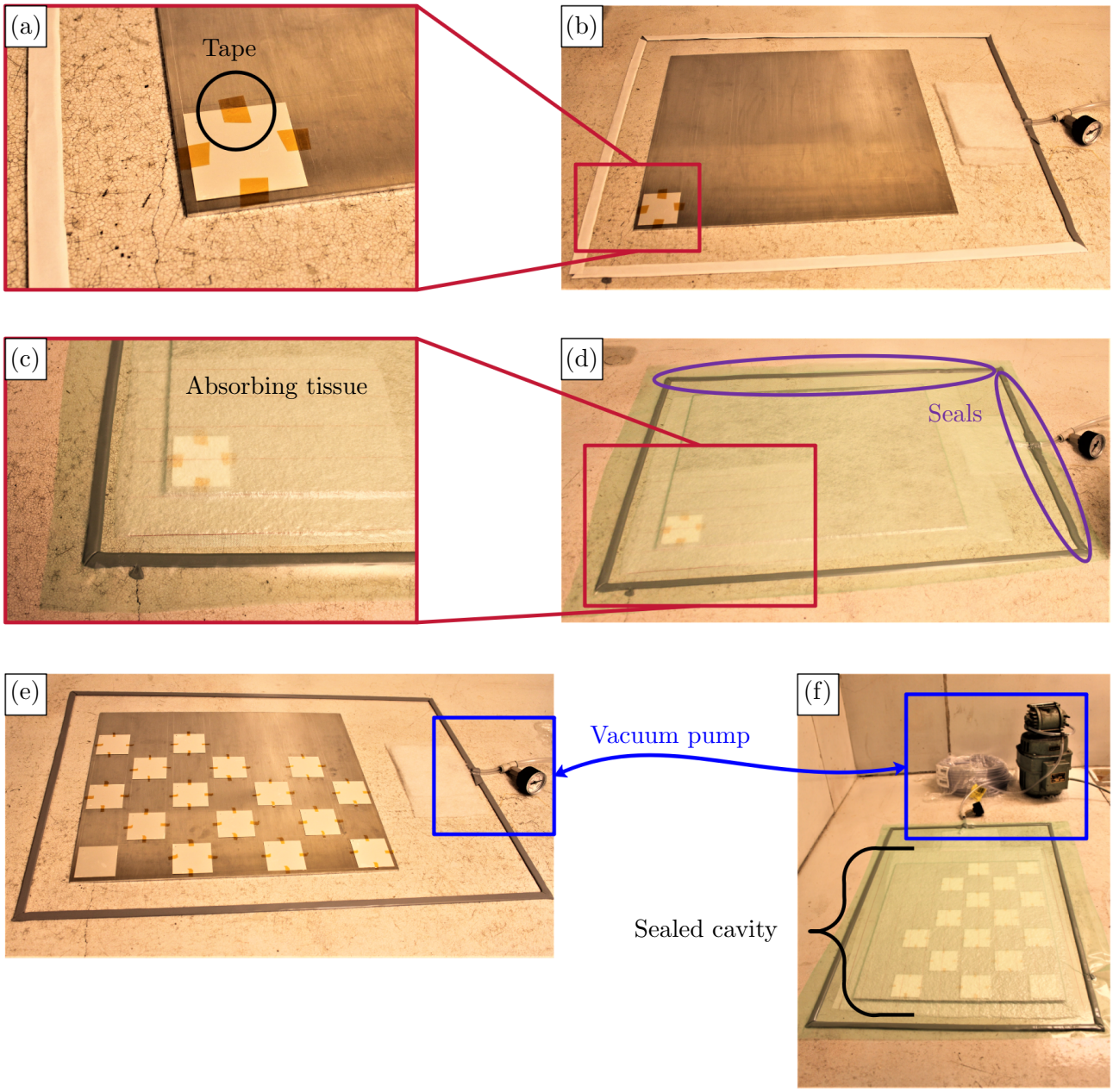

Figure 3.2: Bonding of the piezoelectric patches on the plate: (a), (b) Patch fixation using tape; (c) Absorbing tissue between the plastic layer and the structure; (d) Making up of the sealed cavity; (e) Preparation for the bonding of several patches; (f) Connection of the vacuum pump to the cavity.

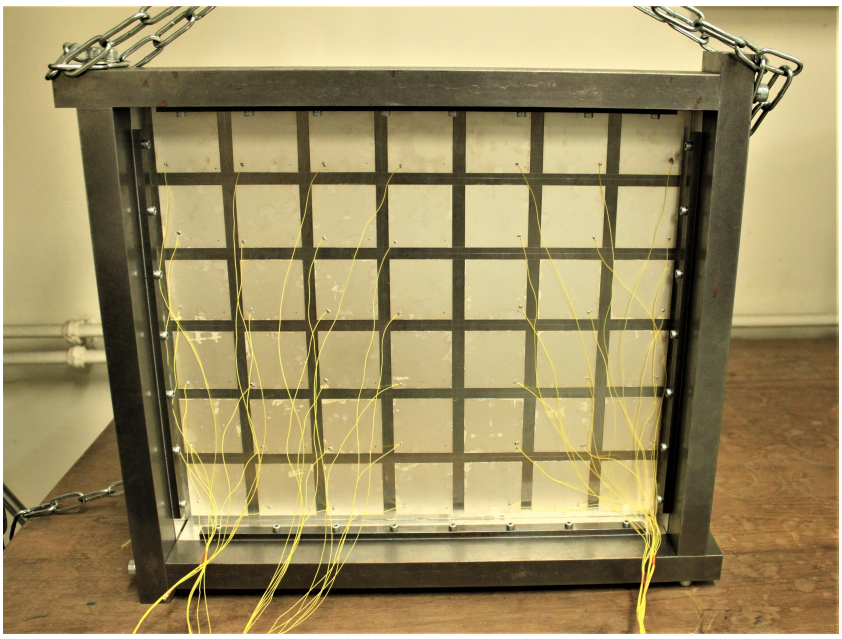

Figure 3.3: Duralumin rectangular plate periodically covered by 42 square piezoelectric patches and simply-supported by a steel frame.

3.3.2 Comparison between simulations and experiments

The simply-supported plate periodically covered with piezoelectric patches is suspended. A shaker applies a point load and a force transducer measures it. A laser vibrometer measures the velocity on the other side of the plate. The (x, y) location of both the excitation and the velocity measurements is drawn in figure 3.4. The excitation is a pseudo-random white noise signal below 5 kHz, and a rectangular window with no overlap is applied to both the excitation and the velocity measurements. These adjustments are typical in modal testing [95], as they ensure that the perceived information is correctly treated [96] while keeping the measurement at an acceptable duration [97]. Moreover, the upper electrodes of the patches are either connected to the ground or independently set in open-circuit.

The structure is modeled with 20-node hexahedral elements. Both the plate and the piezoelectric patches are meshed with one element in depth. In the other directions, the piezoelectric patches as well as the plate beneath them are meshed with $n_x \times n_y$ elements. Taking $n_x = n_y = 3$ leads to converged values for natural frequencies of the undamped structure up to 1 kHz. The maximum remaining difference between natural frequencies estimated with $n_x = n_y = 3$ and $n_x = n_y = 5$ is 0.4 %. Accordingly, the figure 3.4 depicts the mesh used to obtain all the following numerical results.

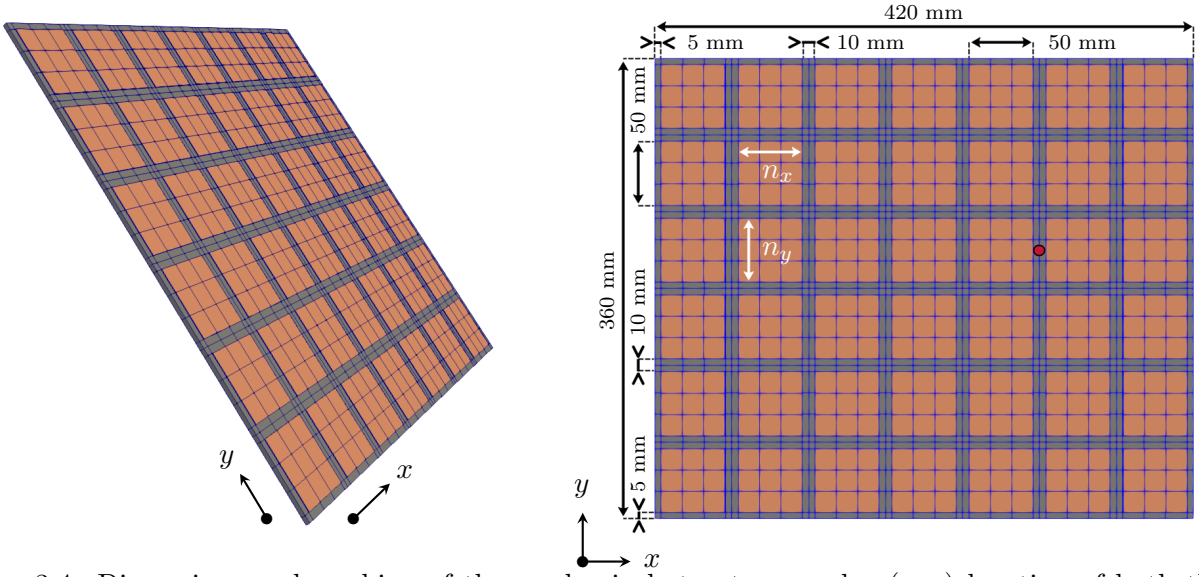

Figure 3.4: Dimensions and meshing of the mechanical structure, and • (x, y) location of both the force and the velocity measurements.

The plate is made of duralumin. Its Poisson's ratio and density are respectively set at 0.35 and 2800 kg/m^3. Its Young's modulus is set at 69 GPa to adjust the eleventh natural frequency of the plate calculated with short-circuited piezoelectric patches to the corresponding resonance in measurements. This corresponds to the last peak below 900 Hz as plotted in figure 3.6.

Mechanical damping is taken into account. This means that a mechanical damping matrix $\boldsymbol{D_m}$ is included in the finite element formulation. Hence, in harmonic motion at angular frequency Ω, the equation (3.27) becomes

$$\left[\begin{pmatrix} \boldsymbol{K_m} & \boldsymbol{K_c} \\ -\boldsymbol{K_c}^{\mathrm{T}} & \boldsymbol{K_e}^{-1} \end{pmatrix} + \mathrm{j}\Omega \begin{pmatrix} \boldsymbol{D_m} & \boldsymbol{0} \\ \boldsymbol{0} & \boldsymbol{0} \end{pmatrix} - \Omega^2 \begin{pmatrix} \boldsymbol{M_m} & \boldsymbol{0} \\ \boldsymbol{0} & \boldsymbol{0} \end{pmatrix}\right] \begin{pmatrix} \boldsymbol{U} \\ \boldsymbol{V} \end{pmatrix} = \begin{pmatrix} \boldsymbol{F} \\ \boldsymbol{Q} \end{pmatrix}. \tag{3.32}$$

Mechanical damping can be included in the other finite element formulations derived in section 3.2 in a similar fashion. Depending on the subtlety of the modeling, various damping models are possible. To avoid infinite resonance peaks, we choose to implement hysteretic damping, which is one of the simplest models available. The mechanical damping matrix $\boldsymbol{D_m}$ is therefore computed according to the mechanical stiffness matrix $\boldsymbol{K_m}$:

$$\boldsymbol{K_m} + \mathrm{j}\Omega\boldsymbol{D_m} = (1 + 2\mathrm{j}\xi)\,\boldsymbol{K_m}, \qquad \text{which is equivalent to} \qquad \boldsymbol{D_m} = \frac{2\xi}{\Omega}\,\boldsymbol{K_m}. \tag{3.33}$$

The damping coefficient ξ is set at 0.3 % so that the amplitude of the first simulated peak is roughly equal to the measured one in figure 3.6.

The piezoelectric patches are made of the PIC 153 PZT material [98]. Few material characteristics are available in the manufacturer's data. Thus these characteristics are either extrapolated from datasheets of other PZT materials, or numerically optimized. This is the case of the piezoelectric coefficients d_{31} and d_{33}. By extrapolation on the basis of other PZT materials whose characteristics are available in [98], it is assumed that $d_{33} \approx -2d_{31}$. Their values are then set in order to minimize the quadratic error on the coupling factors. The modal coupling factor $(k_c)_n$ for the n-th mode is

$$(k_c)_n = \sqrt{\left(\frac{(f_{\mathrm{OC}})_n}{(f_{\mathrm{SC}})_n}\right)^2 - 1}. \tag{3.34}$$

In this expression, $(f_{\mathrm{SC}})_n$ is the n-th natural frequency of the plate when the piezoelectric patches are short-circuited, while $(f_{\mathrm{OC}})_n$ is the n-th natural frequency of the plate when each upper electrode of the piezoelectric patches is left disconnected. As explained in subsection 3.2.7, not interconnecting the upper electrodes of patches in the case of open-circuit allows defining a non-zero coupling factor for all modes, which leads to a more precise estimation for the values of d_{33} and d_{31}.

These frequencies are estimated by using the finite element formulations of equations (3.27) and (3.28). Meanwhile, they are measured at the peak positions of the FRF plotted in figure 3.6. If the structure is slightly damped, then the peak positions are a good approximation of the structure natural frequencies. A more precise method would be to conduct a full experimental modal analysis of the system, for example. Computing the mean squared error (MSE) between simulated and measured values of $(k_c)_n$ for the first eleven modes of the structure results in figure 3.5a. As a consequence, the value of d_{31} is set at -260 pC/N and the value of d_{33} is estimated at 520 pC/N. This d_{33} value is notably smaller than the value of 600 pC/N indicated by the manufacturer's data. This confirms the need to experimentally evaluate the materials characteristics when possible.

As a result, the simulated coupling factors are shown in figure 3.5b. The gap between the simulated and measured coupling factors is less than 5 %. Besides, this maximum overestimation is for the first coupling factor and could be partly explained by the non-ideal experimental boundary conditions. The plate experimental setup is linked to a rigid frame via thin supports, while the plate is the only part of the assembly that is modeled. Therefore the added stiffness owned to the supports is not modeled. Knowing this maximum error of 5 % could be reduced, the prediction of the coupling factors is considered sufficiently precise. All numerical values which are needed for the modeling are summed up in table 3.3.

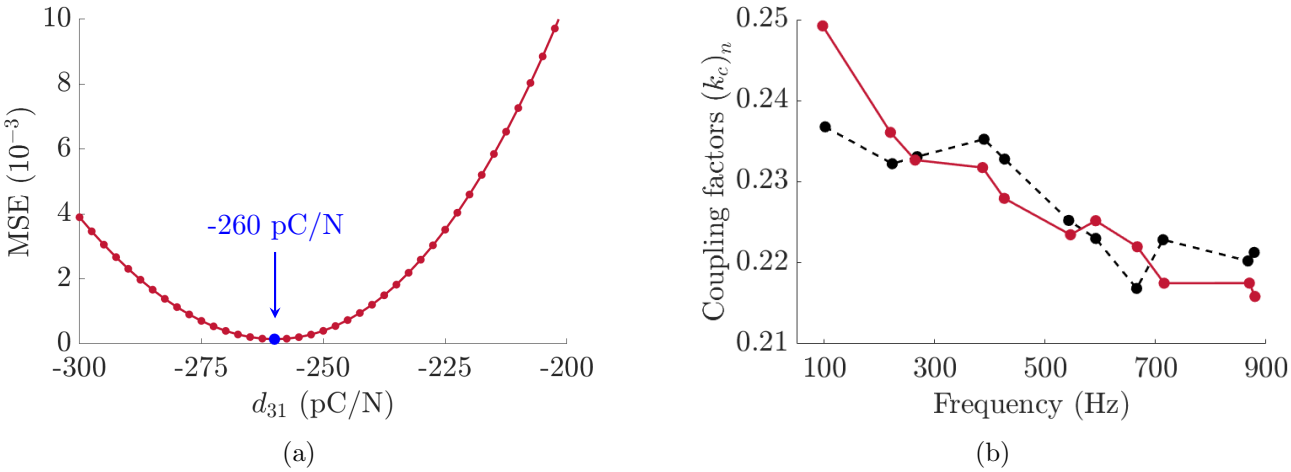

Figure 3.5: (a) MSE on the modal coupling factors for different d_{31} piezoelectric coefficient values and (b) resulting comparison between ---- measured and —— simulated coupling factors of the first eleven plate modes.

Elastic coefficients (10^{-12} N/m^2)				**Poisson's ratios** (-)		**Piezoelectric coefficients** (10^{-12} C/N)		**Relative permittivities** (-)		**Density** (kg/m^3)	
s_{11}^E	16.83[a]	s_{33}^E	$1.15s_{11}^E$[b]	ν_{12}	0.34	d_{31}	-260[c]	$\epsilon_{33}^\sigma/\epsilon_0$	4200	ρ_p	7600
s_{12}^E	$-\nu_{12}s_{11}^E$	s_{44}^E	$1.15s_{66}^E$[b]	ν_{13}	$1.25\nu_{12}$[b]	d_{33}	$-2d_{31}$[b]	$\epsilon_{33}^\varepsilon/\epsilon_0$	2575[d]		
s_{13}^E	$-\nu_{13}s_{11}^E$	s_{66}^E	$2\left(s_{11}^E-s_{12}^E\right)$								

[a] Supposed equal to the s_{11}^E coefficient of the PIC 151 PZT material [98].
[b] Relations extrapolated from other PZT material characteristics [98].
[c] Set to minimize the MSE on the coupling factors (see figure 3.5a).
[d] Measured on an unbonded depolarized patch at 1 kHz and low level of excitation.

Table 3.3: PIC 153 PZT material [98] characteristics used for the finite element modeling.

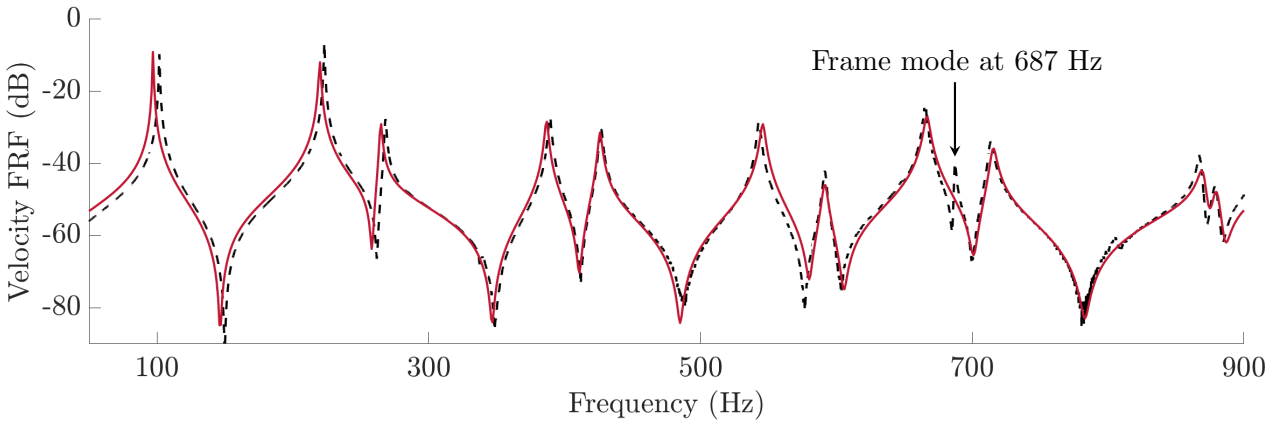

Figure 3.6: ---- Experimental and —— simulated FRFs with short-circuited piezoelectric patches.

The case of short-circuited patches is simulated using the formulation of equation (3.32). The plotted results in figure 3.6 show that the numerical simulation forecasts the dynamics of the structure up to 900 Hz rather well. Moreover, the remaining differences between numerical and experimental results could be reduced. Indeed, the peak at 687 Hz cannot be predicted by our model since it is a frame mode. Furthermore, the gaps between the first simulated and measured peaks can be attributed to the non-ideal experimental boundary conditions, as explained in subsection 3.3.1 and in [94]. As a consequence, the finite element model we have developed of a structure covered by thin piezoelectric transducers is validated at low frequencies.

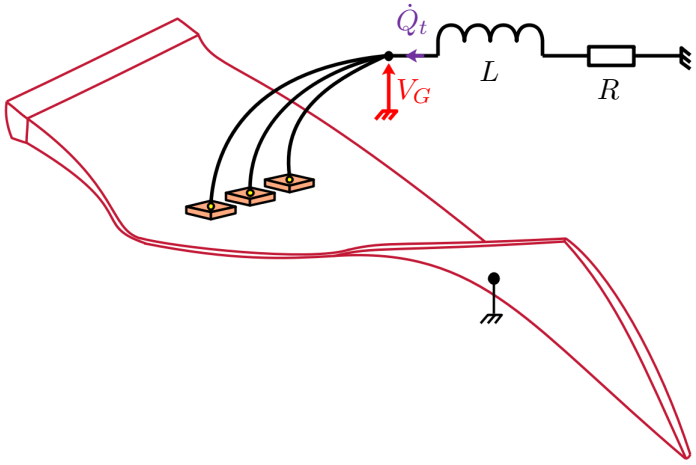

Figure 3.7: Resonant shunt damping of a mechanical structure covered by piezoelectric transducers.

3.4 Piezoelectric coupling to an electrical circuit

3.4.1 Piezoelectric shunting of a structure

Piezoelectric shunt damping has been first described by Hagood and Von Flotow in [5]. The principle is to create an electromechanical tuned mass damper, where the absorber is an electrical system that is added on the vibrating structure. To do so, we must first interconnect all upper electrodes of the piezoelectric transducers covering the structure, and then plug an electrical component between them and the ground. If we consider a resonant shunt, such as drawn in figure 3.7, which is made of a resistance R in series with an inductance L, then a relation is commanded between the common voltage V_G and the total electric charge Q_t:

$$V_G = -\left(R\dot{Q}_t + L\ddot{Q}_t\right). \tag{3.35}$$

Consequently, the finite element formulation of equation (3.31) becomes

$$\begin{pmatrix} \boldsymbol{M_m} & \boldsymbol{0} \\ \boldsymbol{0} & L \end{pmatrix} \begin{pmatrix} \ddot{\boldsymbol{U}} \\ \ddot{Q}_t \end{pmatrix} + \begin{pmatrix} \boldsymbol{0} & \boldsymbol{0} \\ \boldsymbol{0} & R \end{pmatrix} \begin{pmatrix} \dot{\boldsymbol{U}} \\ \dot{Q}_t \end{pmatrix} + \begin{pmatrix} \boldsymbol{K_m} + \dfrac{\left(\sum_{j=1}^{p} \boldsymbol{K_c}^{(j)}\right)\left(\sum_{j=1}^{p} \boldsymbol{K_c}^{(j)}\right)^{\mathrm{T}}}{\sum_{j=1}^{p} C^{\varepsilon(j)}} & \dfrac{\sum_{j=1}^{p} \boldsymbol{K_c}^{(j)}}{\sum_{j=1}^{p} C^{\varepsilon(j)}} \\ \dfrac{\left(\sum_{j=1}^{p} \boldsymbol{K_c}^{(j)}\right)^{\mathrm{T}}}{\sum_{j=1}^{p} C^{\varepsilon(j)}} & \dfrac{1}{\sum_{j=1}^{p} C^{\varepsilon(j)}} \end{pmatrix} \begin{pmatrix} \boldsymbol{U} \\ Q_t \end{pmatrix} = \begin{pmatrix} \boldsymbol{F} \\ 0 \end{pmatrix}. \tag{3.36}$$

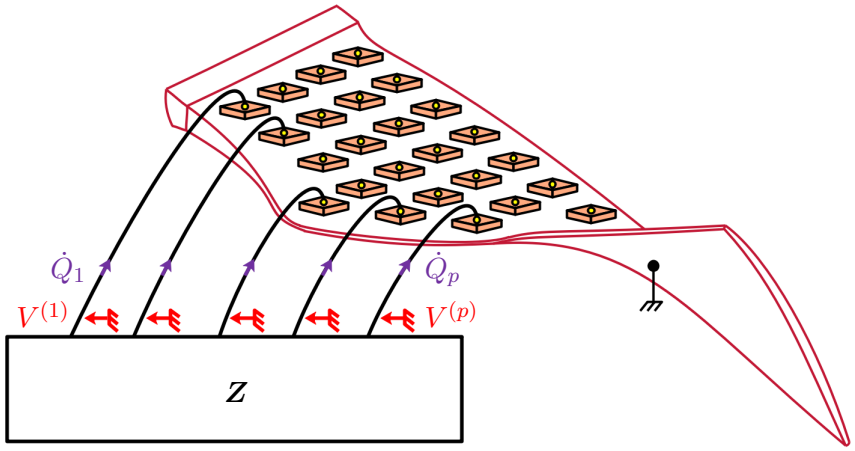

Figure 3.8: Mechanical structure covered by piezoelectric transducers and shunted by a multi-ports impedance controller. For readability purposes, only a few wires connecting the piezoelectric transducers to the network are represented.

In harmonic motion, this equation is similar to the equation (1.1), except from the fact that the resistor induces electrical damping in the coupled system. This means we can expect the mechanical energy that has been transferred in the electrical circuit to be partially dissipated by heat. One can also verify that the inductance plays a role that is analogous to the mass, and that the resistor plays a role that is analogous to viscous damping. This is consistent with the direct electromechanical analogy presented in table 2.1. The coupling of a mechanical structure to a resonant shunt can be interpreted as the first step going towards the coupling to an electrical network, granted that the aforementioned network is in fact a one-degree-of-freedom system, and thus presents only one electrical resonance.

3.4.2 Coupling of a structure to an electrical network

3.4.2.1 Impedance matrix approach

The piezoelectric patches bonded to the structure are now interconnected via an electrical network. A first possibility is to consider that the electrical network is an extension of the case of the resonant shunt previously exhibited. The principle is illustrated in figure 3.8. Indeed, the electrical network can be regarded as a passive electrical controller that commands a relationship between the voltages $\boldsymbol{V}$ and the electrical charges $\boldsymbol{Q}$:

$$\boldsymbol{V} = -\boldsymbol{Z}\boldsymbol{Q}, \tag{3.37}$$

where $\boldsymbol{Z}$ is an impedance matrix whose terms have the same dimension as the inverse of a capacitance. Its terms depend on the inductive and resistive components of the network, which is comparable to the commanded relation of equation (3.35) for the resonant shunt. As a consequence, from equation (3.28) we obtain

$$\begin{pmatrix} \boldsymbol{M_m} & \boldsymbol{0} \\ \boldsymbol{0} & \boldsymbol{0} \end{pmatrix} \begin{pmatrix} \ddot{\boldsymbol{U}} \\ \ddot{\boldsymbol{Q}} \end{pmatrix} + \begin{pmatrix} \boldsymbol{K_m} + \boldsymbol{K_c}\boldsymbol{K_e}\boldsymbol{K_c}^{\mathrm{T}} & \boldsymbol{K_c}\boldsymbol{K_e} \\ (\boldsymbol{K_c}\boldsymbol{K_e})^{\mathrm{T}} & \boldsymbol{K_e} + \boldsymbol{Z} \end{pmatrix} \begin{pmatrix} \boldsymbol{U} \\ \boldsymbol{Q} \end{pmatrix} = \begin{pmatrix} \boldsymbol{F} \\ \boldsymbol{0} \end{pmatrix}. \tag{3.38}$$

Moreover, by applying equations similar as (2.13) it is possible to derive an electrical "mass" matrix $\boldsymbol{M_Z}$, an electrical damping matrix $\boldsymbol{D_Z}$ and an electrical "stiffness" matrix $\boldsymbol{K_Z}$ so that

$$\boldsymbol{V} = -\left(\boldsymbol{M_Z}\ddot{\boldsymbol{Q}} + \boldsymbol{D_Z}\dot{\boldsymbol{Q}} + \boldsymbol{K_Z}\boldsymbol{Q}\right). \tag{3.39}$$

This leads to another finite element formulation highlighting the dynamics of the electrical network:

$$\begin{pmatrix} \boldsymbol{M_m} & \boldsymbol{0} \\ \boldsymbol{0} & \boldsymbol{M_Z} \end{pmatrix} \begin{pmatrix} \ddot{\boldsymbol{U}} \\ \ddot{\boldsymbol{Q}} \end{pmatrix} + \begin{pmatrix} \boldsymbol{0} & \boldsymbol{0} \\ \boldsymbol{0} & \boldsymbol{D_Z} \end{pmatrix} \begin{pmatrix} \dot{\boldsymbol{U}} \\ \dot{\boldsymbol{Q}} \end{pmatrix} + \begin{pmatrix} \boldsymbol{K_m} + \boldsymbol{K_c}\boldsymbol{K_e}\boldsymbol{K_c}^{\mathrm{T}} & \boldsymbol{K_c}\boldsymbol{K_e} \\ (\boldsymbol{K_c}\boldsymbol{K_e})^{\mathrm{T}} & \boldsymbol{K_e} + \boldsymbol{K_Z} \end{pmatrix} \begin{pmatrix} \boldsymbol{U} \\ \boldsymbol{Q} \end{pmatrix} = \begin{pmatrix} \boldsymbol{F} \\ \boldsymbol{0} \end{pmatrix}. \tag{3.40}$$

If the network components are fixed, then the expression of the impedance matrix $\boldsymbol{Z}$ can be theoretically derived. Once $\boldsymbol{Z}$ is known, the equations (3.38) or (3.40) are convenient to simulate the coupled system dynamics. However, the expression of $\boldsymbol{Z}$ may be difficult to derive in the first place. It is a $p \times p$ matrix, whose terms are all different from zero. Deriving the expression of $\boldsymbol{Z}$ involves solving a linear system whose size depends on the amount of components in the network. Besides, another drawback of this approach is that it barely allows modifying the electrical network model. Any parameter whose influence cannot be directly implemented in the available impedance matrix requires to compute a new and more complicated symbolic expression of $\boldsymbol{Z}$, which increases the computing time consequently.

For these reasons, we chose to stay away from this approach. Though it is a natural extension of the resonant shunt to derive a symbolic expression relating the voltages $\boldsymbol{V}$ and the electrical charges $\boldsymbol{Q}$, it is not adapted to the study of non-periodic complex networks, which eventually include non-ideal electrical components. Therefore, another approach is suggested in the next paragraph.

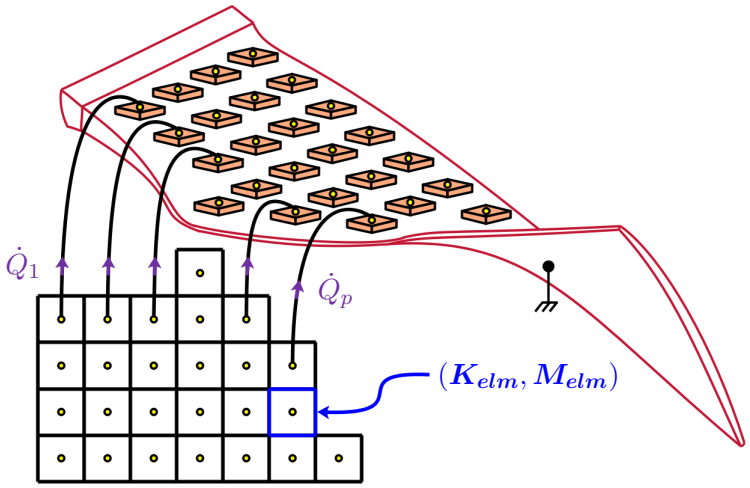

Figure 3.9: Piezoelectric network damping of a mechanical structure covered by piezoelectric transducers. For readability purposes, only a few wires connecting the piezoelectric transducers to the network are represented.

3.4.2.2 Finite element-like approach

Another approach is to assemble unit cells of the electrical network in a similar manner as when applying the finite element method. As seen in figure 3.9, the network is discretized in unit cells, whose elementary matrices of electrical "mass" $\boldsymbol{M_{elm}}$ and electrical "stiffness" $\boldsymbol{K_{elm}}$ are locally defined. Assembling them leads to the dynamic model of the network:

$$\boldsymbol{V_N} = \boldsymbol{M_N}\ddot{\boldsymbol{Q}}_{\boldsymbol{N}} + \boldsymbol{K_N}\boldsymbol{Q_N}. \tag{3.41}$$

The goal is now to couple this finite element-like formulation of the network behavior to the finite element formulation of equation (3.28). Hence we have to relate the vectors of voltages $\boldsymbol{V}$ and electric charges $\boldsymbol{Q}$ of the piezoelectric patches to the vectors of voltages $\boldsymbol{V_N}$ and electric charges $\boldsymbol{Q_N}$ in the network.

Deriving the relationship between $\boldsymbol{Q}$ and $\boldsymbol{Q_N}$ is pretty straight-forward once looking at the available networks. It only implies applying Kirchhoff's current law to the junction between the piezoelectric capacitance and the electrical network. Hence, the j-th electrical charge $Q^{(j)}$ can be expressed in terms of local network charges. The corresponding formulas are summed up in table 3.4. As a consequence, a matrix $\boldsymbol{P}$ can be assembled so that

$$\boldsymbol{Q} = \boldsymbol{P}\boldsymbol{Q_N}. \tag{3.42}$$

Electrical analogue	**Unit cell lumped-element model**	$Q^{(j)}$ **value**
Rod	Figure 2.7b	$q_{x\mathrm{L}}^{(j)} - q_{x\mathrm{R}}^{(j)}$
Bar	Figure 2.9b	$q_{\varphi\mathrm{L}}^{(j)} - q_{\varphi\mathrm{R}}^{(j)}$
Straight beam	Figure 2.11b	$q_{\theta\mathrm{L}}^{(j)} - q_{\theta\mathrm{R}}^{(j)}$
Plate	Figure 2.14	$q_{\theta\mathrm{L}}^{(j)} - q_{\theta\mathrm{R}}^{(j)} + q_{\theta\mathrm{B}}^{(j)} - q_{\theta\mathrm{T}}^{(j)}$
Curved beam (A)	Figure 2.22	$q_{\theta\mathrm{L}}^{(j)} - q_{\theta\mathrm{R}}^{(j)}$
Curved beam (B)	Figures 2.25 and 2.28b	$q_{\theta\mathrm{L}}^{(j)} - q_{\theta\mathrm{R}}^{(j)}$
Tube	Figure 2.36	$q_{\theta\mathrm{L}}^{(j)} - q_{\theta\mathrm{R}}^{(j)} + q_{\theta\mathrm{B}}^{(j)} - q_{\theta\mathrm{T}}^{(j)}$

Table 3.4: Expression of the j-th electrical charge $Q^{(j)}$ in terms of network electric charges.

However, the relation between $\boldsymbol{V}$ and $\boldsymbol{V_N}$ calls for more work. Indeed, the voltage vector $\boldsymbol{V_N}$ is generated by the electrical currents flowing in the network and by the piezoelectric coupling with the vibrating structure. We thus suggest to apply the superposition theorem involving these two voltage sources.

We first consider that $\boldsymbol{U} \neq \boldsymbol{0}$ and $\boldsymbol{Q_N} = \boldsymbol{0}$. This second condition is equivalent to having $\boldsymbol{q_N} = \boldsymbol{0}$ for every unit cell of the network. Moreover, the equation (3.42) induces that $\boldsymbol{Q} = \boldsymbol{0}$. Then, the boundary voltages of each unit cell can be related to the corresponding element of $\boldsymbol{V}$. These relations are deduced by applying Kirchhoff's and Ohm's laws to the network unit cells defined in chapter 2. They are summed up in table 3.5. We consequently show that an assembly process leads to an expression involving the same $\boldsymbol{P}$ matrix as in equation (3.42):

$$\boldsymbol{V_N} = \boldsymbol{P}^{\mathrm{T}} \boldsymbol{V}. \tag{3.43}$$

Therefore, setting $\boldsymbol{Q} = \boldsymbol{0}$ in the finite element formulation of equation (3.27) and remembering that $\boldsymbol{K_e}$ is invertible and symmetric helps relating the voltage vector $\boldsymbol{V_N}$ to the displacement field $\boldsymbol{U}$:

$$\boldsymbol{V_N} = \left(\boldsymbol{K_c} \boldsymbol{K_e} \boldsymbol{P}\right)^{\mathrm{T}} \boldsymbol{U}. \tag{3.44}$$

We then consider that $\boldsymbol{U} = \boldsymbol{0}$ while $\boldsymbol{Q_N} \neq \boldsymbol{0}$. In the case of no piezoelectric coupling with the structure, it has been shown that the voltages and currents in the network are related by equation (3.41).

Electrical analogue	**Unit cell lumped-element model**	**Boundary voltages values**
Rod	Figure 2.7b	$V_{x\mathrm{L}}^{(j)} = V_{x\mathrm{I}}^{(j)}$ $V_{x\mathrm{R}}^{(j)} = V_{x\mathrm{I}}^{(j)}$
Bar	Figure 2.9b	$V_{t\mathrm{L}}^{(j)} = V_{t\mathrm{I}}^{(j)}$ $V_{t\mathrm{R}}^{(j)} = V_{t\mathrm{I}}^{(j)}$
Straight beam	Figure 2.11b	$V_{z\mathrm{L}}^{(j)} = 0$ $\quad V_{\theta\mathrm{L}}^{(j)} = V_{\theta\mathrm{I}}^{(j)}$ $V_{z\mathrm{R}}^{(j)} = 0$ $\quad V_{\theta\mathrm{R}}^{(j)} = V_{\theta\mathrm{I}}^{(j)}$
Plate	Figure 2.14	$V_{z\mathrm{B}}^{(j)} = 0$ $\quad V_{\theta\mathrm{B}}^{(j)} = V_{\theta\mathrm{I}}^{(j)}$ $V_{z\mathrm{L}}^{(j)} = 0$ $\quad V_{\theta\mathrm{L}}^{(j)} = V_{\theta\mathrm{I}}^{(j)}$ $V_{z\mathrm{R}}^{(j)} = 0$ $\quad V_{\theta\mathrm{R}}^{(j)} = V_{\theta\mathrm{I}}^{(j)}$ $V_{z\mathrm{T}}^{(j)} = 0$ $\quad V_{\theta\mathrm{T}}^{(j)} = V_{\theta\mathrm{I}}^{(j)}$
Curved beam (A)	Figure 2.22	$V_{v\mathrm{L}}^{(j)} = 0$ $\quad V_{w\mathrm{L}}^{(j)} = 0$ $\quad V_{\theta\mathrm{L}}^{(j)} = V_{\theta\mathrm{I}}^{(j)}$ $V_{v\mathrm{R}}^{(j)} = 0$ $\quad V_{w\mathrm{R}}^{(j)} = 0$ $\quad V_{\theta\mathrm{R}}^{(j)} = V_{\theta\mathrm{I}}^{(j)}$
Curved beam (B)	Figures 2.25 and 2.28b	$V_{v\mathrm{L}}^{(j)} = 0$ $\quad V_{w\mathrm{L}}^{(j)} = 0$ $\quad V_{\theta\mathrm{L}}^{(j)} = V_{\theta\mathrm{I}}^{(j)}$ $V_{v\mathrm{R}}^{(j)} = 0$ $\quad V_{w\mathrm{R}}^{(j)} = 0$ $\quad V_{\theta\mathrm{R}}^{(j)} = V_{\theta\mathrm{I}}^{(j)}$
Tube	Figure 2.36	$V_{w\mathrm{B}}^{(j)} = 0$ $\quad V_{\theta\mathrm{B}}^{(j)} = V_{\theta\mathrm{I}}^{(j)}$ $V_{v\mathrm{L}}^{(j)} = 0$ $\quad V_{w\mathrm{L}}^{(j)} = 0$ $\quad V_{\theta\mathrm{L}}^{(j)} = V_{\theta\mathrm{I}}^{(j)}$ $V_{v\mathrm{R}}^{(j)} = 0$ $\quad V_{w\mathrm{R}}^{(j)} = 0$ $\quad V_{\theta\mathrm{R}}^{(j)} = V_{\theta\mathrm{I}}^{(j)}$ $V_{w\mathrm{T}}^{(j)} = 0$ $\quad V_{\theta\mathrm{T}}^{(j)} = V_{\theta\mathrm{I}}^{(j)}$

Table 3.5: Expressions of the boundary voltages of the j-th electrical network unit cell.

Applying the superposition principle with equations (3.41) and (3.44) results in the expression of $\boldsymbol{V_N}$ when $\boldsymbol{U} \neq \boldsymbol{0}$ and $\boldsymbol{Q_N} \neq \boldsymbol{0}$:

$$\boldsymbol{V_N} = \boldsymbol{M_N}\ddot{\boldsymbol{Q}}_{\boldsymbol{N}} + \boldsymbol{K_N}\boldsymbol{Q_N} + (\boldsymbol{K_c}\boldsymbol{K_e}\boldsymbol{P})^{\mathrm{T}}\,\boldsymbol{U}. \tag{3.45}$$

Combining the mechanical part of equation (3.28), as well as equations (3.42) and (3.45) leads to a finite element formulation of a structure coupled to an electrical network:

$$\begin{pmatrix} \boldsymbol{M_m} & \boldsymbol{0} \\ \boldsymbol{0} & \boldsymbol{M_N} \end{pmatrix} \begin{pmatrix} \ddot{\boldsymbol{U}} \\ \ddot{\boldsymbol{Q}}_{\boldsymbol{N}} \end{pmatrix} + \begin{pmatrix} \boldsymbol{K_m} + \boldsymbol{K_c}\boldsymbol{K_e}\boldsymbol{K_c}^{\mathrm{T}} & \boldsymbol{K_c}\boldsymbol{K_e}\boldsymbol{P} \\ (\boldsymbol{K_c}\boldsymbol{K_e}\boldsymbol{P})^{\mathrm{T}} & \boldsymbol{K_N} \end{pmatrix} \begin{pmatrix} \boldsymbol{U} \\ \boldsymbol{Q}_{\boldsymbol{N}} \end{pmatrix} = \begin{pmatrix} \boldsymbol{F} \\ \boldsymbol{V}_{\boldsymbol{N}} \end{pmatrix}. \tag{3.46}$$

In harmonic motion, this expression is similar to the equation (1.1), and to a formulation derived in [99] in the case of a single unit cell being periodically assembled along one direction. The present finite element formulation is used for an extension to non-periodic 2D networks, which is a contribution of this thesis. Besides, it allows assembling the network unit cells as in the finite element method. Hence, local modifications of network components can be implemented. This should ease the way going towards non-periodic structures, as it is a more flexible modeling tool than the one developed with the impedance matrix approach in subsection 3.4.2.1. Finally, we point out that that this model only requires the assembled matrices of stiffness, mass and coupling of the structure as starting points. As a consequence, it is convenient to study the impact of a network connection to a structure which is modeled by the finite element method in a commercial software. Note that mechanical damping could also be implemented in this formulation, as will be made in the following chapters.

Hypotheses for finite element modeling of a structure coupled by piezoelectric patches to an electrical network

The main assumptions to derive the finite element formulation of equation (3.46) are:

- The same hypotheses as for the finite element model of equation (3.28) apply. We recall the most important ones:
  - The infinitesimal strain theory applies.
  - The adhesive layers and the electrodes thicknesses are not modeled.
  - The lower electrodes are connected to the ground.
  - The piezoelectric transducers are thin and polarized in the electrodes orthogonal directions, and they exhibit transverse isotropic properties.
- The electrical behavior of network unit cells can be described by elementary matrices of "stiffness" $\boldsymbol{K_{elm}}$ and "mass" $\boldsymbol{M_{elm}}$.
- The electrical network behaves linearly with the excitation sources, so that the superposition principle can be applied. This is ensured by considering linear electrical components and the linear piezoelectricity theory.

3.5 Conclusions

In this chapter, we have developed a finite element model of a structure covered by thin piezoelectric transducers. This model is convenient as it includes the potentials and electrical charges on the upper electrodes of the piezoelectric patches as global variables. Therefore, expressing the cases of setting the piezoelectric transducers in short-circuit and in open-circuit is easy. This finite element model is validated by comparing simulated results to measurements conducted on a simply-supported rectangular plate. The plate is periodically covered by 42 piezoelectric patches, whose materials constants are measured when possible. The good correlation between experimental and numerical results proves that the modeling process is adequate for our situation.

Finally, we consider the case of connecting the structure to a lumped electrical network. We assume that the network can be discretized in unit cells, which can be assembled in a similar way as in the finite element method. A finite element formulation of the structure being coupled to an electrical network via piezoelectric patches is then derived. Besides, this formulation can be applied even if the mechanical and electrical matrices are issued from different numerical sources. In other words, the coupling between the mechanical and electrical systems can be made after their respective assembly processes. One of the objectives of chapter 4 is to validate this model.

Note that the present manuscript does not bring contribution to the topic of finite element modeling of electromechanical coupling via piezoelectric transducers. The originality rather lies on the coupling of a 3D finite element model to a network described by a set of discrete equations.

Chapter 4

Piezoelectric network damping of a plate

The objective of the present chapter is to study the vibration mitigation of a plate coupled to an electrical network via piezoelectric patches. An analogous network of the plate is assembled by considering square plate electrical analogues as unit cells. To do so, magnetic circuits are used to produce passive inductors and transformers for the network, so the design process of magnetic components is recalled. Finally, the network is validated by checking if it meets the frequency and spatial coherence conditions, and multimodal damping is achieved. Besides, comparison between simulations and experiments allows validating the electromechanical model previously developed.

Content

4.1 Introduction

Damping of mechanical vibrations using piezoelectric coupling goes back to the 1990s, when the resonant shunt was described by Hagood and Von Flotow [5]. The efficiency of the resonant shunt to control a single mode of vibration has been extensively studied [13, 8]. The concept of piezoelectric shunt damping has then been extended to multimodal damping. Some passive solutions consider connecting a multi-branch shunt to a single piezoelectric transducer [25, 26, 27, 31]. While adding only one piezoelectric transducer to the structure is barely intrusive, its position and dimensions cannot simultaneously maximize the electromechanical coupling for all modes [35]. As a result, the damping performance might be limited. Moreover, the required inductive components could be difficult to produce [29], and the number of involved electrical components may greatly increase with the number of modes to be controlled [31]. Another solution could use several independent piezoelectric transducers, each one being shunted in order to damp one particular mode of the structure [44, 45]. However, the resulting electromechanical coupling coefficients are inferior to the ones that would be induced by interconnecting all piezoelectric transducers.

Hence, the principle of piezoelectric network damping emerged in the early 2000s [63, 51, 54, 55]. Broadband damping is achieved by bonding piezoelectric patches on a vibrating structure and interconnecting them with electrical components [36]. This way, the inductance requirements are reduced [51]. Besides, the topology of the network to be connected to the plate has a significant impact on the attainable damping performance. It has been shown that connecting the vibrating structure to a network that has the same modal characteristics ensures that there is as much electrical energy as mechanical energy involved in the coupled system [63]. For this reason, the electrical analogues of mechanical structures have been revived for vibration mitigation purposes [64], and piezoelectric network damping of beams [65, 66, 67] and plates [68, 69] has been studied. Most of these works are based on the application of the force-current and velocity-voltage analogy, also called indirect analogy.

Other articles concentrating on using the direct electromechanical analogy have implemented electrical analogues for the vibration mitigation of beams [71] and plates [72, 85]. Based on these recent articles, a plate electrical analogue is produced in this chapter for further measurements. To do so, the design processes of passive inductors and transformers are recalled in sections 4.2 and 4.3. The electrical network is designed to exhibit the same modal properties as the mechanical structure to be damped.

The validation of the network is then made in section 4.4 by comparing measurements to simulations and by conducting an experimental modal analysis. The assembled experimental setup also brings the occasion to develop tools for further analysis of complex structures. Finally, the broadband damping of the plate is addressed in section 4.5. The attained damping performance is promising. Moreover, the experiments bring the opportunity to validate the finite element model of a structure coupled to an electrical network via piezoelectric patches, as developed in chapter 3. The ability to predict the behavior of the coupled system brings hope in forecasting the coupling of complex structures to their electrical analogues in the next chapter.

4.2 Inductors design

All the electrical analogues of the library in section 2.10 include inductive components. Indeed, they are essential at replicating the dynamic behavior of a mechanical structure, since they are analogous to either a mass or a rotational inertia, according to the direct electromechanical analogy in table 2.1. As the present objective is to develop fully passive analogous networks, passive inductors should be designed. Several technical solutions exist to produce passive inductors, such as winding turns of conductive wire around ferrite cylinders, ferrite cores or nanocrystalline toroids. As explained in [100], the range of inductance values required for piezoelectric network damping fits with ferrite cores inductors, which also have the advantage of being easier to automatically wind when compared to toroids. Therefore we only consider this kind of magnetic circuits in this manuscript.

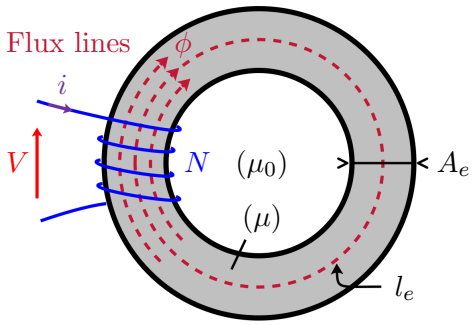

Figure 4.1: Toroidal magnetic circuit.

Electric circuit quantities	**Magnetic circuit quantities**
Voltage V	Magnetomotive force $\mathfrak{F} = Ni$
Electrical current i	Magnetic flux ϕ
Resistance R	Reluctance $\mathfrak{R}$
Conductance $1/R$	Permeance A_L
Conductivity $1/\varrho$	Permeability μ
Ohm's law: $V = Ri$	Hopkinson's law: $\mathfrak{F} = \mathfrak{R}\,\phi$

Table 4.1: Analogy between electric and magnetic circuits.

4.2.1 Laws of magnetic circuits

To design the required inductors, we first recall the rules of magnetic circuits. A magnetic circuit is a medium in which there are one or several loops of magnetic flux. This circuit is mostly made of ferromagnetic material, whose permeability μ is usually much bigger than the vacuum permeability μ_0. This material constant relates the magnetic flux density B to the applied magnetic field strength H, which is generated by the total electrical current surrounding the circuit of magnetic patch length l_e:

$$B = \mu H \qquad \text{with } H = \frac{Ni}{l_e}, \tag{4.1}$$

with N being the number of winding turns. The resulting magnetic flux ϕ in the circuit is

$$\phi = BA_e. \tag{4.2}$$

The geometry of the magnetic circuit is thus characterized by its effective cross-sectional area A_e and by its effective magnetic path length l_e. These quantities are indicated in figure 4.1.

All these equations describing the physical behavior of magnetic circuits are analogous to Ohm's law for electric circuits. This analogy, which is summarized in table 4.1, is verified for static and dynamic variations, as long as the magnetic circuit is not saturated. In other words, the analogy is only suitable for low levels of excitation. In particular, we note that the resistance R and the reluctance $\mathfrak{R}$ of a medium of length l and of cross-section S are expressed by

$$R = \frac{\varrho l}{S} \qquad \text{and} \qquad \mathfrak{R} = \frac{l}{\mu S}. \tag{4.3}$$

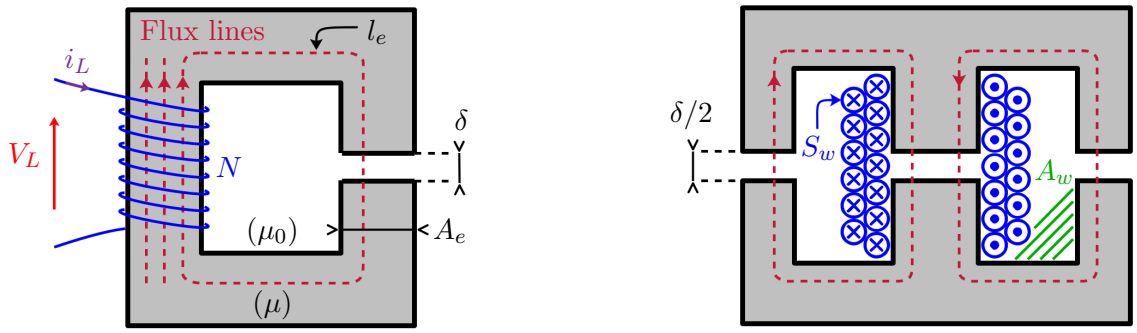

(a) (b)

Figure 4.2: Fully passive inductor made by winding conductive wire around (a) a gapped magnetic core or (b) a gapped RM magnetic core.

4.2.2 Inductors production

We now consider the magnetic circuits in figure 4.2 which include air gaps of length δ. The magnetic flux is related to the applied voltage V_L by Faraday's law of induction:

$$V_L = N \frac{d\phi}{dt}. \tag{4.4}$$

We recall that an inductor is characterized by its constitutive equation:

$$V_L = L \frac{di_L}{dt}. \tag{4.5}$$

One can deduce that passive inductors can be produced by winding N turns of conductive wire around magnetic cores. The resulting inductance value verifies

$$N\phi = Li_L. \tag{4.6}$$

To derive the expression of the inductance, we consider the circuit drawn in figure 4.2a, which can be regarded as a series circuit of two reluctances $\mathfrak{R}_{\text{core}}$ and $\mathfrak{R}_{\text{air}}$. Assuming $\delta \ll l_e$, so that flux lines do not spread out of the circuit cross-section too much when crossing the air gap, one obtains by applying the equation (4.3)

$$\mathfrak{R}_{\text{core}} = \frac{l_e - \delta}{\mu A_e} \qquad \text{and} \qquad \mathfrak{R}_{\text{air}} = \frac{\delta}{\mu_0 A_e}. \tag{4.7}$$

We define the initial relative permeability μ_r of the ferrite material, so that $\mu = \mu_0\mu_r$. Applying Hopkinson's law, which is recorded in table 4.1, leads to the expression of the inductance:

$$L = A_L N^2, \tag{4.8}$$

where A_L is the magnetic circuit permeance:

$$A_L = \frac{\mu_0 \mu_e A_e}{l_e}, \tag{4.9}$$

with μ_e being the effective relative permeability of the magnetic circuit. This quantity depends on the geometric properties of the magnetic circuit and on the ferrite material characteristics [101]:

$$\mu_e = \frac{l_e \mu_r}{l_e + \delta\,(\mu_r - 1)}. \tag{4.10}$$

The series resistance of the inductor, which is owed to the windings, can be estimated as well:

$$R_{sL} = \varrho\,\frac{N l_w}{S_w} \qquad \text{with } S_w = \frac{\pi d_w^2}{4}, \tag{4.11}$$

where ϱ is the resistivity, S_w is the wires cross-section, d_w is the wires diameter and l_w is the average length per turn. If the component is close to fully filled, then l_w is indicated by manufacturer's data.

4.2.3 Air gap and environmental parameters influences

Some environmental parameters modify the relative permeability μ_r, which is a material constant. This is the case of the electrical current [102, 103] and of the temperature [104, 105]. The dependence of the permeability on electrical current is owed to the magnetic saturation of the ferrite material. A typical inductance evolution with the current flowing through it is illustrated in figure 4.3. For any environmental parameter g influencing the relative permeability μ_r, one can compute

$$\begin{aligned} \frac{\partial L}{\partial g} &= \frac{\mu_0 A_e N^2}{l_e}\,\frac{\partial \mu_e}{\partial g} \\ &\approx \frac{\mu_0 A_e N^2}{l_e}\,\left[\frac{l_e}{l_e + \delta\mu_r}\right]^2\,\frac{\partial \mu_r}{\partial g} \qquad \text{if } \delta \ll l_e \text{ and } \mu_r \gg 1. \end{aligned} \tag{4.12}$$

The influence of the air gap on the inductance is interesting to note. Indeed, the equation (4.12) shows that for a ferrite material whose initial relative permeability μ_r variations are given, the greater the air gap δ, the smaller the inductance variations. Consequently, increasing the air gap helps both extending and flattening the linear evolution of the component, such as sketched in figure 4.3. However, as equation (4.10) shows, increasing the air gap δ decreases the relative permeability of the magnetic circuit μ_e. Thus, more turns will be needed to meet the target inductance value, and the equation (4.11) shows that increasing N increases the series resistance value as well.

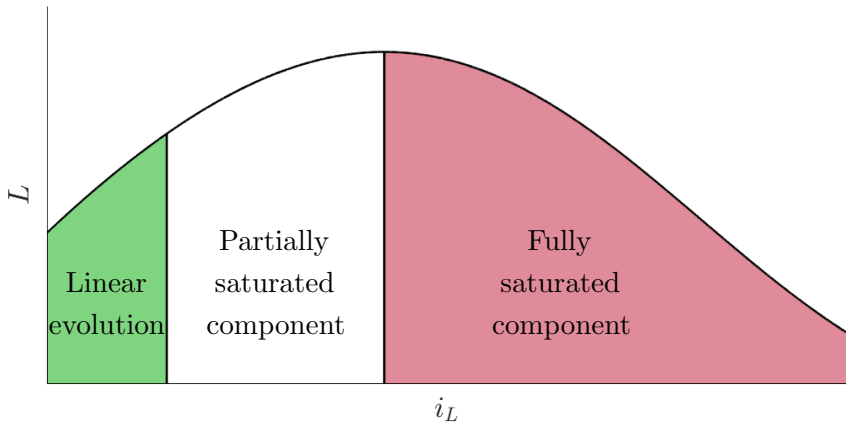

Figure 4.3: Standard dependence on the electrical current of a ferrite-based inductance.

As a conclusion, we show that to produce an inductor, there is a compromise to be found between stability and dissipation: a component with a wider air gap is less sensitive to external parameters variations, but has a larger internal resistance.

4.2.4 Magnetic core selection

The magnetic core should be selected according to energetic and thermal considerations [106, 107]. The objective is to estimate the maximum energy that can be stored in an inductance without exceeding the following limits:

- **The maximum magnetic flux density**: The value of $B^{\max}$ should be set according to the operating area in figure 4.3 which is deemed suitable for the considered application.
- **The maximum current density**: Over $J^{\max}$, the electric energy dissipation by heat is too important, which makes the wire insulation melt and thus ruins the component characteristics.

A convenient way to design the inductor is to make both magnetic flux and current density limits occur for the same electrical current. In other words, we suppose that

$$I_L^{\max} = k_f S_w J^{\max} \qquad \text{and} \qquad \phi^{\max} = B^{\max} A_e = A_L N I_L^{\max}, \tag{4.13}$$

where k_f is the form factor of the electrical current waveform. Hence k_f is equal to the ratio of the signal amplitude $I_L^{\max}$ over its root mean square value. Besides, the magnetic cores have a predefined volume, and so have a capped filling space. As can be seen in figure 4.2b for a Rectangular Modular (RM)

core, the winding surface A_w is filled with cylindrical wires, which generates unoccupied space in the end. Moreover, some space is occupied by the insulation layer of the windings. The filling factor k_u is a convenient indicator about the difficulty to produce a component:

$$k_u = \frac{NS_w}{A_w}. \tag{4.14}$$

A value of k_u superior to 60 % usually indicates that the component is difficult to wind without very well organized winding turns, while having k_u inferior to 30 % corresponds to a barely filled, and as a consequence probably oversized component.

We recall that an inductive component can store a certain amount of energy E_L:

$$E_L = \frac{1}{2} L i_L^2. \tag{4.15}$$

Thus combining equations (4.13), (4.14) and (4.15) results in the expression of the maximum energy $E_L^{\max}$ that the produced inductor can store:

$$E_L^{\max} = \frac{1}{2} k_u k_f \, A_e A_w \, J^{\max} B^{\max}. \tag{4.16}$$

This expression means that for a given application, once $J^{\max}$ and $B^{\max}$ are set, and supposing a standard filling factor, then the energy $E_L^{\max}$ is proportional the area product $A_e A_w$. In other words, the area product is the first quantity to compute to restrain the choices among the available core geometries.

As opposed to what has been written in many articles about resonant shunt damping, for which optimized inductors usually require large inductance and small resistance values, high inductance values are not synonymous with large components. Indeed, passive inductors meeting these requirements can be made following the method described in [3]. Furthermore, the equation (4.16) shows that, for a given application, the size of the component is related to the amount of energy it should store. Therefore, the estimation of $E_L^{\max}$ is critical to adequately design electrical components. Computing the air gap δ and the number of turns N of conductive wire to meet the requirements on the inductance L value and on its series-resistance R_{sL} is made in a second phase.

Range of stored electrical energy for commercially available ferrite cores

We consider standard values of magnetic flux density, current density for copper, filling factor and form factor:

- $B^{\max} = 0.3$ T
- $k_u = 60$ %
- $J^{\max} = 5$ A/mm^2
- $k_f = \sqrt{2}$

In this case, the energy $E_L^{\max}$ stored in an inductor ranges from a few hundreds of microjoules to a few tens of millijoules for most of the ferrite cores which are commercially available [107].

4.2.5 Application to the plate electrical analogue

When the plate electrical analogue was first designed, the electrical energy to be stored in the inductors had not been estimated, since the excitation amplitude had not been set. Hence the 42 desired inductors of the network studied in section 4.4 have been designed so that they:

- **Exhibit an inductance L of 246.6 mH**: The inductance value of the unit cell in figure 4.13a should meet the frequency coherence condition that is derived in subsection 2.7.1. Therefore, the other quantities involved in the equation (2.56) should be estimated beforehand. This process is detailed in section 4.5, and leads to an inductance value of 246.6 mH.
- **Exhibit a series resistance R_{sL} inferior to 30 Ω**: The estimation of this value is explained in the aside at the end of the ongoing subsection.
- **Include an air gap in the magnetic circuit**: We want to limit the variations with environmental parameters of the produced inductance. This is made to ensure that the measurements are as independent as possible from the amplitude of the electrical currents flowing in the network. Consequently, we consider magnetic core geometries involving an air gap, as represented in figure 4.2.
- **Permit the use of an adjustable screw**: To prevent the uncertainties on both the modeling process and on the inductors production, we have decided to use adjustable components. The adjusting screw can be seen from above the realized components, in figure 4.4.
- **Exhibit a filling factor k_u between 30 % and 60 %**: This criterion ensures that the inductors are realizable and not oversized.

Core geometry	l_e (mm)	l_w (mm)	A_e (mm^2)	A_w (mm^2)	A_L (nH)	N (turns)	d_w (μm)	k_u (%)	R_{sL} (Ω)
P 22×13	31.6	44	63	23.4	630	625	150	47	26
RM 8	35.1	42	52	29.2	630	625	150	38	25
P 26×16	37.2	52	93	32	800	555	200	55	15
RM 10	42	52	83	40.2	630	625	200	49	17
P 30×19	45	60	136	48	630	625	200	41	20
					1000	500	200	33	16
P 36×22	52	73	202	63	630	625	200	31	24
					1000	500	200	25	20

Table 4.2: Ferrite core specifications and forecast component characteristics made in N48 ferrite material [108], sorted from the smallest area product A_eA_w to the largest one.

According to the previous criteria, several cores are selected and are recorded in table 4.2. Several wire diameters are sometimes suitable. For example, a P 26×16 core geometry component made with a magnetic circuit of permeance 800 nH could be produced with either a wire diameter d_w of 150 μm or of 200 μm. In this situation, only the best component in terms of low series resistance R_{sL} and filling factor k_u close to 60 % is recorded. Two families of magnetic cores remain among the restrained list in table 4.2: the Rectangular Modular (RM) and Pot (P) cores. The distinction between these two families is that most P cores exhibit larger area products A_eA_w than RM cores. In other words, the P cores are more suited for power electronics than RM cores. Comparing the potential components shows that the one made using the P 26×16 core exhibits the lowest R_{sL} value. However, only RM cores were commercially available when the plate analogue was being designed. The choice was thus made to use RM 10 cores, since it leads to inductors with lower series resistances and higher filling factors.

Energetic validation of the produced inductors

As said above, energetic criteria were not taken into consideration when designing the network inductors. However, once a predictive model of the coupled system is available, it is possible to check if the inductors are well designed for a given excitation. Not to disrupt the flow of the present chapter, an example of such verification is conducted in appendix C.

Figure 4.4: Produced fully passive N48-ferrite based inductor with a RM 10 core geometry.

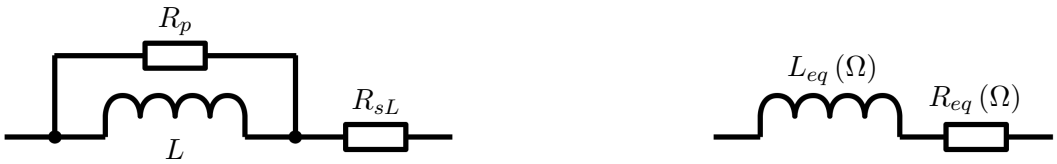

(a) (b)

Figure 4.5: (a) Electrical model of a resistive inductor including magnetic losses and (b) equivalent series representation with frequency-dependent lumped elements.

Finally the 42 inductors of the network are made by winding 610 turns of 200 μm thick copper wire around a RM 10 core of N48 ferrite material, whose nominal permeance is 630 nH. Some turns are taken out from the forecast value of 625 turns in table 4.2, so that the interval over which the inductance can be tuned thanks to an adjusting screw is not limited at one end to the prescribed value of 246.6 mH. In fact, the produced inductance can be set from 240 mH to 270 mH. Besides, while the series resistance was predicted at 17 Ω in table 4.2, it is measured at 13.7 Ω in the end. Once winded, the components look like in figure 4.4.

A realistic electrical model for the produced inductor is sketched in figure 4.5a. It involves an inductance and a series resistance which models copper losses, but also a parallel resistance that models the magnetic losses. We measure these elements thanks to a LCR-meter, however the device identifies the model which is sketched in figure 4.5b. The equivalence between the two models is that

$$L_{eq}\,(\Omega) = \frac{L}{1+\left(\frac{L\Omega}{R_p}\right)^2} \qquad \text{and} \qquad R_{eq}\,(\Omega) = R_{sL} + \frac{R_p}{1+\left(\frac{R_p}{L\Omega}\right)^2}. \tag{4.17}$$

The characteristics of several inductors among the 42 produced are measured. The measurements have been made with a nearly fully engaged adjusting screw, which means that the effective relative permeability μ_e is maximum. According to the equation (4.12), the variations of the component with

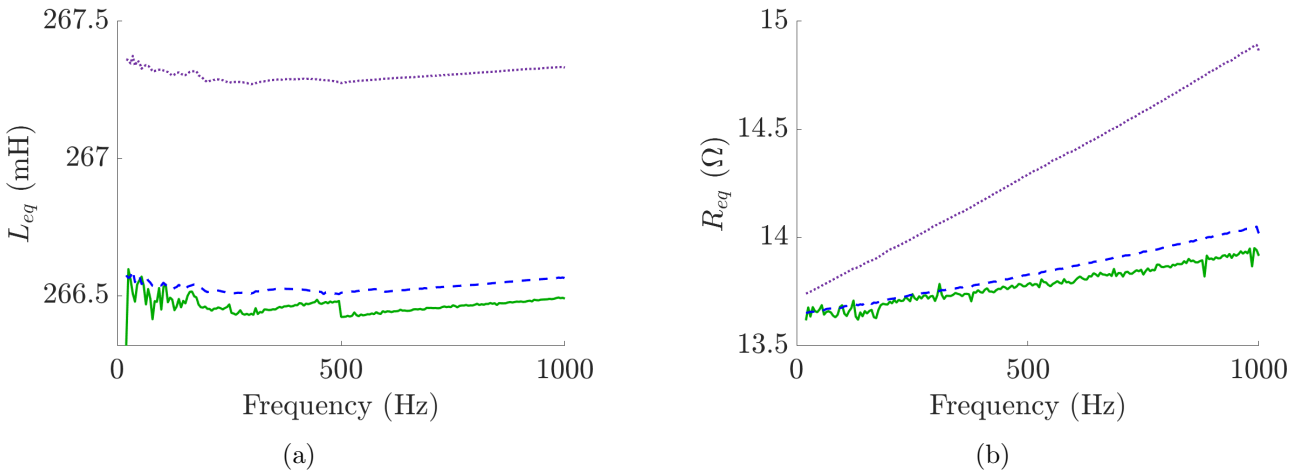

Figure 4.6: Evolution with frequency of (a) the equivalent series inductance L_{eq} and (b) the equivalent series resistance R_{eq} of a produced inductor for an electrical current of —— 10 μA, - - - - 100 μA or ····· 1 mA.

external parameters, such as electrical current and frequency, are thus maximized. The measurements for one inductor are plotted in figure 4.6. The influence of the frequency on the inductor characteristics is consistent with the models in equations (4.17). While this influence can be noticed, note that the electrical behavior of the inductor barely depends on the frequency and on the electrical current, which can be attributed to the air gap and to the relatively low permeance value of the magnetic circuit.

Then, the circuit parameters in figure 4.5a have been fitted with the curves at 10 μA by a least squares method. The identified parameters are $L = 266.6$ mH, $R_{sL} = 13.7\ \Omega$ and $R_p = 8.12\ \text{M}\Omega$. Over the frequency range of interest, the parallel resistance R_p is so much larger than the impedance $2\pi fL$ that it has no influence on the inductor behavior. Consequently, the magnetic losses in the network components can be neglected, and the model sketched in figure 4.5b with frequency-independent lumped elements is deemed adequate going forward.

Series inductor model

The inductor model we have identified is adequate for frequencies under 1 kHz and for electrical currents under 1 mA. In this case, the model consists in:

- Modeling the copper losses by a constant series resistance R_{sL} of 13.7 Ω.
- Modeling the inductive behavior by a constant inductance L, whose value can be tuned from 240 mH to 270 mH.

Presizing of the series resistance of inductors for vibration damping purposes

The series resistance of inductors has the most influence at low frequencies, because the inductor quality factor $L\Omega/R_{sL}$ increases with frequency. Hence the first plate mode has been targeted in terms of damping optimization. The objective is to estimate the value of R_{sL}^{opt} over which the system is overdamped and the infinite norm H_∞ of the system response increases. This phenomenon is illustrated in figure 1.4. We assume that the dissipative elements in transformers are known at this point.

As the coupled electromechanical model developed in section 3.4 had not been validated when designing the plate electrical analogue, the electromechanical model in [72, 85] has first been used to estimate R_{sL}^{opt}. This model is not precisely described in this manuscript, but we recall that it is based on the coupling between a finite difference model of a plate and an electrical network. It has been validated on a setup of piezoelectric network damping of a fully-clamped rectangular plate. A numerical optimization has thus shown that the internal series resistance of the inductors should verify $R_{sL} < R_{sL}^{opt} \approx 30\ \Omega$. Once it is validated in section 4.5, the coupled model we developed in the previous chapter predicts that $R_{sL}^{opt} \approx 30\ \Omega$ as well.

4.3 Transformers design

4.3.1 Laws of magnetic circuits

The electrical analogues of the library in section 2.10 that model bending vibrations include transformers, in the form of lever arm analogues. Transformers usually are the bulkiest components in electrical engineering, therefore their design are of prime importance, which is the topic of the ongoing section. The process is not as detailed as for inductors. Indeed, even though the objectives are different, the rules are mostly similar in the two cases.

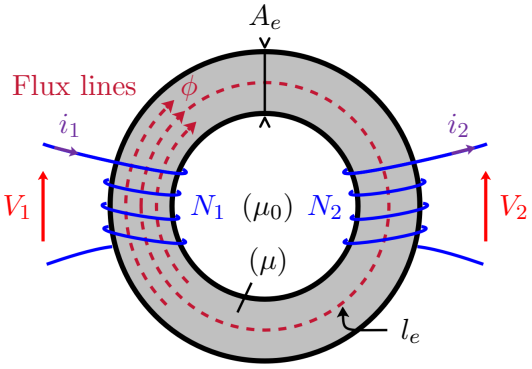

Figure 4.7: Toroidal magnetic circuit with two windings.

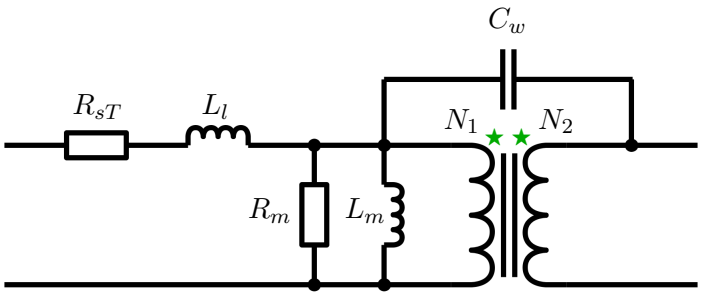

Figure 4.8: Electrical model of a non-ideal transformer at low frequencies.

Transformers can be produced by making several windings around a single magnetic circuit. To demonstrate this, consider the magnetic circuit of figure 4.7 around which two coils of N_1 and N_2 turns are winded. Hopkinson's law, which is recorded in table 4.1, relates the total electrical currents circulating around the magnetic circuit to the magnetic flux ϕ:

$$N_1 i_1 - N_2 i_2 = \mathfrak{R}\,\phi \qquad \text{with } \mathfrak{R} = \frac{l_e}{\mu A_e}. \tag{4.18}$$

Moreover, Faraday's law of induction allows relating the voltages V_1 at the primary side and V_2 at the secondary side to the time-variation of the magnetic flux:

$$\frac{d\phi}{dt} = \frac{V_1}{N_1} = \frac{V_2}{N_2}. \tag{4.19}$$

Assuming the circuit permeability μ is infinite, which is equivalent to set the magnetic reluctance $\mathfrak{R}$ at zero, the two previous equations lead to the constitutive equations of an ideal transformer of ratio $\hat{a}$:

$$\hat{a} = \frac{N_1}{N_2} = \frac{i_2}{i_1} = \frac{V_1}{V_2}. \tag{4.20}$$

4.3.2 Transformers production

While transformers are represented in their ideal form in the derived electrical analogues, the implementation of electrical networks requires to take their imperfections into account. Several models of non-ideal transformers exist, and adequately describe their electrical behaviors depending on the circumstances [101, 109]. The model we have chosen for low frequency applications is sketched in figure 4.8. All the imperfections are referred to the primary side, and include:

- **The leakage inductance** L_l, which stems from the magnetic circuit permeability μ not being infinite. Hence there are flux lines leaking outside of the component. In other words, the two sides of the transformers are imperfectly coupled. This parasitic inductance is mainly affected by the magnetic circuit geometry and by the quality and relative positions of the windings.

- **The magnetizing inductance** L_m, which also results from the circuit permeability μ not being infinite. Indeed, generating a flux in the magnetic circuit requires a non-zero electrical current, as can be understood from equation (4.18) when $\mathfrak{R} \neq 0$. This expresses that some of the electrical current flowing to the primary side of the transformer helps creating the magnetic flux. Thus part of the incoming energy at the primary is not transferred to the secondary.

- **The series resistance** R_{sT}, which models the copper losses in the windings.

- **The core-loss resistance** R_m, which represents the iron losses in the magnetic circuit. Theses losses are due on one hand to variable flux generating eddy currents, which then induce dissipation by heat in the magnetic material. On the other hand, the magnetic losses are due to hysteretic losses that are induced by the reversal of the magnetic flux in the transformer.

- **The winding-to-winding capacitance** C_w, which stems from the electrostatic interaction between the primary and the secondary windings.

These imperfections should be modeled and forecast, to ensure the produced transformers exhibit the desired behavior. If not, they might alter the dynamic behavior of the circuit in which they are integrated, which might then deteriorate the damping performance in the case of a piezoelectric network damping application.

However, several parasitic components in figure 4.8 are quite difficult to foresee. In particular, estimating the winding-to-winding capacitance C_w requires a fine modeling of the electrostatic interaction between windings. Besides, a lumped element does not fully describe the components physics, since the capacitance is distributed along the windings. Moreover, the core-loss resistance R_m is greatly dependent on the frequency and on the flux density in the magnetic circuit. Predicting its value requires advanced electromagnetic modeling tools we have not developed. As a consequence, we proceed to the transformer design by neglecting R_m. Designing transformers for piezoelectric network damping by taking these imperfections into account might be a topic for future works. Nonetheless,

using ungapped toroidal magnetic circuits with high permeability allows minimizing the inductance L_l, while adding an insulation layer between the primary and secondary windings allows minimizing the capacitance C_w. Therefore, we mainly concentrate on designing the magnetizing inductance L_m as well as the windings resistance R_{sT}.

We denote A_L the permeance of the magnetic circuit, which is proportional to the circuit permeability μ. In a non-ideal magnetic circuit, μ is not infinite. This causes A_L, and hence the magnetizing inductance L_m to have finite values as well. Indeed, the expression of L_m is

$$L_m = A_L N_1^2. \tag{4.21}$$

L_m represents the ability of the magnetic circuit to store part of the incident energy in magnetic form, rather than completely transferring it from winding to winding. The goal is for the magnetic circuit to exhibit a large value of μ, which is another reason why we consider ungapped magnetic circuits. Meanwhile, the series resistance referred to the primary side of the transformer is expressed by

$$R_{sT} = \varrho \left[\frac{N_1 l_{w1}}{S_{w1}} + \hat{a}^2 \, \frac{N_2 l_{w2}}{S_{w2}} \right], \tag{4.22}$$

with similar notations to those of equation (4.11), and with the subscripts 1 and 2 referring to the primary and secondary windings, respectively. The design should consequently involve maximizing L_m while keeping R_{sT} under a predefined value.

4.3.3 Magnetic core selection

As for inductors, the design of magnetic circuits for transformers is based on energetic and thermal considerations [106, 107]. However, the criteria are different from those for inductors. Indeed, an ideal transformer does not store energy, but rather transfer it from the primary to the secondary without loss. Therefore, the magnetic circuit should be selected without exceeding:

- **The maximum acceptable magnetic flux density**: In this case as well, the maximum value of flux density should be set to avoid the partial saturation of the ferromagnetic material.
- **The maximum current density**: Over this value, the electric energy dissipation by heat in the windings is too important, which makes the windings insulation layers melt. The component function would thus be ruined.

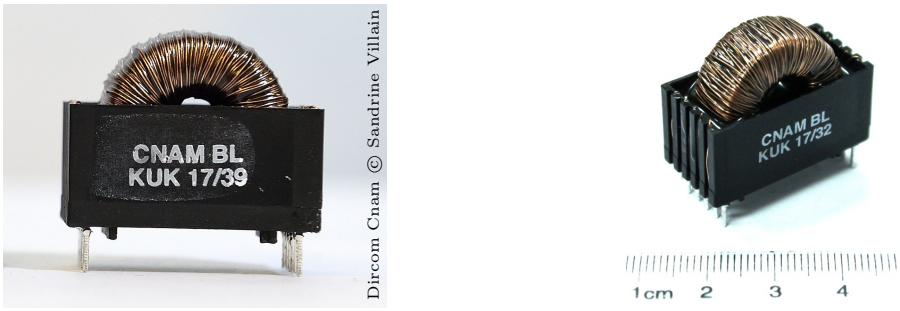

Figure 4.9: Produced nanocrystalline toroidal transformer, whose ratio can be set at 1:1, 2:1 or 4:1.

Finally, the magnetic core selection is restrained by a filling factor k_u whose definition is similar to the filling factor of inductors, expressed by the equation (4.14). It depends on the geometry of the core, the number of turns and the relative positions of windings. Ensuring electrical insulation between windings often results in filling factors between 20 % and 30 %, which is lower than the standard attainable values for inductors [107].

4.3.4 Application to the plate electrical analogue

In the case of piezoelectric network damping, a convenient criterion to ensure that the magnetizing inductance L_m has little to no influence on the network behavior is to tune it according to the local network parameters. All unit cells of the library in section 2.10 that involve transformers also involve at least one inductor of inductance L. We thus suggest to set L_m sufficiently large when compared to L:

$$L_m \geq 50\,\hat{a}^2 L. \tag{4.23}$$

Since the value of L is fixed to meet the frequency coherence condition, it cannot be modified to fit this last inequality. Thus, according to the equation (4.21), one solution to increase L_m is to wind enough turns of conductive wire around the magnetic circuit. However, the same compromise as for the inductors design in section 4.2 applies: for a transformer of ratio $\hat{a}$, increasing N_1 to make L_m bigger also makes the series resistance R_{sT} greater, according to its expression in equation (4.22). This means that the transformer design process can be regarded as trading off some frequency independence of the component for less dissipation. We recall that the final objective in case of a vibration damping application is to avoid overdamping the system, and as a consequence to limit the electrical damping at first.

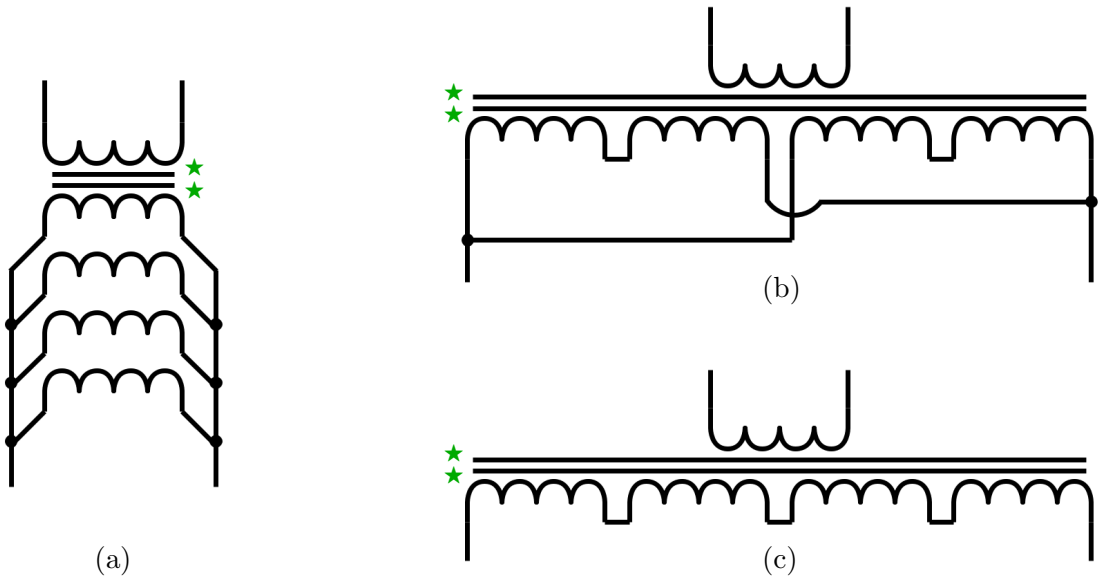

Figure 4.10: Electrical connections of a multi-windings transformer to exhibit (a) a 1:1 ratio, (b) a 2:1 ratio or (c) a 4:1 ratio.

Another solution to meet the requirement of equation (4.23) while limiting the copper losses is to use magnetic cores with a very high permeability μ. This can be done by considering ungapped toroidal circuits made of nanocrystalline material. While this solution is more expensive and the winding requires specific automation, it should lead to the most adequate components in our situation.

For these reasons, we choose to use ungapped nanocrystalline toroidal transformers. The production has been delegated to an external company. The resulting component is pictured in figure 4.9. Without windings, the magnetic circuit has an external radius of 20 mm, an internal radius of 12.5 mm and a thickness of 8 mm. The nanocrystalline material is VITROPERM 500F from VAC. The nominal core permeance at low amplitudes and at 10 kHz is 57 μH. Note that the components have four windings at the primary side, and one winding at the secondary side. All windings have equal number of turns. Therefore, the transformer ratio can be set at 1:1, 2:1 or 4:1 depending on the primary connections. The possible connections are sketched in figure 4.10. This is convenient, as the same nominal transformer can be used for all network transformers.

As all specifications were not available, the transformers have been experimentally characterized. An LCR-meter is used to conduct measurements, as it allows identifying classical electrical component models over given ranges of frequency or electrical current amplitude. The tests are conducted as follows:

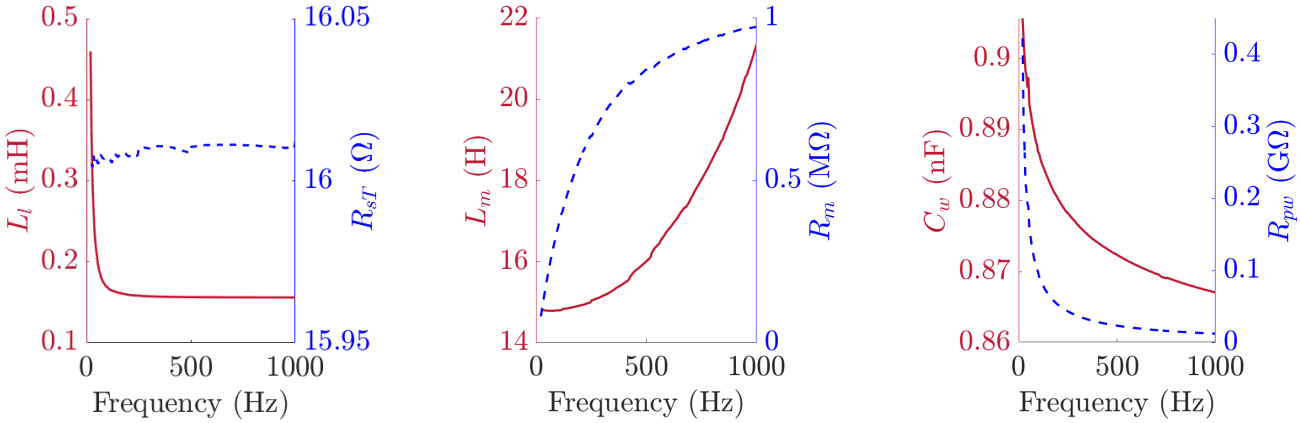

Figure 4.11: Evolution with frequency of (a) —— L_l (mH) and - - - - R_{sT} (Ω) for an electrical current set at 1 mA, of (b) —— L_m (H) and - - - - R_m (MΩ) for an electrical current set at 10 μA, and of (c) —— C_w (nF) and - - - - R_{pw} (GΩ) for a voltage difference set at 500 mV.

- **First test**: The measurement is made at the primary side, while the secondary side is short-circuited. The identified model is a series circuit composed of an inductance and a resistance. By neglecting the capacitance C_w, this allows estimating the values of L_l and R_{sT}.

  The resulting estimations are plotted in figure 4.11a. They show that the leakage inductance L_l is negligible when compared to the other inductances of the network. Meanwhile, the resistance modeling copper losses is almost independent from frequency, which was expected.

  As a side note: The norm of the impedance $R_{sT} + \mathrm{j}L_l\Omega$ is close to 16 Ω even at 1 kHz. To ensure a fine signal-to-noise ratio measurement with a LCR-meter whose upper voltage limit is 2 V, an electrical current of 1 mA is used. This current amplitude is not representative to our application: the amplitude of the network currents during vibration tests is of several μA. Nonetheless, if the value L_l is negligible at high levels of electrical current, it is also negligible at low levels because the magnetic core is further from its saturation state in this case. Therefore, the measurement in figure 4.11a permits neglecting the leakage inductance in any situation.

- **Second test**: The measurement is made at the primary side, while the secondary side is left in open circuit. The identified model is a parallel circuit composed of an inductance and a resistance. By neglecting the capacitance C_w and the series circuit composed of L_l and R_{sT}, whose impedance is negligible when compared to the impedance of the parallel circuit composed of R_m and L_m, this allows estimating the magnetizing inductance and the core-loss resistance.

The results are plotted in figure 4.11b. In this case, the impedance is large enough so that the testing electrical current can be set at a representative value of 10 μA. Both L_m and R_m are frequency-dependent, which was expected [101]. Besides, the impedance $L_m\Omega$ is fifty times larger than R_m at low frequencies, and nearly ten times larger at 1 kHz. Because of this impedance ratio, R_m will be neglected going forward.

- **Third test**: Both transformer sides are short-circuited. Measuring then the impedance between the two sides gives a direct information about the winding capacitance C_w. The LCR-meter allows identifying the parallel circuit composed of the capacitance C_w and a resistance R_{pw}.

  The results are plotted in figure 4.11c. The excitation voltage difference is set at 500 mV, which allows simulating a representative electrical current of around 1 μA in the component. The value of C_w is nearly constant over the considered frequency range, and is small when compared to piezoelectric capacitance measurements conducted on the plate covered by piezoelectric transducers. In the meantime, R_{pw} is virtually infinite. This is consistent with the required electrical insulation between the two transformer sides.

Models of transformer with a 1:1 ratio

Depending on the frequency range of interest and the required accuracy, the transformer model in figure 4.8 can be simplified. A first approximation of the transformer behavior consists in:

- Modeling the copper losses by a series resistance of 31 Ω for each of the four windings at the primary side, and by a series resistance of 9 Ω for the secondary side winding.
- Neglecting the leakage inductance L_l, the core-loss resistance R_m, the magnetizing inductance L_m and the winding capacitance C_w.

Besides, a second order model of the transformer consists in:

- Modeling the copper losses by a series resistance of 31 Ω for each of the four windings at the primary side, and by a series resistance of 9 Ω for the secondary side winding.
- Modeling the magnetizing inductance L_m by a constant value of 16 H.
- Modeling the winding capacitance C_w by a constant value of 0.9 nF.
- Neglecting the leakage inductance L_l and the core-loss resistance R_m.

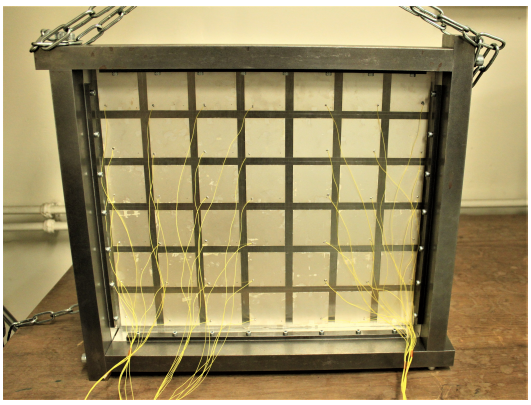

(a)

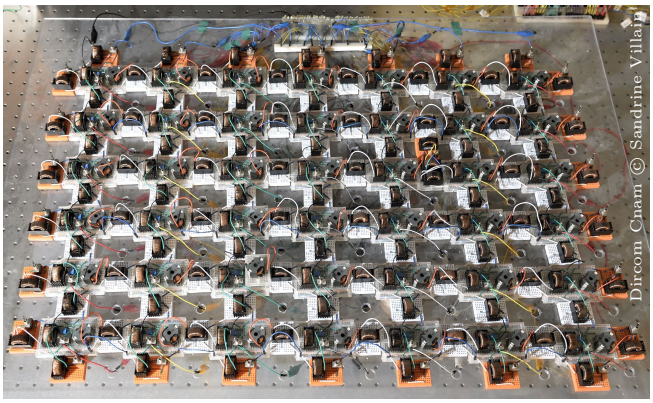

(b)

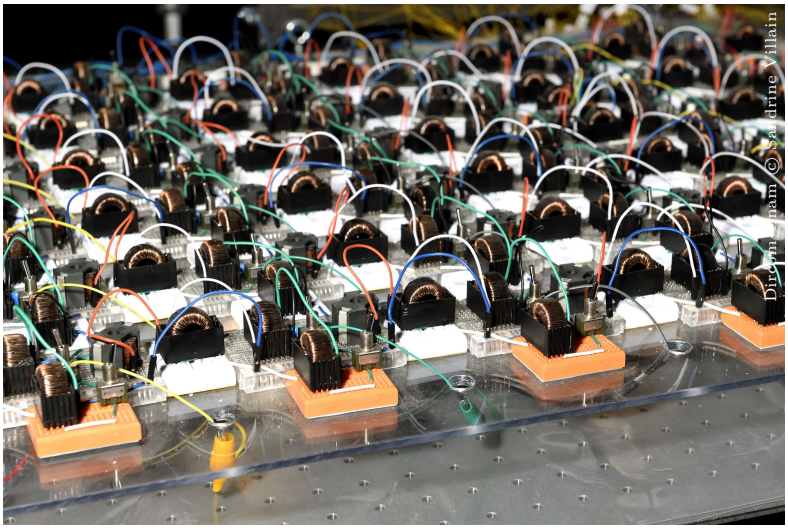

(c)

Figure 4.12: (a) Plate covered with 42 piezoelectric patches and (b) its assembled analogous electrical network made of 42 unit cells. (c) Closeup view, with boundary cells in the foreground.

4.4 Network model and validation

4.4.1 Network description

The objective is to develop the electrical analogue of a simply-supported duralumin plate of dimensions $l_x = 420$ mm, $l_y = 360$ mm and $h_s = 3$ mm. Among the available elements of the library in section 2.10, we select the square plate unit cell to form the electrical network. As a consequence, the plate should be discretized along the x and y directions by respectively $7n_0$ and $6n_0$ elements, n_0 being integer. The choice is to use $n_0 = 1$ because of the significant number of electrical components already

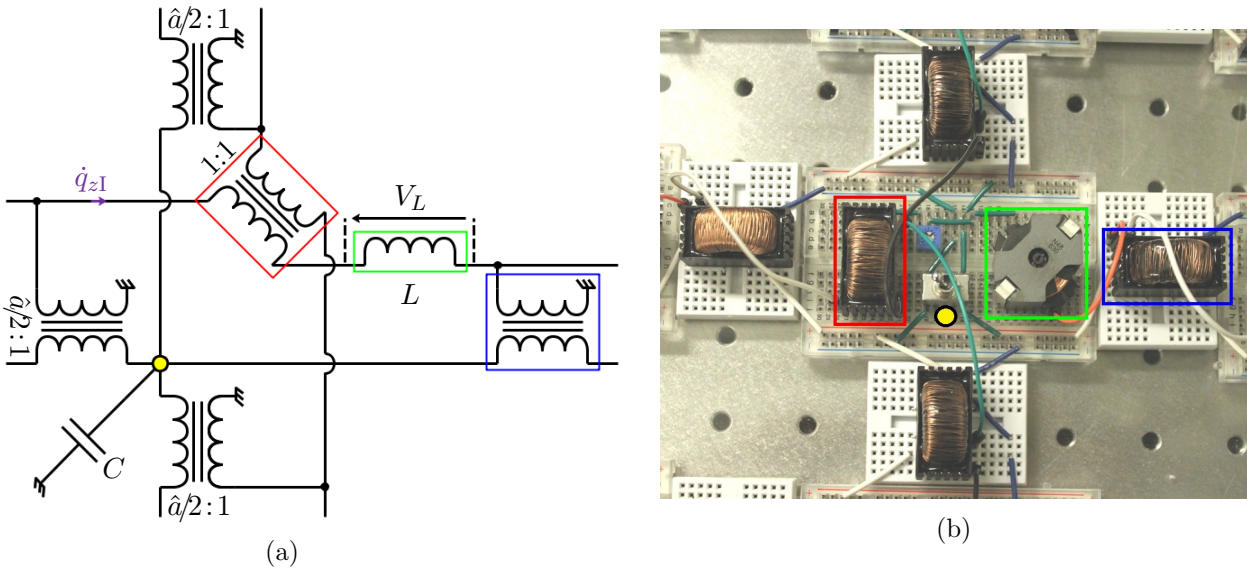

(a) (b)

Figure 4.13: (a) Scheme and (b) picture of the electrical analogue of a square plate, which highlight the central transformer in red, a side transformer in blue, the inductance in green, and the capacitance connection in yellow.

required to produce the plate analogue with this minimal discretization scheme. This justifies that 42 piezoelectric patches have been periodically bonded on one side of the plate. The structure and the bonding process have been described in subsection 3.3.1.

Hence, a network made of 42 identical unit cells has been assembled. It is obtained by assembling the square plate electrical analogous unit cell along the x and y directions. According to the spatial coherence condition expressed by equation (2.6), the resulting analogue should correctly replicate plate modes which exhibit one wavelength or less. The number of unit cells being already higher than in the previous experimental setup in [72] should lead to a wider frequency band upon which the analogy is validated. The structure and its analogous network are pictured in figures 4.12a and 4.12b, respectively. A closer look at a unit cell is shown in figure 4.13b. It can be compared to the unit cell circuit in figure 4.13a, which has been exhibited in section 2.7 as well.

The inductors and transformers of the network are the ones designed and characterized in sections 4.2 and 4.3, respectively. The network testing is made with a nominal inductance for all unit cells of $L = 244$ mH. The central transformers have a 1:1 ratio. Besides, as explained in the aside of subsection 2.8.2, the two transformers of ratio $\hat{a}/2$:1 linking two adjacent cells can be combined into one transformer of ratio $\hat{a}$:1. Combining transformers this way allows limiting the number of

components in the network. Finally, the ratio of the transformers located at the network boundaries is maintained at $\hat{a}$/2:1. All corresponding cable connections are sketched in figure 4.10.

Moreover, the network has been rendered adaptable when possible. Three elements have been added with this in mind and can be seen in figures 4.13b and 4.12c. The first one are toggle switches with three positions, placed next to the capacitances connections. They allow setting the piezoelectric transducers covering the plate to the independent open-circuit condition, connecting them to the network, or connecting them to a common voltage V_G. Then, setting $V_G = 0$ or letting V_G free to evolve leads to the short-circuit and open-circuits conditions, respectively. The other adaptable elements are trimmer resistors, one of which being pictured next to the central transformer in figure 4.13b. The maximum resistance they add in series with the unit cell inductance is 200 Ω. It is one simple way to add local damping in the network. Finally, other toggle switches are integrated in the boundary cells. They allow easily passing from simply-supported to fully clamped analogous boundaries, according to the conditions summed up in table 2.4.

4.4.2 Network model with electrical damping

We recall that an electrical model for the network has been developed in subsection 2.7.1. The principle is to derive an elementary dynamic matrix relating currents and voltages from a unit cell. From there, elementary matrices of "stiffness" $\boldsymbol{K_{elm}}$ and of "mass" $\boldsymbol{M_{elm}}$ are derived by applying the equation (2.13). Assembling them in a similar manner as in the finite element method, we obtained in equation (2.58) the model of the entire network.

However, an accurate model of the network requires to take the components imperfections into account. It has been shown in sections 4.2 and 4.3 that dissipation occurs in the inductors and transformers of the network. A first approximation of the non-ideal network behavior is the circuit represented in figure 4.14. Therefore, it is required to derive an elementary matrix of electrical damping $\boldsymbol{D_{elm}}$. It should depend on R_{sL}, R^c_{sT} and R^s_{sT}, which respectively denote the series resistance of the inductor, of the central transformer of ratio 1:1, and of the side transformers of ratio a/2:1. While the influence of R^c_{sT} and R_{sL} on $\boldsymbol{D_{elm}}$ can be deduced from $\boldsymbol{M_{elm}}$, as explained in the aside of subsection 2.3.6, modeling the influence of the side transformers resistances R^s_{sT} on $\boldsymbol{D_{elm}}$ requires deriving another elementary matrix. Thus we suggest modifying the equation (2.13). If the dynamic matrix $\boldsymbol{D_e}$ can be expressed, then the required elementary matrices can be extracted from it:

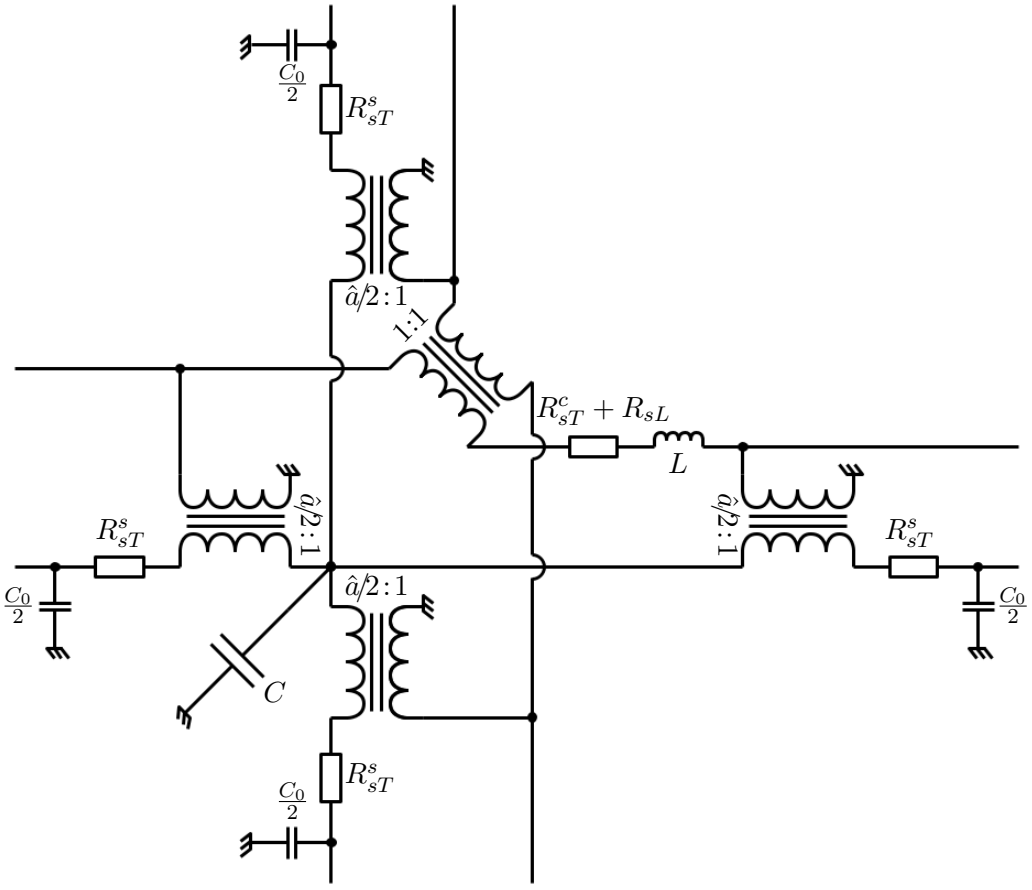

Figure 4.14: Lumped-element model of a unit cell of the assembled network.

$$\boldsymbol{K_{elm}} = \boldsymbol{D_e}|_{\Omega=0}\,, \qquad \boldsymbol{D_{elm}} = \left.\frac{\boldsymbol{D_e} - \boldsymbol{K_{elm}}}{\mathrm{j}\Omega}\right|_{\Omega=0}, \qquad \text{and } \boldsymbol{M_{elm}} = \frac{\boldsymbol{K_{elm}} + \mathrm{j}\Omega\boldsymbol{D_{elm}} - \boldsymbol{D_e}}{\Omega^2}. \quad (4.24)$$

The resulting expression of $\boldsymbol{D_{elm}}$ is given in appendix B.1. Then, assembling these elementary matrices would supplement the equation (2.58) with an assembled electrical damping matrix $\boldsymbol{D_N}$:

$$\boldsymbol{V_N} = \left(\boldsymbol{K_N} + \mathrm{j}\Omega\boldsymbol{D_N} - \Omega^2\boldsymbol{M_N}\right)\boldsymbol{Q_N}. \quad (4.25)$$

4.4.3 Network model validation

Before connecting the network to the plate, we suggest verifying if it behaves as intended. As it should be tested alone, the piezoelectric capacitances cannot be included as the lumped values C in figure 4.14. Thus they are replaced by ceramic capacitors which have a nominal capacitance of 145 nF. In this situation, we propose to validate the network in two manners:

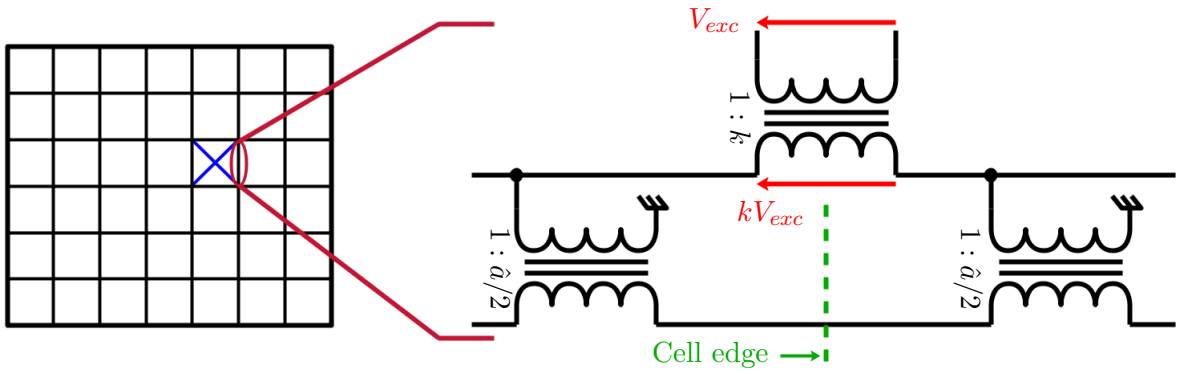

Figure 4.15: Setup of the network excitation through an isolation transformer of ratio k placed between two network unit cells. A marker ⊠ is placed on the location on which the measurements of figures 4.16 and 5.5 are performed.

- **Dynamics validation**: The model should predict the frequency behavior of the network. This is validated by comparing FRFs resulting from experiments and simulations.
- **Modal validation**: The model should exhibit the same mode shapes as the assembled network. This is validated by computing the MAC between measured and simulated current modes.

By analogy with an exciting external force, an external voltage is applied between two unit cells of the network. The voltage V_{exc} is applied through an isolation transformer of ratio k. The corresponding electrical circuit is drawn in figure 4.15. The excitation location, as pointed in the same figure, is chosen so that the first several network modes are excited. At the same time, the voltage drop V_L across each inductor of the network is measured. The numerical FRFs V_L/kV_{exc} obtained using the model of equation (4.25) can thus be compared to measurements.Note that we assume that the network behaves linearly. Therefore we choose to set the excitation as a pseudo-random white noise signal below 2 kHz, which allows estimating the network behavior over the frequency range of interest.

As an example, a comparison is plotted in figure 4.16. The highlighted measured FRF includes resonance peaks and is heavily damped. As explained in the aside of subsection 4.2.5, the dissipative elements of the network have been designed so that the coupling of the network with the plate described in subsection 3.3.1 leads to a slightly underdamped response near the first plate mode. The simulated FRFs are in good agreement with the the measured ones. The remaining differences are gathered at low frequencies. In fact, the antiresonance which is measured at around 25 Hz is owed to the magnetizing branch of the transformers. Indeed, the simulated FRF in the case of a constant

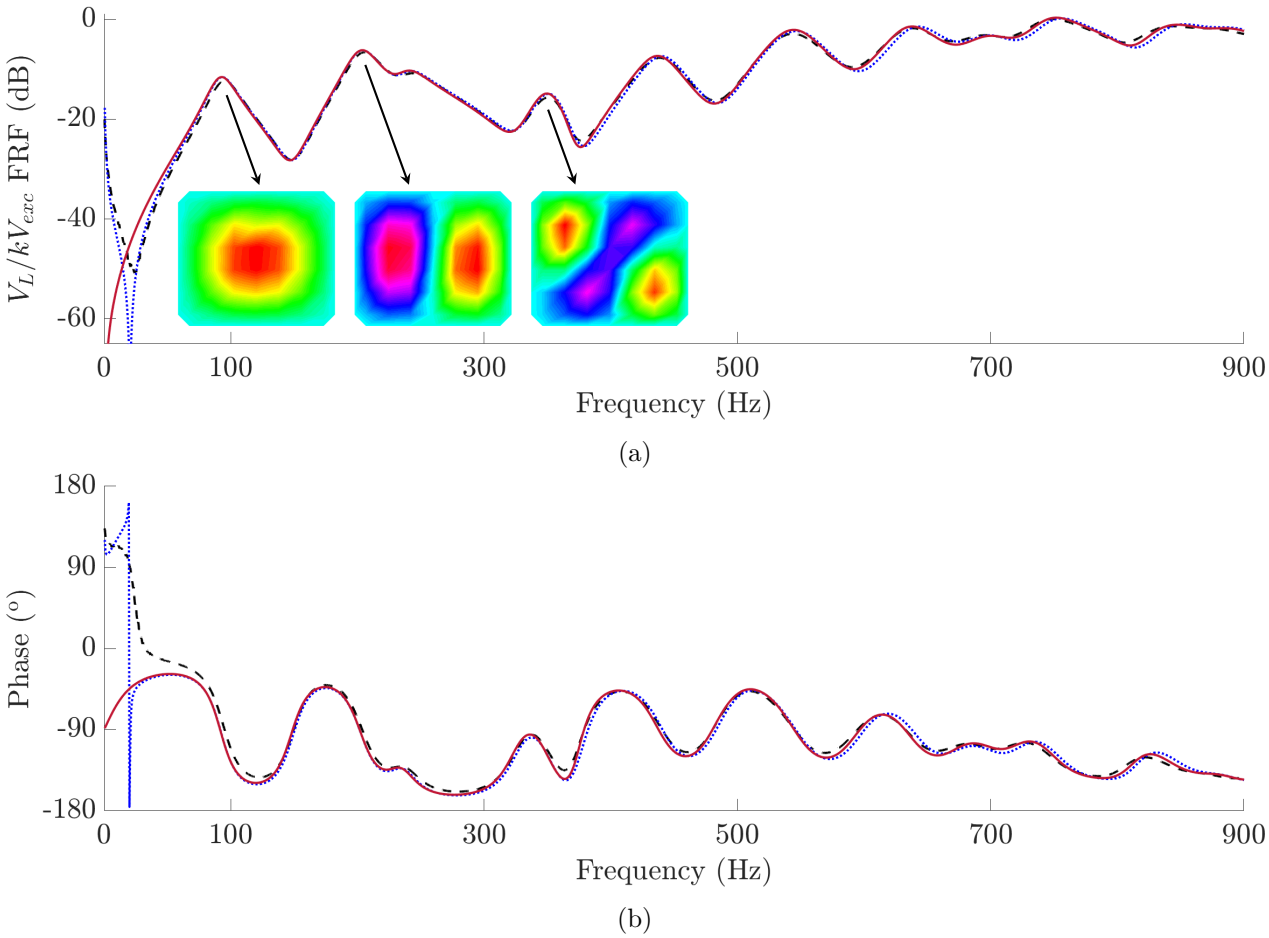

Figure 4.16: (a) Gain and (b) phase of the V_L/kV_{exc} FRF obtained from - - - - measurements, ——— simulations by neglecting the magnetizing branch of transformers, and ····· simulations by considering a constant magnetizing inductance L_m. V_L is measured across the inductor of the unit cell whose location is indicated by a ⊠ marker in figure 4.15. Several operational electrical current shapes at gain peaks are highlighted.

magnetizing inductance L_m is also plotted in figure 4.16. Its effects are to generate an antiresonance at low frequencies and to slightly shift the FRF towards higher frequencies. Though not plotted, we have noticed that this effect is partially compensated when taking the winding capacitance C_w of transformers into account, whose effect near 1 kHz is to shift the FRF to lower frequencies.

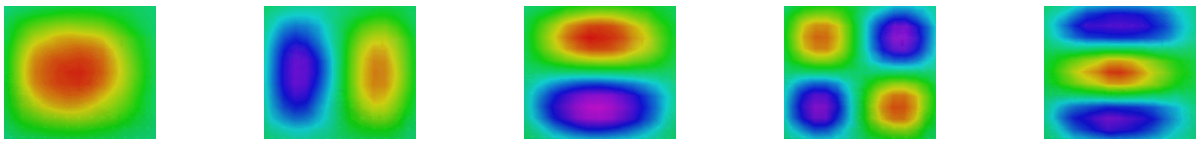

(a) Shape at 102 Hz (b) Shape at 223 Hz (c) Shape at 268 Hz (d) Shape at 389 Hz (e) Shape at 543 Hz

Figure 4.17: Measurement of five operational deflection shapes of the plate.

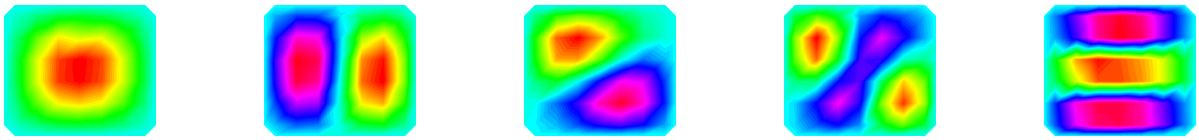

(a) Shape at 101 Hz (b) Shape at 218 Hz (c) Shape at 250 Hz (d) Shape at 376 Hz (e) Shape at 468 Hz

Figure 4.18: Measurement of five operational electrical current shapes of the network.

In the end, slight differences remain between experiments and simulations obtained with the simplest model of non-ideal transformers proposed in section 4.3. These could be reduced by taking other imperfections into account, such as the magnetizing branch and the winding capacitance. However, these refined models are not used later on, because the correlation between the present model and experiments is considered good enough from 50 Hz to 900 Hz.

Besides, we suggest conducting a modal validation of the developed model, by verifying if the model of equation (4.25) generates mode shapes which are consistent with the measured ones. Visualizing the operational electrical current shapes is a first step in doing so. Dividing V_L by the impedance $R_{sL}+\mathrm{j}L\Omega$ leads to the electrical current $\dot{q}_{z\mathrm{I}}$ flowing through each inductor. As a consequence, plotting the shapes of $\dot{q}_{z\mathrm{I}}/kV_{exc}$ is equivalent to plotting the operational deflection shapes of a plate excited by a point load. Several operational deflection shapes of the plate have been measured using a laser vibrometer, and are represented in figure 4.17 for visual comparison with the operational current shapes in figure 4.18. Plotted shapes look alike, even though some are slightly different, such as in figure 4.17c and figure 4.18c. This can be explained by the heavy damping due to resistive components in the electrical network. Hence, operational electrical current shapes may spill over onto each other. It is the case in figure 4.18c, where the measured current distribution looks like a combination of modes (1,2) and (2,1). Anyway, comparing operational shapes offers a first validation of the spatial coherence condition, and exhibits the heavy electrical damping in the network.

An experimental modal analysis of the network is then performed, as suggested in subsection 2.3.7. The experimental mode shapes are extracted using the least-squares rational function estimation method [110]. The first fourteen experimental modes are identified between 50 Hz and 800 Hz, and therefore can be compared to simulated modes in figure 4.20. This MAC matrix shows that experimental and numerical modes are mutually consistent. The only problem is that the eleventh identified mode is a complex mode, whose real part is similar to the eleventh modeled mode, and whose imaginary part is similar to the twelfth modeled mode. This is due to significant and not purely proportional damping in the network. To conduct a complete experimental modal analysis would require refining the extraction of modes as well as the estimation of modal parameters.

In the end, the network model of equation (4.25) is deemed precise enough in terms of modal properties and frequency behavior to be integrated in the coupled model of equation (3.46).

Influence of C_0 capacitors on the network model

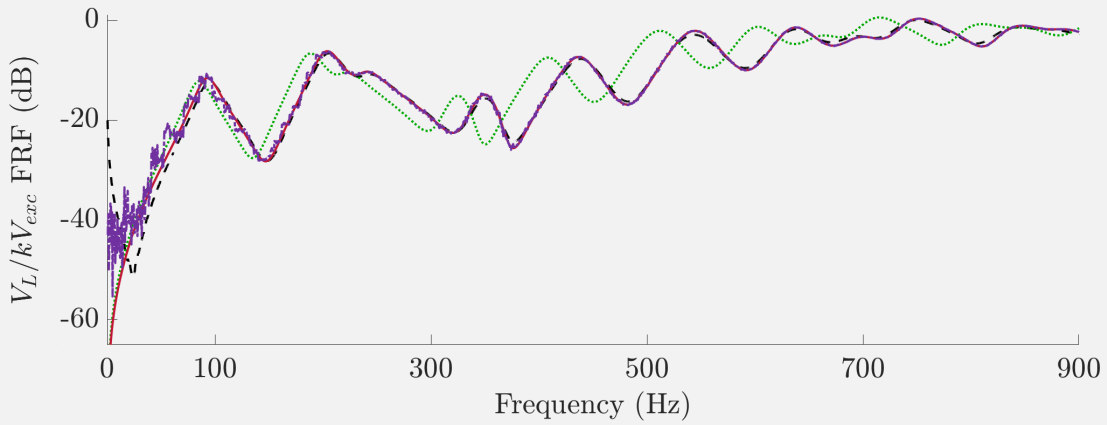

Figure 4.19: Gain of the V_L/kV_{exc} FRF obtained from ---- measurements, and simulations by neglecting the magnetizing branch of transformers with -·-·- $\epsilon = 10^{-13}$, —— $\epsilon = 10^{-6}$ and ····· $\epsilon = 10^{-1}$.

As explained in chapter 2 during the derivation of electrical analogues involving bending phenomena, we suggest connecting additional C_0 capacitors at cells boundaries. The influence of the numerical parameter $\epsilon = C_0/C_\theta$ is illustrated by figure 4.19. If ϵ is too small, then the system is ill-defined and the numerical results are noisy. Then, ϵ has a larger influence on the system dynamics when it becomes closer to 1, since it is equivalent to add electrical compliance between network cells. As previously stated, setting $\epsilon = 10^{-6}$ is a good compromise.

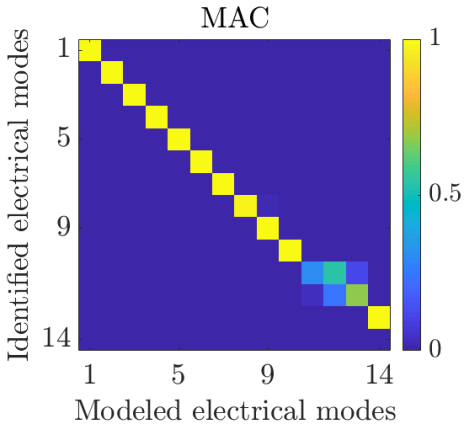

Figure 4.20: MAC matrix between experimental and simulated electrical current modes of the network.

4.5 Broadband damping of a periodic plate

4.5.1 Adapted frequency coherence condition

To ensure identical bending wave propagation in the structure and its analogous network, we recall that the frequency coherence condition derived in subsection 2.7.1 should be met. In the case of the periodic plate covered by piezoelectric patches, the equation (2.56) becomes

$$\frac{1}{a^2}\frac{K_\theta^D}{m} = \frac{1}{\hat{a}^2}\frac{1}{LC^\varepsilon}. \tag{4.26}$$

In this last equation, K_θ^D is the mechanical stiffness when the piezoelectric patches are left in open-circuit. The blocked piezoelectric capacitance C^ε is the capacitance when no bending displacement is allowed. According to the lumped-element electrical model of the piezoelectric coupling [78], such as depicted in figure 4.21, these two quantities can be related to the mechanical stiffness K_θ^E when the piezoelectric patches are short-circuited and to the static piezoelectric capacitance C_{st}:

$$K_\theta^D = K_\theta^E + \frac{e_\theta^2}{C^\varepsilon}, \qquad C_{st} = C^\varepsilon + \frac{e_\theta^2}{K_\theta^E}, \tag{4.27}$$

with e_θ being the coupling coefficient. From the two previous equations, one obtains

$$\frac{C^\varepsilon}{C_{st}} = \frac{K_\theta^E}{K_\theta^D}. \tag{4.28}$$

On that account, the frequency coherence condition of equation (4.26) can also be written

$$\frac{1}{a^2}\frac{K_\theta^E}{m} = \frac{1}{\hat{a}^2}\frac{1}{LC_{st}}. \tag{4.29}$$

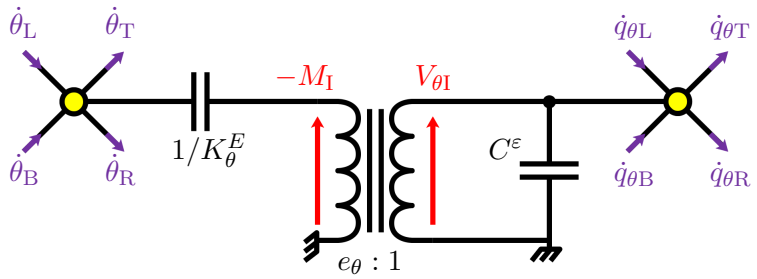

Figure 4.21: Electrical representation of the electromechanical coupling.

The objective is now to tune the electrical components of the network so that the frequency coherence condition is met. The process is the same as in subsection 2.7.2. The side a of the unit cell is fixed once the plate geometry is defined. Moreover, the transformer ratio is set at $\hat{a} = 4$. Thus, all the other parameters involved in the equation (4.29), namely m, K_θ^E and C_{st}, should be estimated before deducing the inductance L, which serves as the tuning parameter:

$$L = \left(\frac{a}{\hat{a}}\right)^2 \frac{m}{K_\theta^E C_{st}}. \tag{4.30}$$

4.5.2 Estimation of the mass

Each unit cell is composed of a square duralumin plate of side a and of thickness h_s, on which a square PIC 153 piezoelectric patch of side l_p and of thickness h_p is bonded. Their respective densities are denoted ρ and ρ_p. Hence, the mass of each unit cell can be computed:

$$m = \rho a^2 h_s + \rho_p l_p^2 h_p. \tag{4.31}$$

4.5.3 Estimation of the bending stiffness

The calculation of the bending stiffness value K_θ^E for a square mechanical plate is based on the model depicted in figure 4.22. It includes a series and parallel combination of discrete rotational springs, so that the bending stiffness $K_{\theta y}^E$ when y is deemed as the normal axis is

$$\frac{1}{K_{\theta y}^E} = \frac{1}{K_{\theta y1}^E} + \frac{1}{K_{\theta y2}^E + K_{\theta y3}^E} + \frac{1}{K_{\theta y4}^E}, \tag{4.32}$$

where $K_{\theta y1}^E$, $K_{\theta y2}^E$ and $K_{\theta y4}^E$ are the stiffnesses of the plate portions indicated in figure 4.22, while $K_{\theta y3}^E$ is the stiffness of the piezoelectric patch. Denoting ν and Y the Poisson's ratio and the Young's

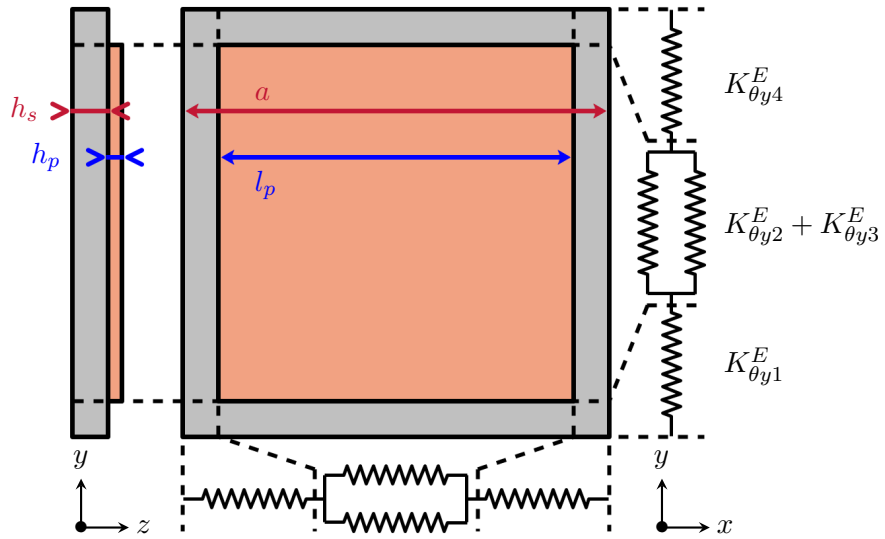

Figure 4.22: Square plate covered by a square piezoelectric patch. The bending stiffness of each portion of the plate and the piezoelectric patch can be modeled as a rotational spring, such as drawn on the right hand-side. The represented thicknesses are not to scale.

modulus of the plate, these stiffnesses values can be computed by the following expressions:

$$\frac{1}{K^E_{\theta y1}} = \frac{1-\nu^2}{Y}\int_0^{(a-l_p)/2} \frac{1}{I(y)}\,dy, \qquad \frac{1}{K^E_{\theta y3}} = \frac{1-\nu_{12}^2}{1/s^E_{11}}\int_{(a-l_p)/2}^{(a+l_p)/2} \frac{1}{I_p(y)}\,dy,$$
$$\frac{1}{K^E_{\theta y2}} = \frac{1-\nu^2}{Y}\int_{(a-l_p)/2}^{(a+l_p)/2} \frac{1}{I(y)}\,dy, \qquad \frac{1}{K^E_{\theta y4}} = \frac{1-\nu^2}{Y}\int_{(a+l_p)/2}^{a} \frac{1}{I(y)}\,dy, \tag{4.33}$$

with I and I_p respectively being the second moments of area of the structure and of the piezoelectric patch. Assuming the piezoelectric patch is thin when compared to the structure, the expressions of I and I_p are computed with respect to the mid-surface of the plate:

$$I(y) = \int_0^a \int_{-h_s/2}^{h_s/2} z^2\,dx\,dz, \qquad I_p(y) = \int_{(a-l_p)/2}^{(a+l_p)/2} \int_{h_s/2}^{h_s/2+h_p} z^2\,dx\,dz. \tag{4.34}$$

Similar equations can be written to estimate the bending stiffness $K^E_{\theta x}$ when x is deemed as the normal axis. In the present case of a square plate being covered by a square piezoelectric transducer, computing the bending stiffness along both in-plane directions gives the same result:

$$K^E_{\theta} = K^E_{\theta x} = K^E_{\theta y}. \tag{4.35}$$

Reference surface for the second moments of area computation

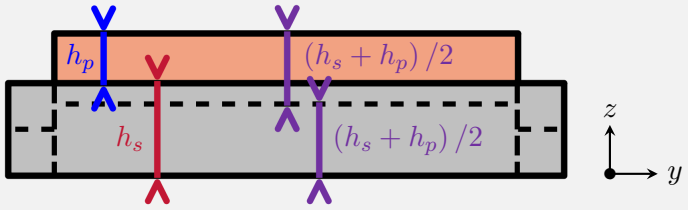

Figure 4.23: 2D sketch of the mid-surface discontinuity of the constant thickness plate partially covered by a constant thickness piezoelectric patch. The represented thicknesses are not to scale.

To compute the expressions of the second moments of area, a reference plane should be fixed. In the actual case, this creates a problem, since the mid-surface of the mechanical unit cell is discontinuous, such as sketched in figure 4.23. The calculation of I and I_p in equations (4.34) is made by using the mid-surface of the plate as the reference, as opposed to what is proposed in [72]:

$$I(y) = \int_0^a \int_{-(h_s+h_p)/2}^{(h_s-h_p)/2} z^2 \, dx \, dz, \qquad I_p(y) = \int_{(a-l_p)/2}^{(a+l_p)/2} \int_{(h_s-h_p)/2}^{(h_s+h_p)/2} z^2 \, dx \, dz. \tag{4.36}$$

For a plate fully covered by a piezoelectric transducer, the equation (4.36) would be more accurate, while the equation (4.34) is convenient for a partially covered plate. In the present situation, the piezoelectric patches cover $l_p^2/a^2 \approx 69$ % of their respective plate portions. Since they are thin, we choose to use the expression of equation (4.34) anyway.

In the end, applying the equations (4.36) rather than the equations (4.34) is a modeling choice, and leads to different identified global values for the unit cell. The differences between the resulting values derived from the two models are recorded in the table 4.3 and are small in this case. Note that a more precise analytical model of piezoelectric beams [111] could also be used to estimate the bending stiffness.

Expressions of I and I_p	K_θ (N.m)	L (mH)
Equations (4.34)	242.9	246.6
Equations (4.36)	241.3	248.2
Difference (%)	0.7	0.7

Table 4.3: Comparison of bending stiffness and inductance values obtained via the two suggested models of second moments of area.

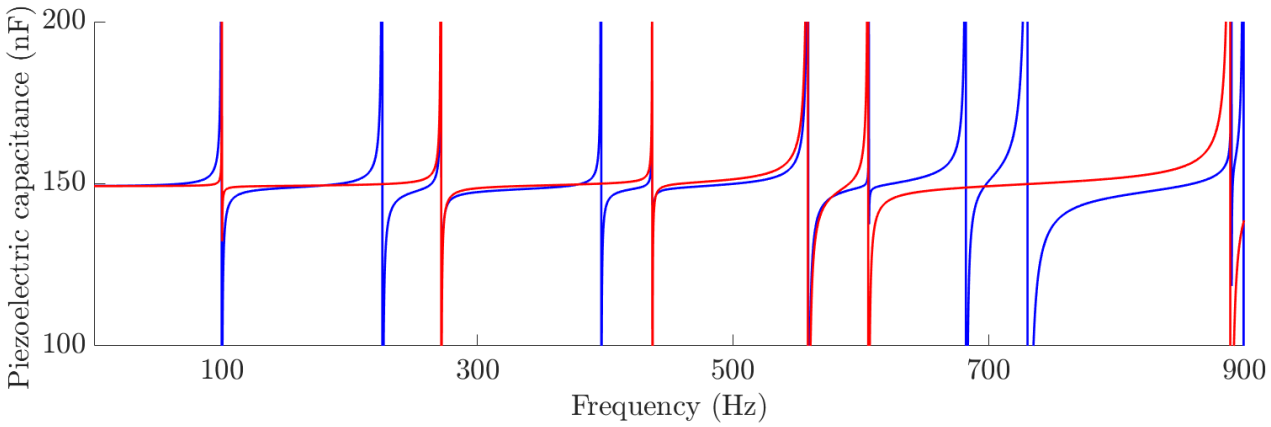

Figure 4.24: Simulated dynamic capacitance for $n_0 = 1$ of two piezoelectric patches covering the plate, whose positions are highlighted in corresponding colors in figure 4.26.

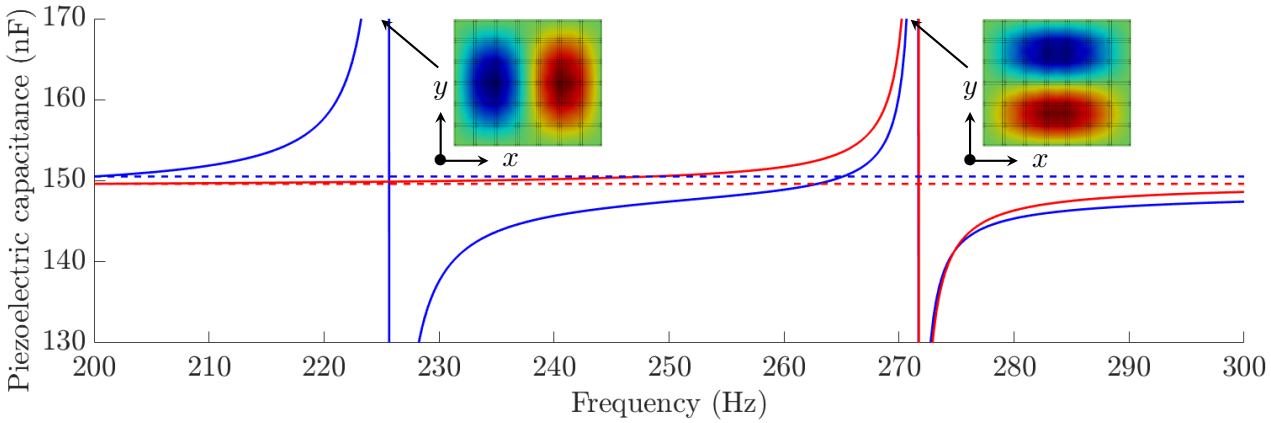

Figure 4.25: Zoom on figure 4.24 around two mechanical resonances. Two short-circuited plate modes are highlighted, on which the piezoelectric patches limits are drawn.

4.5.4 Estimation of the static piezoelectric capacitance

The free piezoelectric capacitance, usually denoted C^{σ}, is the capacitance obtained under zero stress. This value can be estimated by using the relative permittivity ϵ_{33}^{σ} in table 3.3. However, this quantity is notably different from the static capacitance C_{st} that appears in equation (4.29). Indeed, the piezoelectric patches are not entirely free to move since they are bonded to the structure. The static piezoelectric capacitance C_{st} is the capacitance at 0 Hz. To estimate it, we suggest computing the dynamic capacitance $C^{(j)}(\Omega)$:

$$C^{(j)}(\Omega) = \frac{Q^{(j)}}{V^{(j)}}. \tag{4.37}$$

A simulation of $C^{(j)}(\Omega)$ can be obtained by using the finite element formulation of equation (3.28). When considering the j-th piezoelectric patch, $V^{(j)}$ serves as the excitation. Meanwhile, the other patches are left in open-circuit, which means all values in $\boldsymbol{Q}$ are set to 0 except $Q^{(j)}$. This is how the examples of dynamic capacitances are plotted in figures 4.24 and 4.25.

The piezoelectric capacitance is frequency-dependent because of the piezoelectric coupling. This phenomenon has been explained in [33, 84, 34]. Depending on the piezoelectric transducer position, it might generate a strong modal electromechanical coupling factor with some mechanical modes, and none with others [35]. When one crosses a mechanical resonance whose modal coupling factor is non-zero at a piezoelectric transducer position, the corresponding piezoelectric capacitance variations are especially important. This is spotted in figure 4.25: while the mechanical resonance at 271.5 Hz has a significant influence on both considered piezoelectric patches capacitances, only one of them is influenced by the mechanical resonance at 225.5 Hz. This is understandable while comparing the patches positions in figure 4.26 and the mode shapes that illustrate the figure 4.25. Indeed, the electromechanical coupling factor between the piezoelectric patch located near the plate boundary and the second mode plate vanishes for symmetry reasons. Moreover, the constant value to which $C^{(j)}(\Omega)$ seems to converge between resonances in figure 4.24 decreases each time encountering a coupled mechanical resonance. Note that the bigger the modal coupling factor, the bigger the piezoelectric capacitance decrease [34].

Once computed the dynamic capacitance, we propose to estimate the j-th static capacitance C_{st} by the value of $C^{(j)}(\Omega)$ at 0 Hz:

$$C_{st} = C^{(j)}(\Omega)\Big|_{\Omega=0}. \tag{4.38}$$

The resulting C_{st} values distribution for the simply-supported plate produced in subsection 3.3.1 is exhibited in figure 4.26. One can notice the static capacitance values are smaller in the corners than at the center. This stems from the boundary conditions, which restrict the plate movements in the corners more than at its center. However, a reasonable assumption is to set $C_{st} = 149.3$ nF for all piezoelectric patches of the plate in the case of $n_0 = 1$.

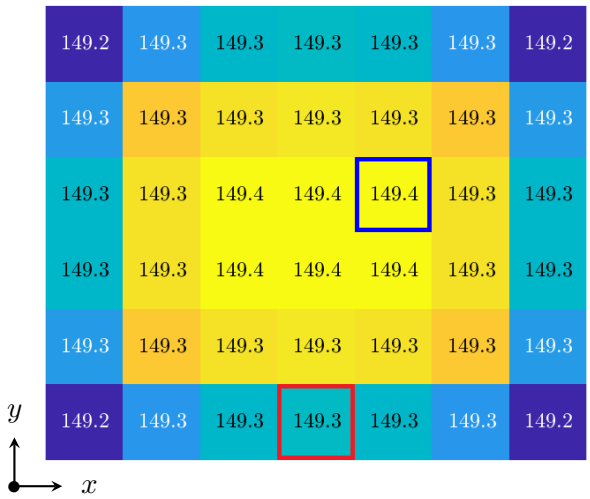

Figure 4.26: Simulated distribution of the C_{st} values (in nF) for the simply-supported plate periodically covered by piezoelectric patches for $n_0 = 1$. The colored frames highlight the piezoelectric transducers whose dynamic capacitances are plotted in figure 4.24.

4.5.5 Network validation

Now that the parameters m, K_θ^E and C_{st} have been estimated, the inductance value L can be derived for each unit cell of the network by applying the frequency coherence condition of equation (4.29). The resulting value is 246.6 mH for the case of $n_0 = 1$. As stated in section 4.2, the produced inductors have a nominal inductance value of 244 mH, which is close enough to the targeted value to attain a significant damping performance in the end. In other words, we have attained the Step 5 of the capsulized method in subsection 2.3.8.

Since their behaviors can be predicted, the analogy between the plate and the network can be verified by checking if the spatial and frequency coherence conditions are met. This corresponds to fulfilling the Step 6 of the electrical analogue design method. This validation is quite important since it is the main verification method that will be available for future numerical examples.

The models in equations (3.30) and (4.25) are used to compute the mode shapes and natural frequencies of the plate and of the network, respectively. To check if there is a similarity between mode shapes, the MAC matrix between the plate and the assembled network is represented in figure 4.28a. It shows that most simulated electrical modes are consistent with mechanical ones. The MAC matrix is not diagonal because of the comparison between results obtained with the model of the lumped

electrical network on one hand, and with the converged finite element model of the plate on the other hand. Indeed, covering the plate with more piezoelectric transducers helps discretizing the structure and its analogous network. The MAC matrix would then tend to a diagonal matrix. We propose to highlight this fact with numerical examples. The density of piezoelectric transducers covering the plate, which is denoted n_0, can be increased to do so. The plate remains discretized by $7n_0 \times 6n_0$ elements, each one being composed of a square plate on which a square piezoelectric patch is bonded. The geometries corresponding to $n_0 = 2$ and $n_0 = 3$ are shown in figure 4.27.

Data comparison for the spatial coherence condition validation

	Plate	Network
Experiments	Figure 4.30	Figure 4.15
Simulations	Equation (3.30)	Equation (4.25)

(a) (b) (c) (d) (e) (f)

Table 4.4: Possibilities of mode shapes comparisons.

Mode shapes of the plate and of the network can be estimated by simulations using equations (3.30) and (4.25). They can also be extracted from measurements thanks to the setups pictured in figure 4.30, or schemed in figure 4.15. Using the notations of table 4.4, the possible comparisons between mode shapes are as follows:

- **(a)** and **(b)**: Comparing measurements to simulations allows validating the developed models in terms of modal properties. This is done for the plate electrical analogue in subsection 4.4.3. However, we did not conduct an experimental modal analysis on mechanical measurements to compare the extracted modes to the forecast ones.
- **(c)** and **(d)**: Comparing measurements or simulations between themselves is the way to validate the spatial coherence condition that we suggest. For future study cases, in particular for those of chapter 5, measurements might not be available. Therefore, the comparison **(c)** is the preferred one to validate an electrical analogue. This is also done in the ongoing subsection in the case of the plate electrical analogue.
- **(e)** and **(f)**: Comparing simulations and measurements of different kinds might lead to discussions about comparing experimental and numerical data. We consequently suggest not conducting these comparisons for the validation of the spatial coherence.

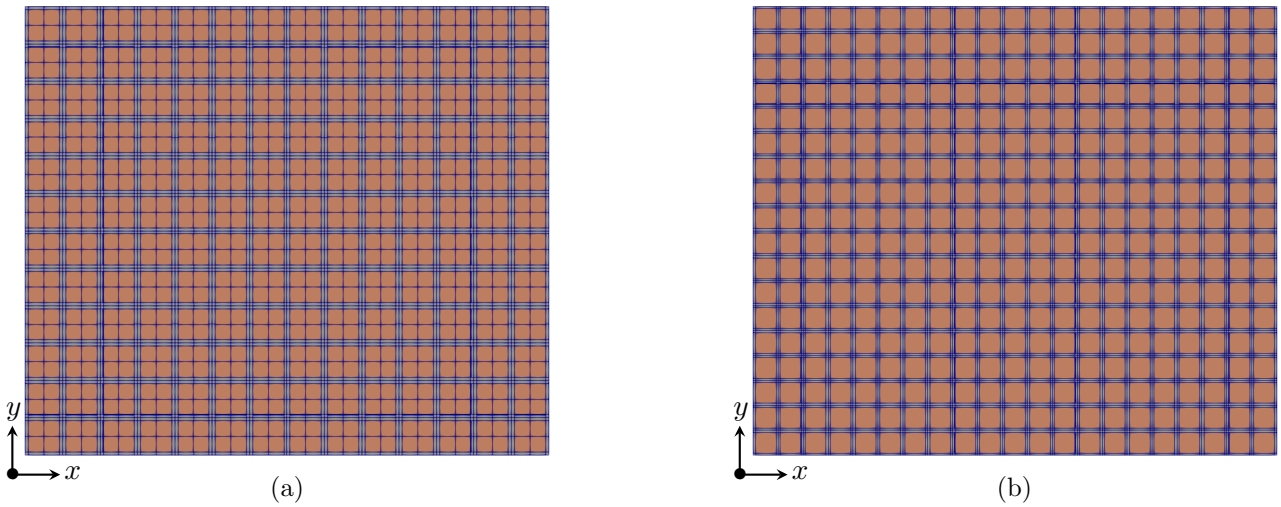

Figure 4.27: Meshes of the plate periodically covered with square piezoelectric patches in the cases of (a) $n_0 = 2$ and (b) $n_0 = 3$.

n_0	**Elements**	**Nodes**	a (mm)	m (g)	C_θ (nF)	L (mH)	**Meshing**	**MAC matrix**	**Marker**
1	7×6	139	60	39.7	149.3	246.6	Fig. 3.4	Fig. 4.28a	♦
2	14×12	530	30	9.9	37.4	61.5	Fig. 4.27a	Fig. 4.28b	▼
3	21×18	795	20	4.4	16.5	27.6	Fig. 4.27b	Fig. 4.28c	●

Table 4.5: Electrical modeling parameters for different discretizations of the plate analogue.

On one hand, the mechanical structure behavior is predicted by the finite element model previously developed. Using the same notation as in figure 3.4, the cases of $n_0 = 1$, $n_0 = 2$ and $n_0 = 3$ are treated with $n_x = n_y = 3$, $n_x = n_y = 2$ and $n_x = n_y = 1$, respectively. We assume the meshes in figure 4.27 lead to converged values for the mechanical simulations. This model is also used to compute the static piezoelectric capacitance C_{st} distributions, which are nearly uniform for all piezoelectric patches. Hence, the mean values of the distributions are recorded in table 4.5.

On the other hand, the global variables m and K_θ^E of the discrete mechanical system are estimated applying the previous equations. We choose to keep $\hat{a} = 4$, and the side length a depends on the geometry. Thus, the networks inductors can be tuned thanks to the frequency coherence condition of equation (4.29). The resulting modeling parameters are gathered in table 4.5.

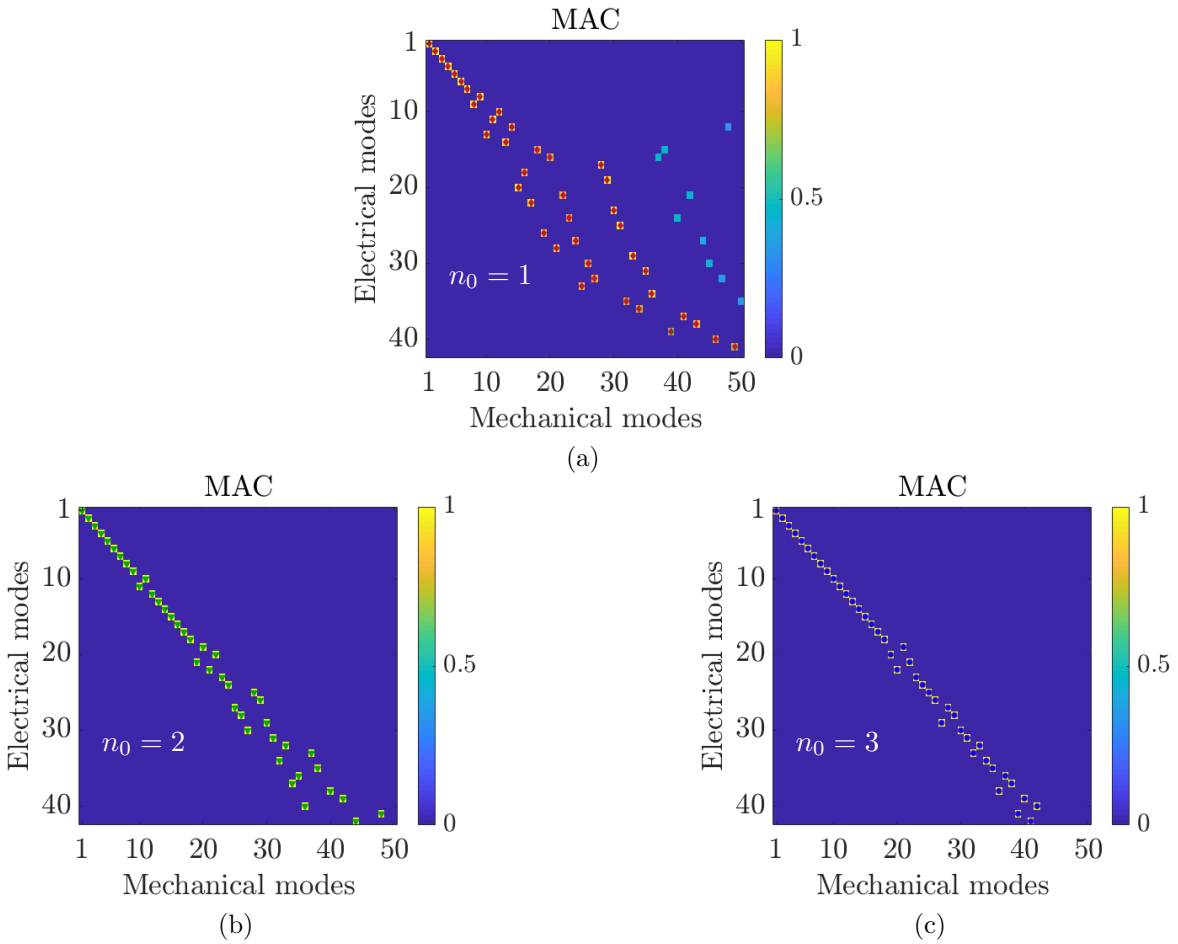

Figure 4.28: MAC between the 50 first velocity modes of the plate covered with piezoelectric patches and the 42 first electrical current modes of the network for (a) $n_0 = 1$, (b) $n_0 = 2$ and (c) $n_0 = 3$. The tiny ♦, ▼ and ● markers indicate which couple of modes are deemed clearly identified, so that they can be plotted in figure 4.29.

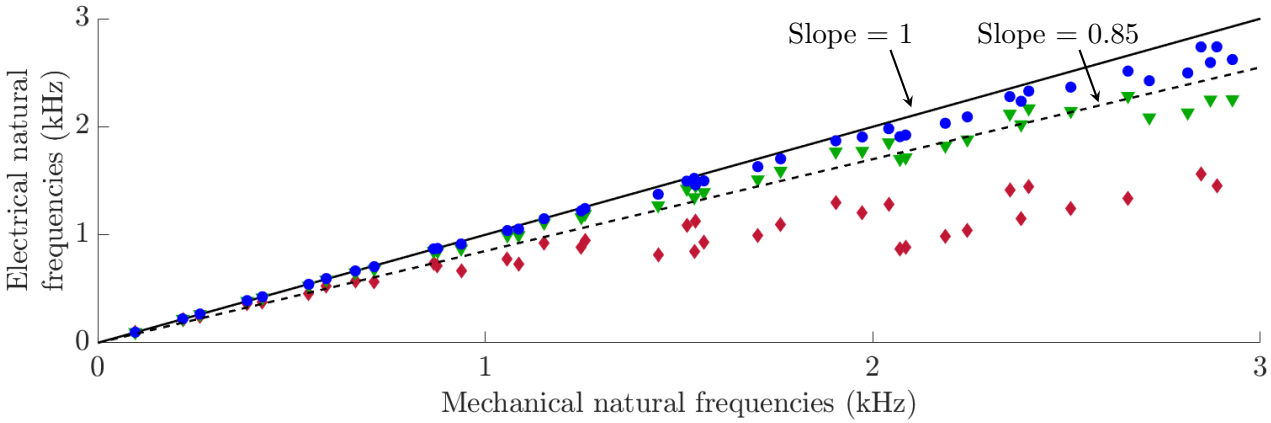

Figure 4.29: Comparison of mechanical and electrical natural frequencies for (♦) $n_0 = 1$, (▼) $n_0 = 2$ and (●) $n_0 = 3$.

Finally, mechanical and electrical modes are compared by computing the MAC matrix. Though they are not represented, the AutoMAC for the mechanical and electrical systems are diagonal up several tens of modes. Then, the MAC matrices comparing mode shapes resulting from models in equations (3.30) and (4.25) are plotted in figures 4.28b and 4.28c. They prove that the spatial coherence condition is met over a large number of modes. This means that the derived plate electrical analogue conveniently represents the behavior of the vibrating structure. Note that even though the electrical modes alignment with mechanical modes when the network is further discretized looks similar to results in figure 2.19, the considered structures are different from one another. Indeed, the analogy validation in subsection 2.7.2 is conducted on a rectangular duralumin plate, and so illustrates that a plate electrical analogue can be designed for such structure. Meanwhile, the ongoing validation is conducted on a duralumin plate with piezoelectric patches bonded on it. In other words, the ongoing validation ensures that a plate electrical analogue can be designed for a layered structure as well.

Besides, the simulated natural frequencies of both systems are compared in figure 4.29. Supposing an acceptable gap of 15 % between them, we expect the frequency coherence condition to be validated for the first eleven modes, which represents a frequency band of nearly 900 Hz. Meanwhile, more than fourty plate modes are correctly replicated by the network for $n_0 = 3$. Increasing the number of network cells makes the finite difference model converge to the finite element model, and hence brings mechanical and electrical natural frequencies closer.

In the end, these results are further arguments in showing that the developed network is an electrical analogue of the plate from 50 Hz to 900 Hz. Both frequency and spatial coherence conditions have been validated over this frequency range.

4.5.6 Broadband damping

The case of the structure being coupled to its passive electrical analogue is finally considered. The setup is pictured in figure 4.30. A shaker applies a point load on the surface of the plate on which the piezoelectric transducers are bonded, and a laser vibrometer measures the resulting movement on the other side of the plate. The parameters of the measurements have been discussed in subsection 3.3.2.

As seen in figure 4.31, broadband vibration damping is achieved. In the meantime, the frame mode at 687 Hz is barely affected by the connection to the network, which was expected. This is a proof that it is possible to mitigate vibrations on a wide frequency range by means of piezoelectric coupling

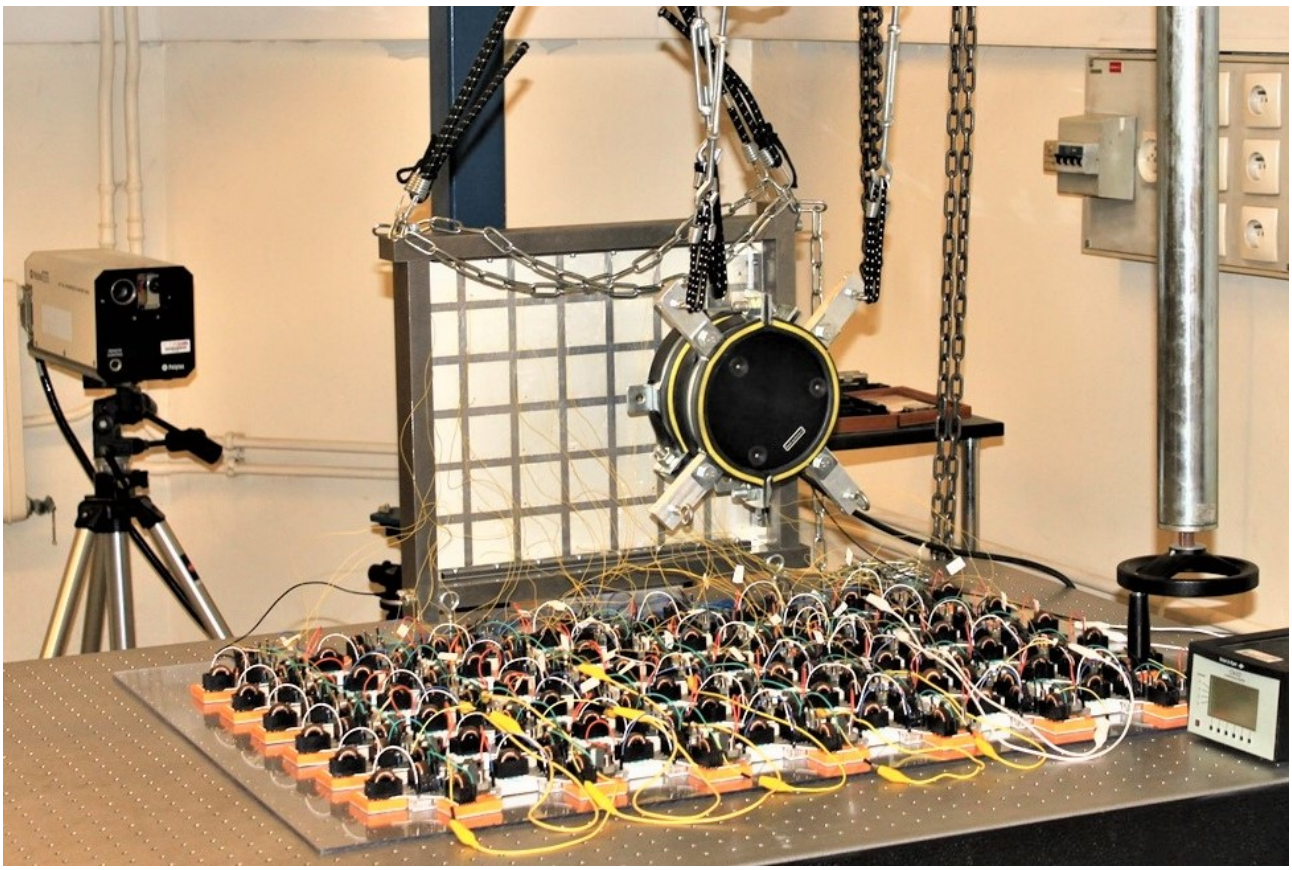

Figure 4.30: Picture of the setup, including the plate covered with piezoelectric transducers, a shaker, a laser vibrometer and the plate electrical analogue developed in section 4.4.

of a plate to its electrical analogue. Piezoelectric network damping has been achieved for a clamped plate in [72], but the network contains more unit cells in the present case. Therefore, the vibration mitigation is visualized upon a wider frequency range.

Besides, the model in equation (3.46) is able to predict the dynamics of the structure coupled to its electrical analogue. This result is of prime importance to go towards complex structures. Indeed, it validates the model we have developed in the previous chapter: while the structure behavior is predicted by a finite element model, an electrical network can be connected to it and be assembled by a finite element-like approach. While a similar model has been developed in [99], it is only applied to the coupling of a 1D finite element mechanical model to a 1D electrical network. In the present work, we have coupled a 3D finite element mechanical model to a 2D electrical network. We can cautiously expect this model to predict the coupling of any 3D mechanical structure modeled by the finite element method to a 1D or a 2D electrical network.

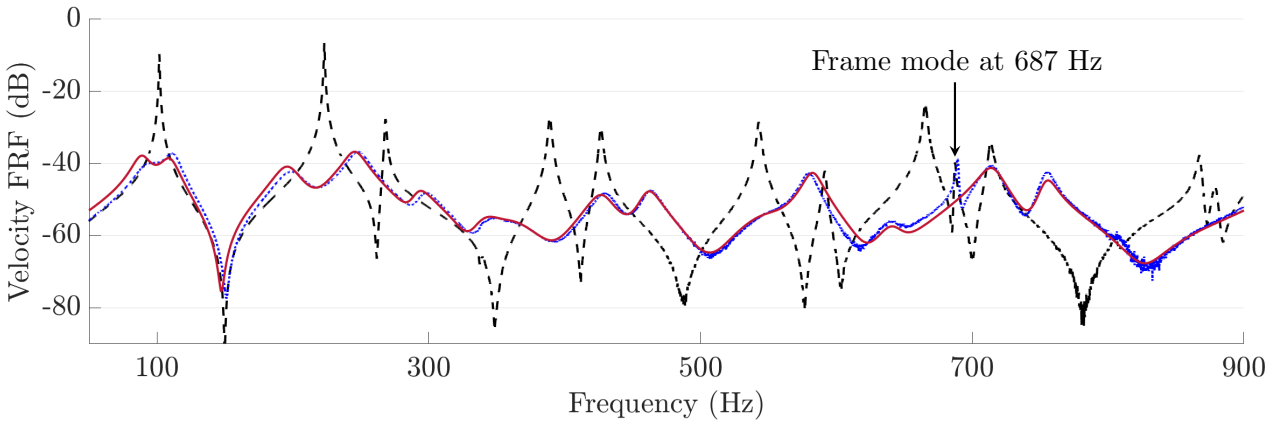

Figure 4.31: Comparison of velocity FRFs : ---- experimental FRF measured with the piezoelectric patches in short-circuit, ····· experimental and —— simulated FRF when the periodic plate is connected to its electrical analogous network.

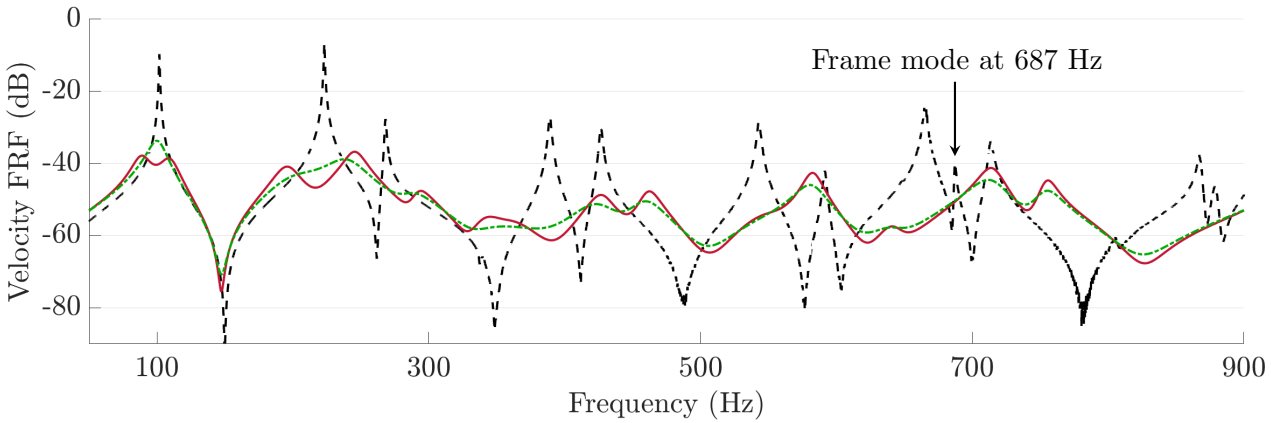

Figure 4.32: Comparison of velocity FRFs : ---- experimental FRF measured with the piezoelectric patches in short-circuit, and simulated FRF when the periodic plate is connected to its electrical analogous network —— without additional dissipative components and - - - with additional resistances of 50 Ω in series with the inductors.

It is now possible to numerically optimize the network components to enhance the damping performance. While we have not conducted such an optimization process, we have changed the value of the series resistance of inductors. This could easily be done in experiments, as trimmer resistors are placed in series with each inductor of the network. This has been explained in subsection 4.4.1, and said resistors are pictured in figure 4.13b. Adding 50 Ω in series with the inductors virtually makes their internal resistance go from 13.7 Ω to 63.7 Ω. The resulting FRF is plotted in figure 4.32. The series resistance of inductors mainly influences the low frequency behavior of the coupled system. Therefore, it makes sense that the first plate mode, which was slightly underdamped in figure 4.31, is now clearly overdamped. This phenomenon has been illustrated in figure 1.4. Moreover, the FRF is flattened at higher frequencies. By combining this effect with dissipative components placed at other locations of the unit cell, the damping performance might further improve. In the case of piezoelectric network damping of structures in bending, tuning the series resistance of transformers might improve the vibration mitigation performance [66, 71, 72].

Quantitative criterion for broadband damping

In the case of unimodal damping, a standard criterion of the vibration mitigation performance is to compute the infinite norm of the damped FRF around the considered mode. In other words, the goal is to minimize the quantity

$$\underset{[f_{\min}:f_{\max}]}{H_\infty}(\mathrm{FRF}) = \mathrm{Max}\left(\left|\mathrm{FRF}\left(2\pi f\right)\right|, f_{\min} \leq f \leq f_{\max}\right). \tag{4.39}$$

Applying this criterion results in one value by frequency range over which it is applied. Therefore, we suggest applying the minimization of the infinite norm to restrained frequency ranges. This corresponds to an optimization of several parameters using as many criteria.

Another performance criterion, which might be more adapted to wide band excitations, is to minimize the total amplitude of the FRF over the frequency range. In other words, the goal is to minimize the quantity

$$\underset{[f_{\min}:f_{\max}]}{H_2}(\mathrm{FRF}) = \int_{f_{\min}}^{f_{\max}} \left|\mathrm{FRF}\left(2\pi f\right)\right| \, df. \tag{4.40}$$

In the end, choosing a broadband damping performance criterion depends on the considered application, as the different criteria will probably lead to different components values.

4.6 Conclusions

This chapter investigates the piezoelectric network damping of a constant thickness plate periodically covered by piezoelectric patches. It consists in coupling a periodic mechanical structure via thin piezoelectric patches to a periodic electrical network for passive broadband damping purposes. The electrical network is designed to exhibit the same modal properties as the mechanical structure to be damped. While its efficiency for plates has been proven before, we use this opportunity to develop tools for the analysis of piezoelectric network damping. These tools will be used for more complex structures later on.

The case of a periodic simply-supported plate is here studied. Its analogous electrical network is implemented by producing passive electrical components, whose design is explained by recalling the laws of magnetic circuits for inductors and transformers. The analogy between the plate and the network is validated by verifying that the spatial and frequency coherence conditions are met. Then, the network is connected to its analogous mechanical structure. Vibration damping of the first eleven modes of the plate, which are spread over a frequency range of nearly 1 kHz, is achieved.

Meanwhile, a behavioral model of the electrical network has been proposed and validated by comparison with experimental results. This model has then been included in the coupled model developed in section 3.4. This larger model has also been validated by comparison with experimental results. Therefore, one can be confident about using it going towards more complex structures in order to forecast their electromechanical dynamics. These structures could be plates with various boundary conditions, arches or tubes. Some of them are treated in the chapter 5. Future works will study the attainable vibration damping performance when these structures are coupled to their respective analogous networks. Furthermore, it is now possible to predict the optimal resistive components to add to the network to optimize the vibration mitigation performance.

Chapter 5

Piezoelectric network damping of complex structures

This chapter is about deriving the electrical analogues of complex structures for vibration mitigation purposes. Three complex plates and two curved structures are treated. The first case plate also helps validating the models previously developed on non-periodic structures by comparison with experiments. In all cases, an electrical network is developed according to the estimated discrete mechanical parameters and by applying the adequate frequency coherence conditions. The analogy between the structure and the network is then validated by comparing their respective modal properties. Finally, a promising broadband vibration damping performance is achieved with realistic electrical components when the modal coupling condition is met.

Content

5.1 Introduction

The efficiency of piezoelectric network damping has been proven on standard mechanical structures, such as rods [70], beams [65, 66, 67, 71] and plates [68, 69, 72]. However, piezoelectric network damping of complex structures has barely been covered in the scientific literature.

The first attempt appears in [112], where dell'Isola et al. developed a finite element model that is adapted to couple two systems respectively governed by a second and fourth order differential equations. On one hand, the bending motion of plates is described by the Kirchhoff-Love theory, so on the other hand adjacent piezoelectric transducers are interconnected by inductors. It is possible to adjust the electrical components values so that one electrical resonance is tuned to a targeted mechanical resonance. By adding resistors in series with the inductors and in parallel with the piezoelectric capacitors, damping can thus be achieved. Then, dell'Isola et al. treated the case of a complex plate, which is not rectangular and include holes. By applying the same method and numerically setting the dissipative elements, they achieved damping of the first complex plate mode.

One limitation of the work presented in [112] is that the spatial coherence condition is not met in some situations. This stems from trying to replicate a mechanical behavior which is governed by a fourth order differential equation by an electrical system that behaves like a second order differential equation system. In other words, the damping solution which can be numerically computed is the coupling of a Kirchhoff-Love plate to an Euler-Bernoulli beam electrical analogue. Hence the network is not analogous to the plate, as explained in section 2.3. Moreover, this network is continuous, which makes it difficult to consider implementing this solution in a practical application. Finally, the developed finite element model is only adapted to structures which are governed by said differential equations, which excludes taking 3D effects into account.

More recently, the plate electrical analogue presented in [72] has been connected to non-periodic plates [100]: a mass is locally added on the initial plate, or some of its boundary conditions are modified. Broadband damping is still achieved when accordingly adapting the network components.

As a consequence, the goal of the present chapter is to study the piezoelectric network damping of complex structures. Since it is inconceivable to produce electrical networks for all study cases before integration, most of treated examples are going to be numerical. For this reason, in chapter 3 we have developed a predictive model of a structure being coupled by piezoelectric patches to an electrical

network. The electrical network to which a complex structure is going to be connected is assembled from known electrical unit cells. To this end, in chapter 2 we have developed a library of electrical circuits whose assemblies behave like electrical analogues of mechanical structures. Using these results allows forecasting the vibration damping performance in complex cases. In other words, the physics of the complex structure is simplified so that the modes to be damped can be modeled by simple mechanical models of rods, bars, beams, plates and curved elements. The structure is then connected to the analogous network of this simplified mechanical model.

Consequently, this chapter is mainly composed of numerical examples, which include complex plates. The first one, in section 5.3, is a plate with a local mass added on its surface. It is the only example of this chapter that contains experimental results. Besides, it helps validating the electromechanical finite element model developed in section 3.4 in a non-periodic case. Then, the section 5.5 studies the vibration damping of a plate with various boundary conditions, while the section 5.4 considers a variable thickness plate. Finally, we treat cases of curved structures such as an arch in section 5.6 and a ring in section 5.7.

What kinds of complexity?

The structure complexities can mostly be classified into the following categories:

- **Non-periodic structures**: Once the structure is discretized, the distribution of discrete parameters might be non-uniform. This can be due to various geometrical parameters, such as the thickness or the curvature. This can also be owed to local modifications induced by contacts with added parts.
- **Boundary conditions complexities**: The only cases we have studied thus far considered the same boundary conditions at all the structure ends. Mixing these boundary conditions is therefore a complexity to look into.
- **Overlapping frequency ranges**: Some structures might exhibit modes which are barely distinct from each others. This is the case of nearly axisymmetric structures, for example. Another complexity is to apply piezoelectric network damping to a structure whose modes of different kinds appear in the frequency range of interest. An example is an arch whose in-plane bending modes and out-of-plane bending modes are included in the frequency range of study.

These sources of complexity might be combined in practice. We choose to consider them separately in order to distinguish their effects on the damping performance.

5.2 Approach

5.2.1 Method

Notations

In this subsection, some of the models which are considered to study the piezoelectric network damping of complex structures are recalled. However, we do not recall the associated notations, which are the same as in chapter 3.

In this chapter, piezoelectric network damping of several complex structures is studied. The process is similar for most of these cases, and consists in the following steps:

- The starting point is a host structure with prescribed boundary conditions, whose first few natural modes require damping. The number of piezoelectric patches to be bonded to the structure is set to avoid spatial aliasing. This means that we consider nearly ten piezoelectric transducers per wavelength of the mode with the smallest wavelength in the frequency range of interest. This discussion has been made in subsection 2.3.5.
- Unit cells from the library in section 2.10 are then selected according to the kind of waves that propagate in the mechanical medium. They are assembled to form an electrical network with as many cells as there are piezoelectric transducers bonded on the host structure.
- The discrete mechanical model resulting from the choice of unit cells is composed of lumped elements, whose values should be computed. This corresponds to estimating geometrical parameters, masses and stiffnesses. While the computation of dimensions and masses is straightforward, the stiffnesses evaluation requires developing mechanical models for layered structures. An example is given in subsection 4.5.3.
- The static piezoelectric capacitance distribution is simulated using the finite element model described in section 3.2. We recall that the finite element formulation allowing this simulation is as follows:

$$\left[\begin{pmatrix} \boldsymbol{K_m} + \boldsymbol{K_c}\boldsymbol{K_e}\boldsymbol{K_c}^{\mathrm{T}} & \boldsymbol{K_c}\boldsymbol{K_e} \\ (\boldsymbol{K_c}\boldsymbol{K_e})^{\mathrm{T}} & \boldsymbol{K_e} \end{pmatrix} - \Omega^2 \begin{pmatrix} \boldsymbol{M_m} & \boldsymbol{0} \\ \boldsymbol{0} & \boldsymbol{0} \end{pmatrix}\right] \begin{pmatrix} \boldsymbol{U} \\ \boldsymbol{Q} \end{pmatrix} = \begin{pmatrix} \boldsymbol{F} \\ \boldsymbol{V} \end{pmatrix}. \tag{5.1}$$

- The characteristics of the remaining electrical components are set by applying the adequate frequency coherence conditions for each unit cell. This allows not modifying the structure, and not increasing the piezoelectric capacitance, which would decrease the overall damping performance [29]. The frequency coherence conditions have been expressed in chapter 2.

- A validation phase which is conducted in all cases but not recorded in this manuscript consists in defining a mesh of the structure that leads to converged results. Then, the mechanical and electrical AutoMAC are each computed to ensure that their respective discretization schemes are fine enough to avoid spatial aliasing.

- We then verify if the frequency and spatial coherence conditions are met. This is done by comparing modal properties of the network and of the structure estimated by their respective uncoupled models. The modal properties of the structure with short-circuited patches are estimated using the equation (5.1). Meanwhile, the modal properties of the electrical network are simulated by the model derived in section 4.4, in which each static capacitance C_{st} replaces the capacitance of the corresponding unit cell:

$$\boldsymbol{V_N} = \left(\boldsymbol{K_N} + \mathrm{j}\Omega\boldsymbol{D_N} - \Omega^2\boldsymbol{M_N}\right)\boldsymbol{Q_N}. \tag{5.2}$$

  The subsection 4.5.5 shows an example of such validation. If both spatial and frequency coherence conditions are met, we say that the **modal coupling condition** is met once the structure and its analogous network are connected. Note that this is a change of vocabulary from [70, 71, 72], where the modal coupling condition expression used to designate what we now call the frequency coherence condition.

- Once the **modal coupling condition** is met, broadband vibration damping is expected if additional resistances are set in the network to adequately add electrical damping. Using the notations of section 3.4, we recall the finite element formulation of a structure being coupled to a lumped electrical network:

$$\left[\begin{pmatrix} \boldsymbol{K_m} + \boldsymbol{K_c}\boldsymbol{K_e}\boldsymbol{K_c}^{\mathrm{T}} & \boldsymbol{K_c}\boldsymbol{K_e}\boldsymbol{P} \\ (\boldsymbol{K_c}\boldsymbol{K_e}\boldsymbol{P})^{\mathrm{T}} & \boldsymbol{K_N} \end{pmatrix} + \mathrm{j}\Omega \begin{pmatrix} \boldsymbol{D_m} & \boldsymbol{0} \\ \boldsymbol{0} & \boldsymbol{D_N} \end{pmatrix} - \Omega^2 \begin{pmatrix} \boldsymbol{M_m} & \boldsymbol{0} \\ \boldsymbol{0} & \boldsymbol{M_N} \end{pmatrix}\right] \begin{pmatrix} \boldsymbol{U} \\ \boldsymbol{Q_N} \end{pmatrix} = \begin{pmatrix} \boldsymbol{F} \\ \boldsymbol{V_N} \end{pmatrix}. \tag{5.3}$$

Not optimized but realistic magnetic components

A good practice for integration would be to design the network inductors and transformers to exhibit optimal electrical damping properties. No additional electrical component would thus be required. While not fully optimized in this chapter, the inductors are developed according to the method described in [3]. Besides, the transformers are similar to the ones of the plate electrical analogue characterized in section 4.3. We verify afterwards that the first targeted mode of the frequency range is slightly underdamped, such as illustrated in figure 1.4. In other words, simulations are conducted with realistic electrical components. This brings hope that integrating fully passive analogous networks in practical applications is possible.

5.2.2 Hypotheses

The main assumptions to study the piezoelectric network damping of complex structures with the previous equations are that:

- The infinitesimal strain theory applies.
- The structure is made of duralumin, and behaves as an isotropic homogeneous linear elastic medium. Its Poisson's ratio, density and Young's modulus are respectively set at 0.35, 2800 kg/m^3 and 69 GPa.
- The piezoelectric transducers are thin and polarized in the electrodes orthogonal directions, and they exhibit transverse isotropic properties. They are made with PIC 153 piezoelectric material, since its characteristics have been adjusted with measurements. The materials properties are recorded in table 3.3.
- The adhesive layers and the electrodes thicknesses are not modeled.
- The lower electrodes are connected to the ground.
- The electrical network behaves linearly with excitation sources, so that the superposition principle can be applied.
- The mechanical damping matrix $\boldsymbol{D_m}$ is computed with a hysteretic damping model. The corresponding damping coefficient ξ is set at 0.3 %. The only exception occurs in section 5.3, where ξ is set at 0.6 %.

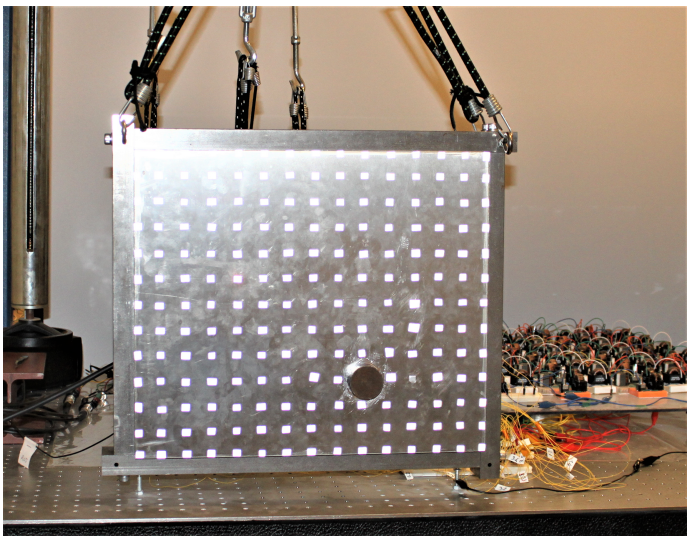

(a)

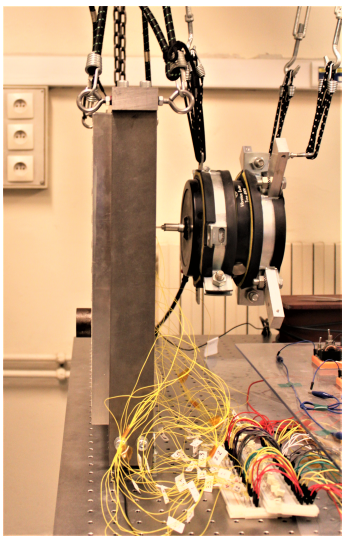

(b)

Figure 5.1: Plate on which a circular mass has been added: (a) front view and (b) side view.

5.3 Plate with a local additional mass

5.3.1 Structure description

The first case of a complex plate here treated is the addition of a mass which is a 22 mm thick, 40 mm diameter cylindrical steel rod of 207 g. This mass is added on the side of the plate which is not covered by piezoelectric patches. The mass addition is pictured in figure 5.1. The bonding is made in two stages: at first, we have glued the mass on the non-adhesive face of a small piece of aluminum tape. The aluminum tape with the mass on it is then attached to the plate, after cleaning the plate surface with acetone. This is the best practice we have empirically found in order to modify the plate behavior without inducing too much damping.

Moreover, this part has been selected for two reasons. The first one is that it covers roughly the same surface as a piezoelectric patch, so the integration in the finite element model later on is facilitated. The other reason is that heavier parts could not be bonded on the plate without the adhesive layer between them and the aluminum tape deteriorating right away. Since the objective is to break the symmetry of the plate, the heaviest part among the available ones has been selected.

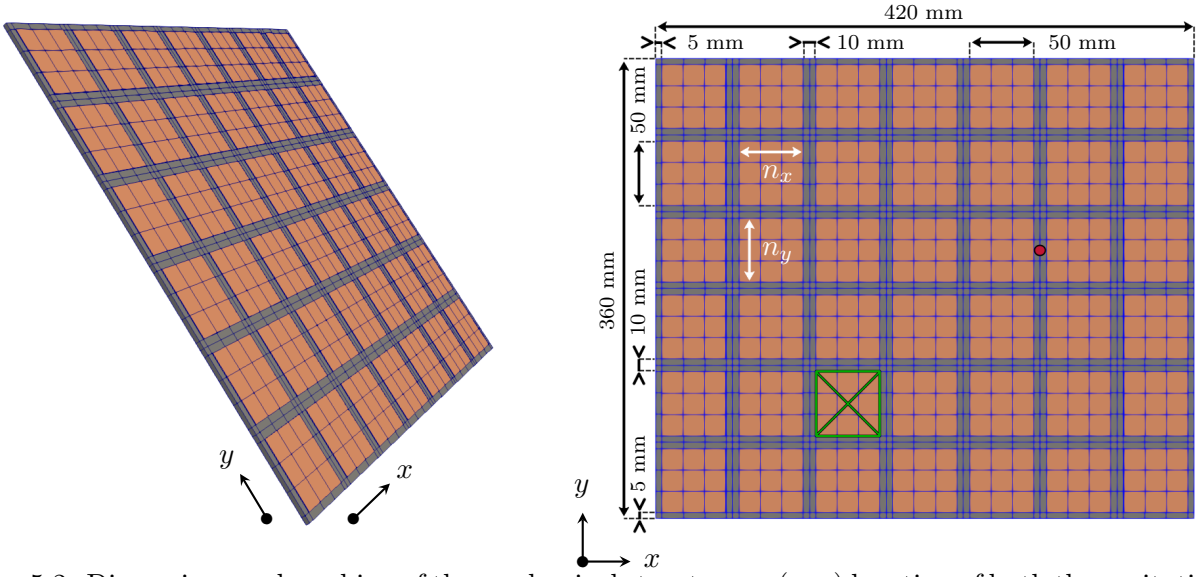

Figure 5.2: Dimensions and meshing of the mechanical structure, • (x, y) location of both the excitation and the velocity measurements, and ⊠ (x, y) position of the added mass.

5.3.2 Finite element model

To take the effect of the added mass into account, elements are added out of the plate plane. The added part is regarded as a 22 mm thick layer covering the same surface as a piezoelectric patch. Its position is indicated on the mesh in figure 5.2 that is used to produce the numerical results. The added mass is discretized in $n_x \times n_y \times 1$ elements. Its Young's modulus is set at 325 MPa. This way, the seventh simulated natural frequency of the plate with short-circuited patches is adjusted to the seventh peak on the measured FRF. Meanwhile, the hysteretic damping coefficient ξ is now set at 0.6 % so that the amplitude of the seventh simulated peak is roughly equal to the measured one.

The correlation between numerical and experimental results in this case is shown in figure 5.3. Measurements are conducted with the same setup as described in subsection 4.5.6. Results are only plotted up to 600 Hz in this case, as they become difficult to interpret at higher frequencies because of the damping induced by the structural modification. When compared to the FRF without the bonded mass, one can notice that the natural frequencies of the plate have been lowered, that the contact with the added mass induces more mechanical damping, and that a frame mode at 203 Hz is now observed. Since the frame is not modeled, its effects cannot be foreseen. In the end, the updated simulated FRF fits quite well with the measured one nonetheless.

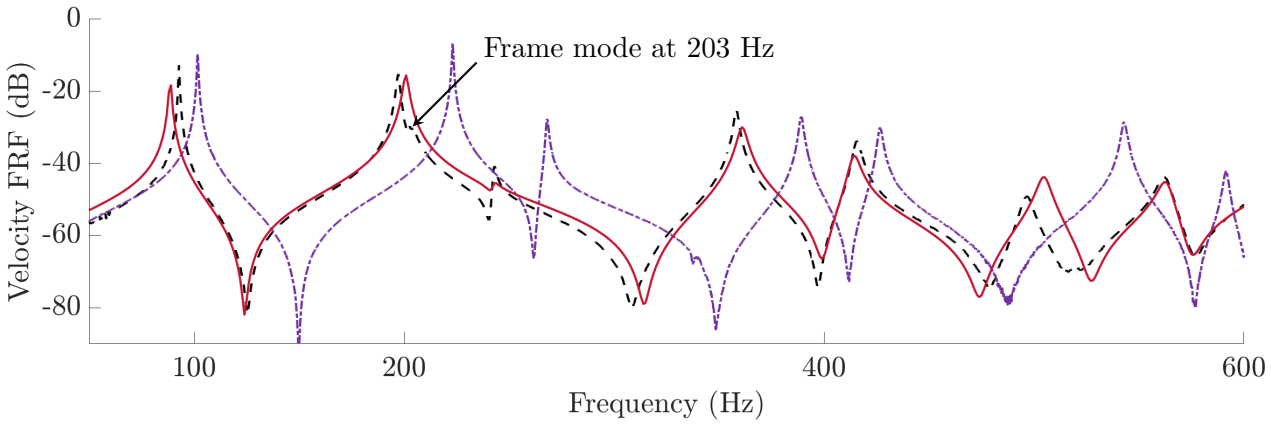

Figure 5.3: FRFs with short-circuited piezoelectric patches: ---- Experimental and —— simulated results with the bonded mass, and ····· experimental results without the bonded mass.

5.3.3 Analogous network

To define the non-periodic plate electrical analogue, the first idea is to keep using the frequency coherence condition which has been expressed in subsection 4.5.1:

$$\frac{1}{a^2}\frac{K_\theta^E}{m} = \frac{1}{\hat{a}^2}\frac{1}{LC_{st}}. \tag{5.4}$$

The mass m of the unit cell in which the added layer has been bonded has locally been changed from 39.7 g to 246.7 g, which is a multiplication by a factor of around 6.2. Therefore the product $\hat{a}^2 LC_{st}$ of the corresponding unit cell should be multiplied by 6.2 as well to adjust the bending wave propagation properties of the network to those of the modified plate. In practice, transformers ratios are fixed. Moreover, increasing C_{st} deteriorates the electromechanical coupling [29]. Hence, the inductance L is chosen as the tuning parameter. The new inductance value is $6.2 \times 0.2466 = 1.53$ H. This value is an overestimation however, as the mechanical stiffness K_θ^E is locally increased as well. Yet the stiffness model drawn in figure 4.22 gives correct results only if the mid-surface of the unit cell is close to the mid-surface of the plate. This has been discussed in the aside of subsection 4.5.3. The added layer being nearly seven times thicker than the plate, the proposed model is not convenient in this case. Modeling the contact of the added mass on the plate would be required to estimate the modifications of the local stiffness. Besides, it would allow estimating the modification of the static capacitance C_{st} distribution as well, even though it is a second order influence. This is out-of-scope of this work, since the potential improvement in modeling accuracy is limited.

Core geometry	l_e (mm)	l_w (mm)	A_e (mm^2)	A_w (mm^2)	A_L (nH)	N (turns)	d_w (μm)	k_u (%)	L (H)	R_{sL} (Ω)
RM 10	42	52	83	40.2	630	1460	150	62	1.34	72

Table 5.1: Ferrite core specifications and forecast component characteristics made in N48 ferrite material [108] for the complex plate electrical analogue.

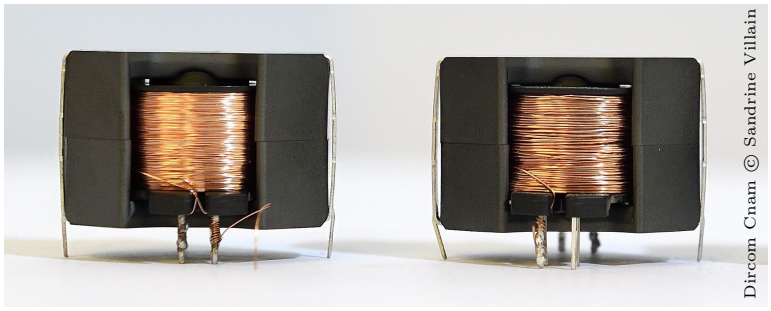

Figure 5.4: Produced fully passive N48-ferrite based inductors with a RM 10 core geometry. On the left: component of inductance 1.34 H, whose specifications are recorded in table 5.1. On the right: component of inductance 244 mH, whose specifications are recorded in table 4.2.

Consequently, in this particular case, we propose not to use the frequency coherence condition to define the electrical analogue. We suggest rather defining the non-periodic plate electrical analogue by tuning its first natural frequency to the first simulated natural frequency of the non-periodic plate. The simulated resonance at around 88 Hz in figure 5.3 is used as a reference value for the structure. Numerical simulations using the equation (5.2) show that the initial inductance of 246.6 mH should be locally replaced by an inductance of 1.34 H to set the first natural frequency of the network to around 88 Hz. One can attest this value is slightly lower than the first approximation of 1.53 H, since the local stiffness modification of the structure is taken into account.

The inductor of 1.34 H is produced by following the same method as described in section 4.2. For practical reasons related to components availability, a gapped RM 10 core with the ferrite material N48 from Epcos TDK has been used in this case as well. The produced inductor has its specifications recorded in table 5.1 and is pictured in figure 5.4. Notice that the newly produced component is more filled than the rest of the network inductors, and is winded with thinner conductive wire. Finally, we have verified that a series circuit composed of an inductance of 1.34 H and a resistance of 75 Ω accurately describes the component behavior at low frequencies and low levels of electrical currents.

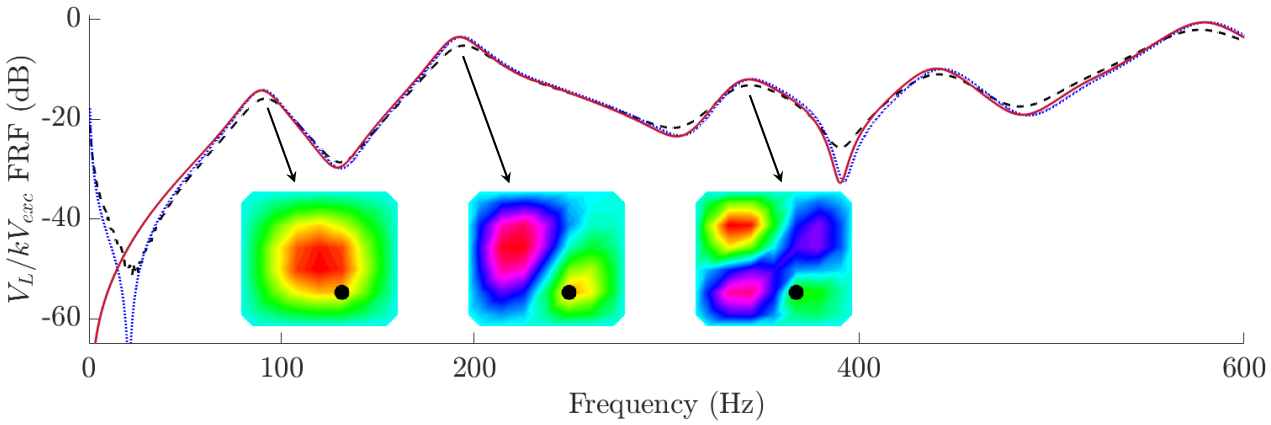

Figure 5.5: FRFs of V_L/kV_{exc} obtained from ---- measurements, —— simulations by neglecting the magnetizing branch of transformers, and ····· simulations by considering a constant magnetizing inductance L_m. V_L is measured across the inductor of the unit cell whose location is indicated by a ⊠ marker in figure 4.15. Several operational electrical current shapes at gain peaks are highlighted.

5.3.4 Network validation

Like in subsection 4.4.3, we suggest verifying if the network behaves as intended before connecting it to the plate. This means that the piezoelectric transducers are replaced by ceramic capacitors of 145 nF of nominal capacitance. The network validation consists in two steps:

- **Dynamics validation**: The model should predict the frequency behavior of the network. This is validated by comparing FRFs resulting from experiments and simulations.
- **Modal validation**: The model should exhibit the same mode shapes as the assembled network. This is validated by computing the MAC between measured and simulated current modes.

Measurements in the network are conducted in a similar fashion as explained in subsection 4.4.3. We do not detail the entire process again, but we recall that an external voltage V_{exc} is imposed between two network unit cells. This is analogous to considering an exciting external force on the plate. The figure 4.15 presents the excitation circuit and its location. Meanwhile, the voltage drop V_L across each inductor of the network is measured. The numerical FRFs V_L/kV_{exc} obtained using the model of equation (5.2) can thus be compared to measurements.

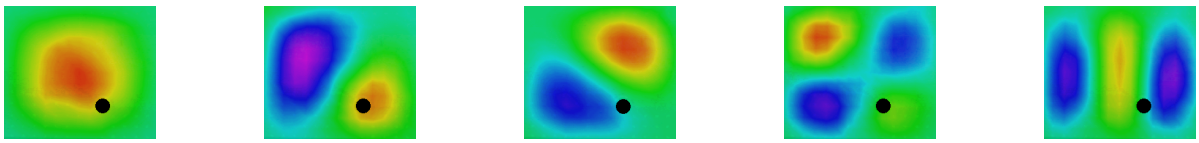

(a) Shape at 102 Hz (b) Shape at 223 Hz (c) Shape at 268 Hz (d) Shape at 389 Hz (e) Shape at 543 Hz

Figure 5.6: Measurement of five operational deflection shapes of the plate with the added mass position indicated in black.

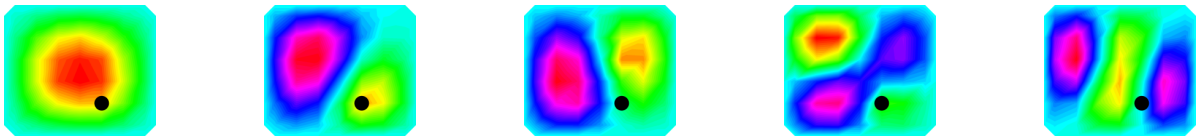

(a) Shape at 101 Hz (b) Shape at 218 Hz (c) Shape at 250 Hz (d) Shape at 376 Hz (e) Shape at 468 Hz

Figure 5.7: Measurement of five operational electrical current shapes of the network with the center of the modified unit cell highlighted in black.

An example of FRFs comparison is plotted in figure 5.5. The simulated FRFs are in good agreement with the measured ones. The few differences can be attributed to neglecting the magnetizing branch and the winding capacitance of transformers. There is also more damping in practice than in the model, which explains the difference in peak heights. Even though these differences could be reduced by taking transformers imperfections into account, we consider that the present network model is accurate enough to predict its frequency behavior from 50 Hz to 600 Hz.

At first, operational current shapes of the network in figure 5.7 can be visually compared to operational deflection shapes of the complex plate in figure 5.6. Operational shapes are obtained by representing the electrical current and velocity distributions at measured FRFs peaks. The visual similarity gives hope that electrical and mechanical modes are consistent. Note that the plate modification is substantial, as shapes are not symmetrical anymore, as opposed to the ones in figure 4.17. Meanwhile, heavy damping in the network explains that the (2,1) and (1,2) electrical shapes spill over each other, and thus are not completely uncorrelated like the corresponding mechanical shapes. This could also be noticed in figure 4.18. These representations highlight that the added mass is heavy enough to regard the modified structure as a complex one when compared to a periodic simply-supported plate.

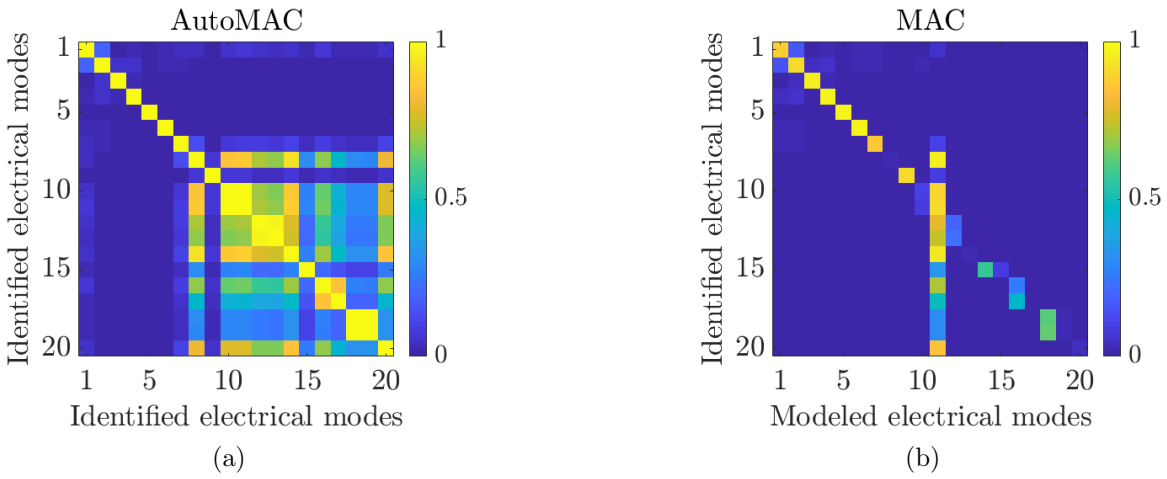

Figure 5.8: (a) AutoMAC of the first 20 electrical current modes identified by performing an experimental modal analysis and (b) MAC matrix between experimental and simulated electrical current modes of the network.

Finally, the modal validation is conducted by comparing the simulated and measured electrical current modes. An experimental modal analysis is performed to extract the network modes from experiments by using the least-squares rational function estimation method [110]. Twenty modes are extracted from experimental data, but only the first seven of them are relevant. Indeed, the identification method is not suitable for systems with significant and not purely proportional damping, which is the case of the developed network. This explains that the identified modes cannot be separated from each other beyond the seventh, as can be seen in figure 5.8a. The identified modes are then compared to simulated ones in figure 5.8b. The represented MAC matrix shows that the first seven experimental and numerical modes are mutually consistent. The modes of smaller wavelengths can hardly be discussed, because of the impossibility to distinguish experimental modes from each others. Using adequate modal analysis tools would improve the quality of modes extraction, and therefore might show that the model is validated over a greater number of modes. However, it is out-of-scope of this work, since the network model of equation (5.2) is deemed precise enough up to 600 Hz in terms of modal properties and frequency behavior to be integrated in the coupled model of equation (5.3).

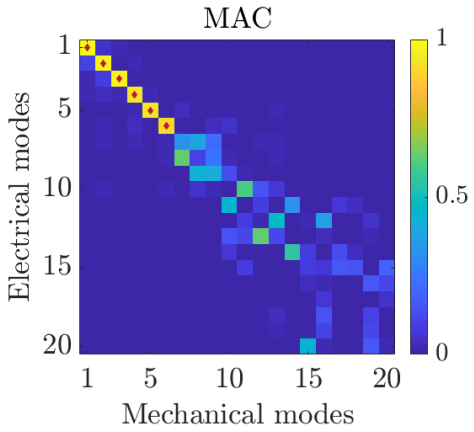

Figure 5.9: MAC between the 20 first simulated velocity modes of the plate covered with piezoelectric patches and the 20 first simulated electrical current modes of the network. The tiny ♦ markers indicate which couple of modes are deemed clearly identified, so that they can be plotted in figure 5.10.

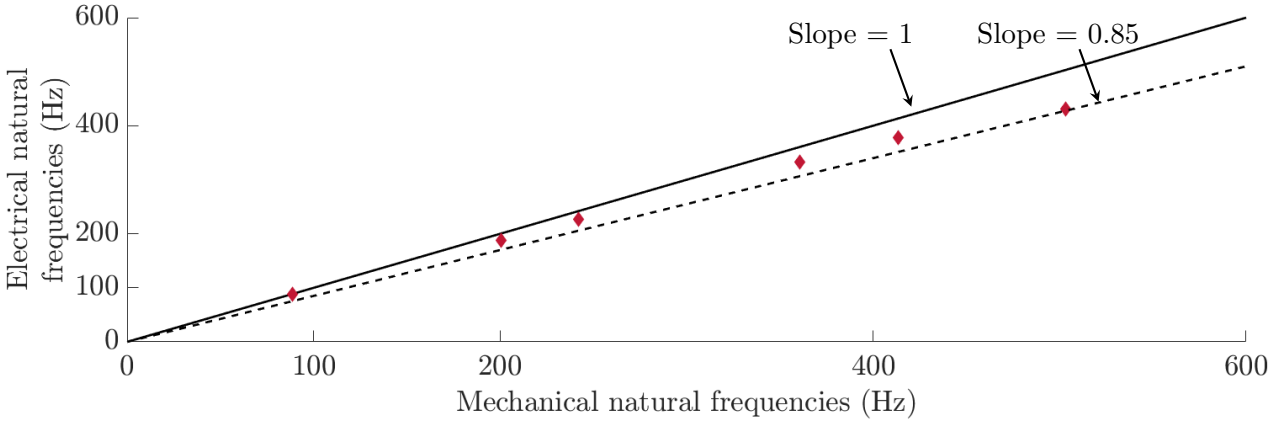

Figure 5.10: Comparison of simulated mechanical natural frequencies of the complex plate, and simulated electrical natural frequencies of its analogous electrical network.

5.3.5 Modal coupling condition

The modal coupling condition is met when coupling two systems for which the spatial and frequency coherence conditions are met. The spatial coherence condition is studied by computing modes of the structure with short-circuited piezoelectric patches, and comparing them to computed electrical modes. This comparison is made in figure 5.9. The analogy seems to be verified between systems up to the sixth mode. Modes at higher frequencies are not mutually consistent. Besides, the natural frequencies of clearly identified couples of modes are plotted against each other in figure 5.10. As a consequence, the modal coupling condition is met when coupling the complex plate to its analogous network, and thus broadband damping is expected.

To obtain a proper analogy at higher frequencies, two solutions are possible. The first one would be to have more piezoelectric patches on the plate, which is equivalent to refine the mesh of the analogous network. The second solution would be to find another analogous unit cell for the plate. Indeed, the significant mass discontinuity induced by the added mass can hardly be predicted by a finite difference model. Hence, the present case can be deemed as the limit case of validity for the plate electrical analogue as developed in sections 4.4 and 4.5. In the end, the analogy between the non-periodic plate and the modified network is still verified up to around 600 Hz.

5.3.6 Broadband damping

The non-periodic plate is now coupled to its passive electrical analogue. The FRF measurement is made with the same setup as described in subsection 4.5.6. As seen in figure 5.11, broadband damping is achieved in this case as well. The case of keeping the network unchanged even though the structure has been modified is plotted as well. In other words, we verify that not adapting the network to the modified structure leads to a deteriorated damping performance. Even though it is not obvious from represented results, it can be understood by looking at the dynamics of the structure around the second bending mode at 197 Hz. If the network is not adapted, then we do not visualize the double peaks that are typical to underdamped tuned mass dampers. Note that this interpretation would be easier if the electromechanical coupling was lower, as a network mistuning would induce a more drastic loss in performance. In the end, these results validate the approach of coupling a non-periodic structure to its fully passive electrical analogue for multimodal damping purposes.

Besides, the simulated results fit rather well with the measured ones. The remaining differences, which were already spotted on results with short-circuited piezoelectric patches, could be reduced by modeling the contact between the added part and the plate, as well as the non-ideal boundary conditions. As it is, we suppose that the finite element model developed in this work and expressed by equation (5.3) can predict the dynamics of a complex structure coupled to an electrical network.

A simple example of modifying the damping in the network is finally shown in figure 5.12. A resistance of 50 Ω is added in series with the network inductors. This brings the series resistance for inductors at 63.7 Ω, except from the modified unit cell which exhibits a series resistance of the inductor of 125 Ω. In this case, the gain in damping performance is not that significant, since the first plate mode becomes overdamped after the resistance addition.

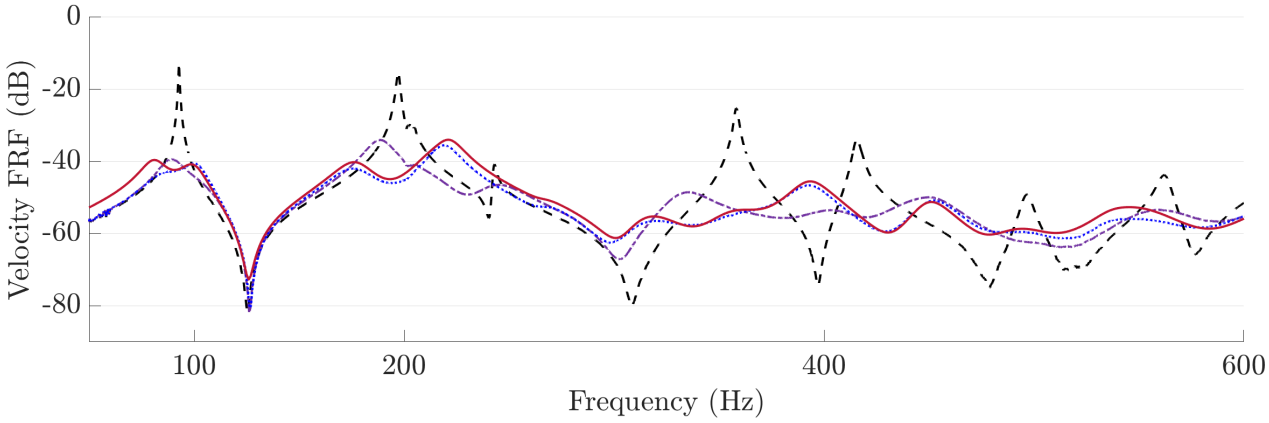

Figure 5.11: Comparison of velocity FRFs : - - - - experimental FRF measured with the piezoelectric patches in short-circuit, ····· experimental and —— simulated FRF when the plate is connected to its electrical analogous network, and – – – experimental FRF when the network uses the same components as before the mass addition for the plate electrical analogue developed in section 4.4.

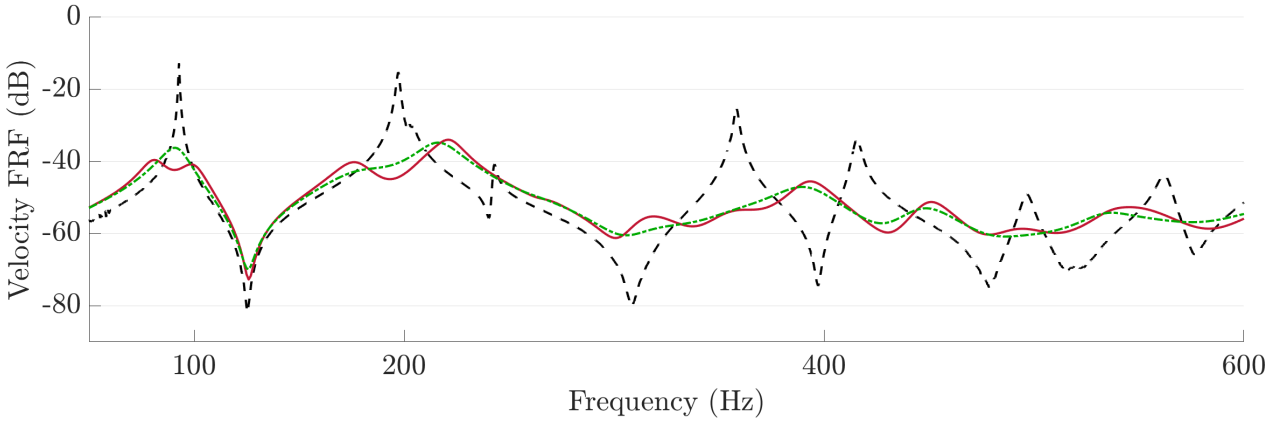

Figure 5.12: Comparison of velocity FRFs : - - - - experimental FRF measured with the piezoelectric patches in short-circuit, and simulated FRF when the plate is connected to its electrical analogous network —— without additional dissipative component and – – – with additional resistances of 50 Ω in series with the inductors.

Position x (mm)	**Position y (mm)**	**Thickness $h_s(x, y)$ (mm)**
0	0	5
420	0	3
0	360	4
420	360	2

Table 5.2: Thicknesses values at the corners of the plate. These four values are enough to set the profile of the plate such as defined in equation (5.5).

5.4 Variable thickness plate

5.4.1 Structure description

The studied case is a simply-supported rectangular plate of sides $l_x = 420$ mm and $l_y = 360$ mm. Square piezoelectric patches are periodically bonded to the plate, and cover $(5/6)^2$ of its surface. For now, it is assumed that the thickness h_s of the plate varies linearly with the x and y coordinates. Therefore, with α, β, γ and δ being real values:

$$h_s\left(x, y\right) = \alpha + \beta x + \gamma y + \delta xy. \tag{5.5}$$

The numerical values of h_s at the plate corners are summed up in table 5.2. The thickness of each piezoelectric patch is constant and is set at 1/6 of the mean thickness of the plate portion it covers.

5.4.2 Analogous network

5.4.2.1 Unit cells selection

The complexity stems from the variable thickness. Indeed, the Kirchhoff-Love equation that we have considered in section 2.7 leads to a discretized mechanical model that includes the same constant bending stiffness K_θ^E along the two main plate directions. This assumption does not fit with the case of a variable thickness plate. Yet, we select the square plate electrical analogue in the library of section 2.10 to make up the structure analogue. We recall the corresponding frequency coherence condition which has been derived in subsection 4.5.1:

$$\frac{1}{a^2}\,\frac{K_\theta^E}{m} = \frac{1}{\hat{a}^2}\,\frac{1}{LC_{st}}. \tag{5.6}$$

This condition should still be locally verified to ensure that the structure and its analogous network have identical bending wave propagation properties. As explained in the method of subsection 5.2.1, the mechanical parameters as well as the static piezoelectric capacitance C_{st} are going to be estimated in the following paragraphs. The transformer ratio $\hat{a}$ and the inductance L of each unit cell then serve as tuning parameters.

5.4.2.2 Mechanical parameters evaluation

As explained in chapter 4 for the constant thickness plate, it is possible to discretize the structure by $7n_0 \times 6n_0$ square elements, n_0 being integer. An example of the geometry and dimensions for $n_0 = 1$ is illustrated in figure 5.2, but with a variable thickness and without the added mass. Hence, the cell side a depends on the considered discretization density:

$$a = \frac{l_x}{7n_0} = \frac{l_y}{6n_0}. \tag{5.7}$$

Denoting ρ and ρ_p the respective mass densities of the structure and of the piezoelectric patches, whose sides l_p is set at 5/6 of a, one can estimate the mass of each unit cell:

$$m = \int_0^a \int_0^a \left(\int_0^{h_s(x,y)} \rho \, dz \right) dx \, dy + \rho_p l_p^2 h_p. \tag{5.8}$$

Then, the method of calculation of the bending stiffness value K_θ^E for a square mechanical plate is based on the model depicted in figure 5.13. The estimation of the bending stiffness along the two main plate directions is based on the same equations as written in subsection 4.5.3. We recall them nonetheless, as they will also be used for the next numerical examples. The model we propose includes a series and parallel combination of discrete springs, so that the bending stiffness $K_{\theta y}^E$ when y is deemed as the normal axis is

$$\frac{1}{K_{\theta y}^E} = \frac{1}{K_{\theta y1}^E} + \frac{1}{K_{\theta y2}^E + K_{\theta y3}^E} + \frac{1}{K_{\theta y4}^E}, \tag{5.9}$$

where $K_{\theta y1}^E$, $K_{\theta y2}^E$ and $K_{\theta y4}^E$ are the stiffnesses of the plate portions indicated in figure 5.13, while $K_{\theta y3}^E$ is the stiffness of the piezoelectric patch. These stiffnesses values can be computed by the following expressions:

$$\begin{aligned}
\frac{1}{K_{\theta y1}^E} &= \frac{1-\nu^2}{Y} \int_0^{(a-l_p)/2} \frac{1}{I(y)} \, dy, & \frac{1}{K_{\theta y3}^E} &= \frac{1-\nu_{12}^2}{1/s_{11}^E} \int_{(a-l_p)/2}^{(a+l_p)/2} \frac{1}{I_p(y)} \, dy, \\
\frac{1}{K_{\theta y2}^E} &= \frac{1-\nu^2}{Y} \int_{(a-l_p)/2}^{(a+l_p)/2} \frac{1}{I(y)} \, dy, & \frac{1}{K_{\theta y4}^E} &= \frac{1-\nu^2}{Y} \int_{(a+l_p)/2}^{a} \frac{1}{I(y)} \, dy,
\end{aligned} \tag{5.10}$$

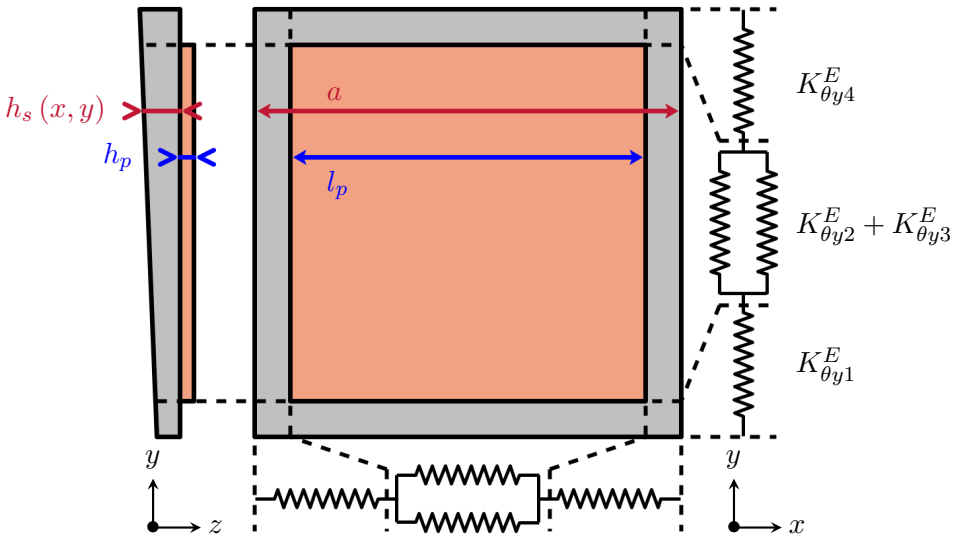

Figure 5.13: Square plate of variable thickness h_s covered by a square piezoelectric patch of constant thickness h_p. The stiffness of each portion of the plate and the piezoelectric patch can be modeled as a spring, such as drawn on the right hand-side. The represented thicknesses are not to scale.

where ν and Y are the Poisson's ratio and the Young's modulus of the plate, and I and I_p are the second moments of area of the structure and of the piezoelectric patch, respectively. As discussed in the aside of subsection 4.5.3, I and I_p can be either computed with respect to the mid-surface of the plate or to the mid-surface of the entire structure. The thickness of each piezoelectric patch being set at 1/6 of the mean thickness of the plate portion it covers, we have shown on the constant thickness plate example that the difference between the two models is negligible. Thus the expressions that we use, which are only valid assuming the piezoelectric patches are thin, are as follows:

$$I(y) = \int_0^a \int_{-h_s(x,y)/2}^{h_s(x,y)/2} z^2 \, dx \, dz, \qquad I_p(y) = \int_{(a-l_p)/2}^{(a+l_p)/2} \int_{h_s(x,y)/2}^{h_s(x,y)/2+h_p} z^2 \, dx \, dz. \tag{5.11}$$

Similar equations can be written to estimate the bending stiffness $K^E_{\theta x}$ when x is deemed as the normal axis. Because of the thickness variations, the bending stiffness $K^E_{\theta x}$ and $K^E_{\theta y}$ along the in-plane directions have two different values. In the end, the stiffness in the frequency coherence condition is calculated as the mean value of $K^E_{\theta x}$ and $K^E_{\theta y}$:

$$K^E_\theta = \frac{1}{2}\left(K^E_{\theta x} + K^E_{\theta y}\right). \tag{5.12}$$

The computed distributions of m and K^E_θ for $n_0 = 1$ are represented in figures 5.14a and 5.14b.

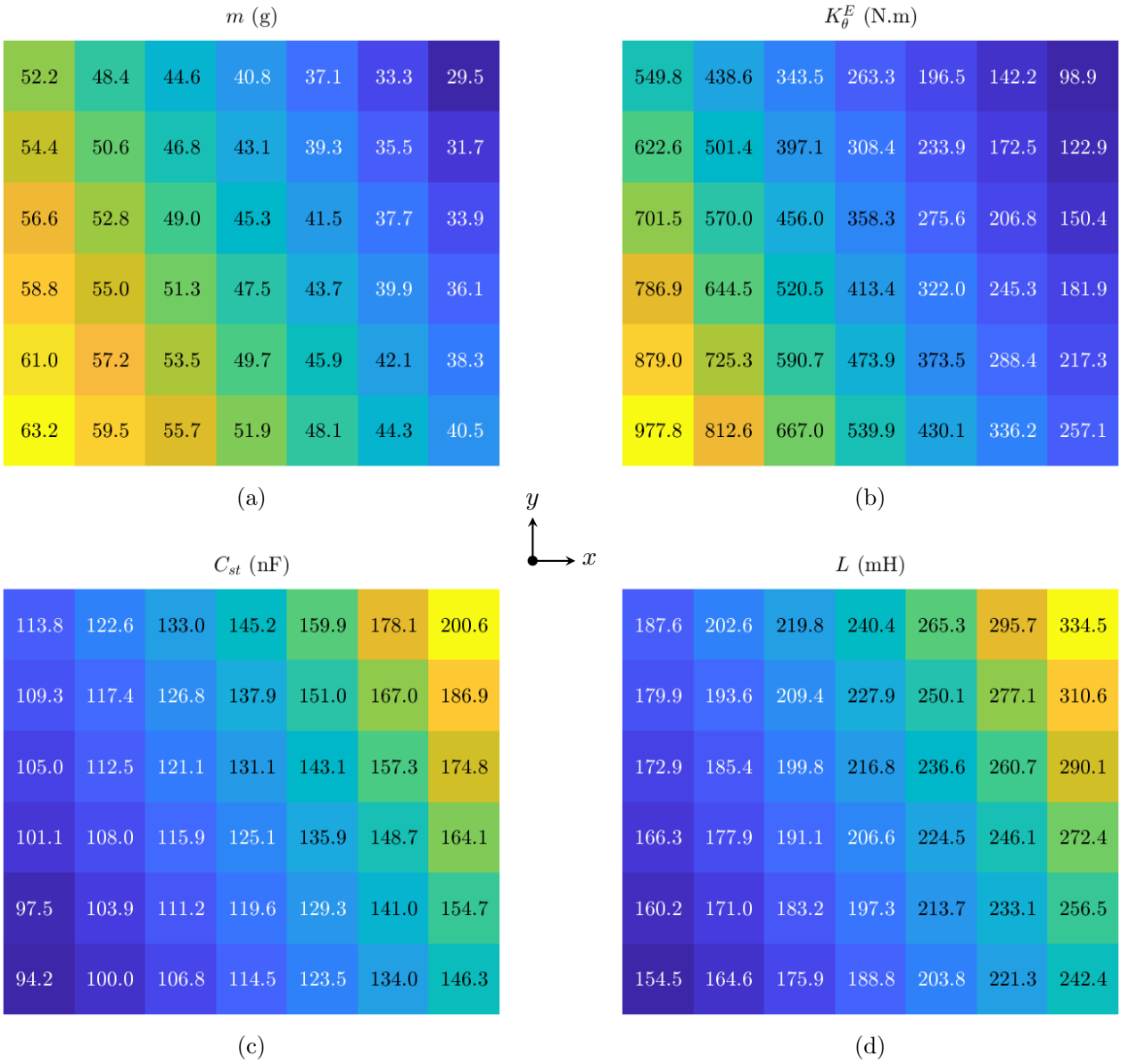

Figure 5.14: Distributions of discrete variables over the unit cells for the variable thickness plate in the case of $n_0 = 1$: (a) discrete mass m (in g), (b) bending stiffness K_θ^E (in N.m), (c) static piezoelectric capacitance C_{st} (in nF), and (d) resulting inductance L (in mH).

5.4.2.3 Electrical parameters evaluation

The static capacitances C_{st} distribution is modeled using the finite element formulation of equation (5.1). Results for $n_0 = 1$ are shown in figure 5.14c. As opposed to the case of a periodic plate in figure 4.26, the distribution is clearly non-uniform. This stems from the structure being non-periodic.

Indeed, the piezoelectric transducers thicknesses are set at 1/6 of the mean thickness of the plate portion they cover. Therefore, the patches on the bottom left and on the top right of the plate are the thickest and the thinnest patches, respectively. This explains that these unit cells exhibit the smallest and largest static capacitances C_{st}, respectively.

Finally, the transformer ratio is arbitrary set at $\hat{a} = 4$. Thus the inductance value L can be derived for each unit cell of the network by applying the frequency coherence condition of equation (5.6):

$$L = \left(\frac{a}{\hat{a}}\right)^2 \frac{m}{K_\theta^E C_{st}}. \tag{5.13}$$

The resulting inductance distribution for $n_0 = 1$, which is plotted in figure 5.14d, is a bit counter-intuitive. Indeed, according to the direct electromechanical analogy that we have applied to derive the plate electrical analogue, inductance is analogous to mass. Therefore we could have expected the inductance distribution to look like the mass distribution in figure 5.14a. However, the ratios of the largest value over the smallest value of the distributions of m and C_{st} is around two, while it is around ten for the distribution of K_θ^E. As a consequence, the distribution of L is more influenced by the bending stiffness distribution than the mass distribution.

5.4.2.4 Network validation

The network validation is conducted by comparing its mode shapes and natural frequencies to those of the structure modeled by the finite element method. These comparisons are represented in figures 5.15 and 5.16, respectively. The analogy between the two systems is ensured up to the tenth mode and nearly 1 kHz even for $n_0 = 1$, which is promising for broadband vibration damping.

5.4.3 Broadband damping

The behavior of the plate of variable thickness being coupled to its electrical analogue is finally studied. We propose a realistic design of the inductive components for $n_0 = 1$ and $n_0 = 2$ in table 5.3. The components of minimum and maximum inductance values are considered. These characteristics, as well as remembering that the produced inductors of 246.6 mH in section 4.2 have a series resistance of 13.7 Ω, show that it is a reasonable expectation for the network inductors to exhibit a series resistance of 15 Ω for $n_0 = 1$ and of 5 Ω for $n_0 = 2$.

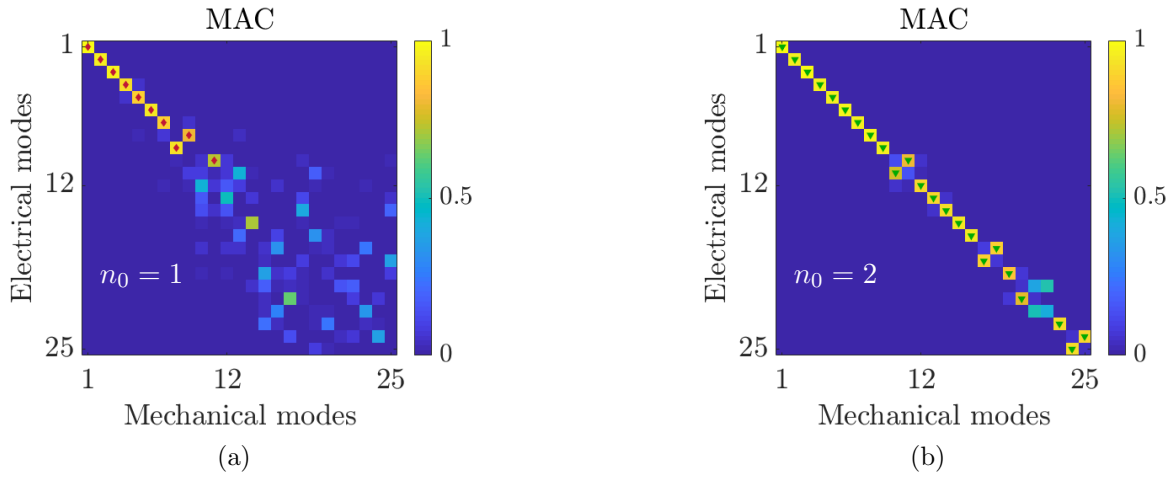

Figure 5.15: MAC between the 25 first velocity modes of the variable thickness plate covered with piezoelectric patches and the 25 first electrical current modes of the network for (a) $n_0 = 1$ and (b) $n_0 = 2$. The tiny ♦ and ▾ markers indicate which couple of modes are deemed clearly identified, so that they can be plotted in figure 5.16.

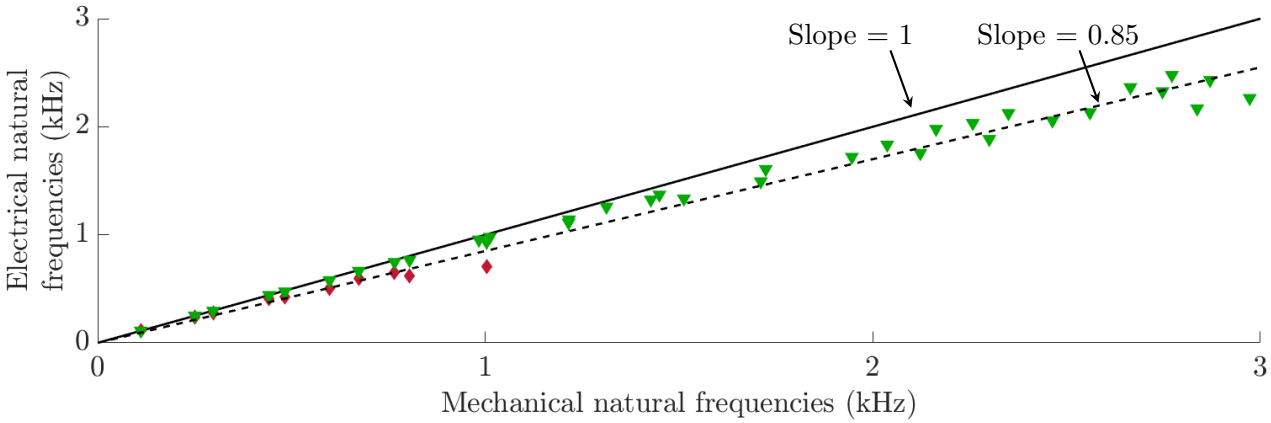

Figure 5.16: Comparison of mechanical and electrical natural frequencies for (♦) $n_0 = 1$ and (▾) $n_0 = 2$.

n_0	Core geometry	l_e (mm)	l_w (mm)	A_e (mm^2)	A_w (mm^2)	A_L (nH)	N (turns)	d_w (μm)	k_u (%)	L (mH)	R_{sL} (Ω)
1	RM 10	42	52	83	40.2	630	495	250	60	154.5	9
							730	200	57	334.5	20
2	RM 10	42	52	83	40.2	630	245	300	43	37.4	3
							375	250	46	87.7	7

Table 5.3: Forecast characteristics of the components of minimum and maximum inductance made in N48 ferrite material [108] for the variable thickness plate electrical analogue with $n_0 = 1$ or $n_0 = 2$.

Besides, for $n_0 = 1$, the same non-ideal transformers as described in section 4.3 are considered. However, simulations show that using them for $n_0 = 2$ leads to the overdamping of the resulting electromechanical system, and thus to a deteriorated damping performance. Therefore other transformers should be designed. The objective remains to produce transformers whose magnetizing inductance L_m is at least fifty times greater than the inductance L when referring to the same transformer side:

$$L_m \geq 50\hat{a}^2 L. \tag{5.14}$$

With the notations of section 4.3, we recall the expressions of the magnetizing inductance L_m and of the series resistance R_{sT} standing for the copper losses, both referred to the primary side:

$$L_m = A_L N_1^2 \qquad \text{and} \qquad R_{sT} = \varrho \left[\frac{N_1 l_{w1}}{S_{w1}} + \hat{a}^2 \, \frac{N_2 l_{w2}}{S_{w2}} \right]. \tag{5.15}$$

For $n_0 = 2$, the network inductors range from three to six times smaller than the inductors of 246.6 mH of the periodic plate analogue. Assuming the inductance is roughly four times smaller in the present application, then according to the equation (5.14), the magnetizing inductance L_m of transformers can be four times smaller as well, while still being large enough not to alter the network dynamics. Hence, the equation (5.15) indicates that the number of turns N_1 can be reduced by a factor of two, which divides R_{sT} by two as well. In addition, dividing N_1 by two also divides the filling factor k_u by two. This means that the wire sections S_{w1} and S_{w2} can be virtually multiply by two to attain a similar filling factor. According to the equation (5.15), thicker wires decrease R_{sT} by another factor of two. In the end, one estimate that the series resistance R_{sT} of transformers could be divided by four if new components had to be produced. This assumption is applied to the model of coupled systems.

The excitation is applied to the plate surface where the piezoelectric patches are bonded, at the same (x, y) location as the point which is drawn in figure 5.2. The driving-point mobility simulated using the model of equation (5.3) for $n_0 = 1$ is plotted in figure 5.17. Note that the hysteretic damping which is applied to the plate induces some damping in the coupled electromechanical system, even when the network is non-dissipative. Meanwhile, the objective of the designed analogous network is met, as the first few modes of the variable thickness plate are damped thanks to the piezoelectric coupling with the network. However, one can notice on figure 5.16 that there is a gap of nearly 15 % between electrical and mechanical natural frequencies of the last few couples of modes for $n_0 = 1$. This

explains that the damping performance at higher frequencies is limited, as can be seen in figure 5.17. The dissipative components of the network still allow mitigating vibrations up to 700 Hz, but the electrical resonance are not coincident with the mechanical ones. Therefore, the damping effect at higher frequencies is closer to the effect that would be achieved with a resistive network [113, 53]. This can be understood by looking at figure 5.18, which considers the piezoelectric network damping of a variable thickness plate with $n_0 = 2$. In this case, the damping performance improves at higher frequencies, which is coherent with the comparison of natural frequencies in figure 5.16 for $n_0 = 2$.

In any case, these results validate the efficiency of the damping solution here proposed. Besides, resistors could be modified or included in different positions of the network in order to enhance the damping performance. Moreover, as written in the aside of section 5.2, the inductors and transformers of the network are not optimized in terms of stored energy, since there is no proposed context for this application. However, the components characteristics are realistic, which gives hope to achieve piezoelectric network damping with fully passive electrical components. This numerical example highlights the feasibility of integrating such a broadband damping solution with purely passive components to a complex structure.

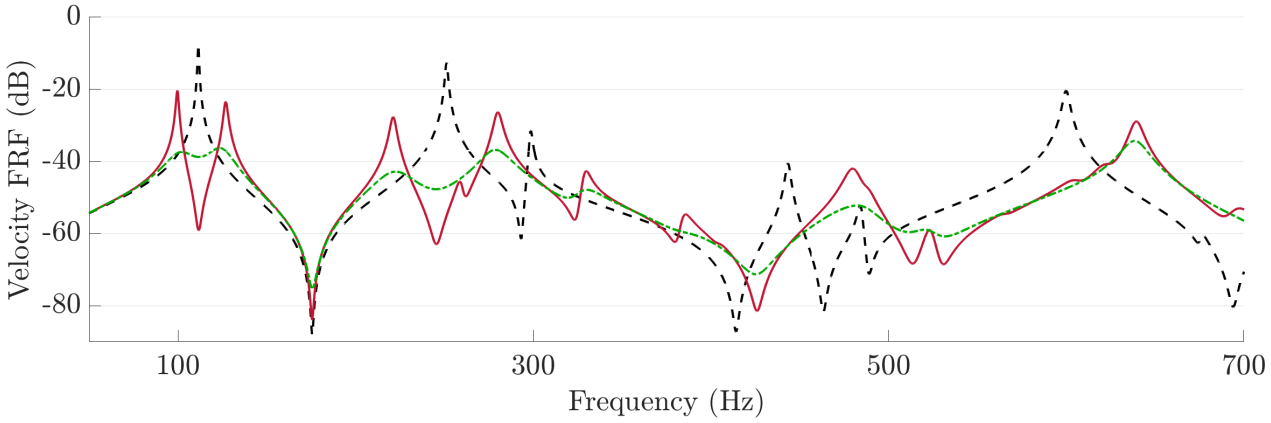

Figure 5.17: Comparison of simulated velocity FRFs for $n_0 = 1$: ---- FRF with short-circuited piezoelectric patches, and FRF when the variable thickness plate is connected to —— a non-dissipative analogous network and – – – a dissipative analogous network.

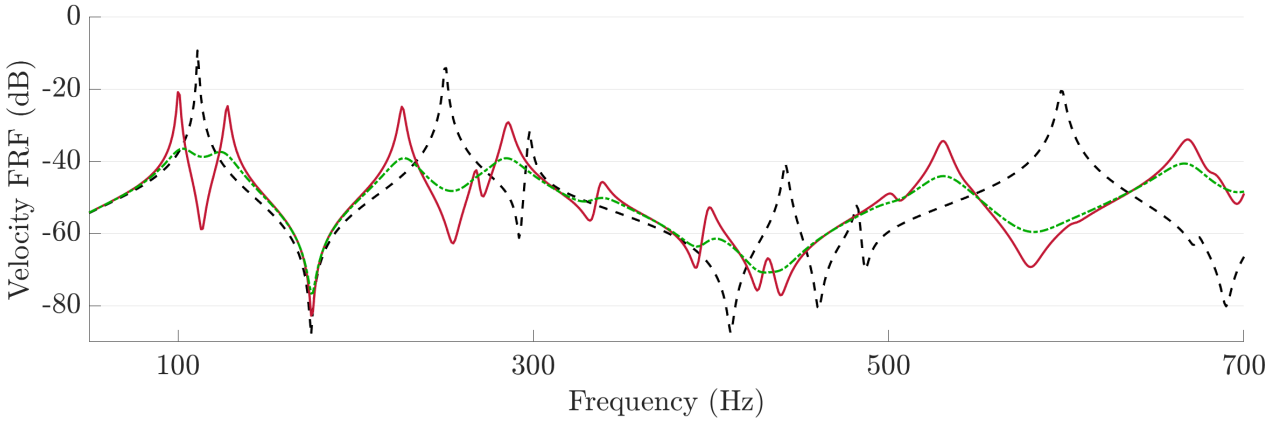

Figure 5.18: Comparison of simulated velocity FRFs for $n_0 = 2$: ---- FRF with short-circuited piezoelectric patches, and FRF when the variable thickness plate is connected to —— a non-dissipative analogous network and – – – a dissipative analogous network.

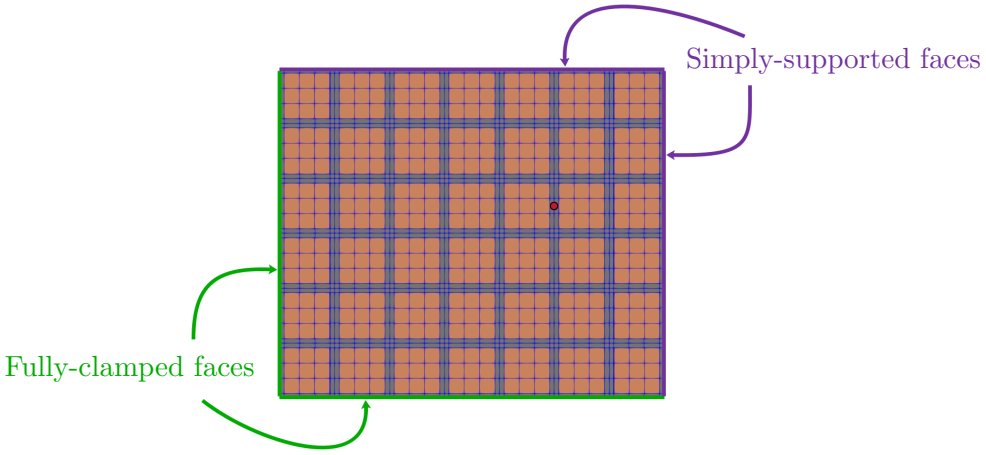

Figure 5.19: Rectangular plate with mixed boundary conditions and • (x, y) location of both the excitation and the velocity measurements.

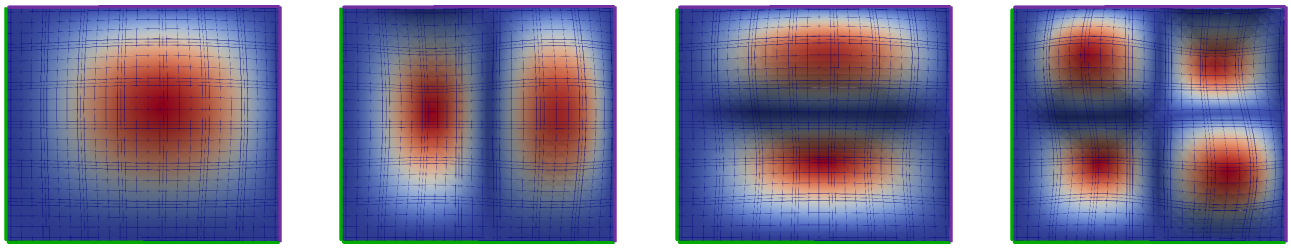

(a) First mode shape at 133.5 Hz

(b) Second mode shape at 270.9 Hz

(c) Third mode shape at 326.8 Hz

(d) Fourth mode shape at 456.3 Hz

Figure 5.20: Shapes of the first four bending modes of the plate with mixed boundary conditions.

5.5 Plate with mixed boundary conditions

5.5.1 Structure description

We consider a case whose geometry is the same as previously studied in chapters 3 and 4: it is a rectangular plate of sides $l_x = 420$ mm and $l_y = 360$ mm and of thickness $h_s = 3$ mm. Square piezoelectric patches are periodically bonded to the plate, and cover $(5/6)^2$ of its surface. A scheme of the structure is proposed in figure 5.19. The complexity comes from the boundary conditions, which are mixed: two adjacent side faces of the structure are fully-clamped, while the two other side faces are simply-supported. It modifies the structure behavior near the edges, as it is illustrated by the first simulated modes which are drawn in figure 5.20. While piezoelectric network damping has been achieved for a fully-clamped plate in [72] and for a fully-supported plate in the chapter 4 of the present manuscript, it has never been applied to a plate with mixed boundary conditions.

5.5.2 Analogous network

5.5.2.1 Unit cells selection

Among the available elements of the library in section 2.10, the square plate electrical analogue remains the one that describes the best the structure dynamics. For this element, we have derived the electrical boundary conditions which are analogous to simply-supported and fully-clamped mechanical boundary conditions. Therefore, the complexity of this numerical example is not induced by an approximation in the structure dynamics, but rather comes from mixing the boundary conditions of the structure. This makes the electrical network to be assembled non-periodic. We recall that the frequency coherence condition expressed by the equation (5.6) should be locally verified so that the structure and its analogous network exhibit similar properties for bending wave propagation. Like in the previous section, the discrete mechanical parameters m and K_θ^E and the static piezoelectric capacitance C_{st} are going to be estimated. The tuning parameters are the remaining electrical components, namely the transformer ratio $\hat{a}$ and the inductance L.

5.5.2.2 Mechanical parameters evaluation

As for the case of the variable thickness plate in section 5.4, the structure can be discretized by $7n_0 \times 6n_0$ square elements, n_0 being integer. The figure 5.19 represents the plate geometry for $n_0 = 1$. As a consequence, the computation of the cell side a and of the discrete mass m are still conducted using equations (5.7) and (5.8), respectively.

Meanwhile, the mechanical model to estimate the value of K_θ^E is mostly the same as in subsection 5.4.2.2. The only differences are that the structure thickness h_s is constant, and that we choose to compute the second moments of area I of the structure and I_p of the piezoelectric transducers with respect to the mid-surface of the entire structure. The reason for this is that we have noticed that the resulting first electrical natural frequency is closer to the mechanical one by doing so. The expressions of said-second moments become

$$I(y) = \int_0^a \int_{-(h_s+h_p)/2}^{(h_s-h_p)/2} z^2 \, dx \, dz, \qquad I_p(y) = \int_{(a-l_p)/2}^{(a+l_p)/2} \int_{(h_s-h_p)/2}^{(h_s+h_p)/2} z^2 \, dx \, dz. \tag{5.16}$$

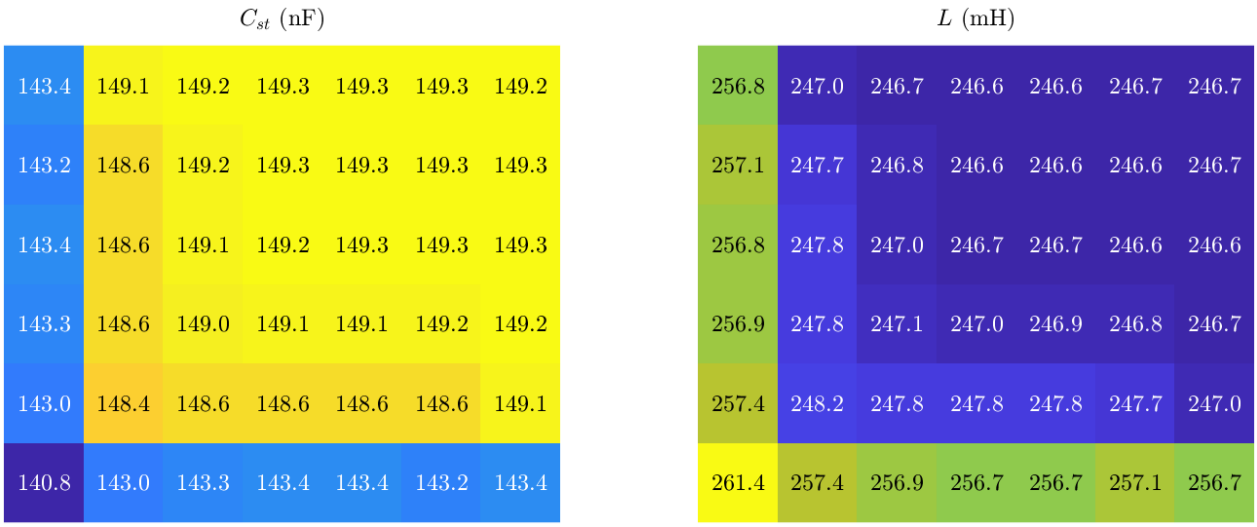

Figure 5.21: Distributions of discrete variables over the unit cells for the plate with mixed boundary conditions in the case of $n_0 = 1$: (a) static piezoelectric capacitance C_{st} (in nF), and (b) resulting inductance L (in mH). Distributions of m and K_θ^E are not represented since they are uniform.

5.5.2.3 Electrical parameters evaluation

The static piezoelectric capacitance C_{st} distribution is modeled using the finite element formulation of equation (5.1). Results for $n_0 = 1$ are shown in figure 5.21a. The distribution is non-uniform because of the mechanical boundary conditions. Indeed, the plate movements are more restrained along its clamped faces than along the supported ones, which influences the static capacitance. One can also notice that the distribution tends towards the fully-supported plate distribution of figure 4.26 distancing from the clamped edges.

Finally, the transformer ratio is arbitrary set at $\hat{a} = 4$. Thus the inductance value L can be derived for each unit cell of the network by applying the frequency coherence condition of equation (5.6). The corresponding expression is the equation (5.13). The resulting distribution for $n_0 = 1$ is plotted in figure 5.21b. The distribution is non-uniform, and we also notice that once we move away from the clamped edges, the distribution also tends towards the mean value of 246.6 mH which has been derived in section 4.5 for the fully-supported plate. Besides, since C_{st} is the only parameter whose distribution is non-uniform over the system, it is consistent with the equation (5.13) that the L and C_{st} distributions are reversed.

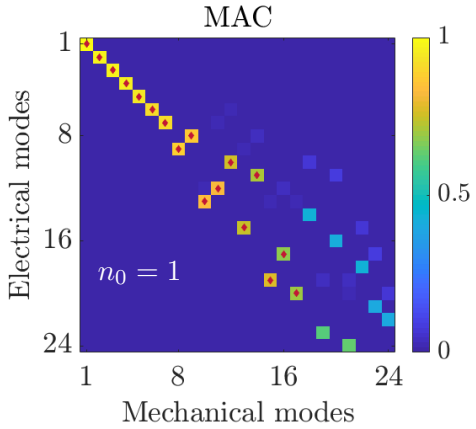

Figure 5.22: MAC between the 24 first velocity modes of the plate with mixed boundary conditions covered with piezoelectric patches and the 24 first electrical current modes of the network for $n_0 = 1$. The tiny ♦ markers indicate which couple of modes are deemed clearly identified, so that they can be plotted in figure 5.23.

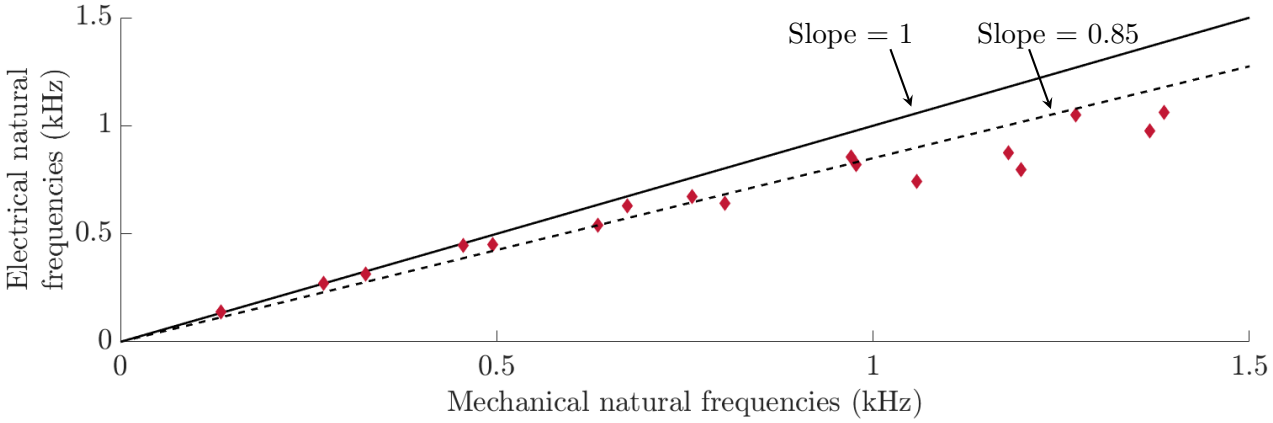

Figure 5.23: Comparison of mechanical and electrical natural frequencies for (♦) $n_0 = 1$.

5.5.2.4 Network validation

The network validation is conducted by comparing its mode shapes and natural frequencies to those of the structure modeled by the finite element method. These comparisons are represented in figures 5.22 and 5.23, respectively. The analogy between the two systems is ensured up to nearly fifteen modes and 1.5 kHz even for $n_0 = 1$, which is promising for broadband vibration damping.

5.5.3 Broadband damping

For the vibration mitigation of the plate with mixed boundary conditions, we suggest using a realistic design of its inductors and transformers. It has been shown in the subsection 5.4.3 that expecting the produced inductors to exhibit a series resistance of 15 Ω for $n_0 = 1$ is reasonable. At the same time, simulations of the coupling between the structure and its analogous network that integrate the transformers designed in section 4.3 have proven that they are adequate for $n_0 = 1$.

Both the excitation and the measurement are made on the plate side which is covered by the piezoelectric transducers, at the position located in figure 5.19. The driving-point mobilities simulated using the model of equation (5.3) for $n_0 = 1$ are plotted in figure 5.24. The information that can be extracted from these simulations is quite similar to the case of the variable thickness plate: broadband vibration damping is achieved, and the damping performance is enhanced at higher frequencies when the network is composed of more elements.

This example brings the opportunity to discuss about the precision of the proposed mechanical models to estimate K_θ^E. Notice in figure 5.24 that two non-equal peaks appear around the first mechanical mode at around 133.5 Hz. They would also appear if $n_0 = 2$, that is if the network has two times more elements along each direction. In the classical theory of tuned mass dampers, this height difference is caused by the first natural frequency of the network not being equal to the first natural frequency of the plate. Estimating the bending stiffness K_θ^E with a more precise analytical model [111] or with a 3D finite element model is probably the way to go to improve the electrical network tuning. Note however that the gap between the first mechanical and electrical natural frequencies is estimated at around 2 % in this case. This is the same order of magnitude that manufacturers exhibit on magnetic

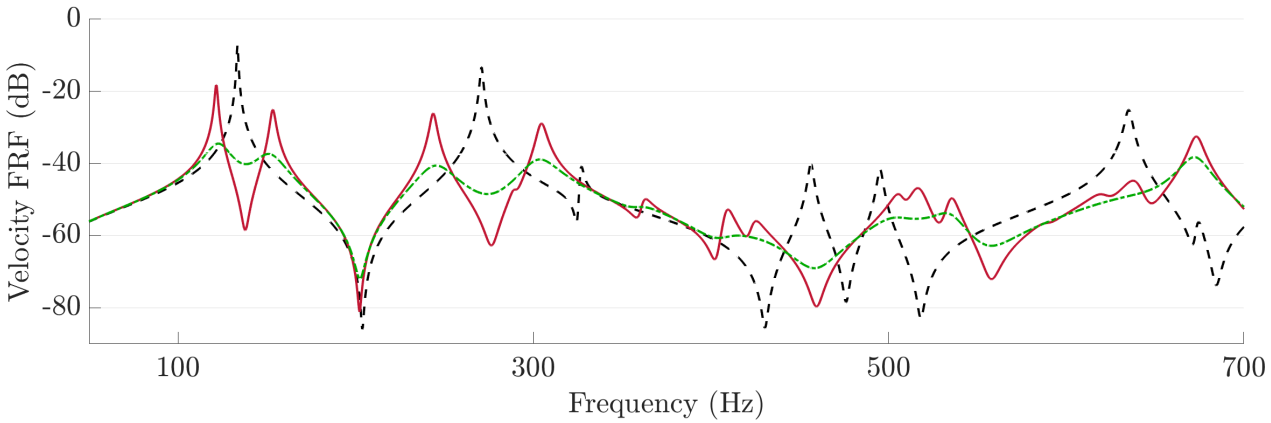

Figure 5.24: Comparison of simulated velocity FRFs for $n_0 = 1$: ---- FRF with short-circuited piezoelectric patches, and FRF when the plate with mixed boundary conditions is connected to —— a non-dissipative analogous network and – – – a dissipative analogous network.

and materials constants of the soft ferrites which are used to produced the network inductors. Hence it is actually not of prime importance to improve the ideal electrical components estimation.

Nonetheless, these results validate that piezoelectric network damping can be applied in a case of a plate with mixed boundary conditions as well. Even though we have not conducted a numerical optimization of the damping performance, considering realistic characteristics for network components makes the present case another example of how broadband damping could be achieved with a fully passive electrical network.

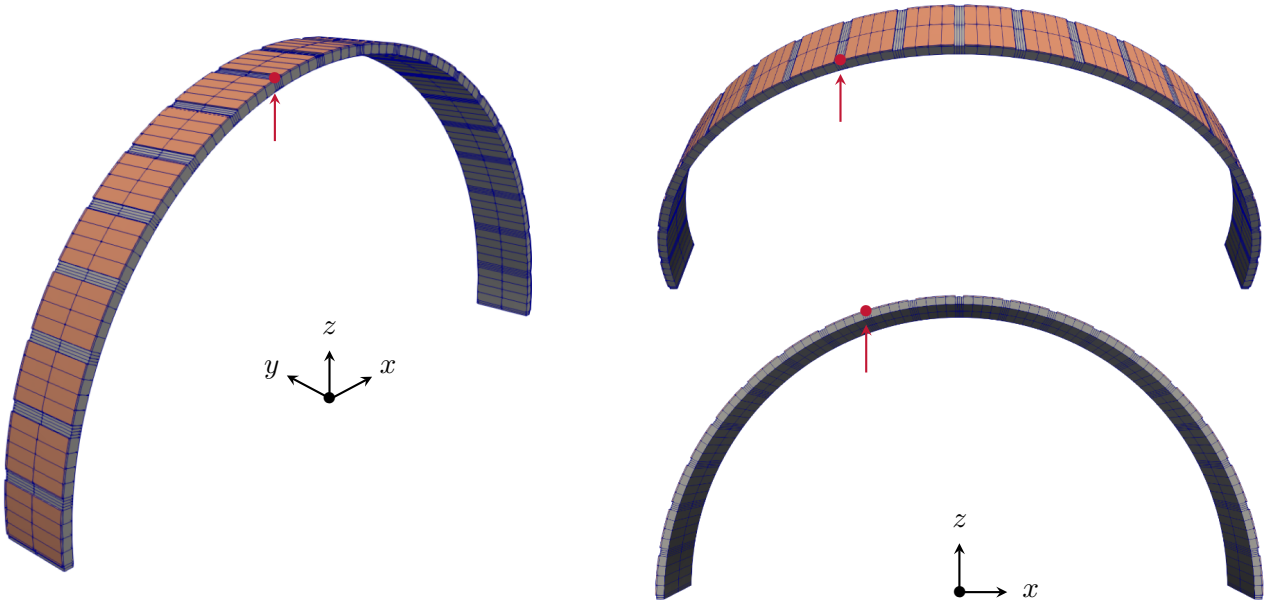

Figure 5.25: Meshing of the semicircular arch periodically covered by $n = 20$ piezoelectric patches, and • location of both the excitation and the velocity measurements for the FRFs plotted in figures 5.32 and 5.33.

5.6 Semicircular arch

5.6.1 Structure description

The studied case is a semicircular arch whose extremities are clamped. As represented in figure 5.25, its dimensions are a radius $R = 200$ mm, a width $b = 40$ mm and a thickness $h_s = 5$ mm. Piezoelectric patches of the same width b and of thickness $h_p = h_s/6$ periodically cover 5/6 of the external surface of the arch. This means that the length l_p of the piezoelectric patches neutral axis is

$$l_p = \frac{5}{6} \frac{\pi \left(R + \frac{h_s}{2} + \frac{h_p}{2} \right)}{n}. \tag{5.17}$$

We predict the assembled electrical analogue to be slightly non-periodic, because of the mechanical boundary conditions effect on the static piezoelectric capacitance. Therefore, the complexity of the present case does not come from non-periodicities. It rather stems from the curvature, which has not been treated in terms of piezoelectric network damping yet, and from the fact that modes of different kinds appear in the frequency range.

Bendable piezoelectric patches

PZT materials are brittle, and thus it is challenging to bond piezoelectric patches to a curved structure. A solution to bend them is to insert a layer of piezoelectric material between layers of polymer material. The polymer serves as an insulation layer and generates a preload on the piezoelectric material. It increases the ultimate tensile strength of the piezoelectric part [114], and hence allows slightly bending it. The commercially available components require a bending radius of several centimeters at least. We do not model additional polymer layers in the present manuscript, since the piezoelectric transducers are bonded to a surface whose radius is $R + h_s/2 = 202.5$ mm. Thus we assume bonding transducers to the considered structure is possible by following the process described in subsection 3.3.1.

5.6.2 Analogous network

5.6.2.1 Unit cells selection

Among the available elements of the library in section 2.10, the curved beam electrical analogue is selected to form the network. The notations we use going forward are the same as in section 2.8. We recall the frequency coherence conditions that should be locally verified so that the structure and the assembled network exhibit similar modal properties:

$$\frac{a}{R} = \frac{\hat{a}}{\hat{R}}, \qquad \frac{K_v}{m} = \frac{1}{LC_v}, \qquad \frac{1}{a^2}\,\frac{K_\theta^E}{m} = \frac{1}{\hat{a}^2}\,\frac{1}{LC_{st}}. \tag{5.18}$$

The objective is now to estimate the mechanical parameters appearing in the previous equations. The static piezoelectric capacitance can be estimated as well by using an adequate finite element formulation. The remaining electrical parameters, namely the transformers ratios parameters $\hat{a}$ and $\hat{R}$, the inductance L and the capacitance C_v, will then be estimated by applying the frequency coherence conditions.

5.6.2.2 Mechanical parameters evaluation

The radius of the arch is $R = 200$ mm. Since it is discretized by n elements, we have

$$a = \frac{\pi R}{n}. \tag{5.19}$$

Knowing the dimensions of the structure, as well as the mass densities of the involved materials, the discrete mass m is

$$m = \rho a b h_s + \rho_p l_p b h_p. \tag{5.20}$$

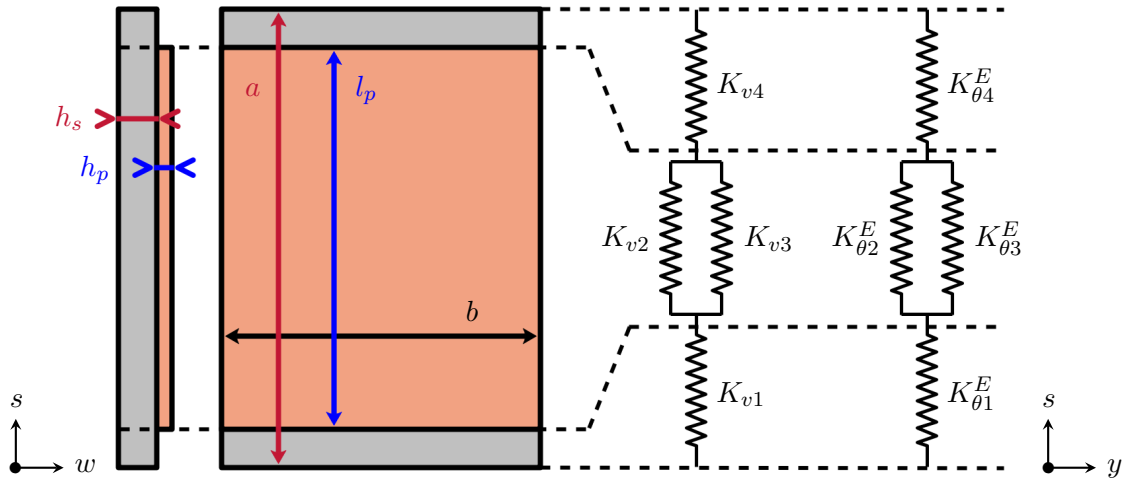

Figure 5.26: Curved beam element of constant thickness h_s covered by a curved piezoelectric patch of constant thickness h_p. The stiffness of each portion of the beam and the piezoelectric patch can be modeled as a spring, such as drawn on the right hand-side. The represented thicknesses are not to scale.

As far as the mechanical stiffnesses go, the discrete mechanical model represented in figure 5.26 is considered. A portion of the arch covered by a piezoelectric patch is sketched in the local frame, with s standing for the arc length direction and w denoting the orthogonal direction to s and y. Each portion of the element is modeled by a discrete spring. This means that we suggest computing the values of the longitudinal stiffness K_v and the bending stiffness K^E_θ with the following equations:

$$\frac{1}{K_v} = \frac{1}{K_{v1}} + \frac{1}{K_{v2}+K_{v3}} + \frac{1}{K_{v4}} \qquad \text{and} \qquad \frac{1}{K^E_\theta} = \frac{1}{K^E_{\theta 1}} + \frac{1}{K^E_{\theta 2}+K^E_{\theta 3}} + \frac{1}{K^E_{\theta 4}}, \tag{5.21}$$

where the involved discrete stiffnesses, which are indicated in figure 5.26, are expressed by

$$\begin{aligned}
\frac{1}{K_{v1}} &= \frac{1}{Y}\int_0^{(a-l_p)/2} \frac{1}{bh_s}\,ds, & \frac{1}{K_{v3}} &= \frac{1}{1/s^E_{11}}\int_{(a-l_p)/2}^{(a+l_p)/2} \frac{1}{bh_p}\,ds,\\
\frac{1}{K_{v2}} &= \frac{1}{Y}\int_{(a-l_p)/2}^{(a+l_p)/2} \frac{1}{bh_s}\,ds, & \frac{1}{K_{v4}} &= \frac{1}{Y}\int_{(a+l_p)/2}^{a} \frac{1}{bh_s}\,ds,\\
\frac{1}{K^E_{\theta 1}} &= \frac{1}{Y}\int_0^{(a-l_p)/2} \frac{1}{I(s)}\,ds, & \frac{1}{K^E_{\theta 3}} &= \frac{1}{1/s^E_{11}}\int_{(a-l_p)/2}^{(a+l_p)/2} \frac{1}{I_p(s)}\,ds,\\
\frac{1}{K^E_{\theta 2}} &= \frac{1}{Y}\int_{(a-l_p)/2}^{(a+l_p)/2} \frac{1}{I(s)}\,ds, & \frac{1}{K^E_{\theta 4}} &= \frac{1}{Y}\int_{(a+l_p)/2}^{a} \frac{1}{I(s)}\,ds,
\end{aligned} \tag{5.22}$$

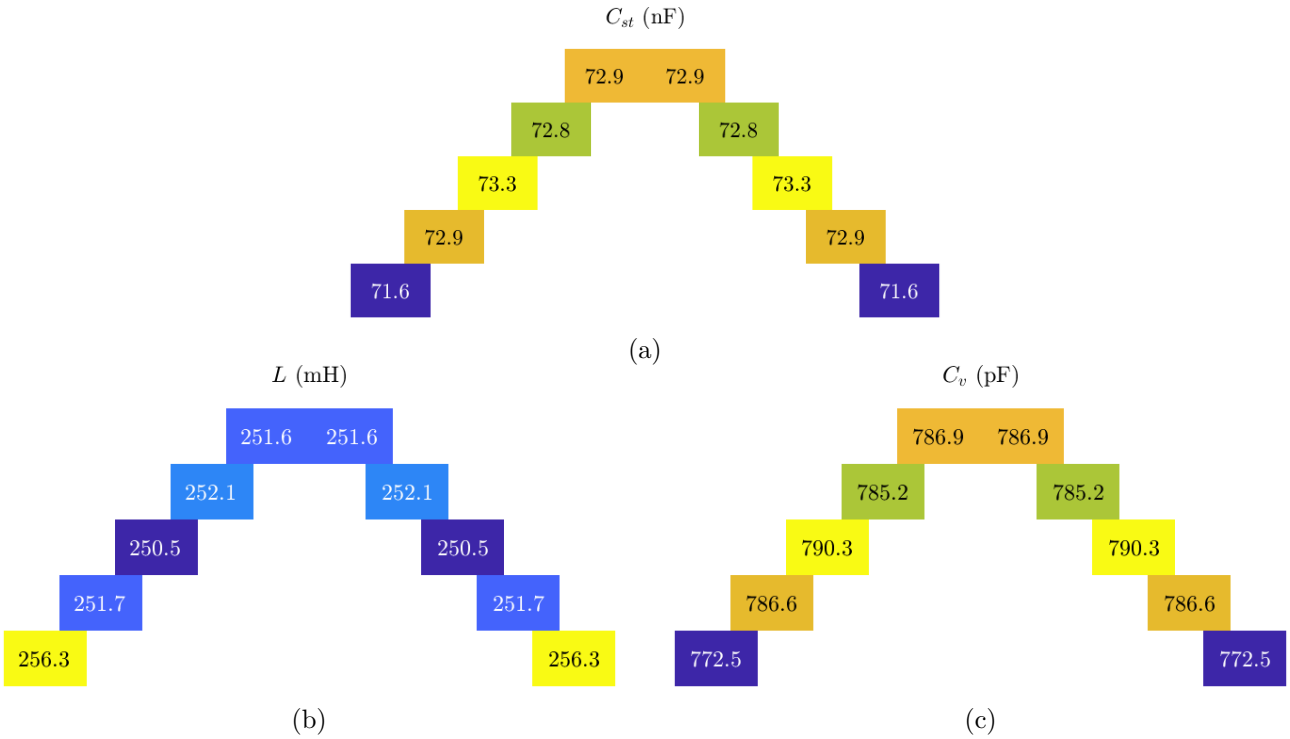

Figure 5.27: Distributions of discrete variables over the unit cells for the clamped semicircular arch in the case of $n = 10$: (a) static piezoelectric capacitance C_{st} (in nF), (b) resulting inductance L (in mH) and (c) resulting capacitance C_v (in pF).

where Y and $1/s_{11}^E$ are the Young's modulus of the structure and of the short-circuited piezoelectric patches. As opposed to the model of calculation for plates in previous examples, the Poisson's ratios are not involved in the beam equations for the bending stiffness. Meanwhile, I and I_p stand for the second moments of area of the structure and of the piezoelectric patch, respectively. In this case, the piezoelectric transducer covering $5/6 \approx 83.3$ % justifies computing I and I_p with respect to the mid-surface of the entire structure:

$$I(s) = \int_0^b \int_{-(h_s+h_p)/2}^{(h_s-h_p)/2} w^2 \, dy \, dw, \qquad I_p(s) = \int_0^b \int_{(h_s-h_p)/2}^{(h_s+h_p)/2} w^2 \, dy \, dw. \tag{5.23}$$

5.6.2.3 Electrical parameters evaluation

The finite element formulation of equation (5.1) can be used to predict the distribution of static piezoelectric capacitances C_{st}. The distribution, which is plotted in figure 5.27a for $n = 10$, is barely non-periodic because of the mechanical boundary conditions that constrain the structure movements at its extremities. Besides, the observed distribution symmetry is coherent with the structure symmetry.

The transformer ratio is arbitrary set at $\hat{a} = 4$. The remaining electrical parameters can then be derived by applying the frequency coherence conditions:

$$\hat{R} = \frac{\hat{a}}{a} R, \qquad L = \left(\frac{a}{\hat{a}}\right)^2 \frac{m}{K_\theta^E C_{st}}, \qquad C_v = \frac{m}{K_v L}. \tag{5.24}$$

Since the static piezoelectric capacitance is the only quantity whose distribution over the arch elements is non-uniform, these equations show that the inductance L distribution is reversed when compared the C_{st} distribution, while the capacitance C_v relative distribution is similar as the C_{st} distribution. Such distributions are represented as an example for $n = 10$ in figures 5.27b and 5.27c.

5.6.2.4 Network validation

The semicircular arch covered with piezoelectric transducers and the assembled electrical network should exhibit the same modal properties, so that the modal coupling condition is met when they are coupled. Their mode shapes and natural frequencies are simulated using the formulations in equations (5.1) and (5.2), respectively.

The comparison of mode shapes is first conducted using the MAC in figure 5.28. The coherence between mechanical and electrical modes is improved when the number of elements n increases. This is expected, as it corresponds to the convergence of a finite difference model towards a finite element model. However, this example highlights that there are mechanical modes which are not replicated by the network. This translates into columns of zeros in the MAC matrix. Looking at several mode shapes of the arch covered with $n = 20$ piezoelectric patches in figure 5.29 helps understanding the physical reasons for this to happen. Indeed, the second and fifth modes of the arch are out-of-plane bending modes. These modes cannot be reproduced in the electrical network, since the considered network unit cell only takes in-plane bending modes into account to be derived. In other words, another more complex network, that takes into account out-of-plane effects and vibrations, would be required to make up the arch electrical analogue over the considered frequency range. Therefore, if they are excited, these modes will appear in the FRFs of the structure and will not be affected by the network coupling.

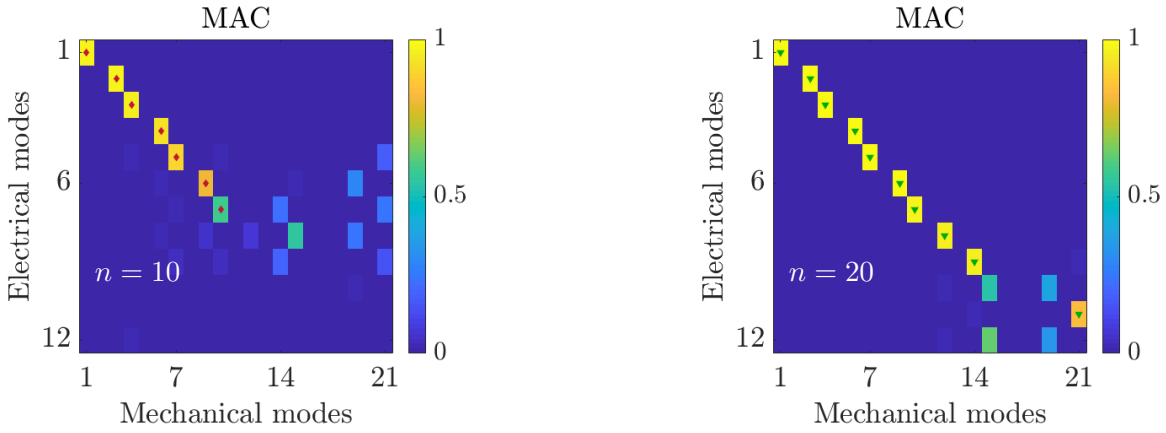

(a) (b)

Figure 5.28: MAC between the 21 first velocity modes of the semicircular arch with clamped extremities covered with piezoelectric patches and the 12 first electrical current modes of the network for (a) $n = 10$ and (b) $n = 20$. The tiny ♦ and ▼ markers indicate which couple of modes are deemed clearly identified, so that they can be plotted in figure 5.30.

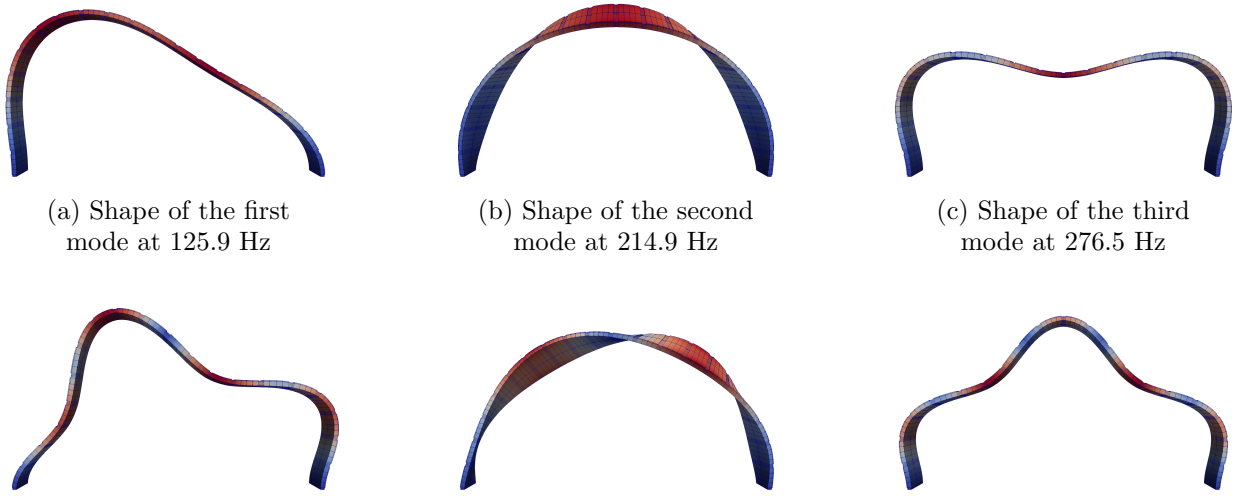

(a) Shape of the first mode at 125.9 Hz

(b) Shape of the second mode at 214.9 Hz

(c) Shape of the third mode at 276.5 Hz

(d) Shape of the fourth mode at 513.1 Hz

(e) Shape of the fifth mode at 635.0 Hz

(f) Shape of the sixth mode at 785.6 Hz

Figure 5.29: Shapes of the first six modes and corresponding natural frequencies of the clamped semicircular arch covered with $n = 20$ piezoelectric patches.

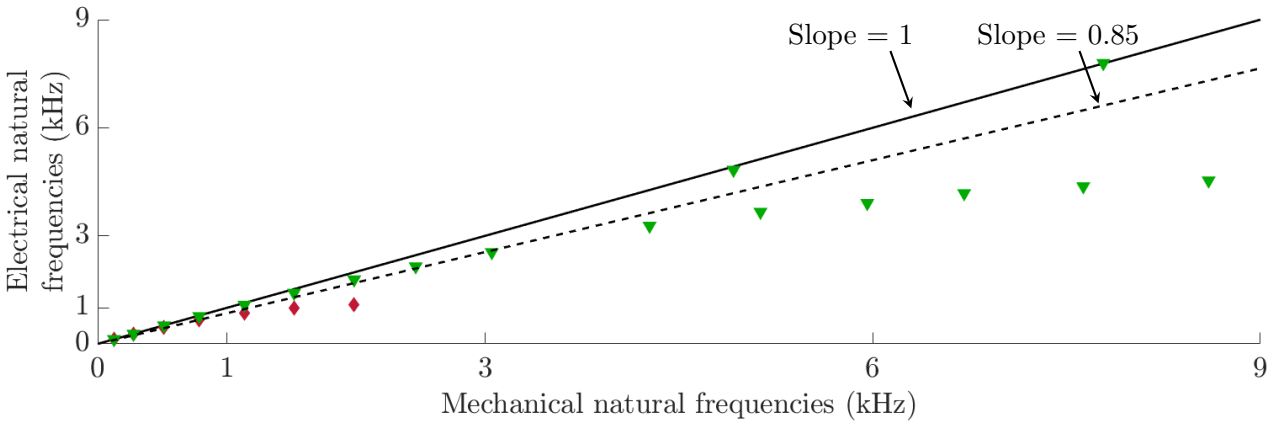

Figure 5.30: Comparison of mechanical and electrical natural frequencies for (♦) $n = 10$ and (▼) $n = 20$.

Finally, the natural frequencies of the assembled network are compared to the natural frequencies of the arch in figure 5.30. The discussion is quite similar to the previous numerical examples: the analogy between the structure and its analogous network is ensured over a given frequency range, which extends when increasing the number of elements n discretizing the network. In the present case, one can consider that the analogy is validated under 1 kHz for the first four modes when $n = 10$, and up to 3 kHz for the first nine modes when $n = 20$.

Overlap of the frequency ranges

The complexity of the case here considered is not inherent to arch-like structures. For example, the plates which have been studied in chapters 4 and 5 exhibit non-bending modes as well, which are not affected by the coupling of their structures to their respective electrical analogues. Indeed, the plate analogues previously developed are assembled from square plate electrical analogues, which only consider the bending of the structure. However, the plate dimensions make these other modes stand at much higher frequencies than the first few bending modes. Thus they did not appear in the analysis.

For the arch case, first in-plane and out-of-plane modes appear in the same the frequency range, as can be seen in figure 5.29. This is one kind of complexity treated in the ongoing numerical example.

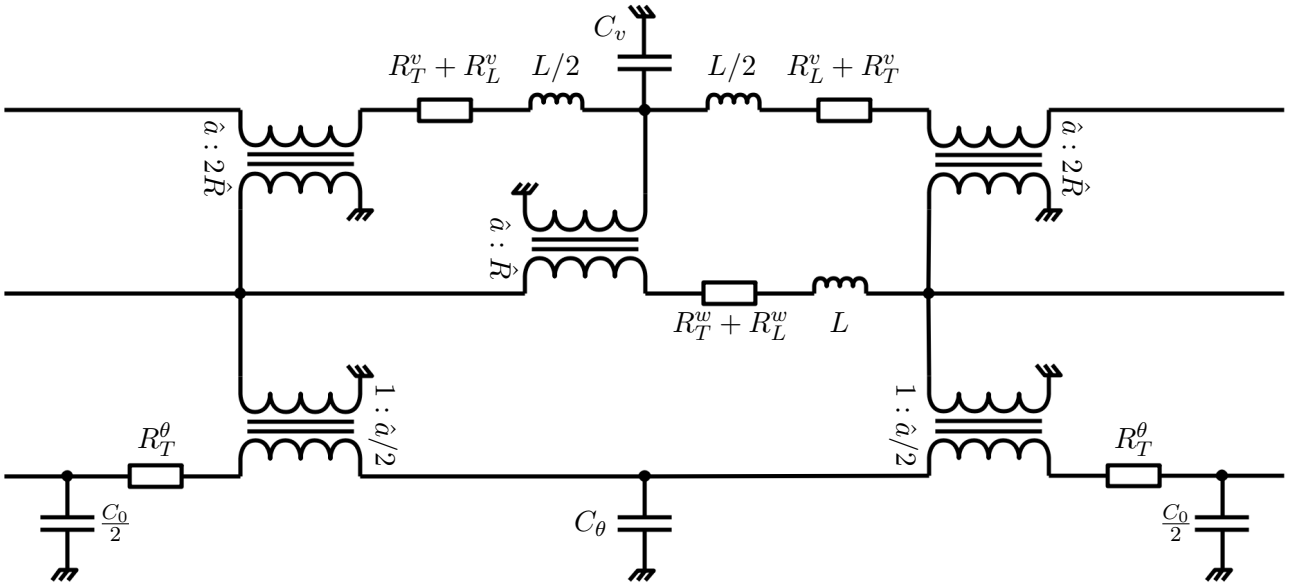

Figure 5.31: Unit cell of the dissipative arch electrical analogue.

5.6.3 Broadband damping

The vibration mitigation of the clamped arch covered by piezoelectric patches is now achieved by coupling the structure to its analogous network. As sketched in figure 5.31, dissipative components are included as series resistances for the inductors and transformers of each unit cell. The subscript T stands for the resistances which are related to transformers, while the subscript L stands for the series resistance of inductors. Meanwhile, the superscripts v, w and θ indicate in which transmission line are located the components they are associated with.

A reasonable assumption for a first design of the network inductors is to assume that the inductance distribution in figure 5.27b is nearly uniform. Therefore, designing the mean components of inductance L and $L/2$ shows that $R_L^w = 15\ \Omega$ and $R_L^v = 5\ \Omega$ for $n = 10$ elements, and $R_L^w = 3\ \Omega$ and $R_L^v = 1\ \Omega$ for $n = 20$ elements are realistic expectations for the produced components.

As far as transformers go, we do not proceed to their full design, but rather suggest setting all series resistance R_T^v, R_T^w and R_T^θ at 10 Ω for $n = 10$. It is a realistic order of magnitude when compared to the transformers produced in section 4.3. Then, for $n = 20$ the value of the inductance L has been divided by around eight, which means that it is reasonable to expect R_T^v, R_T^w and R_T^θ to be divided by eight as well if they are produced in a similar fashion. This comes from the fact that less winding turns

are required to meet the criterion on the magnetizing inductance, and that consequently thicker wires can be used to fill the winding area. This discussion has been made in more details in subsection 5.4.3.

Both the excitation and the measurement are made on the location which is highlighted in figure 5.25. This point has been selected in order to excite all modes of the frequency range. On figures 5.32 and 5.33 are plotted the driving-point mobilities obtained from the model of equation (5.3). Multimodal damping is achieved over a frequency range that increases when the discretization scheme is refined. The main difference with previous examples is that out-of-plane bending modes, which are the second, fifth and eight modes of the frequency range, are not affected by the network. This was predictable, based on the analogy validation previously conducted and the fact that these mechanical modes are not coherent with the electrical ones, as illustrated by figure 5.28. As the mechanical modes are clearly separated nonetheless, the damping performance is barely influenced by these modes which have been neglected in the electrical analogue design.

Note that it would be possible to achieve a multimodal damping performance by connecting the arch to a network resulting from adequately assembling bar and beam electrical analogues. In section 2.8, we suggested using this alternate network, denoted network B as opposed to the network A resulting from assembling curved beam analogues. In other words, an electrical analogue of the arch covered with piezoelectric patches could be described as an assembly of straight bar and beam elements, orientated by rotation matrix analogues. However, the network B requires six transformers per unit cell, while the network A requires only three. As can be seen in figures 5.32 and 5.33, realistic but not optimized components lead to a barely underdamped system. Therefore, even though the transformers design could be adapted, it is probably more challenging to avoid overdamping the first structure modes with network B, since there are more dissipative components involved. Hence using an electrical unit cell that is directly derived from equations describing the structure behavior, such as the unit cell of the network A, is probably advantageous in terms of cost and integration. Nonetheless, more work needs to be done to have definitive conclusions about this comparison between the network assembling possibilities.

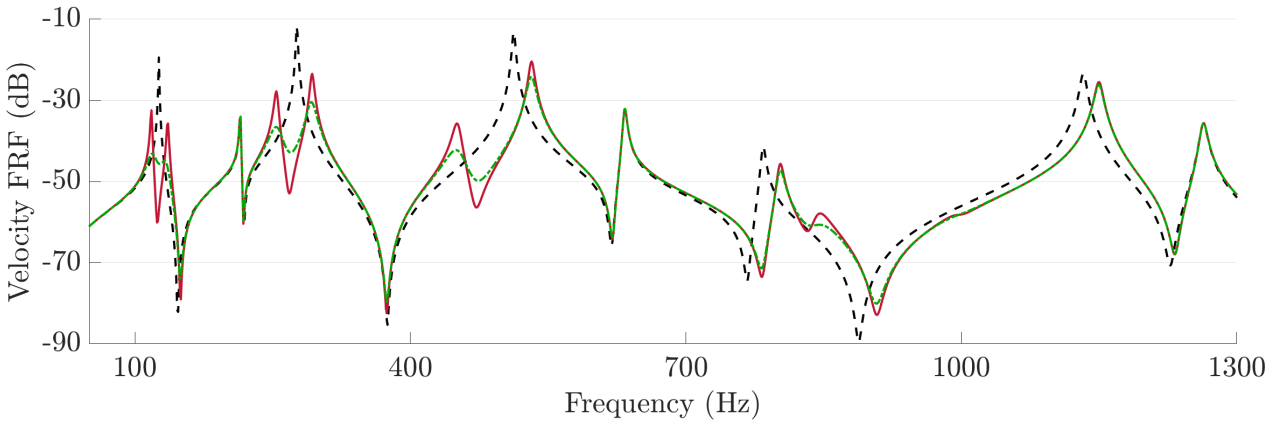

Figure 5.32: Comparison of simulated velocity FRFs for $n = 10$: - - - - with short-circuited piezoelectric patches, and when the arch is connected —— to an ideal network and - - - to a dissipative network.

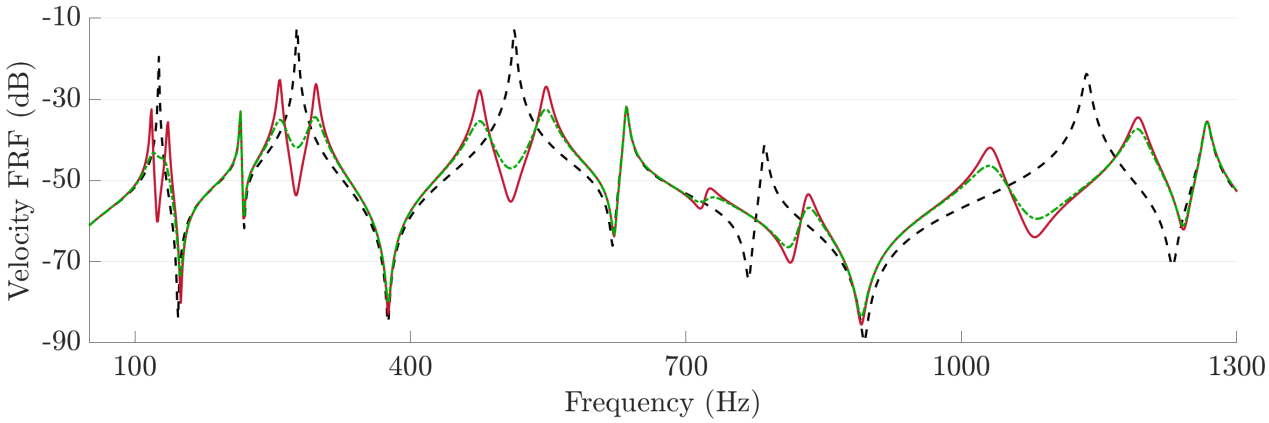

Figure 5.33: Comparison of simulated velocity FRFs for $n = 20$: - - - - with short-circuited piezoelectric patches, and when the arch is connected —— to an ideal network and - - - to a dissipative network.

As a conclusion, this numerical example is the first treated case of broadband vibration mitigation of a curved structure coupled by piezoelectric elements to its electrical analogue. The proposed electrical components are realistic, which means that we have designed a fully passive broadband damping solution for the semicircular arch. The fact that there is an overlap of frequency ranges for modes of different kinds does not affect the damping performance when modes are well-separated, but these additional modes cannot be controlled with the present network. Another unit cell that involves in-plane and out-of-plane analogous bending motions would be needed to do so.

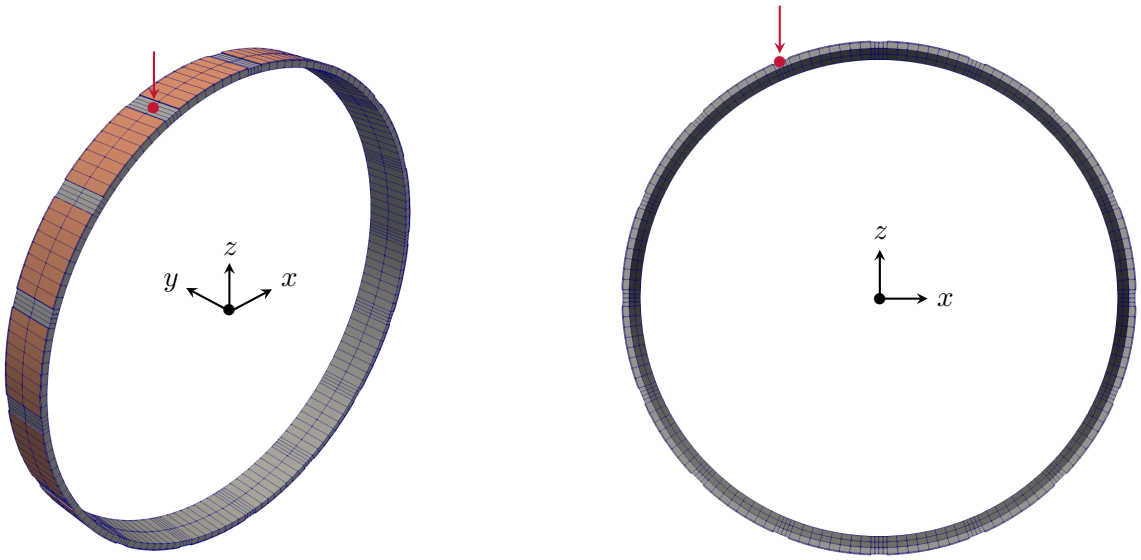

Figure 5.34: Meshing of the circular ring periodically covered by $n = 16$ piezoelectric patches, and • location of both the excitation and the velocity measurements for the FRFs plotted in figures 5.40 and 5.41.

5.7 Ring

5.7.1 Structure description

The last numerical example treated in this chapter is a free ring covered by thin piezoelectric transducers, as illustrated in figure 5.34. Its radius is $R = 200$ mm, its width is $b = 40$ mm and its thickness is $h_s = 5$ mm. There are n piezoelectric patches covering the entire width b of the ring and 5/6 of its external surface. Their thickness h_p is constant and set at 1/6 of h_s. Therefore the length l_p of the neutral axis of each piezoelectric element is

$$l_p = \frac{5}{6} \frac{2\pi \left(R + \frac{h_s}{2} + \frac{h_p}{2} \right)}{n}. \tag{5.25}$$

In the present case, the assembled electrical network should be periodic. Moreover the case of a curved structure has been studied in the previous section with the piezoelectric network damping of an arch. As a consequence, the main complexity here stems from the structure being closed on itself. This signifies that the unit cells of the electrical network should form a closed loop. Besides, because of the structure symmetry, there are pairs of mechanical modes to be damped. These two sources of complexity have not been considered before.

5.7.2 Finite element model

Since the structure presents no boundary conditions, rigid body motion is allowed. In terms of numerical simulation, this means that six natural frequencies at 0 Hz are expected. In the meantime, the structure exhibits double modes because of its symmetries: for each non-zero natural frequency, there are two modes with similar mode shapes which are shifted from one another by an angle of $\pi/(2n_l)$, with n_l being the mode shape lobes number. We prefer avoiding uncertainties related to the numerical treatment of the lack of boundary conditions and of double modes. Hence, we choose to add a numerical parameter K_0^m to the stiffness of one element of the mesh, so that its elementary mechanical stiffness matrix $\boldsymbol{K_{elm}^m}$ is replaced by $\boldsymbol{K_{elm}^m} + K_0^m \cdot \|\boldsymbol{K_{elm}^m}\| \cdot \boldsymbol{I_d}$, with $\boldsymbol{I_d}$ being the identity matrix. Increasing some terms of the diagonal of the assembled mechanical stiffness matrix $\boldsymbol{K_m}$ is equivalent to connect springs between a fixed point and the corresponding nodes of the structure mesh. The value of K_0^m is then manually set between 10^{-13} and 10^{-12}. This way, the rigid body modes are not at 0 Hz anymore, but K_0^m is small enough that they are left below 1 Hz, so they have no influence on the first structure modes. Meanwhile, even though the double modes are not equal anymore, the gap between couples of modes is maximum for the first couple, and remains inferior to 0.6 %. We consequently assume that this numerical trick does not alter the structure dynamics.

5.7.3 Analogous network

5.7.3.1 Unit cells selection

The curved beam electrical analogue is chosen among the developed unit cells in the library of section 2.10. To ensure that the assembled network exhibits the same modal properties as the ring, the frequency coherence conditions expressed in the equation (5.18) should be used to design the network components. The goal is thus to estimate the parameters of these frequency coherence conditions which are set once the structure geometry is defined. The transformers parameters $\hat{a}$ and $\hat{R}$, the inductance L and the capacitance C_v serve then as the tuning parameters.

5.7.3.2 Mechanical parameters evaluation

The radius of the arch is $R = 200$ mm. Since it is discretized by n elements, we have

$$a = \frac{2\pi R}{n}. \tag{5.26}$$

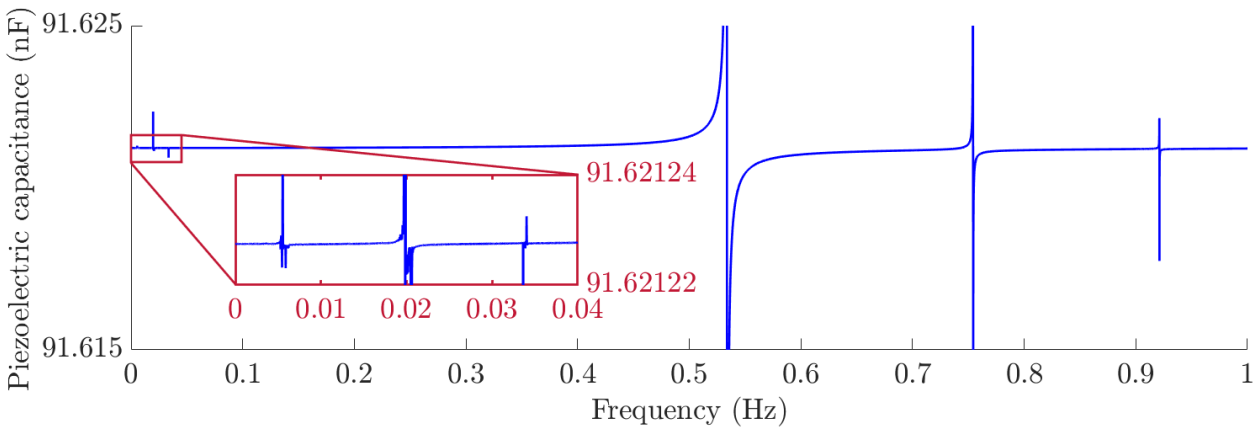

Figure 5.35: Simulated dynamic capacitance at very low frequencies of one piezoelectric patch covering the ring for $n = 16$ elements. Notice the scale of the y-axis.

Meanwhile, the discrete mass m remains expressed by the equation (5.20), and the longitudinal stiffness K_v and the bending stiffness K_θ^E are estimated using the same model of layered materials as for the arch in the previous section. The model for stiffnesses computation is sketched in figure 5.26 and is expressed from equations (5.21) to (5.23).

5.7.3.3 Electrical parameters evaluation

The finite element formulation of equation (5.1) can be used to predict the distribution of static piezoelectric capacitances C_{st}. This brings the opportunity to compute the effect of the numerical parameter K_0^m at low frequencies. As can be seen in figure 5.35, six peaks corresponding to the quasi-rigid body modes appear below 1 Hz. Like for the other modes, the dynamic capacitance decreases after each rigid body mode. Notice however on the y-axis of the graph that this decrease is negligible.

The distribution of the static piezoelectric capacitance, which is plotted in figure 5.36 for $n = 16$ elements, is barely non-periodic. This is due to digital noise, as the difference between the largest and the smallest C_{st} values is less than 0.4 % for $n = 16$ elements and 0.2 % for $n = 32$ elements. Therefore it makes sense to assume that the distribution is uniform and equal to its mean value. Since distributions of m, K_v, K_θ^E and C_{st} are uniform over the structure unit cells, the distributions of L and C_v are uniform as well. They can be derived by applying the frequency coherence conditions in equation (5.24) after setting the transformer ratio at $\hat{a} = 4$.

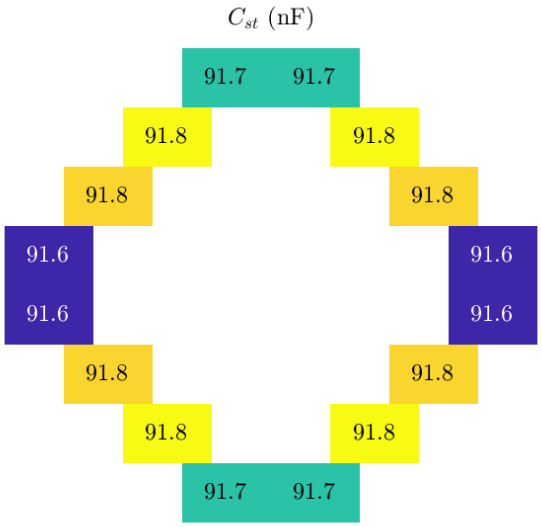

Figure 5.36: Distribution of the static piezoelectric capacitance C_{st} (in nF) over the unit cells for the ring covered with $n = 16$ piezoelectric patches.

5.7.3.4 Network validation

To achieve the modal coupling condition when the ring and the network are connected, they should exhibit the same modal properties. Their mode shapes are compared using the MAC, whose matrix representations are drawn in figure 5.37. Like in the case of the arch treated in section 5.6, several mechanical modes are not replicated by the electrical network. Indeed, the assembled network has been developed by only taking in-plane modes into account, while modes with out-of-plane strains also appear among the first structure modes. For example, the figure 5.38 illustrates why the third and fourth columns on one hand, and the ninth and tenth columns on the other hand, of the MAC matrix remain at zero. Excluding these modes, whose physics cannot be predicted by the assembled electrical circuit, the network modes are consistent with the structure modes. Besides, increasing the number of elements n helps extending the frequency range over which the electromechanical analogy is validated. Finally, the figure 5.39 shows that the natural frequencies of the network tend towards the mechanical ones. Note that there are two times less points of comparison in this figure than identified on the MAC matrices representations of figure 5.37. This is explained by the fact that the structure exhibits pairs of modes, which generates coincident points in figure 5.39.

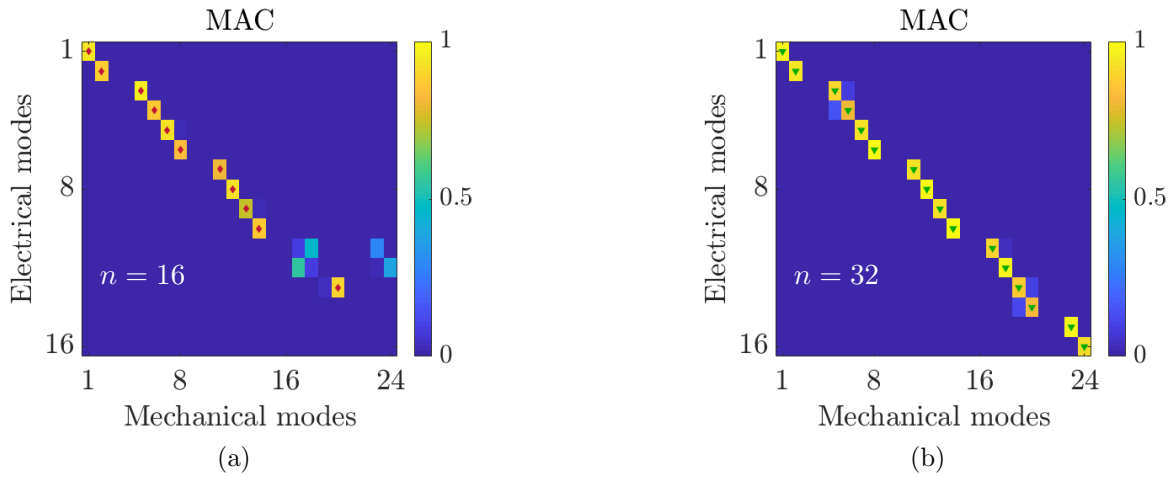

(a) (b)

Figure 5.37: MAC between the 24 first velocity modes of the free ring covered with piezoelectric patches and the 16 first electrical current modes of the network for (a) $n = 16$ and (b) $n = 32$. The tiny ♦ and ▼ markers indicate which couple of modes are deemed clearly identified, so that they can be plotted in figure 5.39.

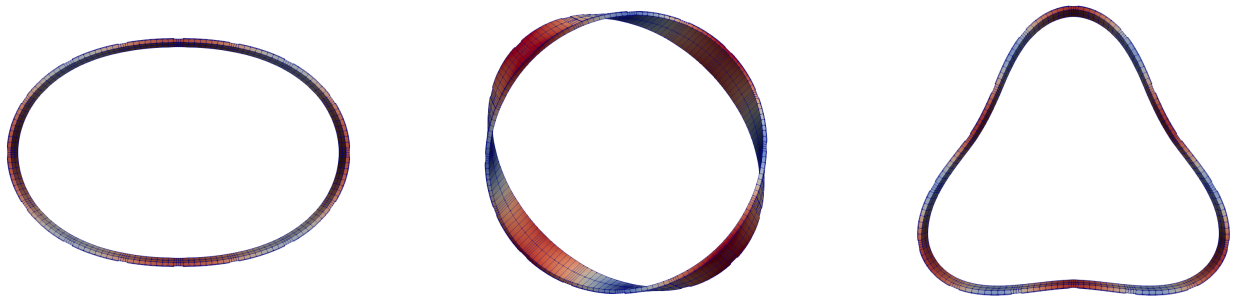

(a) Shape of the first modes pair at 76.6 Hz

(b) Shape of the second modes pair at 186.6 Hz

(c) Shape of the third modes pair at 216.9 Hz

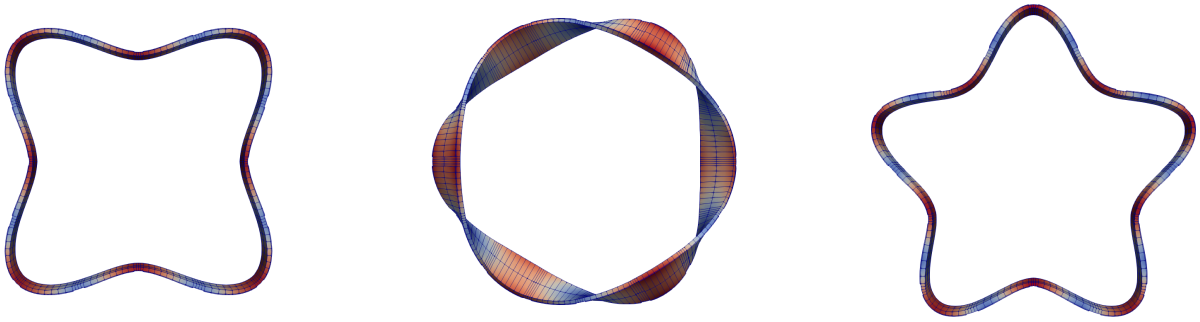

(d) Shape of the fourth modes pair at 416.4 Hz

(e) Shape of the fifth modes pair at 651.2 Hz

(f) Shape of the sixth modes pair at 674.2 Hz

Figure 5.38: Shapes of the first six modes pairs and corresponding natural frequencies of the ring covered with $n = 16$ piezoelectric patches.

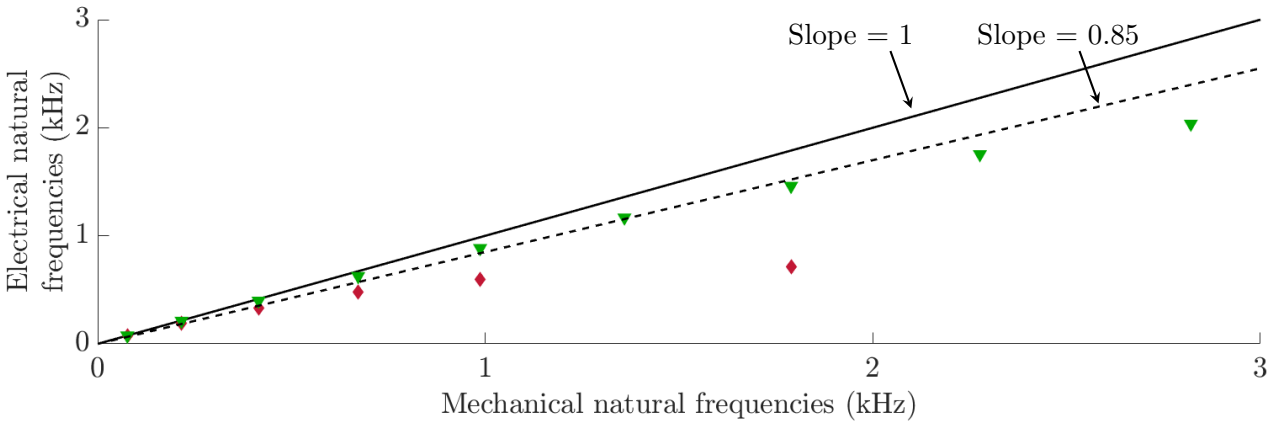

Figure 5.39: Comparison of mechanical and electrical natural frequencies for (♦) $n = 16$ and (▼) $n = 32$.

Electrical modes at 0 Hz

As for the mechanical structure, there are modes at 0 Hz for the electrical network. Moreover, the periodically assembled network exhibits double modes. To avoid uncertainties related to the numerical treatment of these double modes and of the electrical analogues of the rigid body modes, we add a numerical parameter in the network model as well. Just like the parameter K_0^m for the finite element model of the ring, a negligible parameter, which is of the same unit as the inverse of a capacitance, is added to some diagonal terms of the assembled electrical "stiffness" matrix $\boldsymbol{K_N}$ of equation (5.2). Its value is set between 10^{-13} and 10^{-12} to keep the three quasi-"rigid" electrical modes under 1 Hz.

5.7.4 Broadband damping

Vibration damping is now considered by coupling the structure to its analogous network. The same dissipative components as sketched in figure 5.31 bring electrical damping to the coupled system. It is realistic to consider electrical components that exhibit series resistances of $R_L^w = 15\ \Omega$ and $R_L^v = 5\ \Omega$ for $n = 16$ elements, and $R_L^w = 4\ \Omega$ and $R_L^v = 2\ \Omega$ for $n = 32$ elements. Moreover, just like for the arch electrical analogue of section 5.6, we do not proceed to a detailed transformers design. We rather suggest setting R_T^v, R_T^w and R_T^θ at 10 Ω for $n = 16$ elements, and at a eighth of this value for $n = 32$ elements. The reasons for dividing the transformers resistances when n increases have been discussed for previously treated numerical examples. Note that these values of resistances are of the same order of magnitude than the transformers designed in section 4.3, which is why we deem them as realistic components.

A marker in figure 5.34 indicates at which position both the excitation and the measurement are made for the FRFs below. It has been selected so that ring modes which are not coherent with network modes are not excited. In other words, the second mode at 186.6 Hz and the fifth mode at 651.2 Hz, which are illustrated in figure 5.38, will not appear on the incoming graphs. Indeed, the case of having unwanted mechanical modes in the frequency range has been treated in section 5.6 already. The simulated driving-point mobilities are represented in figures 5.40 and 5.41. The achieved damped results are promising, even though the network components have not been optimized in terms of damping performance. Besides, the fact that several modes are very close to each other does not alter the network behavior, as both modes of every couple are damped.

As a conclusion, this numerical example is another example of piezoelectric network damping of a curved structure. It is also the first example of a structure whose electrical analogue forms a closed-loop, and which exhibits double modes. We have shown that these complexities can be overcome, since broadband vibration damping of a ring is possible by connecting it to a fully passive electrical analogue.

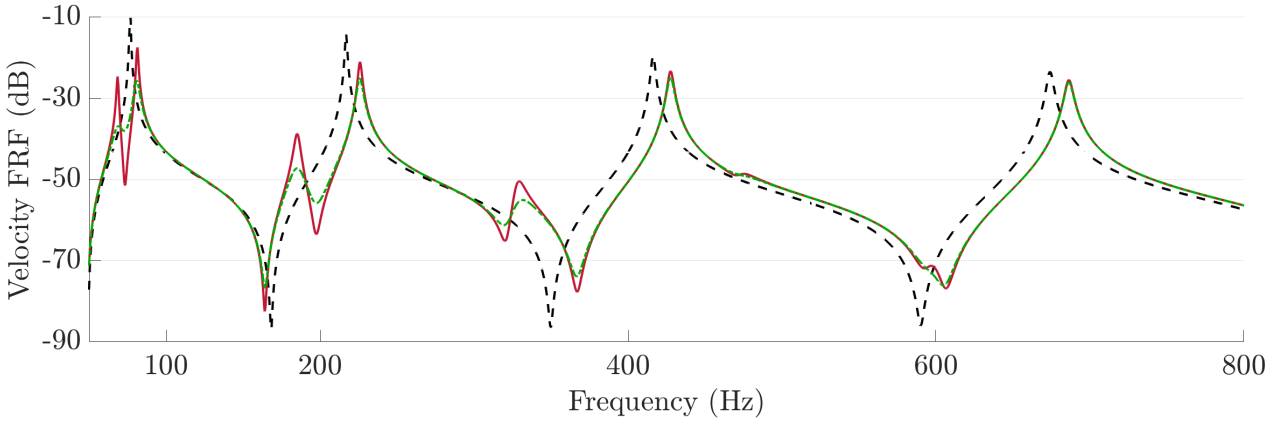

Figure 5.40: Comparison of simulated velocity FRFs for $n = 16$: - - - - with short-circuited piezoelectric patches, and when the ring is connected ——— to an ideal network and - - - to a dissipative network.

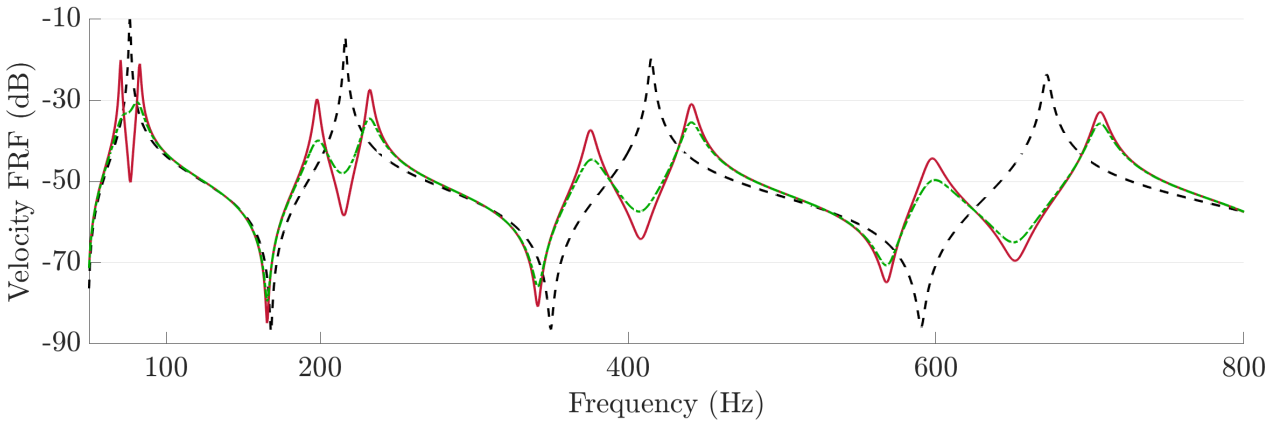

Figure 5.41: Comparison of simulated velocity FRFs for $n = 32$: - - - - with short-circuited piezoelectric patches, and when the ring is connected ——— to an ideal network and - - - to a dissipative network.

5.8 Conclusions

This chapter investigates the piezoelectric network damping of complex structures. The first treated example involves a local mass addition on the plate surface. The natural frequencies and the mode shapes of the structure change because of this addition. The electrical analogue produced in chapter 4 is modified accordingly. Broadband damping is achieved over the first modes of the structure. Moreover, this example is used to ensure that the models developed in previous chapters can be extended to non-periodic cases. We thus have validated by comparison with experimental results on this specific complex case the behavioral model of the electrical network, the finite element model of a structure covered by thin piezoelectric transducers, and the finite element formulation of the coupled system. Therefore, we assume these models can be used going towards other complex structures.

The next numerical examples are complex plates as well. A fully-supported plate of variable thickness, and a constant thickness plate with two supported sides and two clamped sides are considered. Then, numerical examples involve curved structures. The semicircular arch example stands as the first approach to curved structures and to cases in which uncoupled modes appear in the frequency range of interest. Meanwhile, the ring example is a first approach to structures with pairs of modes, and with an electrical analogue that forms a closed-loop and exhibits no boundaries. In all studied cases, the electrical components of the networks are designed by respecting the frequency coherence conditions previously derived. Connecting the structures to their respective analogous networks with dissipative components allows damping the first few targeted modes. Besides, all simulations are conducted with non-optimized but realistic components. This means that piezoelectric network damping of complex structures may be implemented with fully passive components. It is a first successful step towards coupling a complex structure to its electrical analogue for multimodal damping purposes.

Among the complex but periodic structures, the remaining numerical example that could be treated is the tube. We have proposed a tube electrical unit cell in the library of section 2.10, which should be first validated. Then the piezoelectric network damping of a tube could be investigated. Other numerical examples could also include mixed complexities. For example, an arch with a varying curvature and mixed boundary conditions would be a non-periodic structure with curvature.

Chapter 6

Conclusions and perspectives

In this last chapter, we gather the most important contributions of this manuscript. We also give prospects for future works. These include applying piezoelectric network damping to other complex structures on one hand, and taking integration issues into account on the other hand. More specifically, we highlight the potential studies on electrical components design, on the passive tuning in case of temperature variations, and on the comparison with other passive broadband damping solutions.

Content

6.1 Conclusions

Piezoelectric network damping of a structure consists in covering a mechanical structure with piezoelectric transducers and to connect it to an adequate electrical network. To ensure a multimodal vibration mitigation, the network can be an electrical analogue, which means that it exhibits the same modal properties as the structure it is intended to damp. The objective of the present work was to extend the concept of piezoelectric network damping to complex structures. While it had been applied to cases of rods, beams and flat plates both numerically and experimentally, more complex structures had not been treated. For this reason, in chapter 2 we have gathered electrical unit cells which reproduce in the electrical domain the propagation of different kinds of mechanical waves. Electrical analogues of rods, bars, straight and curved beams, plates and tubes have been described. To derive them, the direct electromechanical analogy has been applied to discrete mechanical models. We have then expressed the spatial and frequency coherence conditions that an assembly of electrical unit cells should verify to exhibit similar modal properties as a given structure. Based on these results, we have produced a simply-supported rectangular plate electrical analogue in chapter 4. The assembled network has been validated by comparing its mode shapes and natural frequencies to plate modal properties. We have then shown that connecting the plate to this electrical network allows mitigating its first mechanical bending modes. This experimental setup stands as another proof of concept for the piezoelectric network damping of academic structures.

Meanwhile, in chapter 3 we have developed a numerical tool to predict the dynamics of a structure being coupled to an electrical network via thin piezoelectric transducers. This model is based on coupling a finite element model of a mechanical structure to a behavioral model of an electrical network. The experiments conducted in chapters 3 and 4 have brought the opportunity to validate this approach by comparing simulations to measurements. Besides, this model has been validated in chapter 5 on a complex case as well, which confirms that it can be used as a predictive tool going towards even more complex cases. Finally, note that this model requires the assembled stiffness, mass and coupling matrices of the structure in order to connect a network to it. This means that this model is convenient to apply piezoelectric network damping to a structure whose finite element model is issued from a commercial software.

In the chapter 5, complex cases of piezoelectric network damping are finally treated. The first examples are complex plates. The principle was to start from the known case of a periodic plate and to gradually make it non-periodic, either by locally adding a mass on its surface, by making its thickness variable, or by mixing its boundary conditions. The other complex cases are curved structures, namely a clamped semicircular arch and a free ring. This has allowed studying the problems related to the structure exhibiting double modes in the frequency range of interest, modes which generate no coupling with the electrical network, or having a closed-loop electrical circuit as an electrical analogue. For all these five examples, piezoelectric network damping has been proven as a multimodal vibration damping solution. Moreover, even though the network components have not been optimized in terms of stored energy or damping performance, we have made sure that the predicted vibration mitigation is attainable with realistic components. Hence they represent the first successful steps towards coupling complex structures to their fully passive electrical analogues for multimodal damping purposes.

Main contributions of the present manuscript

Allow us to sum up the main results obtained during this PhD and recorded in this manuscript:

- Description of a method for the design of passive electrical analogues.
- Definition of a library of electrical analogues, which notably includes 1D and 2D curved elements.
- Development of a numerical tool for modeling the coupling of a 3D structure covered with thin piezoelectric transducers to an electrical network.
- Validation of this tool by comparison with experimental results on periodic and non-periodic structures.
- Numerical proof of the efficiency of piezoelectric network damping for complex plates and 1D curved structures.
- Achievement of broadband damping by considering realistic and thus fully passive electrical components.

List of publications

The results presented in this thesis were partially published in journal papers [104, 115] and conference proceedings [105, 116, 117]. A list of publications is available in appendix D.

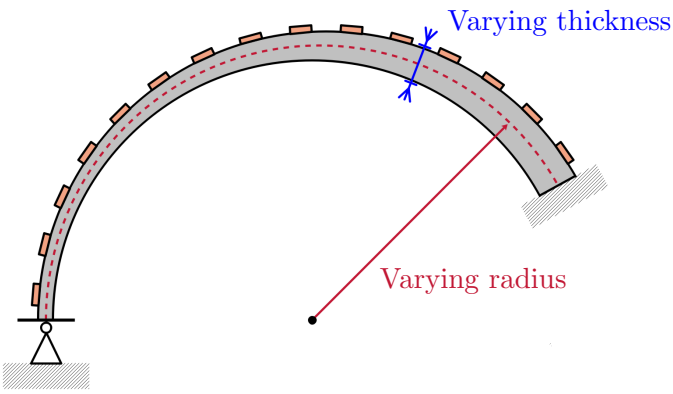

Figure 6.1: Segmental arch of varying radius and thickness covered by piezoelectric transducers.

6.2 Piezoelectric network damping of more complex structures

On one hand, it is possible to mix the complexities already studied, to make sure that combining them does not ruin the damping performance. A numerical example that we are interested in is an arch covered with piezoelectric transducers which is characterized by varying dimensions, a central angle different from 180 degrees, and different boundary conditions. A sketch of such structure is proposed in figure 6.1. This study case gathers most of the complexities treated thus far, and as a consequence represents the most complex structure based on already validated analogues.

As a perspective, note that there are many cases which can be deemed as complex that we have not treated. One of them is a tube periodically covered by piezoelectric patches, such as depicted in figure 6.2. In the library of section 2.10, we have proposed an electrical circuit for a tube electrical analogue. A validation should first be conducted for the electrical network without coupling, such as for the plate and the curved beam analogues in subsections 2.7.2 and 2.8.3, respectively. Then, piezoelectric network damping could be investigated. In this case, the structure would exhibit double modes and its analogous electrical network would be a 2D network that forms a closed-loop along one direction. Moreover, the tube dimensions can be set so that bending modes along the curvature and bending modes along the longitudinal direction appear in the same frequency range. This kind of complexity has been highlighted in the semicircular arch example in section 5.6. We are confident that the network assembled from tube analogous unit cells would damp the targeted modes.

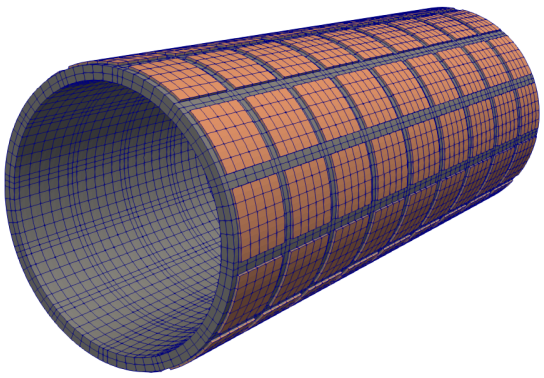

Figure 6.2: Meshing of a circular tube periodically covered by 12 piezoelectric transducers along its curvature and 9 piezoelectric transducers along its length.

Besides, we recall that we suggest using networks which are issued from a degraded version of the structure dynamics. We have proposed a method to produce an electrical analogue of any complex structure that results from the assembly of simple elements recorded in the library of section 2.10. This is what has been done for the variable thickness plate in section 5.4, whose analogous unit cell is a square plate of constant thickness. In order to go towards more realistic structures, there is interest in considering even more complex geometries. To this end, the works of MacNeal [73] on electrical analogues of plates with non-parallel edges sound like a fitting starting point.

Moreover, investigating the connection of a structure to several distinct networks in order to damp different types of modes might prevent from defining electrical analogues for combined loads. The principle is that different types of piezoelectric transducers can be bonded to the structure. Connecting these patches to the adequate electrical networks, such as in figure 6.3, should allow damping different types of modes by combining the effects of several independent analogues. The interest in such a solution stems from the possibility to enhance the coupling for all targeted modes, and optimize the damping performance as a consequence.

Nonetheless, the development of new electrical analogues might be required for the situations where the structure behavior cannot be reproduced in the electrical domain by the unit cells recorded in the library of section 2.10. Examples that come to mind include a 2D membrane element or a rectangular plate bending element. Finally, the development of new electrical analogues might also be required for some boundary conditions, such as the passive analogue of a free plate edge, which is discussed in appendix A.

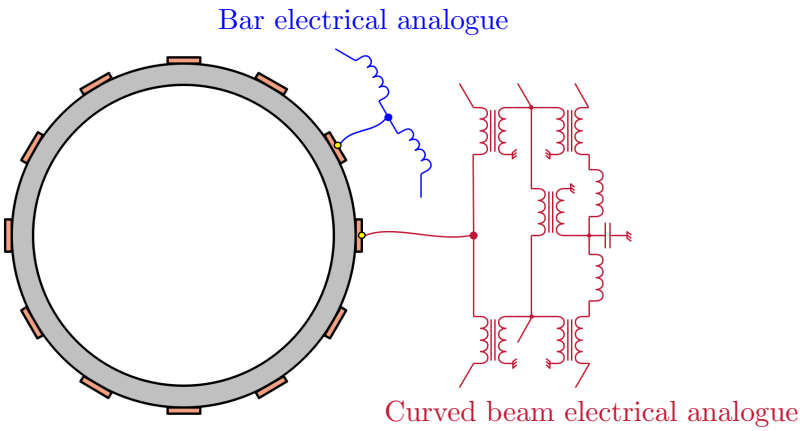

Figure 6.3: Ring covered by piezoelectric transducers which are connected to two distinct electrical networks.

6.3 Electrical components design for piezoelectric network damping

6.3.1 Mass reduction of the analogous network

In fields of transports, especially aeronautics or aerospace, the payload is a criterion of prime importance. Admittedly, the network developed in chapter 4 is too heavy to be integrated as of today, since the table 6.1 indicates that it is nearly three times heavier than the structure it damps. While it is only an example, it highlights that integrating piezoelectric network damping as a fully passive vibration mitigation solution requires some kind of mass optimization of the electrical components.

Note that the electromechanical models which have been developed in this work can be used to design the inductors and transformers of the network. Indeed, these components should be designed according to the electrical current flowing through them. In particular, the mass of an inductor is not driven by its inductance value, as opposed to what has been written in many articles about piezoelectric shunt damping, but by the energy it should store. Two design methods are then possible. The first one is to consider that the distribution of piezoelectric transducers on the structure is given data. Then the electromechanical coupling is set, the constraints are to meet the frequency coherence condition and to achieve an optimized vibration mitigation performance, and the objective function to minimize is the mass. The other method is to consider that either a maximum payload or a maximum added mass is fixed and the objective function to optimize is then the electromechanical coupling. Developing a numerical tool that estimates the potential damping performance for a given added mass, or that estimates the minimum added mass for a given damping performance, would allow investigating the practical limitations of piezoelectric network damping integration.

Structure		**Analogous network**	
Plate	1270 g	Inductors	42×35 g $= 1470$ g
PZT patches	42×9.5 g $= 399$ g	Transformers	139×25 g $= 3475$ g
Approximate total	1.7 kg	Approximate total	5.0 kg

Table 6.1: Mass comparison of the piezoelectric network damping setup described in chapters 3 and 4.

Distinction between added mass and payload

One of the main drawbacks for the integration of piezoelectric network damping is that it might represent a significant mass addition. However, note that even though piezoelectric network damping increases the payload, it might not be synonymous with added mass to the vibrating structure. Indeed, it is possible to set the network aside from the structure, thus not altering the mass of its moving parts too much. Depending on the application, increasing the payload but not the added mass might be acceptable.

6.3.2 Design of inductors for various excitations

We already explained that the design of an inductor depends on the energy it should store, and hence on the electrical current flowing through it. In the case of vibration damping using piezoelectric coupling, the electrical current is generated by the mechanical excitation. As a consequence, the inductors design should take the excitation spectral density into account:

- **Harmonic excitation**: In this case, the design of the inductor can be conducted at fixed frequency. This is what has already been described in section 4.2.
- **Sweep-sine excitation**: Assuming the excitation variations are slow when compared to the frequency at which the electromechanical system behaves, then the network is virtually in steady state at each moment. Therefore the method for harmonic excitation applies as well.
- **Broadband random excitation**: In this case, the excitation and the resulting electrical current have to be described by their power spectral densities. The energy to be stored by the inductive component should thus be computed by integrating its continuous power spectrum over the frequency range of interest.

6.3.3 Non-linear piezoelectric network damping

Finally, we want to highlight the difference between a complex structure and a complex situation: a complex situation might occur even for a simple structure. Non-linear vibrations fall in this category. Indeed, all mechanical structures behave non-linearly if the excitation amplitude is large enough. If it occurs, then there is a modification of the mechanical natural frequencies. Besides, we have shown that the characteristics of the electrical components we have developed evolve with the electrical current flowing through them. Consequently, electrical non-linearities may occur as well, and they may alter the network dynamics. For these reasons, the electrical damping device that is coupled to the structure should be adapted according to mechanical and electrical non-linearities to ensure maintaining the damping performance. Solutions have been proposed for resonant shunts [103] and 1D piezoelectric networks [118]. The principle is to design electrical components, such as inductors or capacitors, which exhibit electrical non-linear behaviors which are similar to the mechanical non-linearities. Integrating these considerations to derive a fully passive non-linear 2D network might be possible using the predictive model we have developed in this work.

6.4 Passive tuning in case of temperature variations

A fully passive integrated solution of vibration mitigation via piezoelectric coupling should be designed so that the damping performance is robust against environmental parameters variations. One environmental parameter that has a significant impact on the electromechanical system behavior is temperature. Indeed, piezoelectric materials properties vary with temperature [119, 120, 19], which in turn modifies the piezoelectric capacitance.

6.4.1 Resonant shunt damping

In the case of resonant shunt damping, a commonly accepted result to achieve an optimal damping performance is to tune the electrical resonance frequency at the targeted mechanical resonance frequency in open-circuit [5, 8, 9]. Park and Han [16] have shown that the degradation of resonant shunts performance when temperature evolves is mainly caused by variations of the piezoelectric materials constants. Several adaptive solutions [20, 18, 30] have been suggested, but they are not autonomous passive solutions since they require external power supply. For this reason, we have developed two

solutions of a piezoelectric resonant shunt that passively adapts to temperature variations. Both solutions assume that the variations with temperature of all involved parameters are given data, which in practice might require going back-and-forth between measurements and models.

The first one, which is described in [104, 105], involves designing the shunt inductor according to temperature characteristics of the system. The ferrite material which makes up the inductor magnetic circuit is characterized by its magnetic permeability. This material constant evolving with temperature, it can be chosen so that the resulting inductance exhibits the desired variations when temperature evolves. Tuning variations of a resonant shunt can thus be passively counterbalanced. A drawback of this solution is that the inductance of a ferrite-based inductor depends on the electrical current [102], and we explained in subsection 4.2.3 that designing an inductor with large variations of inductance with temperature may lead to large variations with the electrical current as well. As a consequence, the produced component might behave in a non-linear fashion.

The second solution, which is studied in [105], keeps the shunt inductance constant. We explained in subsection 4.2.3 that an inductor can be produced to be barely dependent on environmental parameters by including a wide enough air gap. The network tuning is instead maintained by adding capacitors in parallel with the shunt impedance to counterbalance its temperature variations. The drawback of such a solution is that increasing the shunt capacitance deteriorates the coupling [29], and so the overall damping performance. Hence a small capacitance with large temperature variations is required. This can be achieved by adequately selecting ceramic capacitors of class 2 [121].

6.4.2 Piezoelectric network damping

The passive adaptation of electrical components for piezoelectric network damping in case of temperature variations has not been considered yet. However, we suggest that the method proposed in [105] for resonant shunt damping can be extended to it. To ensure maintaining the vibration damping performance in case of temperature variations, the main condition is to keep meeting the frequency coherence condition. As an example, this means that for the plate electrical analogue we have

$$\frac{1}{a\left(T\right)^{2}}\,\frac{K_{\theta}^{E}\left(T\right)}{m}=\frac{1}{\hat{a}^{2}}\,\frac{1}{L\left(T\right)C_{st}\left(T\right)}, \tag{6.1}$$

with T denoting the temperature. By connecting a capacitance C_p in parallel with the piezoelectric capacitance, C_{st} is virtually replaced by $C_{st}+C_p$. Therefore, if the added capacitance is the tuning

parameter, it should verify the following equation:

$$C_p(T) = \left(\frac{a(T)}{\hat{a}}\right)^2 \frac{m}{K_\theta^E(T)\, L(T)} - C_{st}(T). \tag{6.2}$$

Assuming that the variations with temperature of all involved quantities are known, the parallel capacitance can be designed to exhibit the required temperature profile $C_p(T)$. As explained in the previous subsection, adding a capacitance in parallel with the piezoelectric capacitance decreases the electromechanical coupling [28], and so the attainable damping performance. This is the main drawback of the presented method. Capacitors of class 2 have large temperature variations [121] and could thus be used in practice to limit the capacitance increase.

Another complexity to consider is that the analogous network might be separated from the vibrating structure in practice. This means that the structure and the network might be subjected to different temperature fields. The assumption for equations (6.1) and (6.2) is that the mechanical unit cell and its analogous electrical unit cell are both at temperature T, which might not be true in a practical application. Consequently, integrating this solution becomes a multiphysics engineering problem.

As a conclusion, note that solutions of fully passive components adapting to temperature variations have been experimentally validated in the case of piezoelectric shunt damping. As of today, conducting temperature experiments for piezoelectric network damping is challenging because of the size of the involved systems. Therefore, methods may first be numerically validated in future works.

6.5 Comparison to other passive broadband damping solutions

Another perspective for future works is to compare piezoelectric network damping to other passive broadband damping solutions. Comparisons could be made with resistive networks. Another well-spread solution is viscoelastic damping, which consists in bonding constrained viscoelastic layers on a structure. Some elements of comparison between solutions have been written in [117]. We have shown on the simply-supported plate example that piezoelectric network damping might lead to a better vibration mitigation on the first vibration modes. The comparison of the influence of other parameters such as temperature and cost on their damping performances has yet to be rigorously conducted.

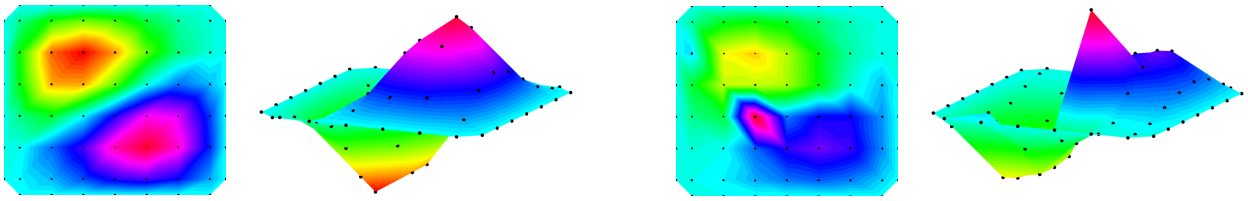

(a) (b)

Figure 6.4: Measurement at fixed frequency of operational electrical current shapes in (a) the fully developed network of chapter 4 and (b) in a network with a defect appearing in one unit cell. The tiny black points indicate the measurements locations.

6.6 Defects detection in an electrical network

While assembling the plate electrical analogue in chapter 4, several wiring mistakes were committed before getting to the final setup. Indeed, nearly two thousands wires were needed to produce the full network. Even though the important amount of connections is not synonymous with complexity, it makes the probability to commit a wiring error significant. The tool we have used to track down defects in the network is a visual one: plotting the distribution of electrical currents at a fixed frequency near an expected natural frequency of the network should result in a shape looking like a plate mode. On figure 6.4 is an example of this visual tool applied near the natural frequency of the (1,2) plate mode. When compared to a defect-free network in figure 6.4a, whose electrical current shape has been shown in subsection 4.4.3 already, a defect is clearly visible in figure 6.4b. While this tool is convenient to detect a defect location, it barely informs about the kind of defect producing the visualized shape.

The development of this visual tool gives us the idea to work on the detection of defects in electrical networks. While there is interest in tracking down the wiring mistakes, it is also important to realize if some components deteriorate over time. Indeed, ensuring that the network behaves as intended is of prime importance for the integration of piezoelectric network damping solutions. Detection techniques exist for mechanical structures [122, 123]. These techniques may be extended to the case of detecting defects in electrical networks.

6.7 Final thoughts

In this manuscript, the interest in piezoelectric network damping has been illustrated by forecasting broadband vibration mitigation of several thin mechanical structures. Even though the achievable damping performance thanks to piezoelectric networks should be rigorously compared to other fully passive multimodal damping solutions, the experimental and simulated results are promising.

It now seems crucial to focus on the integration of piezoelectric networks in industrial applications. Questions arise when the effects on the coupled system dynamics of external parameters such as the excitation amplitude and temperature have to be taken into account. Furthermore, the design of bulky passive components such as inductors and transformers requires further investigations. Indeed, these magnetic components represent a significant mass addition to the vibrating system, which stands as the main limitation of piezoelectric network damping. While solutions have been suggested, a proper mass optimization under external parameters constraints has not been conducted yet. We are hopeful that the numerical tools which have been developed in this work can be used to this end. Finally, other manufacturing processes for electrical components might be investigated. In particular, the recent developments in additive printing of layers with prescribed electrical behaviors generate intriguing potential for the integration of densely discretized electrical networks.

Bibliography

[1] A. Erturk and D. J. Inman, *Piezoelectric energy harvesting*. John Wiley & Sons, 2011.

[2] J. A. B. Gripp and D. A. Rade, "Vibration and noise control using shunted piezoelectric transducers: A review," *Mechanical Systems and Signal Processing*, vol. 112, pp. 359–383, 2018.

[3] B. Lossouarn, M. Aucejo, J.-F. Deü, and B. Multon, "Design of inductors with high inductance values for resonant piezoelectric damping," *Sensors and Actuators A: Physical*, vol. 259, pp. 68–76, 2017.

[4] R. L. Forward, "Electronic damping of vibrations in optical structures," *Applied Optics*, vol. 18, no. 5, pp. 690–697, 1979.

[5] N. W. Hagood and A. Von Flotow, "Damping of structural vibrations with piezoelectric materials and passive electrical networks," *Journal of Sound and Vibration*, vol. 146, no. 2, pp. 243–268, 1991.

[6] J. P. Den Hartog, *Vibrations*. McGraw-Hill Book Company, 1956.

[7] G. Caruso, "A critical analysis of electric shunt circuits employed in piezoelectric passive vibration damping," *Smart Materials and Structures*, vol. 10, no. 5, pp. 1059–1068, 2001.

[8] O. Thomas, J. Ducarne, and J.-F. Deü, "Performance of piezoelectric shunts for vibration reduction," *Smart Materials and Structures*, vol. 21, no. 1, p. 015008, 2012.

[9] M. Berardengo, A. Cigada, S. Manzoni, and M. Vanali, "Vibration control by means of piezoelectric actuators shunted with LR impedances: performance and robustness analysis," *Shock and Vibration*, vol. 2015, pp. 1–30, 2015.

[10] K. Yamada, "Complete passive vibration suppression using multi-layered piezoelectric element, inductor, and resistor," *Journal of Sound and Vibration*, vol. 387, pp. 16–35, 2017.

[11] S. Wu, "Piezoelectric shunts with a parallel R-L circuit for structural damping and vibration control," in *Proceedings SPIE*, vol. 2720, pp. 259–269, 1996.

[12] U. Andreaus and M. Porfiri, "Effect of electrical uncertainties on resonant piezoelectric shunting," *Journal of Intelligent Material Systems and Structures*, vol. 18, no. 5, pp. 477–485, 2007.

[13] K. Yamada, H. Matsuhisa, H. Utsuno, and K. Sawada, "Optimum tuning of series and parallel LR circuits for passive vibration suppression using piezoelectric elements," *Journal of Sound and Vibration*, vol. 329, no. 24, pp. 5036–5057, 2010.

[14] P. Soltani, G. Kerschen, G. Tondreau, and A. Deraemaeker, "Piezoelectric vibration damping using resonant shunt circuits: an exact solution," *Smart Materials and Structures*, vol. 23, no. 12, p. 125014, 2014.

[15] J. Høgsberg and S. Krenk, "Calibration of piezoelectric RL shunts with explicit residual mode correction," *Journal of Sound and Vibration*, vol. 386, pp. 65–81, 2017.

[16] J.-W. Park and J.-H. Han, "Sensitivity analysis of damping performances for passive shunted piezoelectrics," *Aerospace Science and Technology*, vol. 33, no. 1, pp. 16–25, 2014.

[17] M. Berardengo, J. Høgsberg, S. Manzoni, M. Vanali, A. Brandt, and T. Godi, "LRLC-shunted piezoelectric vibration absorber," *Journal of Sound and Vibration*, vol. 474, p. 115268, 2020.

[18] J. J. Hollkamp and T. F. Starchville, "A self-tuning piezoelectric vibration absorber," *Journal of Intelligent Material Systems and Structures*, vol. 5, no. 4, pp. 559–566, 1994.

[19] A. Belloli, D. Niederberger, S. Pietrzko, M. Morari, and P. Ermanni, "Structural vibration control via R-L shunted active fiber composites," *Journal of Intelligent Material Systems and Structures*, vol. 18, no. 3, pp. 275–287, 2006.

[20] D. Niederberger and M. Morari, "An autonomous shunt circuit for vibration damping," *Smart Materials and Structures*, vol. 15, no. 2, pp. 359–364, 2006.

[21] M. Lallart, E. Lefeuvre, C. Richard, and D. Guyomar, "Self-powered circuit for broadband, multimodal piezoelectric vibration control," *Sensors and Actuators A: Physical*, vol. 143, no. 2, pp. 377–382, 2008.

[22] J. Ducarne, O. Thomas, and J.-F. Deü, "Structural vibration reduction by switch shunting of piezoelectric elements: modeling and optimization," *Journal of Intelligent Material Systems and Structures*, vol. 21, no. 8, pp. 797–816, 2010.

[23] Y.-Y. Chen, D. Vasic, F. Costa, C.-K. Lee, and W.-J. Wu, "Self-powered semi-passive piezoelectric structural damping based on zero-velocity crossing detection," *Smart Materials and Structures*, vol. 22, no. 2, p. 025029, 2013.

[24] Y.-P. Liu and D. Vasic, "Semi-passive piezoelectric structural damping based on a pulse-width modulation switching circuit," *Journal of Mechanical Science and Technology*, vol. 27, no. 12, pp. 3625–3633, 2013.

[25] J. J. Hollkamp, "Multimodal passive vibration suppression with piezoelectric materials and resonant shunts," *Journal of Intelligent Material Systems and Structures*, vol. 5, no. 1, pp. 49–57, 1994.

[26] S. Wu, "Method for multiple mode piezoelectric shunting with single PZT transducer for vibration control," *Journal of Intelligent Material Systems and Structures*, vol. 9, no. 12, pp. 991–998, 1998.

[27] S. Behrens, S. O. R. Moheimani, and A. J. Fleming, "Multiple mode current flowing passive piezoelectric shunt controller," *Journal of Sound and Vibration*, vol. 266, no. 5, pp. 929–942, 2003.

[28] A. J. Fleming and S. O. R. Moheimani, "Adaptive piezoelectric shunt damping," *Smart Materials and Structures*, vol. 12, no. 1, pp. 36–48, 2003.

[29] A. J. Fleming, S. Behrens, and S. O. R. Moheimani, "Reducing the inductance requirements of piezoelectric shunt damping systems," *Smart Materials and Structures*, vol. 12, no. 1, pp. 57–64, 2003.

[30] D. Niederberger, A. J. Fleming, S. O. R. Moheimani, and M. Morari, "Adaptive multi-mode resonant piezoelectric shunt damping," *Smart Materials and Structures*, vol. 13, no. 5, pp. 1025–1035, 2004.

[31] M. Berardengo, S. Manzoni, and A. M. Conti, "Multi-mode passive piezoelectric shunt damping by means of matrix inequalities," *Journal of Sound and Vibration*, vol. 405, pp. 287–305, 2017.

[32] S. Behrens, A. J. Fleming, and S. O. R. Moheimani, "A broadband controller for shunt piezoelectric damping of structural vibration," *Smart Materials and Structures*, vol. 12, no. 1, pp. 18–28, 2003.

[33] B. de Marneffe and A. Preumont, "Vibration damping with negative capacitance shunts: theory and experiment," *Smart Materials and Structures*, vol. 17, no. 3, p. 035015, 2008.

[34] M. Berardengo, O. Thomas, C. Giraud-Audine, and S. Manzoni, "Improved resistive shunt by means of negative capacitance: new circuit, performances and multi-mode control," *Smart Materials and Structures*, vol. 25, no. 7, p. 075033, 2016.

[35] J. Ducarne, O. Thomas, and J.-F. Deü, "Placement and dimension optimization of shunted piezoelectric patches for vibration reduction," *Journal of Sound and Vibration*, vol. 331, no. 14, pp. 3286–3303, 2012.

[36] I. Giorgio, L. Galantucci, A. D. Corte, and D. D. Vescovo, "Piezo-electromechanical smart materials with distributed arrays of piezoelectric transducers: current and upcoming applications," *International Journal of Applied Electromagnetics and Mechanics*, vol. 47, no. 4, pp. 1051–1084, 2015.

[37] O. Thorp, M. Ruzzene, and A. Baz, "Attenuation and localization of wave propagation in rods with periodic shunted piezoelectric patches," *Smart Materials and Structures*, vol. 10, no. 5, pp. 979–989, 2001.

[38] L. Airoldi and M. Ruzzene, "Design of tunable acoustic metamaterials through periodic arrays of resonant shunted piezos," *New Journal of Physics*, vol. 13, no. 11, p. 113010, 2011.

[39] G. Wang, S. Chen, and J. Wen, "Low-frequency locally resonant band gaps induced by arrays of resonant shunts with Antoniou's circuit: experimental investigation on beams," *Smart Materials and Structures*, vol. 20, no. 1, p. 015026, 2010.

[40] G. Wang, J. Wang, S. Chen, and J. Wen, "Vibration attenuations induced by periodic arrays of piezoelectric patches connected by enhanced resonant shunting circuits," *Smart Materials and Structures*, vol. 20, no. 12, p. 125019, 2011.

[41] C. Sugino, S. Leadenham, M. Ruzzene, and A. Erturk, "An investigation of electroelastic bandgap formation in locally resonant piezoelectric metastructures," *Smart Materials and Structures*, vol. 26, no. 5, p. 055029, 2017.

[42] K. Yi, M. Ouisse, E. Sadoulet-Reboul, and G. Matten, "Active metamaterials with broadband controllable stiffness for tunable band gaps and non-reciprocal wave propagation," *Smart Materials and Structures*, vol. 28, no. 6, p. 065025, 2019.

[43] O. Thorp, M. Ruzzene, and A. Baz, "Attenuation of wave propagation in fluid-loaded shells with periodic shunted piezoelectric rings," *Smart Materials and Structures*, vol. 14, no. 4, pp. 594–604, 2005.

[44] A. Spadoni, M. Ruzzene, and K. Cunefare, "Vibration and wave propagation control of plates with periodic arrays of shunted piezoelectric patches," *Journal of Intelligent Material Systems and Structures*, vol. 20, no. 8, pp. 979–990, 2009.

[45] F. Casadei, M. Ruzzene, L. Dozio, and K. A. Cunefare, "Broadband vibration control through periodic arrays of resonant shunts: experimental investigation on plates," *Smart Materials and Structures*, vol. 19, no. 1, p. 015002, 2009.

[46] F. Casadei, T. Delpero, A. Bergamini, P. Ermanni, and M. Ruzzene, "Piezoelectric resonator arrays for tunable acoustic waveguides and metamaterials," *Journal of Applied Physics*, vol. 112, no. 6, p. 064902, 2012.

[47] S. Chen, G. Wang, J. Wen, and X. Wen, "Wave propagation and attenuation in plates with periodic arrays of shunted piezo-patches," *Journal of Sound and Vibration*, vol. 332, no. 6, pp. 1520–1532, 2013.

[48] F. Tateo, M. Collet, M. Ouisse, and K. A. Cunefare, "Design variables for optimizing adaptive metacomposite made of shunted piezoelectric patches distribution," *Journal of Vibration and Control*, vol. 22, no. 7, pp. 1838–1854, 2014.

[49] F. Tateo, M. Collet, M. Ouisse, M. N. Ichchou, K. A. Cunefare, and P. Abbe, "Experimental characterization of a bi-dimensional array of negative capacitance piezo-patches for vibroacoustic control," *Journal of Intelligent Material Systems and Structures*, vol. 26, no. 8, pp. 952–964, 2014.

[50] C. Sugino, M. Ruzzene, and A. Erturk, "An analytical framework for locally resonant piezoelectric metamaterial plates," *International Journal of Solids and Structures*, vol. 182-183, pp. 281–294, 2020.

[51] C. Maurini, F. dell'Isola, and D. D. Vescovo, "Comparison of piezoelectronic networks acting as distributed vibration absorbers," *Mechanical Systems and Signal Processing*, vol. 18, no. 5, pp. 1243–1271, 2004.

[52] T. Valis, A. H. von Flotow, and N. W. Hagood, "An acoustic-electromagnetic piezoelectric waveguide coupler," *Journal of Sound and Vibration*, vol. 178, no. 5, pp. 669–680, 1994.

[53] G. Rosi, J. Pouget, and F. dell'Isola, "Control of sound radiation and transmission by a piezoelectric plate with an optimized resistive electrode," *European Journal of Mechanics - A/Solids*, vol. 29, no. 5, pp. 859–870, 2010.

[54] F. dell'Isola, C. Maurini, and M. Porfiri, "Passive damping of beam vibrations through distributed electric networks and piezoelectric transducers: prototype design and experimental validation," *Smart Materials and Structures*, vol. 13, no. 2, pp. 299–308, 2004.

[55] P. Bisegna, G. Caruso, and F. Maceri, "Optimized electric networks for vibration damping of piezoactuated beams," *Journal of Sound and Vibration*, vol. 289, no. 4-5, pp. 908–937, 2006.

[56] Y. Lu and J. Tang, "Electromechanical tailoring of structure with periodic piezoelectric circuitry," *Journal of Sound and Vibration*, vol. 331, no. 14, pp. 3371–3385, 2012.

[57] A. E. Bergamini, M. Zündel, E. A. F. Parra, T. Delpero, M. Ruzzene, and P. Ermanni, "Hybrid dispersive media with controllable wave propagation: A new take on smart materials," *Journal of Applied Physics*, vol. 118, no. 15, p. 154310, 2015.

[58] H. Yu, K. W. Wang, and J. Zhang, "Piezoelectric networking with enhanced electromechanical coupling for vibration delocalization of mistuned periodic structures — theory and experiment," *Journal of Sound and Vibration*, vol. 295, no. 1-2, pp. 246–265, 2006.

[59] M. Lallart, L. Yan, C. Richard, and D. Guyomar, "Damping of periodic bending structures featuring nonlinearly interfaced piezoelectric elements," *Journal of Vibration and Control*, vol. 22, no. 18, pp. 3930–3941, 2016.

[60] L. Yan, B. Bao, D. Guyomar, and M. Lallart, "Periodic structure with interconnected nonlinear electrical networks," *Journal of Intelligent Material Systems and Structures*, vol. 28, no. 2, pp. 204–229, 2016.

[61] B. Bao, D. Guyomar, and M. Lallart, "Piezoelectric metacomposite structure carrying nonlinear multilevel interleaved-interconnected switched electronic networks," *Composite Structures*, vol. 161, pp. 308–329, 2017.

[62] B. Bao, D. Guyomar, and M. Lallart, "Vibration reduction for smart periodic structures via periodic piezoelectric arrays with nonlinear interleaved-switched electronic networks," *Mechanical Systems and Signal Processing*, vol. 82, pp. 230–259, 2017.

[63] S. Vidoli and F. dell'Isola, "Modal coupling in one-dimensional electromechanical structured continua," *Acta Mechanica*, vol. 141, no. 1-2, pp. 37–50, 2000.

[64] S. Alessandroni, F. dell'Isola, and M. Porfiri, "A revival of electric analogs for vibrating mechanical systems aimed to their efficient control by PZT actuators," *International Journal of Solids and Structures*, vol. 39, no. 20, pp. 5295–5324, 2002.

[65] U. Andreaus, F. dell'Isola, and M. Porfiri, "Piezoelectric passive distributed controllers for beam flexural vibrations," *Modal Analysis*, vol. 10, no. 5, pp. 625–659, 2004.

[66] M. Porfiri, F. dell'Isola, and F. M. F. Mascioli, "Circuit analog of a beam and its application to multimodal vibration damping, using piezoelectric transducers," *International Journal of Circuit Theory and Applications*, vol. 32, no. 4, pp. 167–198, 2004.

[67] M. Porfiri, F. dell'Isola, and E. Santini, "Modeling and design of passive electric networks interconnecting piezoelectric transducers for distributed vibration control," *International Journal of Applied Electromagnetics and Mechanics*, vol. 21, no. 2, pp. 69–87, 2005.

[68] S. Alessandroni, U. Andreaus, F. dell'Isola, and M. Porfiri, "Piezo-ElectroMechanical (PEM) Kirchhoff–Love plates," *European Journal of Mechanics - A/Solids*, vol. 23, no. 4, pp. 689–702, 2004.

[69] S. Alessandroni, U. Andreaus, F. dell'Isola, and M. Porfiri, "A passive electric controller for multimodal vibrations of thin plates," *Computers & Structures*, vol. 83, no. 15-16, pp. 1236–1250, 2005.

[70] B. Lossouarn, M. Aucejo, and J.-F. Deü, "Multimodal coupling of periodic lattices and application to rod vibration damping with a piezoelectric network," *Smart Materials and Structures*, vol. 24, no. 4, p. 045018, 2015.

[71] B. Lossouarn, J.-F. Deü, and M. Aucejo, "Multimodal vibration damping of a beam with a periodic array of piezoelectric patches connected to a passive electrical network," *Smart Materials and Structures*, vol. 24, no. 11, p. 115037, 2015.

[72] B. Lossouarn, J.-F. Deü, M. Aucejo, and K. A. Cunefare, "Multimodal vibration damping of a plate by piezoelectric coupling to its analogous electrical network," *Smart Materials and Structures*, vol. 25, no. 11, p. 115042, 2016.

[73] R. H. MacNeal, *The solution of partial differential equations by means of electrical networks*. PhD thesis, California Institute of Technology, 1949.

[74] S. U. Benscoter and R. H. MacNeal, "Introduction to electrical-circuit analogies for beam analysis," *NACA Technical Note 2785*, 1952.

[75] S. U. Benscoter and R. H. MacNeal, "Equivalent-plate theory for a straight multicell wing," *NACA Technical Note 2786*, 1952.

[76] R. H. MacNeal, "Electrical analogies for stiffened shells with flexible rings," *NACA Technical Note 3280*, 1954.

[77] A. Bloch, "Electromechanical analogies and their use for the analysis of mechanical and electromechanical systems," *Journal of the Institution of Electrical Engineers - Part I: General*, vol. 92, no. 52, pp. 157–169, 1945.

[78] L. L. Beranek, *Acoustics*. Acoustical Society of America, 1954.

[79] R. H. MacNeal, G. D. McCann, and C. H. Wilts, "The solution of aeroelastic problems by means of electrical analogies," *Journal of the Aeronautical Sciences*, vol. 18, no. 12, pp. 777–789, 1951.

[80] J. Ducarne, *Modeling and optimisation of non-linear vibration damping by switch shunting of piezoelectric elements*. Theses, Conservatoire national des arts et metiers - Cnam, 2009.

[81] J. C. Schönfeld, "Analogy of hydraulic, mechanical, acoustic and electric systems," *Applied Scientific Research*, vol. 3, no. 1, pp. 417–450, 1954.

[82] G. Raze, A. Paknejad, G. Zhao, V. Broun, C. Collette, and G. Kerschen, "Suppression of delay-induced instabilities of digital piezoelectric vibration absorbers," in *Proceedings of the 9th ECCOMAS Thematic Conference on Smart Structures and Materials-SMART 2019*, pp. 991–1001, International Centre for Numerical Methods in Engineering (CIMNE), 2019.

[83] A. Preumont, B. de Marneffe, A. Deraemaeker, and F. Bossens, "The damping of a truss structure with a piezoelectric transducer," *Computers & Structures*, vol. 86, no. 3-5, pp. 227–239, 2008.

[84] A. Preumont, *Vibration control of active structures*. Springer Netherlands, 3rd ed., 2011.

[85] B. Lossouarn, M. Aucejo, J.-F. Deü, and K. A. Cunefare, "Design of a passive electrical analogue for piezoelectric damping of a plate," *Journal of Intelligent Material Systems and Structures*, p. 1045389X1773123, 2017.

[86] M. Paschero, *Modeling and synthesis of circuits analogue to generalized ondulatory phenomena giroscopically coupled*. PhD thesis, Sapienza University of Rome, 2007.

[87] R. J. Allemang, "The modal assurance criterion - Twenty years of use and abuse," *Sound & Vibration*, vol. 37, pp. 14–23, 2003.

[88] S. P. Timoshenko and S. Woinowsky-Krieger, *Theory of plates and shells*. McGraw-Hill, 1959.

[89] P. Chidamparam and A. W. Leissa, "Vibrations of planar curved beams, rings, and arches," *Applied Mechanics Reviews*, vol. 46, no. 9, pp. 467–483, 1993.

[90] A. Benjeddou, "Advances in piezoelectric finite element modeling of adaptive structural elements: a survey," *Computers & Structures*, vol. 76, no. 1-3, pp. 347–363, 2000.

[91] J. Mackerle, "Smart materials and structures—a finite element approach—an addendum: a bibliography (1997–2002)," *Modelling and Simulation in Materials Science and Engineering*, vol. 11, no. 5, pp. 707–744, 2003.

[92] O. Thomas, J.-F. Deü, and J. Ducarne, "Vibrations of an elastic structure with shunted piezoelectric patches: efficient finite element formulation and electromechanical coupling coefficients," *International Journal for Numerical Methods in Engineering*, vol. 80, no. 2, pp. 235–268, 2009.

[93] "IEEE standard on piezoelectricity," 1988.

[94] O. Robin, J.-D. Chazot, R. Boulandet, M. Michau, A. Berry, and N. Atalla, "A plane and thin panel with representative simply supported boundary conditions for laboratory vibroacoustic tests," *Acta Acustica united with Acustica*, vol. 102, no. 1, pp. 170–182, 2016.

[95] P. Avitabile, *Modal testing: a practitioner's guide*. John Wiley & Sons, 2017.

[96] J. Schoukens, R. Pintelon, E. van der Ouderaa, and J. Renneboog, "Survey of excitation signals for FFT based signal analyzers," *IEEE Transactions on Instrumentation and Measurement*, vol. 37, no. 3, pp. 342–352, 1988.

[97] G. Heinzel, A. Rüdiger, and R. Schilling, "Spectrum and spectral density estimation by the Discrete Fourier transform (DFT), including a comprehensive list of window functions and some new at-top windows," 2002.

[98] PI Ceramic, "Piezoelectric ceramic products: Fundamentals, characteristics and applications," 2016.

[99] B. Lossouarn, M. Aucejo, and J.-F. Deü, "Electromechanical wave finite element method for interconnected piezoelectric waveguides," *Computers & Structures*, vol. 199, pp. 46–56, 2018.

[100] B. Lossouarn, *Multimodal vibration damping of structures coupled to their analogous piezoelectric networks*. Theses, Conservatoire national des arts et metiers - Cnam, 2016.

[101] E. C. Snelling, *Soft ferrites*. CRC Press, 2nd ed., 1969.

[102] V. E. Legg, "Magnetic measurements at low flux densities using the alternating current bridge," *Bell System Technical Journal*, vol. 15, no. 1, pp. 39–62, 1936.

[103] B. Lossouarn, J.-F. Deü, and G. Kerschen, "A fully passive nonlinear piezoelectric vibration absorber," *Philosophical Transactions of the Royal Society A: Mathematical, Physical and Engineering Sciences*, vol. 376, no. 2127, p. 20170142, 2018.

[104] R. Darleux, B. Lossouarn, and J.-F. Deü, "Passive self-tuning inductor for piezoelectric shunt damping considering temperature variations," *Journal of Sound and Vibration*, vol. 432, pp. 105–118, 2018.

[105] R. Darleux, B. Lossouarn, and J.-F. Deü., "Effect of temperature on the tuning of a piezoelectric resonant shunt composed of variable inductance or variable capacitance," in *Proceedings of the 28th International Conference on Noise and Vibration Engineering (ISMA 2018)*, 2018.

[106] C. W. T. McLyman, *Transformer and inductor design handbook*. CRC press, 2017.

[107] B. Multon, "COMPOSANTS PASSIFS DE L'ÉLECTRONIQUE DE PUISSANCE (magnétiques et capacitifs)." Lecture, 2015.

[108] TDK Epcos, "Ferrite and accessories - general definitions," 2017.

[109] B. Multon, "Modèles électriques du transformateur électromagnétique," *La Revue 3 E. I*, pp. 31–36, 1997.

[110] A. A. Ozdemir and S. Gumussoy, "Transfer function estimation in system identification toolbox via vector fitting," *IFAC-PapersOnLine*, vol. 50, no. 1, pp. 6232–6237, 2017.

[111] C. Maurini, J. Pouget, and F. dell'Isola, "On a model of layered piezoelectric beams including transverse stress effect," *International Journal of Solids and Structures*, vol. 41, no. 16-17, pp. 4473–4502, 2004.

[112] F. dell'Isola, E. Santini, and D. Vigilante, "Purely electrical damping of vibrations in arbitrary PEM plates: a mixed non-conforming FEM-Runge-Kutta time evolution analysis," *Archive of Applied Mechanics*, vol. 73, pp. 26–48, 2003.

[113] G. Rosi, *Control of sound radiation and transmission by means of passive piezoelectric networks : modelling, optimization and experimental implementation.* Theses, Université Pierre et Marie Curie - Paris VI, 2010.

[114] F. Bachmann and P. Ermanni, "Integration of encapsulated piezoelectric actuators in highly loaded CFRP structures," in *Active and Passive Smart Structures and Integrated Systems 2010* (M. N. Ghasemi-Nejhad, ed.), SPIE, 2010.

[115] R. Darleux, B. Lossouarn, and J.-F. Deü, "Broadband vibration damping of non-periodic plates by piezoelectric coupling to their electrical analogues," *Smart Materials and Structures*, vol. 29, no. 5, p. 054001, 2020.

[116] R. Darleux, B. Lossouarn, and J.-F. Deü, "Broadband vibration damping of a non-periodic plate by piezoelectric coupling to its electrical analogue," in *9th ECCOMAS Thematic Conference on Smart Structures and Materials, SMART 2019*, 2019.

[117] L. Rouleau, B. Lossouarn, R. Darleux, and J.-F. Deü, "Comparison of damping performances of constrained viscoelastic layers and passive piezoelectric networks," in *48th International Congress and Exposition on Noise Control Engineering, INTERNOISE 2019*, 2019.

[118] B. Lossouarn, G. Kerschen, and J.-F. Deü, "Vibration mitigation of multiple nonlinear resonances through an analogous piezoelectric network," in *9th ECCOMAS Thematic Conference on Smart Structures and Materials, SMART 2019*, 2019.

[119] M. W. Hooker, "Properties of PZT-based piezoelectric ceramics between -150°C and 250°C," tech. rep., NASA, 1998.

[120] C. Miclea, C. Tanasoiu, L. Amarande, C. F. Miclea, C. Plavitu, M. Cioangher, L. Trupina, C. T. Miclea, and C. David, "Effect of temperature on the main piezoelectric parameters of a soft PZT ceramic," *Romanian Journal of Information Science and Technology*, vol. 10, no. 3, pp. 243–250, 2007.

[121] M. J. Pan and C. A. Randall, "A brief introduction to ceramic capacitors," *IEEE Electrical Insulation Magazine*, vol. 26, no. 3, pp. 44–50, 2010.

[122] M. Aucejo and O. D. Smet, "A multiplicative regularization for force reconstruction," *Mechanical Systems and Signal Processing*, vol. 85, pp. 730–745, 2017.

[123] M. Aucejo and O. D. Smet, "An optimal Bayesian regularization for force reconstruction problems," *Mechanical Systems and Signal Processing*, vol. 126, pp. 98–115, 2019.

Appendix A

Electrical analogue of a plate free boundary condition

A free edge of a plate is the boundary condition whose electrical analogue remains undefined with the method described in section 2.3. This brief aside explains the problem and highlights what has been done to try to overcome this limitation.

A.1 Classical plate theory

In the plate theory [88], other intermediate quantities than used in equations (2.53) are considered. The classical notations for this digression are as follows: the bending moments along the x and y directions are respectively denoted M_x and M_y, the twisting moment is denoted M_{xy}, the shear forces are denoted Q_x and Q_y, and ν is the material Poisson's ratio. Meanwhile, θ_x and θ_y are the slopes along the x and y directions, respectively. The plate dynamics in harmonic motion and these intermediate quantities are expressed by

$$\begin{aligned}
M_x &= -aK_\theta \left(\frac{\partial \theta_x}{\partial x} + \nu \frac{\partial \theta_y}{\partial y} \right), & Q_x &= \frac{\partial M_x}{\partial x} - \frac{\partial M_{xy}}{\partial y}, & \theta_x &= \frac{\partial U_z}{\partial x}, \\
M_y &= -aK_\theta \left(\frac{\partial \theta_y}{\partial y} + \nu \frac{\partial \theta_x}{\partial x} \right), & Q_y &= \frac{\partial M_y}{\partial y} - \frac{\partial M_{xy}}{\partial x}, & \theta_y &= \frac{\partial U_z}{\partial y}, \\
M_{xy} &= aK_\theta (1-\nu) \frac{\partial^2 U_z}{\partial x \partial y}, & -\rho h a \Omega^2 U_z &= \frac{\partial Q_x}{\partial x} + \frac{\partial Q_y}{\partial y}.
\end{aligned} \tag{A.1}$$

The boundary condition for a free edge parallel to the y direction at the x_e abscissa is described by the following equations [88]:

$$M_x(x_\mathrm{e}, y) = 0, \tag{A.2}$$

$$Q_x(x_\mathrm{e}, y) - \frac{\partial M_{xy}}{\partial y}(x_\mathrm{e}, y) = 0. \tag{A.3}$$

A.2 Limitation of the present plate electrical analogue

The intermediate quantities we have defined in equations (2.53) are different from the ones defined in equations (A.1). Admittedly, the shear force Q_x has the same expression in both cases, but the set of differential equations used in section 2.7 does not include the bending moment M_x and the twisting moment M_{xy}. Since they appear in the equations that define the free edge behavior, their expressions should be related to our notations.

From the equation (A.2) and the expression of M_x in the set of equations (A.1), we deduce that along the free edge we have

$$\frac{\partial \theta_x}{\partial x}(x_\mathrm{e}, y) + \nu \frac{\partial \theta_y}{\partial y}(x_\mathrm{e}, y) = 0, \qquad \text{or also} \qquad \frac{\partial \theta_x}{\partial x}(x_\mathrm{e}, y) = -\nu \frac{\partial \theta_y}{\partial y}(x_\mathrm{e}, y). \tag{A.4}$$

Hence, the bending moment M that is defined in equations (2.53) becomes

$$\begin{aligned} M(x_\mathrm{e}, y) &= aK_\theta \left(\frac{\partial \theta_x}{\partial x}(x_\mathrm{e}, y) + \frac{\partial \theta_y}{\partial y}(x_\mathrm{e}, y) \right) \\ &= (1-\nu)\, aK_\theta \frac{\partial^2 U_z}{\partial y^2}(x_\mathrm{e}, y). \end{aligned} \tag{A.5}$$

Furthermore, the derivative of the twisting moment M_{xy} is

$$\begin{aligned} \frac{\partial M_{xy}}{\partial y} &= (1-\nu)\, aK_\theta \frac{\partial}{\partial y} \left(\frac{\partial^2 U_z}{\partial x \partial y} \right) \\ &= (1-\nu)\, aK_\theta \frac{\partial^2 \theta_x}{\partial y^2}. \end{aligned} \tag{A.6}$$

So the equation (A.3) can be rewritten:

$$Q_x(x_\mathrm{e}, y) = (1-\nu)\, aK_\theta \frac{\partial^2 \theta_x}{\partial y^2}(x_\mathrm{e}, y). \tag{A.7}$$

The next step is to apply a finite difference scheme to the equations (A.5) and (A.7). Assuming the right position in figure 2.2b corresponds to the free edge, the centered finite difference scheme at position R for a second order differential equation is required:

$$\left(\frac{\partial^2 g}{\partial y^2}\right)_{\mathrm{I}} = \frac{g_{\mathrm{R}_+} - 2g_{\mathrm{R}} + g_{\mathrm{R}_-}}{a^2}, \tag{A.8}$$

where g is the quantity to derive, and g_{R_+} and g_{R_-} are the values of g on the right-hand side of the above and below unit cells, respectively. As a consequence, discretizing equations (A.5) and (A.7) leads to the free edge discrete conditions expressed with our system of intermediate quantities:

$$M_{\mathrm{R}} = (1-\nu)\ \frac{K_\theta}{a}\ \left(U_{z\mathrm{R}_+} - 2U_{z\mathrm{R}} + U_{z\mathrm{R}_-}\right), \tag{A.9}$$

$$Q_{\mathrm{R}} = (1-\nu)\ \frac{K_\theta}{a}\ \left(\theta_{\mathrm{R}_+} - 2\theta_{\mathrm{R}} + \theta_{\mathrm{R}_-}\right). \tag{A.10}$$

Applying the direct electromechanical analogy summed up in table 2.1 results in the analogous electrical boundary condition for a free plate edge:

$$\frac{aC_\theta}{1-\nu}\, V_{\theta\mathrm{R}} = 2q_{z\mathrm{R}} - q_{z\mathrm{R}_+} - q_{z\mathrm{R}_-}, \tag{A.11}$$

$$\frac{aC_\theta}{1-\nu}\, V_{z\mathrm{R}} = 2q_{\theta\mathrm{R}} - q_{\theta\mathrm{R}_+} - q_{\theta\mathrm{R}_-}. \tag{A.12}$$

These equations can be interpreted as capacitors characteristics. However, they cannot be integrated in the network made of the unit cells represented in figure 2.14. Indeed, meeting the equations (A.11) and (A.12) would require to implement nodes where three electrical currents converge without prescribing the voltages on the corresponding terminals. A powered active circuit would probably be needed to meet these conditions. As a conclusion, the actual unit cell drawn in figure 2.14 does not allow for a fully passive electrical representation of a plate free edge.

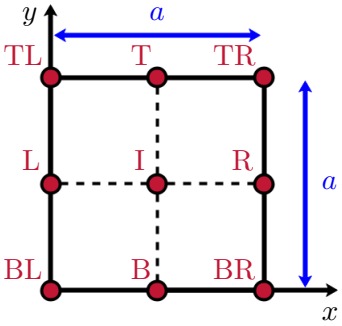

Figure A.1: 2D discretization scheme, where I, B, L, R, T, BL, BR, TL and TR refer to the central, bottom, left, right, top, bottom left, bottom right, top left and top right positions, respectively.

A.3 Potential solutions

The difficulty to passively represent a free edge for the developed square plate electrical analogue stems from trying to discretize a second order differential equation. Hence applying a discretization grid that allows representing in discrete fashion differential equations of higher order might be of help during the analogous network design process. Many other 2D grids are helpful in modeling a plate dynamics [88]. An example of refined grid is sketched in figure A.1. This way, discretized versions of equations (A.5) and (A.7) might be passively integrated in the network.

Another solution to model mechanical boundary conditions using the finite difference method is to create a continuation of the discrete model beyond the boundary [88]. An example of such continuation is represented in figure A.2. The continuation depth, as well as the command of the added fictive degrees of freedom, depends on the boundary condition to model. For example, one node beyond the boundary is enough to model a simply-supported or a clamped plate boundary condition. For a free edge, two fictive nodes are needed. From an electrical point of view, this continuation method has the potential to be an easy-to-integrate solution, even though it might significantly increase the number of electrical components in the network.

Finally, a solution might be to design a new plate electrical analogue, which would retain as intermediate quantities the bending moment M_x and the effective shear force V_x, whose expression

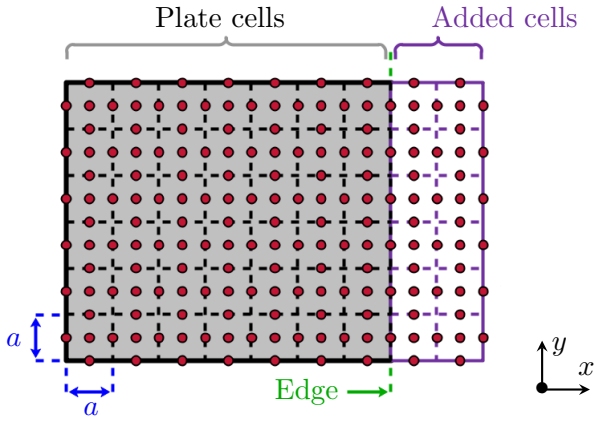

Figure A.2: Continuation of the plate discretization grid beyond the boundary.

with the classical plate dynamics notations of section A.1 is

$$V_x = Q_x - \frac{\partial M_{xy}}{\partial y}. \tag{A.13}$$

Short-circuit electrical connections could then be sufficient to represent a free plate edge in the electrical domain. While such a solution could exist, the number of electrical components would probably significantly increase when compared to the actual plate electrical analogue. Moreover, connecting this new unit cell to the present one might be impossible, which would negate all the advantages of the actual solution in terms of limited number of components.

As a side note: The electrical analogue of a free edge boundary condition for a plate is derived by MacNeal in [73]. To do so, more intermediate quantities are kept, including the twisting and bending moments, a more complex discretization grid is used near the boundary, and a continuation method beyond the boundary is applied. In other words, all three solutions we have mentioned in the ongoing section are studied. The only differences with the present work is that a model of a variable thickness plate is required to define the analogous free edge condition, and that the indirect electromechanical analogy (see table 2.1) is considered. This result gives hope that a fully passive solution might exist by applying the direct electromechanical analogy, but it highlights that extensive work should be conducted to obtain it.

Appendix B

Elementary matrices for the plate, curved beam and tube electrical analogues

The elementary matrices of several electrical analogues of chapter 2 are quite complex. Their full expressions are large and do not present a significant interest by themselves. Therefore, we have chosen to record them in this aside. The elementary matrices for the square plate electrical analogue (see section 2.7), the curved beam electrical analogue (see section 2.8) and the tube electrical analogue (see section 2.9) are written below.

B.1 Square plate electrical analogue

The derivation of the square plate electrical analogue elementary matrices is explained in subsection 2.7.1. The matrix $\boldsymbol{B}$ is invertible as long as $C_0 \neq 0$, in which case the dynamic matrix $\boldsymbol{D_e}$ can be computed. Equations (2.13) are then applied. The resulting electrical elementary matrices of electrical "mass" $\boldsymbol{M_{elm}}$ and electrical "stiffness" $\boldsymbol{K_{elm}}$ corresponding to figure 2.15 are

$$\boldsymbol{K_{elm}} = \frac{1}{\hat{a}C_0}\begin{pmatrix} \frac{6}{\hat{a}} & 3 & \frac{-2}{\hat{a}} & -1 & \frac{-2}{\hat{a}} & 1 & \frac{-2}{\hat{a}} & 1 \\ 3 & \frac{\hat{a}(8C_0+3C_\theta)}{2(2C_0+C_\theta)} & -1 & \frac{-\hat{a}C_\theta}{2(2C_0+C_\theta)} & -1 & \frac{\hat{a}C_\theta}{2(2C_0+C_\theta)} & -1 & \frac{\hat{a}C_\theta}{2(2C_0+C_\theta)} \\ \frac{-2}{\hat{a}} & -1 & \frac{6}{\hat{a}} & 3 & \frac{-2}{\hat{a}} & 1 & \frac{-2}{\hat{a}} & 1 \\ -1 & \frac{-\hat{a}C_\theta}{2(2C_0+C_\theta)} & 3 & \frac{\hat{a}(8C_0+3C_\theta)}{2(2C_0+C_\theta)} & -1 & \frac{\hat{a}C_\theta}{2(2C_0+C_\theta)} & -1 & \frac{\hat{a}C_\theta}{2(2C_0+C_\theta)} \\ \frac{-2}{\hat{a}} & -1 & \frac{-2}{\hat{a}} & -1 & \frac{6}{\hat{a}} & -3 & \frac{-2}{\hat{a}} & 1 \\ 1 & \frac{\hat{a}C_\theta}{2(2C_0+C_\theta)} & 1 & \frac{\hat{a}C_\theta}{2(2C_0+C_\theta)} & -3 & \frac{\hat{a}(8C_0+3C_\theta)}{2(2C_0+C_\theta)} & 1 & \frac{-\hat{a}C_\theta}{2(2C_0+C_\theta)} \\ \frac{-2}{\hat{a}} & -1 & \frac{-2}{\hat{a}} & -1 & \frac{-2}{\hat{a}} & 1 & \frac{6}{\hat{a}} & -3 \\ 1 & \frac{\hat{a}C_\theta}{2(2C_0+C_\theta)} & 1 & \frac{\hat{a}C_\theta}{2(2C_0+C_\theta)} & 1 & \frac{-\hat{a}C_\theta}{2(2C_0+C_\theta)} & -3 & \frac{\hat{a}(8C_0+3C_\theta)}{2(2C_0+C_\theta)} \end{pmatrix}, \tag{B.1a}$$

$$\text{and } \boldsymbol{M_{elm}} = \frac{L}{16}\begin{pmatrix} 1 & \frac{\hat{a}}{2} & 1 & \frac{\hat{a}}{2} & 1 & \frac{-\hat{a}}{2} & 1 & \frac{-\hat{a}}{2} \\ \frac{\hat{a}}{2} & \frac{\hat{a}^2}{4} & \frac{\hat{a}}{2} & \frac{\hat{a}^2}{4} & \frac{\hat{a}}{2} & \frac{-\hat{a}^2}{4} & \frac{\hat{a}}{2} & \frac{-\hat{a}^2}{4} \\ 1 & \frac{\hat{a}}{2} & 1 & \frac{\hat{a}}{2} & 1 & \frac{-\hat{a}}{2} & 1 & \frac{-\hat{a}}{2} \\ \frac{\hat{a}}{2} & \frac{\hat{a}^2}{4} & \frac{\hat{a}}{2} & \frac{\hat{a}^2}{4} & \frac{\hat{a}}{2} & \frac{-\hat{a}^2}{4} & \frac{\hat{a}}{2} & \frac{-\hat{a}^2}{4} \\ 1 & \frac{\hat{a}}{2} & 1 & \frac{\hat{a}}{2} & 1 & \frac{-\hat{a}}{2} & 1 & \frac{-\hat{a}}{2} \\ \frac{-\hat{a}}{2} & \frac{-\hat{a}^2}{4} & \frac{-\hat{a}}{2} & \frac{-\hat{a}^2}{4} & \frac{-\hat{a}}{2} & \frac{\hat{a}^2}{4} & \frac{-\hat{a}}{2} & \frac{\hat{a}^2}{4} \\ 1 & \frac{\hat{a}}{2} & 1 & \frac{\hat{a}}{2} & 1 & \frac{-\hat{a}}{2} & 1 & \frac{-\hat{a}}{2} \\ \frac{-\hat{a}}{2} & \frac{-\hat{a}^2}{4} & \frac{-\hat{a}}{2} & \frac{-\hat{a}^2}{4} & \frac{-\hat{a}}{2} & \frac{\hat{a}^2}{4} & \frac{-\hat{a}}{2} & \frac{\hat{a}^2}{4} \end{pmatrix}. \tag{B.1b}$$

From the equation (B.1b), we can define the matrix $\boldsymbol{M_0}$ verifying $\boldsymbol{M_{elm}} = L\boldsymbol{M_0}$. Then, applying equations (4.24) leads to the expression of the elementary damping matrix $\boldsymbol{D_{elm}}$:

$$\boldsymbol{D_{elm}} = \left(R^c_{sT} + R_{sL}\right)\boldsymbol{M_0} + \frac{R^s_{sT}}{\hat{a}^2}\begin{pmatrix} 3 & 0 & -1 & 0 & -1 & 0 & -1 & 0 \\ 0 & \frac{\hat{a}^2}{4} & 0 & \frac{\hat{a}^2}{4} & 0 & -\frac{\hat{a}^2}{4} & 0 & -\frac{\hat{a}^2}{4} \\ -1 & 0 & 3 & 0 & -1 & 0 & -1 & 0 \\ 0 & \frac{\hat{a}^2}{4} & 0 & \frac{\hat{a}^2}{4} & 0 & -\frac{\hat{a}^2}{4} & 0 & -\frac{\hat{a}^2}{4} \\ -1 & 0 & -1 & 0 & 3 & 0 & -1 & 0 \\ 0 & -\frac{\hat{a}^2}{4} & 0 & -\frac{\hat{a}^2}{4} & 0 & \frac{\hat{a}^2}{4} & 0 & \frac{\hat{a}^2}{4} \\ -1 & 0 & -1 & 0 & -1 & 0 & 3 & 0 \\ 0 & -\frac{\hat{a}^2}{4} & 0 & -\frac{\hat{a}^2}{4} & 0 & \frac{\hat{a}^2}{4} & 0 & \frac{\hat{a}^2}{4} \end{pmatrix}. \tag{B.2}$$

B.2 Curved beam electrical analogue

The derivation of the curved beam electrical analogue elementary matrices is explained in subsection 2.8.1. The matrix $\boldsymbol{B}$ is invertible as long as $C_0 \neq 0$, in which case the dynamic matrix $\boldsymbol{D_e}$ can be computed. Equations (2.13) are then applied. We recall the nondimensionalized parameters which remain in the following expressions:

$$\delta = \frac{\hat{a}}{\hat{R}}, \qquad \beta = LC_v\Omega^2, \qquad \gamma = \hat{a}^2 LC_\theta \Omega^2, \qquad \epsilon = \frac{C_0}{C_\theta}. \tag{B.3}$$

As a consequence, the elementary matrices corresponding to the unit cell of the curved beam electrical analogue represented in figure 2.23 are

$$\boldsymbol{M_{elm}} = \frac{L}{4}\begin{pmatrix} 2+\frac{\delta^2}{4} & \frac{\delta}{2} & \frac{\hat{a}\delta}{4} & -\frac{\delta^2}{4} & \frac{\delta}{2} & -\frac{\hat{a}\delta}{4} \\ \frac{\delta}{2} & 1 & \frac{\hat{a}}{2} & -\frac{\delta}{2} & 1 & -\frac{\hat{a}}{2} \\ \frac{\hat{a}\delta}{4} & \frac{\hat{a}}{2} & \frac{\hat{a}^2}{4} & -\frac{\hat{a}\delta}{4} & \frac{\hat{a}}{2} & -\frac{\hat{a}^2}{4} \\ -\frac{\delta^2}{4} & -\frac{\delta}{2} & -\frac{\hat{a}\delta}{4} & 2+\frac{\delta^2}{4} & -\frac{\delta}{2} & \frac{\hat{a}\delta}{4} \\ \frac{\delta}{2} & 1 & \frac{\hat{a}}{2} & -\frac{\delta}{2} & 1 & -\frac{\hat{a}}{2} \\ -\frac{\hat{a}\delta}{4} & -\frac{\hat{a}}{2} & -\frac{\hat{a}^2}{4} & \frac{\hat{a}\delta}{4} & -\frac{\hat{a}}{2} & \frac{\hat{a}^2}{4} \end{pmatrix}, \tag{B.4a}$$

$$\text{and } \boldsymbol{K_{elm}} = \frac{1}{\hat{a}^2 C_0}\,\frac{1}{\epsilon\gamma\delta^2 + 16\beta\,(\epsilon+1)}\,\boldsymbol{K_0}, \tag{B.4b}$$

where $\boldsymbol{K_0}$ is a 6×6 symmetric matrix, whose terms above the diagonal are written below:

$$\boldsymbol{K_0}^{(1)} = \begin{pmatrix} 16\,\epsilon\,\gamma + 16\,\beta\,\delta^2 + 16\,\epsilon^2\,\gamma - 8\,\delta^2\,\epsilon^2\,\gamma + \delta^4\,\epsilon^2\,\gamma + 16\,\beta\,\delta^2\,\epsilon - 8\,\delta^2\,\epsilon\,\gamma + 2\,\delta^4\,\epsilon\,\gamma \\ * \end{pmatrix},$$

$$\boldsymbol{K_0}^{(2)} = \begin{pmatrix} 2\,\delta\,\left(16\,\beta + 16\,\beta\,\epsilon - 4\,\epsilon\,\gamma - 4\,\epsilon^2\,\gamma + \delta^2\,\epsilon^2\,\gamma + 2\,\delta^2\,\epsilon\,\gamma\right) \\ 4\,\gamma\,\delta^2\,\epsilon^2 + 8\,\gamma\,\delta^2\,\epsilon + 64\,\beta\,\epsilon + 64\,\beta \\ * \end{pmatrix},$$

$$\boldsymbol{K_0}^{(3)} = \begin{pmatrix} 2\,\hat{a}\,\delta\,\left(\epsilon\,\gamma\,\delta^2 + 8\,\beta + 8\,\beta\,\epsilon - 2\,\epsilon\,\gamma\right) \\ 4\,\hat{a}\,\left(\epsilon\,\gamma\,\delta^2 + 8\,\beta + 8\,\beta\,\epsilon\right) \\ 2\,\hat{a}^2\,\left(\epsilon\,\gamma\,\delta^2 + 8\,\beta + 16\,\beta\,\epsilon\right) \\ * \end{pmatrix},$$

$$\boldsymbol{K_0}^{(4)} = \begin{pmatrix} 16\,\beta\,\delta^2 - 16\,\epsilon\,\gamma - 16\,\epsilon^2\,\gamma + 8\,\delta^2\,\epsilon^2\,\gamma - \delta^4\,\epsilon^2\,\gamma + 16\,\beta\,\delta^2\,\epsilon + 8\,\delta^2\,\epsilon\,\gamma \\ 2\,\delta\,\left(16\,\beta + 16\,\beta\,\epsilon + 4\,\epsilon\,\gamma + 4\,\epsilon^2\,\gamma - \delta^2\,\epsilon^2\,\gamma\right) \\ 4\,\hat{a}\,\delta\,\left(4\,\beta + 4\,\beta\,\epsilon + \epsilon\,\gamma\right) \\ 16\,\epsilon\,\gamma + 16\,\beta\,\delta^2 + 16\,\epsilon^2\,\gamma - 8\,\delta^2\,\epsilon^2\,\gamma + \delta^4\,\epsilon^2\,\gamma + 16\,\beta\,\delta^2\,\epsilon - 8\,\delta^2\,\epsilon\,\gamma + 2\,\delta^4\,\epsilon\,\gamma \\ * \end{pmatrix},$$

$$\boldsymbol{K_0}^{(5)} = \begin{pmatrix} -2\,\delta\,\left(16\,\beta + 16\,\beta\,\epsilon + 4\,\epsilon\,\gamma + 4\,\epsilon^2\,\gamma - \delta^2\,\epsilon^2\,\gamma\right) \\ 4\,\gamma\,\delta^2\,\epsilon^2 - 64\,\beta\,\epsilon - 64\,\beta \\ -32\,\hat{a}\,\beta\,\left(\epsilon + 1\right) \\ -2\,\delta\,\left(16\,\beta + 16\,\beta\,\epsilon - 4\,\epsilon\,\gamma - 4\,\epsilon^2\,\gamma + \delta^2\,\epsilon^2\,\gamma + 2\,\delta^2\,\epsilon\,\gamma\right) \\ 4\,\gamma\,\delta^2\,\epsilon^2 + 8\,\gamma\,\delta^2\,\epsilon + 64\,\beta\,\epsilon + 64\,\beta \\ * \end{pmatrix},$$

$$\boldsymbol{K_0}^{(6)} = \begin{pmatrix} 4\,\hat{a}\,\delta\,\left(4\,\beta + 4\,\beta\,\epsilon + \epsilon\,\gamma\right) \\ 32\,\hat{a}\,\beta\,\left(\epsilon + 1\right) \\ 16\,\hat{a}^2\,\beta \\ 2\,\hat{a}\,\delta\,\left(\epsilon\,\gamma\,\delta^2 + 8\,\beta + 8\,\beta\,\epsilon - 2\,\epsilon\,\gamma\right) \\ -4\,\hat{a}\,\left(\epsilon\,\gamma\,\delta^2 + 8\,\beta + 8\,\beta\,\epsilon\right) \\ 2\,\hat{a}^2\,\left(\epsilon\,\gamma\,\delta^2 + 8\,\beta + 16\,\beta\,\epsilon\right) \end{pmatrix}.$$

B.3 Tube electrical analogue

The first steps of the tube electrical analogue elementary matrices derivation are explained in section 2.9. The matrix $\boldsymbol{B}$ is invertible as long as $C_0 \neq 0$, in which case the dynamic matrix $\boldsymbol{D_e}$ can be computed. Equations (2.13) are then applied. We recall the nondimensionalized parameters which remain in the following expressions:

$$\delta = \frac{\hat{a}}{\hat{R}}, \qquad \beta = LC_v\Omega^2, \qquad \gamma = \hat{a}^2 LC_\theta \Omega^2, \qquad \epsilon = \frac{C_0}{C_\theta}. \tag{B.5}$$

We consider the unit cell of the tube electrical analogue represented in figure 2.36, to which side capacitors $C_0/2$ are connected. The corresponding elementary matrices are

$$\boldsymbol{M_{elm}} = \begin{pmatrix}
1 & \frac{\hat{a}}{2} & \frac{\delta}{2} & 1 & \frac{\hat{a}}{2} & -\frac{\delta}{2} & 1 & -\frac{\hat{a}}{2} & 1 & -\frac{\hat{a}}{2} \\
\frac{\hat{a}}{2} & \frac{\hat{a}^2}{4} & \frac{\hat{a}\delta}{4} & \frac{\hat{a}}{2} & \frac{\hat{a}^2}{4} & -\frac{\hat{a}\delta}{4} & \frac{\hat{a}}{2} & -\frac{\hat{a}^2}{4} & \frac{\hat{a}}{2} & -\frac{\hat{a}^2}{4} \\
\frac{\delta}{2} & \frac{\hat{a}\delta}{4} & 8+\frac{\delta^2}{4} & \frac{\delta}{2} & \frac{\hat{a}\delta}{4} & -\frac{\delta^2}{4} & \frac{\delta}{2} & -\frac{\hat{a}\delta}{4} & \frac{\delta}{2} & -\frac{\hat{a}\delta}{4} \\
1 & \frac{\hat{a}}{2} & \frac{\delta}{2} & 1 & \frac{\hat{a}}{2} & -\frac{\delta}{2} & 1 & -\frac{\hat{a}}{2} & 1 & -\frac{\hat{a}}{2} \\
\frac{\hat{a}}{2} & \frac{\hat{a}^2}{4} & \frac{\hat{a}\delta}{4} & \frac{\hat{a}}{2} & \frac{\hat{a}^2}{4} & -\frac{\hat{a}\delta}{4} & \frac{\hat{a}}{2} & -\frac{\hat{a}^2}{4} & \frac{\hat{a}}{2} & -\frac{\hat{a}^2}{4} \\
-\frac{\delta}{2} & -\frac{\hat{a}\delta}{4} & -\frac{\delta^2}{4} & -\frac{\delta}{2} & -\frac{\hat{a}\delta}{4} & 8+\frac{\delta^2}{4} & -\frac{\delta}{2} & \frac{\hat{a}\delta}{4} & -\frac{\delta}{2} & \frac{\hat{a}\delta}{4} \\
1 & \frac{\hat{a}}{2} & \frac{\delta}{2} & 1 & \frac{\hat{a}}{2} & -\frac{\delta}{2} & 1 & -\frac{\hat{a}}{2} & 1 & -\frac{\hat{a}}{2} \\
-\frac{\hat{a}}{2} & -\frac{\hat{a}^2}{4} & -\frac{\hat{a}\delta}{4} & -\frac{\hat{a}}{2} & -\frac{\hat{a}^2}{4} & \frac{\hat{a}\delta}{4} & -\frac{\hat{a}}{2} & \frac{\hat{a}^2}{4} & -\frac{\hat{a}}{2} & \frac{\hat{a}^2}{4} \\
1 & \frac{\hat{a}}{2} & \frac{\delta}{2} & 1 & \frac{\hat{a}}{2} & -\frac{\delta}{2} & 1 & -\frac{\hat{a}}{2} & 1 & -\frac{\hat{a}}{2} \\
-\frac{\hat{a}}{2} & -\frac{\hat{a}^2}{4} & -\frac{\hat{a}\delta}{4} & -\frac{\hat{a}}{2} & -\frac{\hat{a}^2}{4} & \frac{\hat{a}\delta}{4} & -\frac{\hat{a}}{2} & \frac{\hat{a}^2}{4} & -\frac{\hat{a}}{2} & \frac{\hat{a}^2}{4}
\end{pmatrix}, \tag{B.6a}$$

$$\text{and } \boldsymbol{K_{elm}} = \frac{\gamma\epsilon^2\delta^2}{\hat{a}^4 C_0^3} \frac{1}{\gamma\epsilon\delta^2 + 32\beta\,(1+2\epsilon)} \boldsymbol{K_0}, \tag{B.6b}$$

where $\boldsymbol{K_0}$ is a 10×10 symmetric matrix, whose terms above the diagonal are written below:

$$\boldsymbol{K_0}^{(1)} = \begin{pmatrix} 4\,\gamma\,\delta^2\,\epsilon^2 + 8\,\gamma\,\delta^2\,\epsilon + 384\,\beta\,\epsilon + 192\,\beta \\ * \end{pmatrix},$$

$$\boldsymbol{K_0}^{(2)} = \begin{pmatrix} 4\,\hat{a}\ (\epsilon\,\gamma\,\delta^2 + 24\,\beta + 48\,\beta\,\epsilon) \\ 2\,\hat{a}^2\ (\epsilon\,\gamma\,\delta^2 + 24\,\beta + 64\,\beta\,\epsilon) \\ * \end{pmatrix},$$

$$\boldsymbol{K_0}^{(3)} = \begin{pmatrix} -2\,\delta\ (16\,\beta + 32\,\beta\,\epsilon + 4\,\epsilon\,\gamma + 8\,\epsilon^2\,\gamma - \delta^2\,\epsilon^2\,\gamma) \\ -4\,\hat{a}\,\delta\ (4\,\beta + 8\,\beta\,\epsilon + \epsilon\,\gamma) \\ 32\,\epsilon\,\gamma + 48\,\beta\,\delta^2 + 64\,\epsilon^2\,\gamma - 16\,\delta^2\,\epsilon^2\,\gamma + \delta^4\,\epsilon^2\,\gamma + 96\,\beta\,\delta^2\,\epsilon - 8\,\delta^2\,\epsilon\,\gamma + 2\,\delta^4\,\epsilon\,\gamma \\ * \end{pmatrix},$$

$$\boldsymbol{K_0}^{(4)} = \begin{pmatrix} 4\,\gamma\,\delta^2\,\epsilon^2 - 128\,\beta\,\epsilon - 64\,\beta \\ -32\,\hat{a}\,\beta\ (2\,\epsilon + 1) \\ 2\,\delta\ (48\,\beta + 96\,\beta\,\epsilon - 4\,\epsilon\,\gamma - 8\,\epsilon^2\,\gamma + \delta^2\,\epsilon^2\,\gamma + 2\,\delta^2\,\epsilon\,\gamma) \\ 4\,\gamma\,\delta^2\,\epsilon^2 + 8\,\gamma\,\delta^2\,\epsilon + 384\,\beta\,\epsilon + 192\,\beta \\ * \end{pmatrix},$$

$$\boldsymbol{K_0}^{(5)} = \begin{pmatrix} -32\,\hat{a}\,\beta\ (2\,\epsilon + 1) \\ -16\,\hat{a}^2\,\beta \\ 2\,\hat{a}\,\delta\ (\epsilon\,\gamma\,\delta^2 + 24\,\beta + 48\,\beta\,\epsilon - 2\,\epsilon\,\gamma) \\ 4\,\hat{a}\ (\epsilon\,\gamma\,\delta^2 + 24\,\beta + 48\,\beta\,\epsilon) \\ 2\,\hat{a}^2\ (\epsilon\,\gamma\,\delta^2 + 24\,\beta + 64\,\beta\,\epsilon) \\ * \end{pmatrix},$$

$$\boldsymbol{K_0}^{(6)} = \begin{pmatrix} 2\,\delta\ (16\,\beta + 32\,\beta\,\epsilon + 4\,\epsilon\,\gamma + 8\,\epsilon^2\,\gamma - \delta^2\,\epsilon^2\,\gamma) \\ 4\,\hat{a}\,\delta\ (4\,\beta + 8\,\beta\,\epsilon + \epsilon\,\gamma) \\ 16\,\beta\,\delta^2 - 32\,\epsilon\,\gamma - 64\,\epsilon^2\,\gamma + 16\,\delta^2\,\epsilon^2\,\gamma - \delta^4\,\epsilon^2\,\gamma + 32\,\beta\,\delta^2\,\epsilon + 8\,\delta^2\,\epsilon\,\gamma \\ 2\,\delta\ (16\,\beta + 32\,\beta\,\epsilon + 4\,\epsilon\,\gamma + 8\,\epsilon^2\,\gamma - \delta^2\,\epsilon^2\,\gamma) \\ 4\,\hat{a}\,\delta\ (4\,\beta + 8\,\beta\,\epsilon + \epsilon\,\gamma) \\ 32\,\epsilon\,\gamma + 48\,\beta\,\delta^2 + 64\,\epsilon^2\,\gamma - 16\,\delta^2\,\epsilon^2\,\gamma + \delta^4\,\epsilon^2\,\gamma + 96\,\beta\,\delta^2\,\epsilon - 8\,\delta^2\,\epsilon\,\gamma + 2\,\delta^4\,\epsilon\,\gamma \\ * \end{pmatrix},$$

$$\boldsymbol{K_0}^{(7)} = \begin{pmatrix} 4\,\gamma\,\delta^2\,\epsilon^2 - 128\,\beta\,\epsilon - 64\,\beta \\ -32\,\hat{a}\,\beta\,\left(2\,\epsilon + 1\right) \\ -2\,\delta\,\left(16\,\beta + 32\,\beta\,\epsilon + 4\,\epsilon\,\gamma + 8\,\epsilon^2\,\gamma - \delta^2\,\epsilon^2\,\gamma\right) \\ 4\,\gamma\,\delta^2\,\epsilon^2 - 128\,\beta\,\epsilon - 64\,\beta \\ -32\,\hat{a}\,\beta\,\left(2\,\epsilon + 1\right) \\ -2\,\delta\,\left(48\,\beta + 96\,\beta\,\epsilon - 4\,\epsilon\,\gamma - 8\,\epsilon^2\,\gamma + \delta^2\,\epsilon^2\,\gamma + 2\,\delta^2\,\epsilon\,\gamma\right) \\ 4\,\gamma\,\delta^2\,\epsilon^2 + 8\,\gamma\,\delta^2\,\epsilon + 384\,\beta\,\epsilon + 192\,\beta \\ * \end{pmatrix},$$

$$\boldsymbol{K_0}^{(8)} = \begin{pmatrix} 32\,\hat{a}\,\beta\,\left(2\,\epsilon + 1\right) \\ 16\,\hat{a}^2\,\beta \\ 4\,\hat{a}\,\delta\,\left(4\,\beta + 8\,\beta\,\epsilon + \epsilon\,\gamma\right) \\ 32\,\hat{a}\,\beta\,\left(2\,\epsilon + 1\right) \\ 16\,\hat{a}^2\,\beta \\ 2\,\hat{a}\,\delta\,\left(\epsilon\,\gamma\,\delta^2 + 24\,\beta + 48\,\beta\,\epsilon - 2\,\epsilon\,\gamma\right) \\ -4\,\hat{a}\,\left(\epsilon\,\gamma\,\delta^2 + 24\,\beta + 48\,\beta\,\epsilon\right) \\ 2\,\hat{a}^2\,\left(\epsilon\,\gamma\,\delta^2 + 24\,\beta + 64\,\beta\,\epsilon\right) \\ * \end{pmatrix}, \qquad \boldsymbol{K_0}^{(10)} = \begin{pmatrix} 32\,\hat{a}\,\beta\,\left(2\,\epsilon + 1\right) \\ 16\,\hat{a}^2\,\beta \\ 4\,\hat{a}\,\delta\,\left(4\,\beta + 8\,\beta\,\epsilon + \epsilon\,\gamma\right) \\ 32\,\hat{a}\,\beta\,\left(2\,\epsilon + 1\right) \\ 16\,\hat{a}^2\,\beta \\ -4\,\hat{a}\,\delta\,\left(4\,\beta + 8\,\beta\,\epsilon + \epsilon\,\gamma\right) \\ 32\,\hat{a}\,\beta\,\left(2\,\epsilon + 1\right) \\ -16\,\hat{a}^2\,\beta \\ -4\,\hat{a}\,\left(\epsilon\,\gamma\,\delta^2 + 24\,\beta + 48\,\beta\,\epsilon\right) \\ 2\,\hat{a}^2\,\left(\epsilon\,\gamma\,\delta^2 + 24\,\beta + 64\,\beta\,\epsilon\right) \end{pmatrix},$$

$$\boldsymbol{K_0}^{(9)} = \begin{pmatrix} 4\,\gamma\,\delta^2\,\epsilon^2 - 128\,\beta\,\epsilon - 64\,\beta \\ -32\,\hat{a}\,\beta\,\left(2\,\epsilon + 1\right) \\ -2\,\delta\,\left(16\,\beta + 32\,\beta\,\epsilon + 4\,\epsilon\,\gamma + 8\,\epsilon^2\,\gamma - \delta^2\,\epsilon^2\,\gamma\right) \\ 4\,\gamma\,\delta^2\,\epsilon^2 - 128\,\beta\,\epsilon - 64\,\beta \\ -32\,\hat{a}\,\beta\,\left(2\,\epsilon + 1\right) \\ 2\,\delta\,\left(16\,\beta + 32\,\beta\,\epsilon + 4\,\epsilon\,\gamma + 8\,\epsilon^2\,\gamma - \delta^2\,\epsilon^2\,\gamma\right) \\ 4\,\gamma\,\delta^2\,\epsilon^2 - 128\,\beta\,\epsilon - 64\,\beta \\ 32\,\hat{a}\,\beta\,\left(2\,\epsilon + 1\right) \\ 4\,\gamma\,\delta^2\,\epsilon^2 + 8\,\gamma\,\delta^2\,\epsilon + 384\,\beta\,\epsilon + 192\,\beta \\ * \end{pmatrix}.$$

Appendix C

Inductors design validation in terms of stored energy

C.1 Design principle

In subsection 4.2.4, we have explained that estimating the magnetic energy that an inductor should be able to store is of prime importance in its design. Indeed, the equation (4.16) shows that, for a given application, the maximum energy $E_L^{\max}$ that an inductor can store is proportional to the area product $A_e A_w$. Thus, any uncertainty on the system behavior or on the excitation leads to not optimal components from an energetic point of view, and as a consequence in terms of mass and occupied volume as well. Therefore, a predictive model is required to proceed to a fine inductor design.

The design of the plate electrical analogue inductors in section 4.2 has been conducted without energetic considerations. Indeed, specifications in terms of mechanical excitation were not fixed. Now that the formulation in equation (3.46) has been validated by comparison with experiments in subsection 4.5.6, it is possible to use it to estimate the mechanical loads to which the plate can be subjected without saturating the network components. In other words, the present appendix marks a step towards the potential integration of piezoelectric network damping in industrial applications.

C.2 Application to the developed plate electrical analogue

C.2.1 Electrical currents and stored energies distributions

The resulting electrical current $i_L = \dot{q}_{z\mathrm{I}}$ flowing through each inductor can be computed thanks to the values of the other electrical currents of the unit cell in figure 2.14:

$$\left\{\begin{array}{l} i_L = \dot{q}_{z\mathrm{B}} + \frac{\hat{a}}{2}\,\dot{q}_{\theta\mathrm{B}} \\ i_L = \dot{q}_{z\mathrm{L}} + \frac{\hat{a}}{2}\,\dot{q}_{\theta\mathrm{L}} \\ i_L = \dot{q}_{z\mathrm{R}} - \frac{\hat{a}}{2}\,\dot{q}_{\theta\mathrm{R}} \\ i_L = \dot{q}_{z\mathrm{T}} - \frac{\hat{a}}{2}\,\dot{q}_{\theta\mathrm{T}} \end{array}\right. \quad \Longrightarrow \quad i_L = \frac{1}{4}\left[\dot{q}_{z\mathrm{B}} + \dot{q}_{z\mathrm{L}} + \dot{q}_{z\mathrm{R}} + \dot{q}_{z\mathrm{T}} + \frac{\hat{a}}{2}\,\left(\dot{q}_{\theta\mathrm{B}} - \dot{q}_{\theta\mathrm{T}} + \dot{q}_{\theta\mathrm{L}} - \dot{q}_{\theta\mathrm{R}}\right)\right]. \tag{C.1}$$

The electrical currents i_L FRFs flowing through the network inductors are frequency-dependent because of the piezoelectric coupling. Then, the maximum electrical current value over the considered frequency range of interest is

$$I_L^{\max} = \underset{[f_{\min}:f_{\max}]}{H_\infty}\left(i_L\right) = \mathrm{Max}\left(\left|i_L\left(2\pi f\right)\right|, f_{\min} \leq f \leq f_{\max}\right). \tag{C.2}$$

Consequently, the value of $I_L^{\max}$ allows estimating the electrical energy $E_L^{\max}$ that the component should be able to store. We recall that the maximum magnetic energy that an inductive component can store is

$$E_L^{\max} = \frac{1}{2}\,L\,(I_L^{\max})^2\,. \tag{C.3}$$

C.2.2 Application around the first plate mode

The inductors we have produced in section 4.2 are RM 10 core components, whose specifications are extracted from manufacturer's data and recorded in table 4.2. Their filling factor is $k_u = 47$ %. Moreover, the maximum electrical current density $J^{\max}$ is about 5 A/mm^2. Finally, we want to avoid saturating the component, such as illustrated in figure 4.3, so the maximum admissible density flux $B^{\max}$ is set at a tenth of the standard saturation limit of 0.3 T for ferrite materials. For a harmonic excitation, by applying the following equation which has already been derived in subsection 4.2.4:

$$E_L^{\max} = \frac{1}{2}\,k_u k_f\,A_e A_w\,J^{\max} B^{\max}, \tag{C.4}$$

we estimate that the produced inductors can store an energy of nearly 170 μJ.

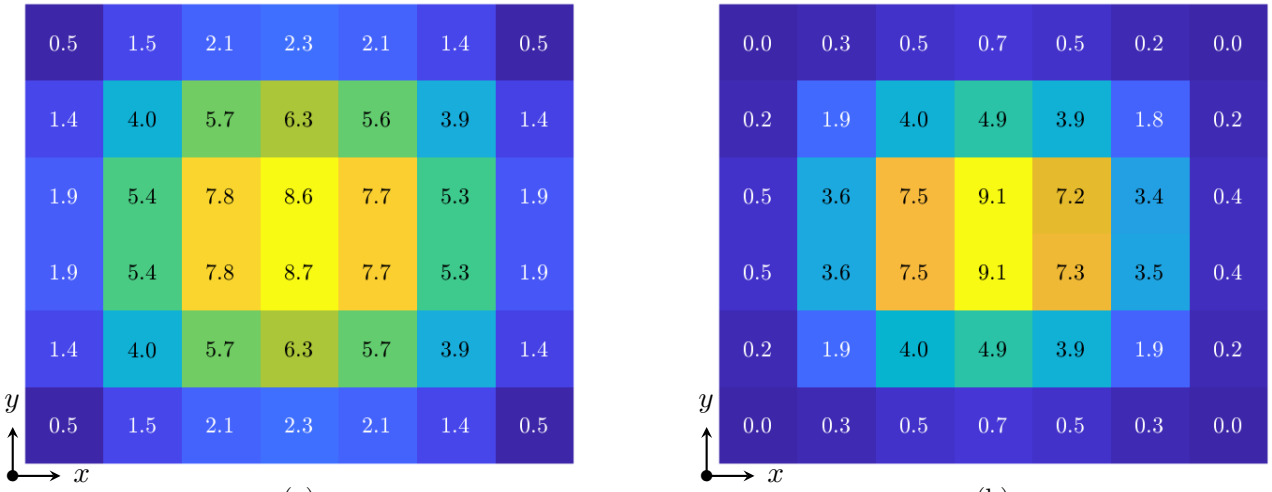

Figure C.1: Simulated distribution of the (a) maximum electrical currents $I_L^{\max}$ (in μA) and of the (b) maximum energy $E_L^{\max}$ (in pJ) to be stored in the plate electrical analogue for a given excitation.

We propose to compare this value to the energy that should be stored in the inductors for a harmonic nominal effort between $f_{\min} = 90$ Hz and $f_{\max} = 91$ Hz of 1 N of amplitude. It is applied at the location highlighted in figure 3.4. The coupled model predicts that the corresponding driving-point deflection is 23 μm. Besides, the same parameters as in section 4.5 are considered. Even though the inductance values could be numerically optimized to enhance the damping performance, the corresponding modifications are small enough that they would barely alter the digression to come.

The distribution of $I_L^{\max}$ is represented in figure C.1a. It is similar to the the first plate mode, which is consistent with the network being a plate electrical analogue. The distribution of $E_L^{\max}$ is then represented in figure C.1b. The values are much lower than the limit we have fixed of 170 μJ. Note that the distribution does not reflect the conditions over which the experiments recorded in this manuscript have been conducted. Indeed, the mechanical excitation which was generated by the shaker was not a harmonic signal, but a low-level pseudo-random white noise signal.

Moreover, the distribution is not homogeneous over the network though the inductors share the same characteristics. This example illustrates that, even for periodic structures, the network inductors could be produced differently from one another for a harmonic excitation. In other words, smaller, and thus lighter magnetic cores could have been considered to damp the first plate mode, especially for cells near the network boundaries. Note however that designing small passive components with high quality factors might be challenging.

Appendix D

Publications

D.1 Journal papers

- R. Darleux, B. Lossouarn, J.-F. Deü, "Passive self-tuning inductor for piezoelectric shunt damping considering temperature variations", Journal of Sound and Vibration, vol. 432, pp. 105-118, 2018

- R. Darleux, B. Lossouarn, J.-F. Deü, "Broadband vibration damping of non-periodic plates by piezoelectric coupling to their electrical analogues", Smart Materials and Structures, vol. 29, no. 5, p. 054001, 2020

D.2 Conference proceedings

- *Acknowledgments in* O. Robin, A. Berry, N. Atalla, M. Aucejo, B. Lossouarn, L. Rouleau, J.-F. Deü, C. Marchetto, L. Maxit, "Setting up plane and thin panels with representative simply supported boundary conditions: comparative results and applications in three laboratories", Inter-Noise 2018, Chicago (USA)

- R. Darleux, B. Lossouarn, J.-F. Deü, "Effect of temperature on the tuning of a piezoelectric resonant shunt composed of variable inductance or variable capacitance", ISMA 2018, Leuven (Belgium)

- L. Rouleau, B. Lossouarn, R. Darleux, J.-F. Deü, “Comparison of damping performances of constrained viscoelastic layers and passive piezoelectric networks”, Inter-Noise 2019, Madrid (Spain)
- R. Darleux, B. Lossouarn, J.-F. Deü, “Broadband vibration damping of a non-periodic plate by piezoelectric coupling to its electrical analogue”, SMART 2019, Paris (France)

D.3 Posters and presentations

- “Plate electrical analogue for multimodal energy transfer”, JNRSE 2018, Besançon (France)
- “Amortissement vibratoire multimodal de plaques non périodiques par couplage à leurs réseaux piézoélectriques analogues”, JJCAB 2019, Besançon (France)
- “Amortissement vibratoire par couplage à un réseau piézoélectrique analogue”, Journée F2M janvier 2020, Gif-sur-Yvette (France)

le cnam

Robin DARLEUX

Development of analogous piezoelectric networks for the vibration damping of complex structures

HESAM UNIVERSITÉ

Résumé: **Cette thèse de doctorat s'intéresse au développement de réseaux piézoélectriques analogues pour l'amortissement vibratoire de structures complexes. L'objectif est d'atténuer les vibrations des modes de plus grandes longueurs d'ondes de structures qu'on recouvre de patchs piézoélectriques, afin de les coupler à des réseaux qui présentent des propriétés identiques de propagation d'onde. Pour ce faire, on détaille une méthode permettant de définir l'analogue électrique de toute structure mécanique. On applique cette méthode à des cas standards de propagation d'ondes mécaniques pour former une bibliothèque de cellules électriques analogues. Le cas d'une plaque rectangulaire recouverte de patchs piézoélectriques est ensuite traité. On assemble un réseau analogue à l'aide d'éléments de la bibliothèque précédemment obtenue. Un dimensionnement adéquat des composants magnétiques du réseau assure qu'il soit de nature purement passive. La connexion de la plaque à son réseau analogue résulte en un amortissement multimodal, ce qui illustre l'efficacité de cette solution d'amortissement. En parallèle, un modèle éléments finis d'une structure couplée à un réseau électrique par des patchs piézoélectriques est développé. La comparaison entre résultats expérimentaux et simulés permet de valider ce modèle. Il est par conséquent utilisé pour finalement aborder l'amortissement large bande de structures complexes à travers des exemples numériques de plaques complexes et de structures à une courbure. Les résultats sont prometteurs, puisqu'ils illustrent la possibilité d'appliquer à des structures complexes l'amortissement multimodal par couplage à des réseaux piézoélectriques analogues purement passifs.**

Mots-clefs: Couplage piézoélectrique, Amortissement vibratoire multimodal, Réseau analogue passif, Structures complexes, Analogie électromécanique directe, Modélisation éléments finis, Comparaisons calculs-essais.

Abstract: **This doctoral thesis focuses on the development of analogous piezoelectric networks for broadband damping of complex structures. The objective is to damp the modes of largest wavelengths of mechanical structures, which are covered by piezoelectric patches in order to couple them to fully passive electrical networks which exhibit similar wave propagating properties. To do so, we first propose a method to derive the electrical analogue of any mechanical structure. It is applied to create a library of elementary analogues that represent classical wave propagation cases. Then, the electrical analogue of a rectangular plate covered by piezoelectric transducers is assembled with elements from the library. Following design methods of passive inductors and transformers, the produced network is fully passive. Vibration tests highlight the mitigation efficiency of the concept when the plate is connected to its analogous network. Meanwhile, we develop a finite element model of a structure covered with thin piezoelectric transducers connected to a lumped electrical network. Comparisons with experiments validate this model. Thus it is used to finally investigate the achievable performance of piezoelectric network damping applied to complex structures, such as complex plates and single curved structures numerical examples. Results are promising: they highlight it might be possible to develop fully passive piezoelectric analogous networks to damp vibrations of complex structures.**

Keywords: Piezoelectric coupling, Broadband vibration mitigation, Passive analogous network, Complex structures, Direct electromechanical analogy, Finite element modeling, Experimental comparisons.